THE ISO HANDBOOK

Volume V:

SWS –
The Short Wavelength Spectrometer

Kieron Leech[1], Do Kester[2], Russell Shipman[2], Douwe Beintema[2], Helmut Feuchtgruber[3], Ana Heras[1], Rik Huygen[4], Fred Lahuis[2], Dieter Lutz[3], Patrick Morris[5], Peter Roelfsema[2], Alberto Salama[1], Stephan Schaeidt[3], Edwin Valentijn[2], Bart Vandenbussche[4], Ekkehard Wieprecht[3] and Thijs de Graauw[2].

SAI/2000-008/Dc, Version 2.0.1

June, 2003

[1] ISO Data Centre, Science Operations and Data Systems Division, Research and Scientific Support Department of ESA, Villafranca del Castillo, P.O. Box 50727, E-28080 Madrid, Spain
[2] Space Research Organisation of The Netherlands, P.O. Box 800, NL-9700 AV Groningen, The Netherlands
[3] Max-Planck-Institut für extraterrestrische Physik, Postfach 1312, D-85741 Garching, Germany
[4] Instituut voor Sterrenkunde, Katholieke Universiteit Leuven, Celestijnenlaan 200B, B-3001 Heverlee, Belgium
[5] Space Research Organisation of The Netherlands, Sorbonnelaan 2, NL-3584 CA Utrecht, The Netherlands

Document Information

Document:	The ISO Handbook
Volume:	V
Title:	SWS – The Short Wavelength Spectrometer
Reference Number:	SAI/2000-008/Dc
Issue:	Version 2.0
Issue Date:	June 2003
Authors:	K. Leech, D. Kester, R. Shipman et al.
Editors:	T. Müller, J. Blommaert & P. Garca-Lario
Web-Editor:	J. Matagne

Document History

The ISO Handbook, Volume V: SWS – The Short Wavelength Spectrometer is based on the following documents:

- The *ISO Short Wavelength Spectrometer Observer's Manual*, K. Leech (with contributions from Th. de Graauw, the SWS Instrument Dedicated Team & S. Sidher, based on V2.0 produced by K.A. van der Hucht, D. Lutz and the SWS consortium), Issue 3.0, July 22, 1996.
- The *SWS Instrument & Data Manual*, K. Leech (with contributions from the SWS Instrument Dedicated Team and the SWS Instrument Support Team), Issue 1.0, SAI/98-095/Dc, November 3, 1998.
- Earlier versions of *The ISO Handbook on SWS – The Short Wavelength Spectrometer* (previously called Volume VI), SAI-2000-008/Dc.
- All other documents listed in the Bibliography.

Document Change Record

Date	Revision	Comments
Jan 2000	Version 1.0	Derived from SWS Instrument Data Manual
Jan 2001	Version 1.1	update
Jul 2001	Version 1.2	update to OLP 10 standard
Apr 2002	Version 2.0	update, now Volume V
Jun 2003	Version 2.0.1	minor editorial changes, printed version

Acknowledgements

The Short Wavelength Spectrometer was a joint effort by:

- Space Research Organisation of the Netherlands in Groningen (SRON-G) and Utrecht (SRON-U)
- Max Planck Institut für extraterrestrische Physik (MPE), Garching, Germany.

With contributions from:

- Instituut voor Sterrenkunde, Katholieke Universiteit Leuven (KUL), Belgium
- Steward Observatory, University of Arizona, AZ, USA
- Air Force Research Laboratory (AFRL), Hanscom AFB, MA, USA.

Many other groups contributed to the success of this instrument. In particular:

- The ISO Data Centre (IDC) in Villafranca, Spain
- Astronomical Institute *Anton Pannekoek*, University of Amsterdam (UvA), The Netherlands
- Kapteyn Astronomical Institute, University of Groningen (RUG), The Netherlands
- Leiden Observatory, University of Leiden, The Netherlands.

The SWS Proposal Team

The ISO Short Wavelength Spectrometer proposal team consisted of:

Principal Investigator

Thijs de Graauw	SRON-G

Co-Investigators

Douwe Beintema	SRON-G
Siegfried Drapatz	MPE
Miller Goss	RUG
Gerhard Haerendel	MPE
Leo Haser	MPE
Karel van der Hucht	SRON-U
Theo Kamperman	SRON-U
Henny Lamers	SRON-U
Paul Wesselius	SRON-G
Jan Wijnbergen	SRON-G

Instrument Development Team

Hans Imhof	SRON-U
Willem Luinge	SRON-G
Friedhelm Melzner	MPE
Ger Ploeger	SRON-G
Jacob Stöcker	MPE
Jan van Rooyen	SRON-U
Klaas Wildeman	SRON-G

Collaborators

Herman van Agthoven	TPD, Delft
Reinhard Genzel	UCB, USA
Wim Werner	TPD, Delft

The SWS Instrument Consortium

Principal Investigator

Thijs de Graauw	SRON-G

Scientific Support

Thijs van der Hulst	RUG
Steve Price	AFRL/VSBC
Reinhard Genzel	MPE
Dieter Lutz	MPE
Henny Lamers	SRON-U
Xander Tielens	SRON-G
Ewine van Dishoeck	Leiden
Rens Waters	UvA
Christoffel Waelkens	KUL

The Instrument Hardware Development Team

Herman van Agthoven (TPD-Delft)	FPU mechanical design
Lothar Barl (MPE)	Detector evaluation
Albert-Jan Boonstra (SRON-G)	FPU AIT
Stephan Czempiel (MPE)	FP manufacture
Carel van Dijkhuizen (SRON-U)	Warm electronics
Siegfried Drapatz (MPE)	Instrument development support
Henk Doedens (SRON-G)	Harness, amp design
Jaap Evers (SRON-G)	Ground support equipment, AIV, PA
Martin Frericks (SRON-U)	EMC, signal chain development
Werner Goebel (MPE)	FP development
Piet de Groene (SRON-U)	EMC, warm electronics manager
Leo Haser (MPE)	MPE project leader, FP developer
Wim Horinga (SRON-G)	FP test assistant
Herman Jacobs (SRON-U)	Consortium PA
Gerd Jakob (MPE)	ILT cryogenics
Norbert Kamm (MPE)	ILT cryogenics
Theo Kamperman (SRON-U)	SWS project manager
Reinhard Katterloher (MPE)	SWS test manager
Daniel Kussendrager (SRON-G)	PI assistant
Siep van der Lei (SRON-G)	ILT assistant
Rien van der Linden (SRON-G)	ILT testing
Hans Loidl (MPE)	Detector testing
Willem Luinge (SRON-G)	Detector evaluation, detector block design
Friedhelm Melzner (MPE)	FP development
Bernhard Merz (MPE)	Detector testing
Jörg Niekerke (MPE)	Test equipment support
Duc van Nguyen (SRON-G)	FPU integration, Int. Amp. integration
Uwe Pagel (MPE)	FP development
Günther Pfaller (MPE)	FP manufacture
Ger Ploeger (SRON-G)	Scanner/detector block designer

Peter Reiss (MPE)	Test equipment support
Christel Schäfer (MPE)	FP/ILT documentation
Kees Smoorenburg (TPD-Delft)	FPU opto-mechanical structure manager
Heinrich Späth (MPE)	FP development
Wilhelm. Stöberl (MPE)	FP testing
Jacob Stöcker (MPE)	FP mechanical design
Ulrich Thiele (MPE)	Test equipment support
Huib Visser (TPD-Delft)	FPU opto-mechanical design
Johan Wensink (SRON-G)	Detector testing
Jan Wijnbergen (SRON-G)	FPU optical design
Klaas Wildeman (SRON-G)	FPU manager
Erick Young (Steward Obs.)	FP detectors
Frans Zwart (SRON-U)	Warm electronics

The SWS Test, Calibrations, Operations Team

Mario van den Ancker (UvA)	Line profile observations
Otto Bauer (MPE)	Operations leader 1992–2001
Harald Baumgartner (MPE)	Computer support
Kurt Becher (MPE)	Software development
Douwe Beintema (SRON-G)	SIDT, beam profiles
Hilco Bekenkamp (SRON-G)	Software development
Geert Bex (KUL)	Software development
Danny Boxhoorn (SRON-G)	SIDT
Jacqueline Coté (SRON-G)	SWS Observation Time Estimator (SOTE)
Helmut Feuchtgruber (MPE)	SIDT leader 1996–1997, FP
Menne Glas (SRON-G)	Software
Norbert Heinecke (MPE)	Software, Computer support
Ana Heras (ESA)	SIDT, Trend Analysis, calibration
Sacha Hony (UvA)	SWS-IA feedback
Rik Huygen (KUL)	Author CoCo
Kay Justtanont (SRON-G)	SWS-IA feedback
Do Kester (SRON-G)	Software development, λ cal., system modelling
Jan Koornneef (SRON-G)	Calibration support, spectral line catalog
Dietmar Kunze (MPE)	ISOSDC, Software
Fred Lahuis (SRON-G)	SIDT, Software
Kieron Leech (ESA)	SIDT, Documentation
Rosario Lorente (INSA)	SIDT, Beam profiles
Dieter Lutz (MPE)	ISOSDC, Calibration, line profiles
Patrick Morris (SRON-U)	SIDT, Photometric calibration
Georg Orthuber (MPE)	Computer support
Sabine Osterhage (MPE)	Software development, Computer support
Dimitra Rigopoulou (MPE)	SWS-IA feedback
Peter Roelfsema (SRON-G)	SIDT leader 1995–1996
Dirk Rosenthal (MPE)	SWS-IA feedback
Alberto Salama (ESA)	SIDT leader 1997–1998, beam profiles
Stephan Schaeidt (MPE)	SIDT, Photometric calibration
Berhard Scheiner (MPE)	Administrative Support
Karla Seidenschwang (MPE)	Software development
Russell Shipman (SRON-G)	DIDAC, Photometric calibration
Nico Sijm (SRON-U)	Software development
Henrik Spoon (MPE)	Code development

Michael Steinmayer (MPE)	RTA/QLA
Eckhard Sturm (MPE)	Software, ISOSDC
Edwin Valentijn (SRON-G)	SIDT, (pre-)flight cal., SWS development
Bart Vandenbussche (KUL)	SIDT, RSRF calibration
Karel van der Hucht (SRON-U)	Spectral line catalog
Aprajita Verma (MPE)	ISOSDC
Binne Viersen (SRON-G)	Software
Paul Wesselius (SRON-G)	Operations leader 1987–1992
Ekkehard Wieprecht (MPE)	SIDT, Software
Erich Wiezorrek (MPE)	RTA/QLA
Issei Yamamura (SRON-G)	SWS-IA feedback

Contents

List of Figures

List of Tables

Chapter 1

Introduction

1.1 Purpose

The SWS Handbook is one in a series of five[1] documents that explain the operations of the Infrared Space Observatory (ISO) and its four instruments, the data received from the instruments and the processing carried out on the data. Volume I gives an overview of the entire ISO mission and it explains the operations of the ISO satellite while the remaining four explain the individual instruments (CAM, LWS, PHT and SWS). The SWS document describes data processed with version 10 of the Off-Line Processing (OLP) system, available from the ISO Data Archive (IDA) at:

`http://www.iso.vilspa.esa.es/`

The Explanatory Documentation provides information relevant to the ISO data user, concerning the satellite, the instruments and the observational and technical data products. It is a comprehensive description of systems and parameters relevant to ISO data products, how these products were derived, and what are the known limitations. This information will enable the SWS data users to do further data analysis beyond the scope of the automatic Off Line Processing (OLP).

1.2 Structure

The SWS Handbook is divided into 9 chapters, each of which describe some aspects of the instrument. It is intended that the handbook can be read from cover to cover, although some forward references were necessary.

An overview of the SWS instrument is given in Chapter 2. In Chapter 3 the modes in which SWS could observe are presented with some examples of resulting data products. The wavelength calibration is described in Chapter 4. Chapters 5 and 6 present the photometric calibration; the latter concerns the so-called 'Post-Helium' Phase of the mission. The pipeline, also called the Off-Line Processing system (OLP), is a system where the contents of the previous chapters is moulded into software. The pipeline and the data products are discussed in Chapter 7, with additional details in Appendix A.

Pointing issues and beam profiles are given in Chapter 8. Finally, the last Chapter 9 addresses several instrumental effects and caveats the user should be aware of that bear upon the understanding of SWS but could not find a logical place in any of the other chapters.

In addition to the 9 chapters there are several appendices, describing in detail the data products, calibration concerns, the uplink history, acronyms and symbols used throughout the handbook.

[1] Originally six documents were planned with Volume I on the *ISO Mission* and II on the *ISO Satellite* but both have now been merged in Volume I in Version 2.0.

Typographical conventions

- Programmes (within OSIA or ISAP) are written in small caps. Eg. DYNADARK.
- Keywords within (FITS) products are written in capital teletype like `SWAASTAT`.

1.3 How to Contact Us

Should you need further help from ESA concerning ISO or the instrument you can:

1. Send a question to the ISO helpdesk at: `helpdesk@iso.vilspa.esa.es`.
2. Look at the SWS web pages, available from:
   `http://www.iso.vilspa.esa.es/` → `ISO Explanatory Library` → `SWS`.

American observers can also obtain information from IPAC by:

1. Sending a question to the IPAC helpdesk: `iso@ipac.caltech.edu`.
2. Looking at the IPAC ISO WWW page:
   `http://www.ipac.caltech.edu/` → `ISO`.

The Short Wavelength Spectrometer teams maintain three websites through which they may be contacted. The Dutch ISO Data Analysis Centre (DIDAC) at SRON, Groningen has its home page at:

`http://www.sron.rug.nl/didac/`

The ISO Spectrometer Data Centre at the Max-Planck-Institut für extraterrestrische Physik (MPE), Garching, Germany has a web page at:

`http://www.mpe-garching.mpg.de/iso/`

and the Catholic University at Leuven, Belgium, maintains the ISO SWS consortium homepage at:

`http://sws.ster.kuleuven.ac.be/`

Specific documents of interest to SWS users are cited in this Handbook and can be accessed via the web at the URLs given in the Bibliography.

There are two software packages specifically written to further process SWS data beyond the standard pipeline products: the Observers SWS Interactive Analysis (OSIA) and the ISO Spectral Analysis Package (ISAP) for SWS and LWS Auto Analysis Results (AAR). Both these packages can be accessed and retrieved from the ISO Web site:

`http://www.iso.vilspa.esa.es/` → `ISO Data Analysis Software`.

Documentation is also available at this web site to guide you in the reduction of your data using these packages.

1.4 SWS Publications

1.4.1 Acknowledgements and guidelines

Any paper published based on **ISO data** should contain the following text, as a footnote to the title:

Based on observations with ISO, an ESA project with instruments funded by ESA Member States (especially the PI countries: France, Germany, the Netherlands and the United Kingdom) and with the

participation of ISAS and NASA.

Should the journal in question not permit footnotes to the title, the above text should appear as a footnote the first time ISO is mentioned.

The preferred reference for the ISO mission is:

The Infrared Space Observatory (ISO) mission, Kessler, M.F. et al. 1996, A & A 315, L27

Any paper published based on **SWS data** should acknowledge the instrument with the following reference:

Observing with the ISO Short Wavelength Spectrometer, de Graauw T. et al. 1996, A&A 315, L49

If you use OSIA to reduce your SWS data please write in the acknowledgements:

OSIA is a joint development of the SWS consortium. Contributing institutes are SRON, MPE, KUL and the ESA Astrophysics Division.

If you use ISAP to reduce your SWS or LWS data please write in the acknowledgments:

The ISO Spectral Analysis Package (ISAP) is a joint development by the LWS and SWS Instrument Teams and Data Centres. Contributing institutes are CESR, IAS, IPAC, MPE, RAL and SRON.

1.4.2 Inventory of publications

In order to offer a complete bibliographic information to the ISO Data Archive users, we try to keep track of all publications involving ISO data, and of all observations used for these publications. As a result, in IDA next to any selected observation, the button 'Articles' provides the references of the publications involving this particular observation and a link to their Astrophysics Data System (ADS) entry[2]. Your contribution in this matter can greatly help keeping an information as comprehensive as possible and we therefore ask you to kindly provide the following information for each of your publications:
- complete reference of the article (or preprint)
- list of TDT numbers and instrument modes of the observations that you have exploited for the publication.

You can send the information either by e-mail to:
helpdesk@iso.vilspa.esa.es
or by normal mail to:
ISO Project Scientist
(ISO Preprints)
ESA Satellite Tracking Station
Villafranca del Castillo
P.O. Box 50727
28080 Madrid

[2] `http://adswww.harvard.edu/`

Chapter 2

Instrument overview

This chapter describes the mechanical design, optical layout and detector systems of the SWS instrument.

2.1 General Introduction to SWS

The Short Wavelength Spectrometer (SWS, see Figure 2.1) on board ESA's Infrared Space Observatory (ISO) provided medium and high spectral resolution in the wavelength region 2.38–45.2 μm. Its two largely independent grating spectrometers had a spectral resolution of $R \approx 1000$–2000, corresponding to a velocity resolution of $\Delta v \approx 150$–300 km/s. By inserting Fabry-Pérot (FP) filters, one for the range 15–26 μm (with capability down to 11.4 μm at reduced resolution) and the other for the region 26–35 μm (with capability to 44.5 μm at reduced sensitivity), the resolution could be increased to $R \approx 30,000$, $\Delta v \approx 10$ km/s.

The SWS wavelength range is of great scientific interest, not only because it is here that cool objects in the temperature range 80–1500 K radiate the bulk of their energy, but also because of its rich variety of atomic, ionic, molecular and solid-state spectral features. These provide unique and excellent tools for studies of the physical and chemical processes in the universe, especially of those regions optically hidden by interstellar dust. The SWS spectral resolution allows kinematic processes to be probed in a variety of objects ranging from nuclei of galaxies to planetary atmospheres. SWS made 3763 scientific observations during the lifetime of ISO, or 13% of the total number. These SWS observations lasted a total of 2694 hours, or 25% of the observing time of ISO. After helium depletion some 400 additional observations were done with SWS band 1 only. See Chapter 6.

Astronomers observed with ISO using what were known as Astronomical Observation Templates (AOT). There were four science templates for SWS, each devoted to a different sort of observation. Users filled in a template with the expected fluxes of their target, the wavelength range or lines they wanted to observe etc, and the logic that ran behind the template generated the necessary instrumental parameters and commands. There was one AOT to observe the entire SWS spectral range at low resolution (SWS01), another was for observing specific spectral lines (SWS02), a third to observe spectral ranges (SWS06), and a final one to observe targets using the FP (SWS07). As well as these four AOTs, a more flexible system was designed for calibration, the Calibration Uplink System (CUS). The CUS was not normally used by observers. The AOTs are discussed in detail in Chapter 3.

Data obtained by SWS was telemetered down by the satellite and collected at the ground station. For each observation several data files were generated containing raw data, instrument status, pointing information etc. The file containing the detector readouts in time order, was called the Edited Raw Data (ERD) file, edited because it was a reordered subset of the telemetry stream sent down from the satellite. The raw data was processed by an automatic pipeline to two further reduction levels. The first stage is known as Standard Processed Data (SPD). It contains the uncalibrated signal and pertaining wavelengths, still

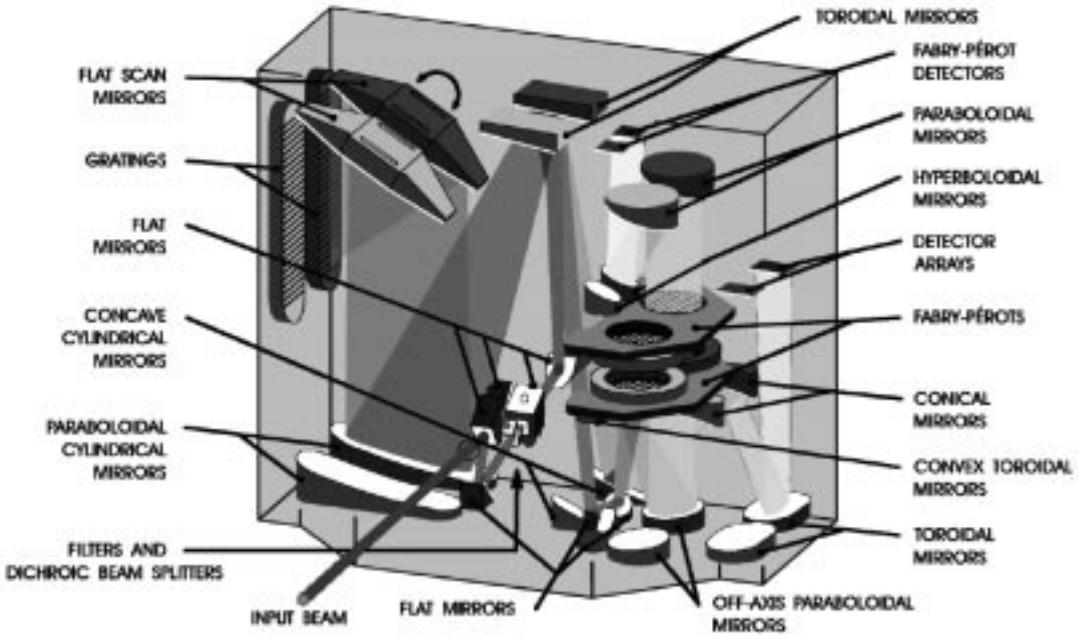

Figure 2.1: *The SWS instrument. Physically it was small, about the size of an overhead projector, and hung, upside down, just under ISO's primary mirror. It was inside the cryostat, together with the three other instruments.*

in time order. The second stage is called Auto-Analysis Results (AAR). Data at the AAR level has been processed to a level where it can normally be used for scientific analysis (flux versus wavelength), although further processing with interactive tools, like OSIA, generally improve the quality.

2.2 Instrument Design

Figure 2.1 gives an impression of the layout of the SWS, while Figure 2.2 shows an expanded view of the optical systems. Light from the telescope was reflected into the SWS by the ISO pyramidal mirror (not shown in Figures 2.1 or 2.2). The SWS had three entrance apertures, each with its own dichroic beam splitter feeding the Short Wavelength (SW) section and the Long Wavelength (LW) section. The entrance aperture appropriate to the wavelength range of the requested observation was automatically selected by specific pointing of the ISO satellite, with the relationship between aperture and wavelength ranges given in Table 2.1. A four-position selection mechanism permitted opening of any one of these apertures or blocking of all three – see Section 8.2.1 for further details.

Each grating had its own scanning mechanism, enabling the use of both parts of the spectrograph at the same time, albeit through the same aperture. Changing the wavelength of light falling on the detectors was achieved by rotating the flat mirrors close to each grating in discrete scan steps. A qualification model of one of the scanners is shown in Figure 2.3. (Their location is shown in Figures 2.1 and 2.2).

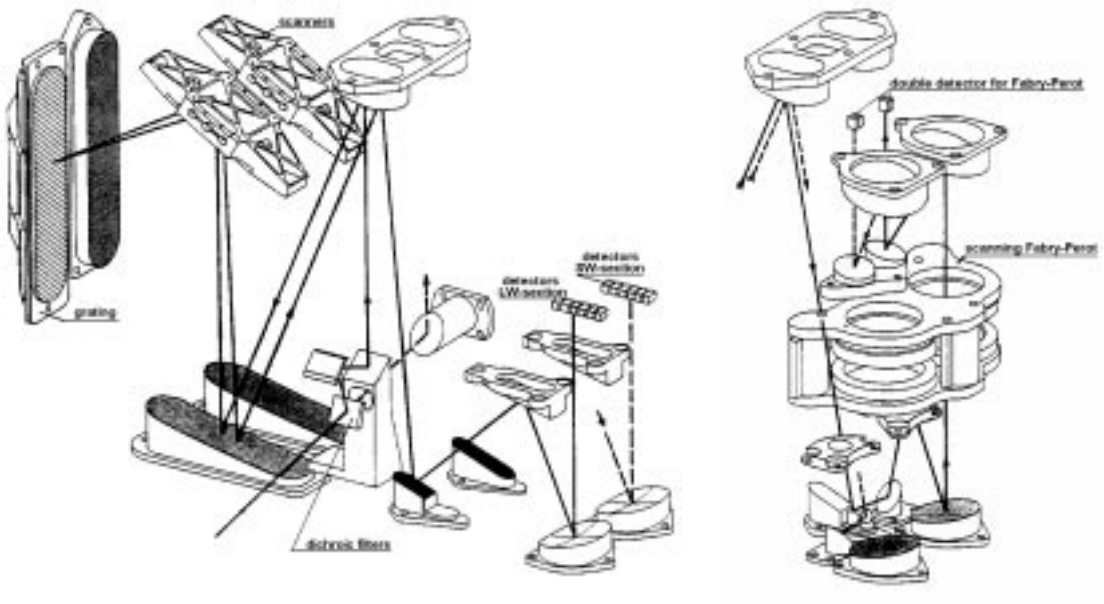

Figure 2.2: *Internal layout of the Short Wavelength Spectrometer (SWS). On the left is the light-path for grating observations, while on the right an abbreviated light-path for Fabry-Pérot observations is shown.*

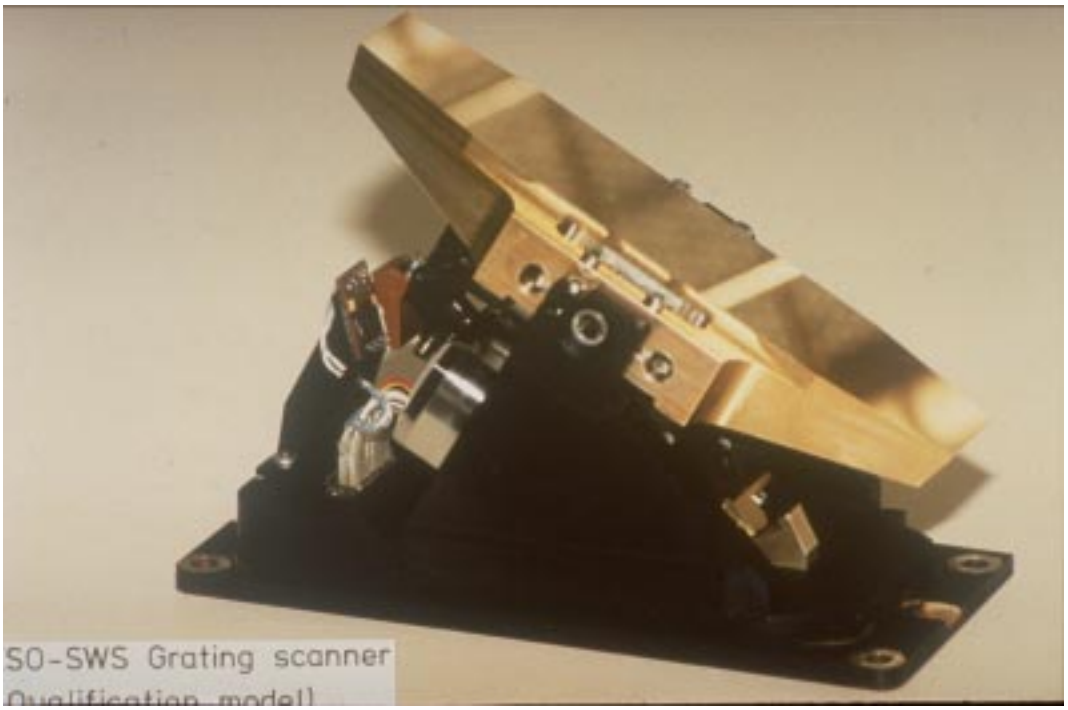

Figure 2.3: *A qualification model of one of the SWS grating scanners.*

After reflection from the gratings, the light more or less retraced its path and, by means of small-diameter re-imaging relay optics, the high resolution spectral image of each wavelength band was re-imaged onto the detector block. These relay optics have various functions:

- They relayed the high resolution image to a more easily-accessible location on the detector block.
- They changed the relative opening of the beam to a value that was optimised to the detector dimensions.
- They enabled efficient straylight rejection.

To use the FPs, the radiation returning from the LW grating was collimated again, transmitted through a tunable FP interference filter and imaged onto separate detectors in the detector block. This second light path is also shown in Figure 2.2. The two FPs were mounted on a single pair of parallel plates. Their separation and parallelism could be varied by changing the currents in three pull coils.

2.3 The Wavelength Range Covered

The design of the SWS instrument subdivides the 2.38–45.2 μm wavelength range into several different bands. There are 12 grating bands and, for the reduced FP spectral range, 5 FP bands. Sometimes these bands are also referred to as AOT bands. The bands, listed in Table 2.1, are combinations of detector array, aperture and grating orders such that for each band its detector array sees a unique order of light, and hence a unique wavelength. Therefore, a request to observe one wavelength of light defines which array, aperture and grating order to use. At any given time, the astronomical source of interest to the observer was centred on one and only one of the three SWS apertures, feeding light on many, or all, of the 52 detector elements via the two rotatable scanning mirrors. While it was possible to find scanner settings such that all of the detector arrays would contain valid data, the instrument was normally operated such that only one or two of the detector arrays received *one* order of the grating spectrometer, the other four or five receiving a mixture of orders (and hence producing no valid data). However, the observer or archive user will receive data from all 52 detectors.

2.4 Signal Detection

2.4.1 Design of the signal chain

The SW and LW gratings are associated with 4 different detector arrays of 12 elements each, and the 2 SWS Fabry-Pérots are associated with 2 double detectors (only one of each pair being used to gather valid data). More information on the detectors is given in Table 2.1. All $4 \times 12 + 2 \times 2 = 52$ detectors are operated simultaneously. The InSb, the Si:As (BIBIB) and the Si:Ga detectors are operated at a temperature of 4 K, which is the temperature of the spectrometer unit. The Si:Sb detectors for the FP are heated to 10 K and the Ge:Be detectors are cooled to 2.5 K by a thermal strap to the helium tank of the cryostat.

Except for the InSb photo-diodes, the detectors are photo-conductors that require a finite bias voltage. The detectors are connected to discrete integrating-amplifier chains. The first amplifier stages are heated-JFET buffer amplifiers located close to the detectors. The remaining electronics are located in the warm amplifier box in the service module of the satellite.

A schematic diagram of the detector electronics is shown in Figure 2.6. The detector current charges the small capacitor formed by the finite capacitance of the JFET gate and of the electrical leads between the detector and the gate. The resulting voltage ramp is amplified and digitised, to be read out 'non-destructively'. Every 1, 2 or 4 seconds (selected by the AOT logic) the pre-amplifier is reset by removing

Table 2.1: *Detector definition for the SWS bands*

Sect.[1]	Band	Order	Aper.	Filter[2]	Area[3] [″×″]	Detector type	Detector number	Wavelength[4] [μm]	Resolution[5] ($R = \lambda/\Delta\lambda$)	L[6] AOT
SW	1A	4	1	Al_2O_3	14–20	InSb	1 – 12	2.38 – 2.60	1870 – 2110	756
SW	1B	3	1	Al_2O_3	14–20	InSb	1 – 12	2.60 – 3.02	1470 – 1750	1043
SW	1D	3	2	LiF	14–20	InSb	1 – 12	3.02 – 3.52	1750 – 2150	1282
SW	1E	2	2	LiF	14–20	InSb	1 – 12	3.52 – 4.08	1290 – 1540	867
SW	2A	2	2	LiF	14–20	Si:Ga	13 – 24	4.08 – 5.30	1540 – 2130	2115
SW	2B	1	2	LiF	14–20	Si:Ga	13 – 24	5.30 – 7.00	930 – 1250	1377
SW	2C	1	3	SrF_2	14–20	Si:Ga	13 – 24	7.00 – 12.0[7]	1250 – 2450	4276
LW	3A	2	1	Al_2O_3	14–27	Si:As[8]	25 – 36	12.0 – 16.5	1250 – 1760	2047
LW	3C	2	2	LiF	14–27	Si:As[8]	25 – 36	16.5 – 19.5	1760 – 2380	1879
LW	3D	1	2	LiF	14–27	Si:As[8]	25 – 36	19.5 – 27.5	980 – 1270	2524
LW	3E	1	3	SrF_2	20–27	Si:As[8]	25 – 36	27.5 – 29.0	1300	500
LW	4	1	3	SrF_2	20–33	Ge:Be	37 – 48	29.0 – 45.2	1020 – 1630	4324
LW	4A[9]	2	1	Al_2O_3	20–33	Ge:Be	37 – 48	12.0 – 16.6	1250 – 1760	2047
LW	4C[9]	2	2	LiF	20–33	Ge:Be	37 – 48	16.0 – 19.7	1760 – 2380	1879
LW	4D[9]	1	2	LiF	20–33	Ge:Be	37 – 48	19.6 – 27.6	980 – 1270	2524
FP1	5A	3	1	Al_2O_3	10–39	Si:Sb	49 – 50[10]	11.4 – 12.2	20600 – 24000	
FP1	5B	2	1	Al_2O_3	10–39	Si:Sb	49 – 50[10]	12.2 – 16.0	24000 – 32000	
FP1	5C	2	2	LiF	10–39	Si:Sb	49 – 50[10]	16.0 – 19.0	32000 – 34500	
FP1	5D	1	2	LiF	10–39	Si:Sb	49 – 50[10]	19.0 – 26.0	34500 – 35500	
FP2	6	1	3[12]	SrF_2	17–40	Ge:Be	51 – 52[11]	26.0 – 44.5	29000 – 31000	

Notes:

1. SW = short-wavelength grating section, LW = long-wavelength grating section, FP = Fabry-Pérot.
2. The SW section is seen in transmission through the filters while the LW section and the FPs are seen in reflection.
3. 'Aperture area' refers to the dimensions of the SWS detectors projected through the entrance apertures projected onto the sky. The first number refers to the size in the dispersion direction and the second refers to the cross dispersion direction.
4. These are the validated ranges of the bands. The actual wavelength ranges are slightly greater.
5. The resolution given is that obtained when observing an extended source
6. L_{AOT} = total number of scanner steps in band.
7. Band 2C ends at 13.16 μm for SWS07.
8. Band 3 uses Back-Illuminated Blocked Impurity Band (BIBIB) detectors.
9. The three extra bands were added as a check to the band 3 data. Data from them are not produced by the standard OLP pipeline, but can only be generated using the Observers SWS Interactive Analysis (OSIA).
10. Detector 49 is used for FP observations in band 5.
11. Detector 51 is used for FP observations in band 6.
12. FP2 observations in band 6 are made through the virtual aperture 4 (see Section 3.6) but are flagged in the data as being through aperture 3.

the charge from the input gate. The residual charge after a a reset is minimised by a compensation pulse immediately following the reset.

The heated-JFET pre-amplifiers of each grating detector array are combined in a single integrated circuit. A side-effect of this arrangement is that stray capacitance between the input leads of the pre-amplifiers causes significant cross-talk between neighbouring array elements. Since the only involved impedances are capacitive, the cross-talk percentage is independent of frequency and can be accounted for in the data analysis.

The pre-amplifier resets are sufficiently compensated to avoid overloading of the first stages of the warm amplifiers. To avoid dynamic-range problems due to remaining offsets, the signals pass through an AC filter that removes the DC offset. This filter affects the shape of the ramps in a predictable and correctable

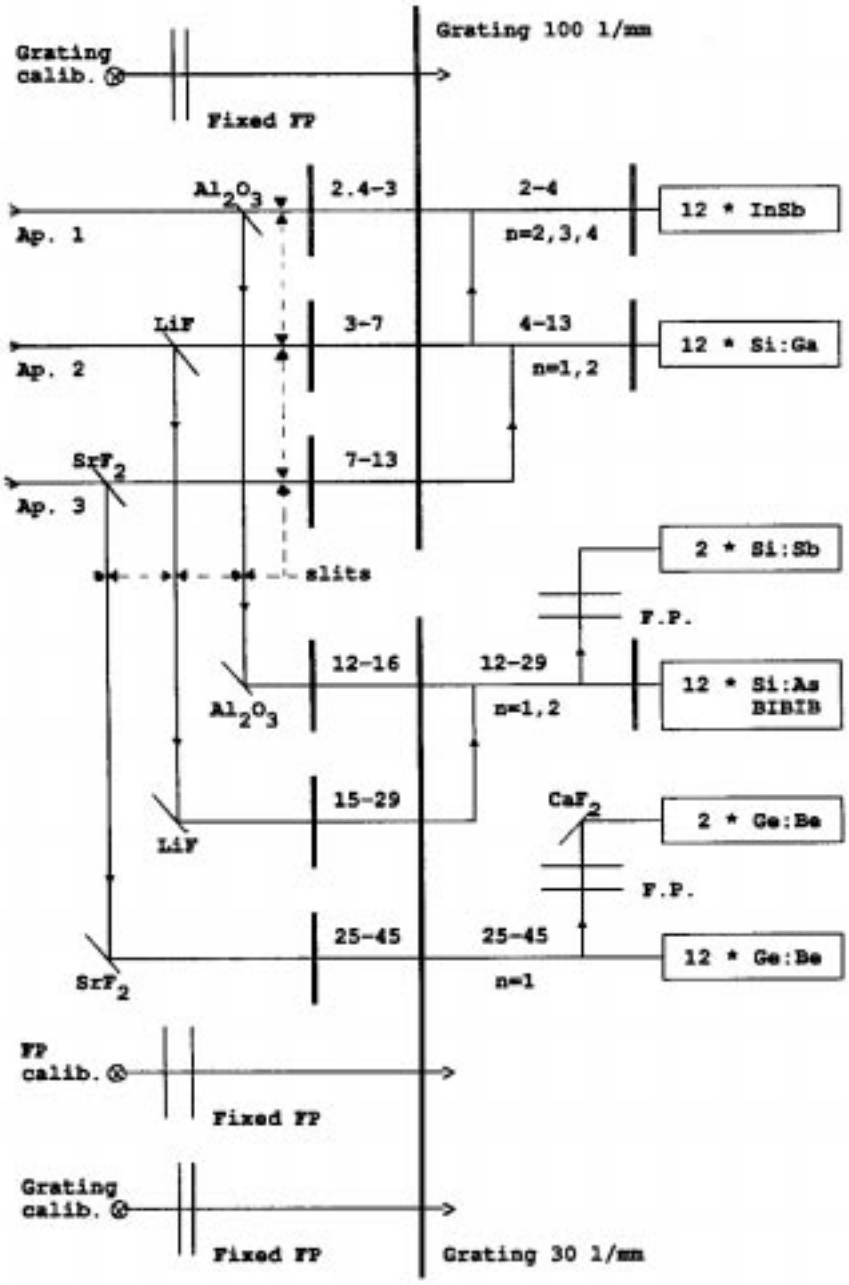

Figure 2.4: *Block diagram of the SWS. The diagram shows the optical functions of the spectrometer, excluding its internal calibration sources, but including the shutter, the collimation and the imaging optics. It excludes band 3E.*

fashion.

The filter outputs are sampled 24 times per second, and then they are multiplexed. They pass through an amplifier with selectable gain factor of (1, 4 or 16) times 225. The gain for FP detectors is an overall

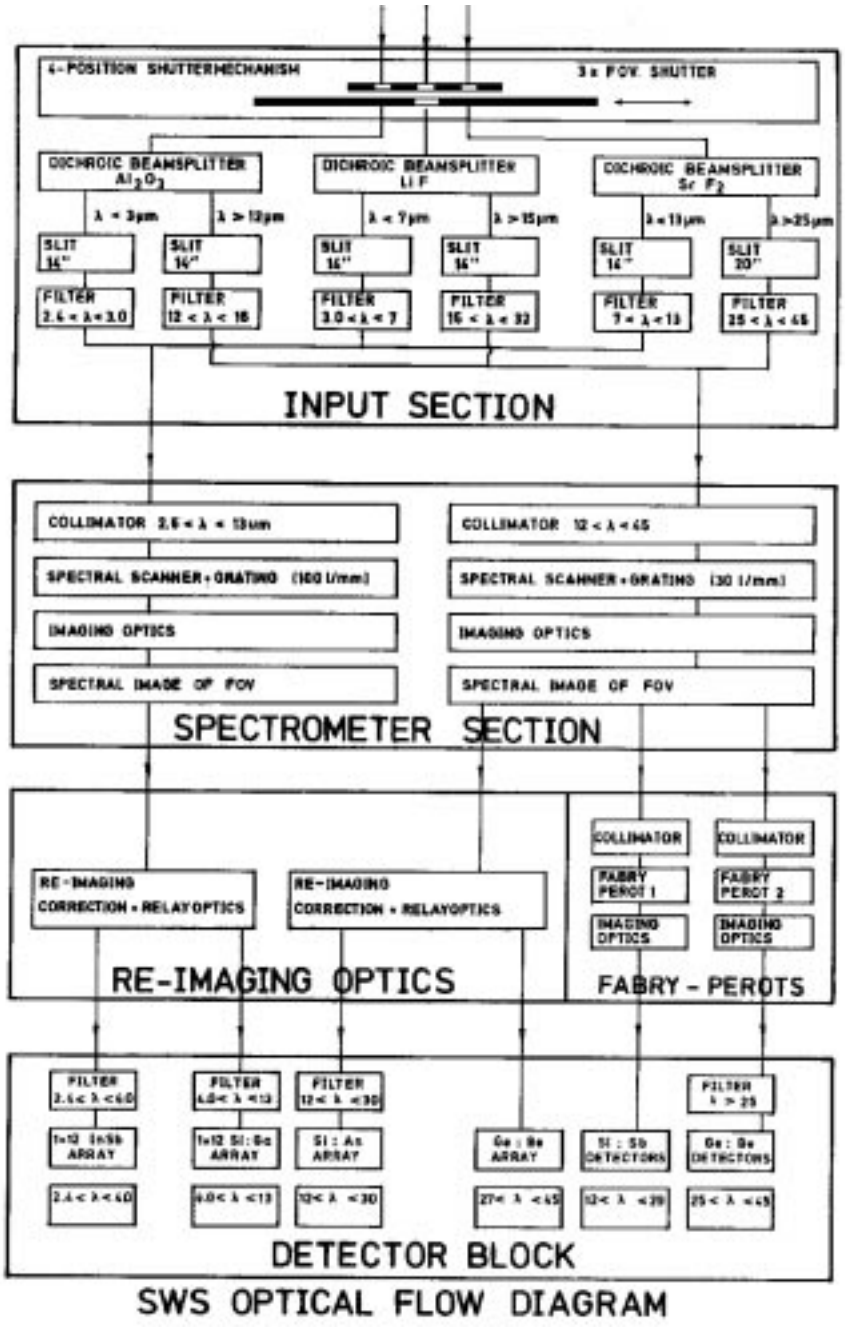

Figure 2.5: *The diagram indicates the six separate entrance slits behind the dichroics after the three apertures. It shows all the spectral order-separation filters and the internal wavelength calibrators. The shutters, collimation and imaging optics and band 3E have been left out.*

factor of 2 higher. Finally they are digitised into 12-bit numbers (covering a 20-V range). At the highest gain setting, the digitisation is precise enough to sample the pre-amplifier noise. At the lowest gain setting, the gain of the warm amplifiers is 225 for the grating detectors and 450 for the FP detectors.

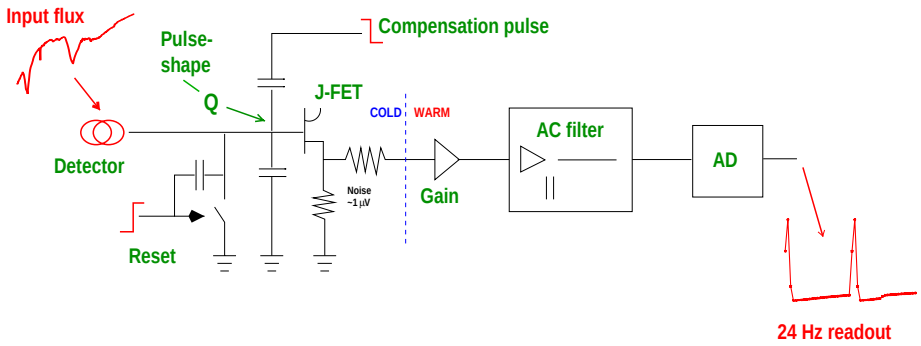

Figure 2.6: *Simplified scheme of the SWS electronics showing all components known to affect the integrated signal from the detectors.*

Figure 2.7 gives a data example in which the individual datapoints from the non-destructive readouts and reset pulses can be seen. The plot starts with a reset pulse, where the capacitor is short-circuited causing the bit readout to spike high. The system stabilises after about four readouts, and as light falls on the detector the charge on the integrating capacitor slowly increases. Careful analysis shows the system to require more than four readouts to stabilise. All the slopes are slightly curved, due to the limited time constant of the AC filter – see Chapter 7. The second slope suffers from a glitch approximately half way along its length, where the measured voltage suddenly jumps instead of following the (curved) slope. Some extra charge is dumped on the capacitor due to e.g. a cosmic ray hit. The rest of this readout is not affected by the glitch as the slope just continues on its curved path, as can be seen by comparing it with the other four slopes.

Data examples for each AOT are shown in Sections 3.3 to 3.6. The automatic data processing chain (OLP) is discussed in Chapter 7.

2.4.2 Processes in the signal chain

In this section all processes that can be identified in the 24 Hz data or in the extracted spectrum induced by the detectors and electronics will be briefly described. This is adapted from Lahuis et al. 2001, [25].

Detectors: detector cross-talk

The cross-talk between adjacent grating detectors amounts to between 10 and 15 %. The correction for this is discussed in Section 7.2.7.

Detectors: memory effects

The SWS Si:Ga, Si:Sb and Ge:Be detectors all suffer from memory effects or transients, whereas the InSb and Si:As detectors are both free from transient effects.

Transient effects were observed in the laboratory prior to launch and have been taken into account in the design of the observing templates used for all general observations. The templates were designed such that the influence of transient effects were minimised. There is sufficient redundancy in each observation so that transient effects can be recognised in the time domain and possibly corrected for. Memory effects are discussed further in Sections 7.3.3.2 and 9.2.

Detectors: de-biasing

During the integration of the detector current, the voltage rise across the detector reduces the bias voltage so that the responsivity of the detector drops slightly during the reset interval. This effect is predicted for all detectors except the InSb photo-diodes. It has been seen only for the Ge:Be grating detectors, and only at very high input signals ($>$ few 10^4 Jy).
This effect is under study. Currently no correction is available.

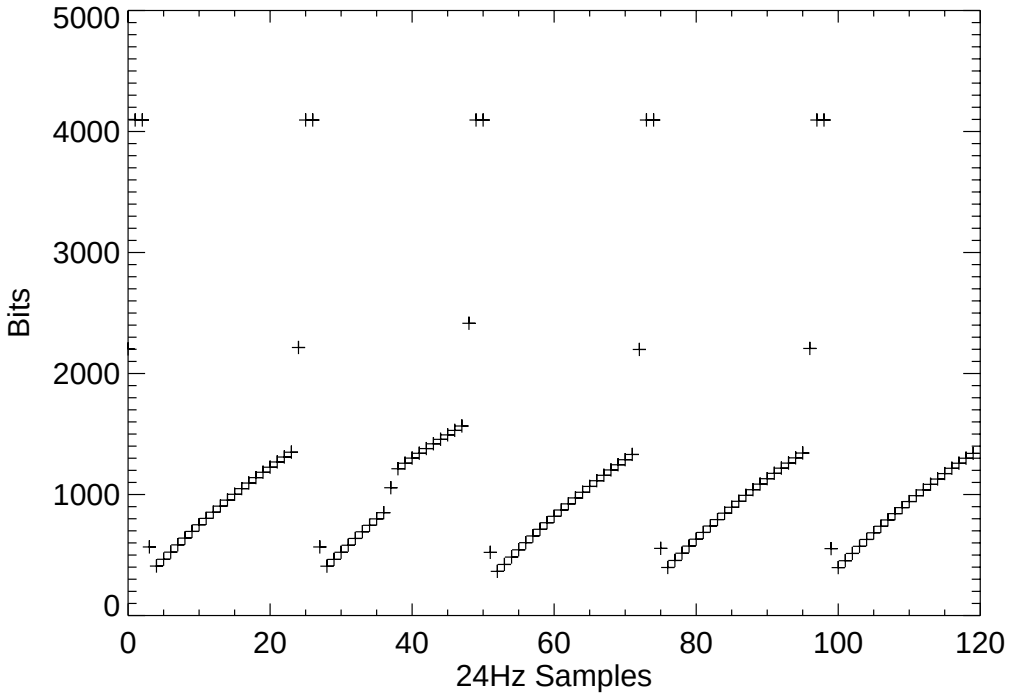

Figure 2.7: *Example readouts, from part of an SWS06 observation. Note the glitch approximately halfway through the second slope, where the output suddenly increases. Also note the curvature in the slopes, caused by the AC filter. Both these effects are removed in the OLP processing chain.*

Detectors: particle impacts

All SWS detectors suffer from the impacts of charged particles. When a particle impact occurs, the additional charge released in the detector causes a jump in the 24-Hz readout signal, constituting a 'glitch' in the data. A secondary effect of the particle impact might be a transient behaviour after the impact where, on time scales of a few seconds, transient tails are observed in particular for the Ge:Be and the FP detectors.

These jumps are recognised and corrected for in the pipeline, see Section 7.2.8. The transient tails, however, are not corrected. For more information on glitch tails see Section 9.2.4.

Reset: saturation

The application of the reset/compensation pulse is never perfect. A fraction of the compensation pulse is fed into the first few samples and these may go into saturation in the amplifier chain, e.g. in the operational amplifier in the high-pass filter. See Figure 2.7, the points at 4095 bits. The reset time of this saturation is fast, less than a quarter of a second. The direct consequence however is that the first samples of the integration ramp cannot be used in the slope fit.

Reset: reset-pulse aftermath

After the reset/compensation pulse has been applied a charge can be left before the input gate of the JFET. This charge will decay over the combined capacitance of the cold electronics and be added to the charge built up by the integration of the detector current. This is seen as an additional exponentially decaying signal onto the integrated 24 Hz signal, usually referred to as the pulse-shape effect. The pulse-shape is an additive effect and only important for low-flux cases. The correction for this effect is discussed in Section 7.2.6

Readout: high-pass filter
The high-pass filter which removes DC offsets has a typical time constant of 2 seconds. Individual time-constants were derived for all 52 detectors from laboratory data. The correction for this is discussed in Section 7.2.5.

Readout: gain amplification
Accounting for the selected gain setting is trivial. The gains are selectable per detector array to values of 225 times (1, 4 or 16). The FP gains are an overall factor of 2 higher. No deviations from the nominal gain ratios have been detected.

Readout: A-D conversion
At the end the analogue signal is digitised. The amplified analogue signal ranges from ± 12 V, and is converted to a bitrange from 0 to 4095 corresponding to ± 10 V. Any analogue signal outside the ± 10 V range is therefore set to 0 or 4095 and flagged as out of limit in the first stage of the processing – see Section 7.2.2.

Readout: saturation
At very high signal levels ($10^5 \mu$V/s), saturation effects come into play. First, parts of the ramps become saturated and at even higher signal levels the complete ramp can become saturated. In the last case the ramp will be outside the bitrange already after the first sample.

Unless otherwise noted, these effects are corrected for in the pipeline in the reverse order in which they occur, to undo their effects and to reconstruct the incoming signal. See Section 7.2.

Chapter 3

Instrument Observing Modes

3.1 Introduction

Astronomical observations with ISO were carried out via pre-planned observing modes. These are modes in which the basic operating parameters for the instrument are predefined (e.g. which sub-instrument to use at what wavelength resolution), leaving the user to select wavelengths to scan between, enter flux levels etc. Almost all observations entered by observers used one of four Astronomical Observation Templates, AOTs, while calibration observations used a variety of AOTs and Calibration Uplink System, (CUS) observations. The AOTs are fully described in Beintema & Kunze 1999, [1], to which users are pointed if this section does not provide them with sufficient information. CUS was a very flexible system to define observations for calibration purposes which very well could contain valuable astronomical information. It was also used to define a specialized AOT for the Post-Helium Phase.

The `EOHAAOTN` keyword, present in the product files (see Appendix A), indicates what type of observation was performed. For normal AOTs it will take the value S01, S02, S06 or S07. For CUS or post-helium observations it will take the value S99, while S90 – S98 were reserved for engineering operations such as activation and de-activation. During the mission changes were made to the AOTs as experience with the instrument increased. A list of these changes is given in Appendix C.

In this book the AOTs will be indicated by their official designation: SWS01, SWS02, ... SWS99 to distinguish them from AOTs with possibly similar names in use by the other instruments.

3.2 AOT Overview

There were two main observing modes with the SWS.

1. **Grating-Only Observations (Medium spectral resolution)** – SWS01, SWS02 and SWS06
   The spectral region of interest was directed to an array of 12 detectors. The spectral range instantaneously covered by the array was about 8 grating resolution elements, with gaps between the individual detectors (except for Band 3). For an observation, the grating was scanned in small steps to fully sample the desired wavelength range and provide a certain redundancy in case of detector failures or detector memory effects. Different scan schemes were used to obtain high fidelity line profiles, scans of wavelength ranges, and quick low-resolution full scans of the SWS wavelength range.

2. **Fabry-Pérot / Grating Combination Observations (High spectral resolution)** – SWS07
   The wavelength was selected by setting the Fabry-Pérot (FP) unit to a gap where one of the transmitting orders matched the correct wavelength. The FP unit was then scanned in steps of

about 1/4 FP resolution element. The grating was used as an order sorter, with the maximum of the grating transmission tuned to the desired wavelength so that unwanted FP orders were suppressed. Because the two detectors of a FP detector pair look at slightly different grating resolution elements, this tuning could normally be done only for one detector. The other detector would not simultaneously deliver a useful signal as use of this redundant detector would require commanding of a slightly different grating position.

Figure 3.1 gives an overview of the wavelength ranges that could be simultaneously covered by the SW and LW or FP detector systems.

During an AOT observation, the source spectrum was measured by rotating the scanning mirror of the grating or varying the gap of the Fabry-Pérot (FP). Each AOT may have done one or more exposures with an internal calibrator for a photometric check and a number of dark current measurements with the aperture closed. Hence, the data produced by any single AOT was generally of several different types.

Four AOTs, listed below, were defined for SWS. Operating modes changed during the mission, and any such changes are noted in Appendix C.

- **SWS01**: a single up-down scan for each aperture. It had four possible scan speeds and was primarily intended to quickly scan the entire SWS wavelength range at degraded resolution.
- **SWS02**: slow short up-down scans, designed to measure line profiles.
- **SWS06**: medium length grating scans with various options. Programmed as long up-down scan, possibly with reference scan. Used to observe long wavelength regions at full resolution.
- **SWS07**: LW section devoted to FP observations. The SW section did almost the same as in SWS06. In this AOT priority was given to the FP.

Example outputs from all AOTs are given in Sections 3.3 to 3.6. For all AOTs the measurements of photometric check, dark current and science data are interleaved in the ERD and SPD, while the AAR only contains science detector data for which a unique wavelength is assigned to the light falling on that detector.

3.2.1 Up-Down scans

All grating observations employed what were known as up-down scans. In these, the grating initially scans a wavelength range in one direction, then reverses direction to cover the same wavelength region again. e.g. the scanner may start at 35 μm, scan down to 30 μm and then go back up to 35 μm. Having two scans, in different directions, enables a discrimination to be made between real spectral structure and detector memory effects, as the latter can mimic the former. They are called up-down scans, rather than down-up scans, as it is the scanner step number (aka LVDT) that increases then decreases, and wavelength is inversely correlated with LVDT. Note that 'up-down scans' only refer to what the grating was doing. For FP observations both the grating and the FP always increased in position, hence decreased in wavelength, with time. An example of an up-down scan is shown in Figure 3.2, taken from an SWS01 observation.

For observations of bright sources ($>$ 100 Jy) the uncalibrated fluxes seen in bands 2 and 4 in the up-scan can differ by 20% compared to the that seen in the down-scan due to memory effects – see Sections 9.2 and 5.7.2. The other grating bands did not suffer from memory effects.

3.2.2 Reference scans

SWS06 and SWS07 observations planned before July 10, 1997 employed what was known as 'reference scans'. These were supposed to enable a determination of the detector drifts caused by memory effects.

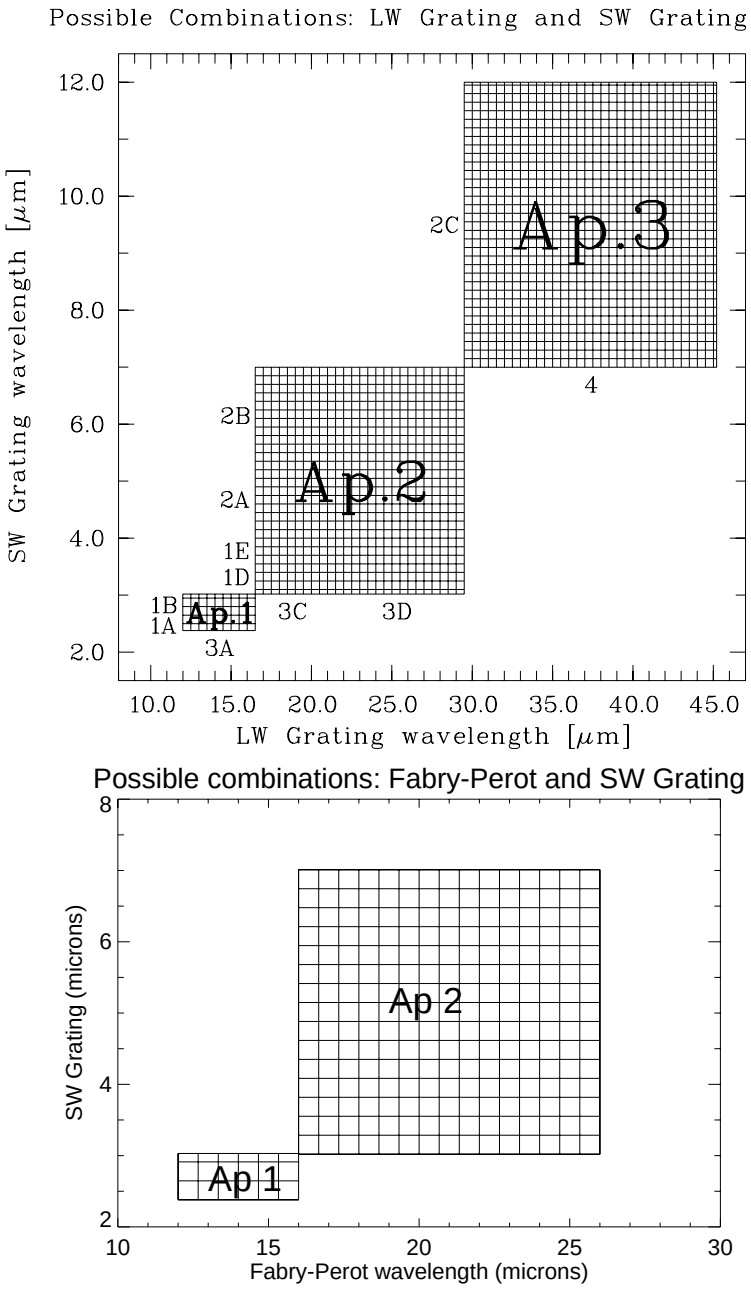

Figure 3.1: *Overview of possibilities for simultaneous use of LW grating and SW grating (top) and FP and SW grating (bottom). Only combinations within the hatched area were allowed, and simultaneous observations through aperture 3 when observing with the FP were not allowed. The corresponding band designations and aperture numbers are indicated.*

The method used, was for the grating to occasionally switch back to a fixed grating position, and hence wavelength. Any changes in the detector response at this wavelength over the time scale of the observation were due to detector memory effects, which could therefore be calibrated out. These reference scans were

only present in long AOTs.

However, no proper method based on the reference scans could be devised to correct the memory effects while on the other hand a good method was found for band 2 using the Fouks-Schubert model. Furthermore, it was found that including such reference scans actually harmed observations due to the interplay of reference scans and memory effects, described in Section 9.2.3. The time span between reference scans was therefore increased from observations planned from July 10, 1997 such that most SWS06's did not suffer from them.

3.3 SWS01 – Full Scan

SWS01 was designed to perform a quick scan over the entire SWS spectral range to get the broad continuum shape of the object under study. It could scan at one of four user-selected speeds, resulting in four possible durations for the AOT. The scans are effectively continuous, using small and frequent steps, and on a time scale much shorter than the selected reset interval of the detector pre-amplifiers. The integration in time translates into a smoothing of the spectrum, which prevents aliasing problems due to insufficient sampling. It was accepted that the spectral resolution it could achieve, would be lower than nominal. The degradation of resolution with respect to the full resolution provided by AOT SWS02 is a function of wavelength and source structure. Table 3.1 gives approximate average values for this resolution degradation. See Section 4.5.1.2 for further discussion.

Table 3.1 shows the reset intervals, dwell times, stepsize and number of up-down scans for SWS01. The reset interval is the time between detector resets, the dwell time is the time during which the grating does not move (and hence each detector is seeing a fixed wavelength) and the stepsize, in LVDT, is the amount by which the grating moves every dwell time. An LVDT is an internal unit of measurement of the grating position and is given the name because it is measured by a Linear Voltage Differential Transducer. A movement of 1 LVDT corresponds to approximately 1/8 of a resolution element.

Table 3.1: *SWS01 parameters*

Speed	Duration [s]	Reset interval [s]	Dwell time [s]	Stepsize LVDT	Number of up-down scans	Pipeline resolution degradation
1	1172	1	1/8	4	1	≈ 4
2	1944	2	1/8	2	1	≈ 4
3	3846	2	1/8	1	1	≈ 2.5
4	6570	2	1/4	1	1	≈ 1.4

For an SWS01 measurement, where the grating moves during a reset interval, the grating position in the `SWSPGPOS` field of the SPD is set to the start position of the grating during the reset interval. This contrasts with the wavelength in the `SWSPWAVE` field of the SPD which is the effective wavelength, i.e. calculated for the grating position averaged over the valid samples.

Example of an SWS01 observation:

The timeline of an SWS01 observation using the fastest speed 1 was as follows:

1. Acquisition - point aperture 1 to target
2. Dark current measurement (20 sec)
3. Single scan up, bands 1A, 1B, 3A (70 sec)
4. Single scan down, bands 1A, 1B, 3A (70 sec)

5. Dark current (20 sec)
6. Internal photometric calibration (40 sec)
7. Switch to aperture 2 (10 sec)
8. Dark current measurement (20 sec)
9. Single scan up, bands 1D, 1E, 2A, 2B, 3C, 3D (170 sec)
10. Single scan down, bands 1D, 1E, 2A, 2B, 3C, 3D (170 sec)
11. Dark current measurement (20 sec)
12. Switch to aperture 3 (10 sec)
13. Dark current (20 sec)
14. Single scan up, bands 2C, 3E, 4 (150 sec)
15. Single scan down, bands 2C, 3E, 4 (150 sec)
16. Dark current (20 sec)
17. Internal photometric calibration (40 sec)

Figure 3.2 shows the layout of an SWS01 speed 3 ERD. It displays how the complete wavelength range is covered in time by the 4 grating bands. It also shows the relation between the LVDTs in the SW/LW sections, the wavelengths and the selected apertures (in the bottom panel). The nature of up-down scans (see Section 3.2.1) can be seen clearly. The periods when apertures 1, 2 and 3 are used, times of dark current measurements and photometric checks are indicated in colours at the bottom: red, green and blue for apertures, black for dark and yellow for the photometric check.

Figure 3.3 shows only a small fraction of the ERD data for detectors 1, 13, 25 and 37 (bands 1, 2, 3 & 4) of the same SWS01 observation. The signal is shown in bit values against time (ITK).

Figure 3.4 shows SPD data, in μV/s, for detector 1 of each band against time. Figure 3.5 shows the AAR for the same observation, now as flux (Jy) against wavelength (upper panel). The spread of flux between different detectors in the same band can be seen in the band 4 data. In the lower panel it is shown what further processing can achieve.

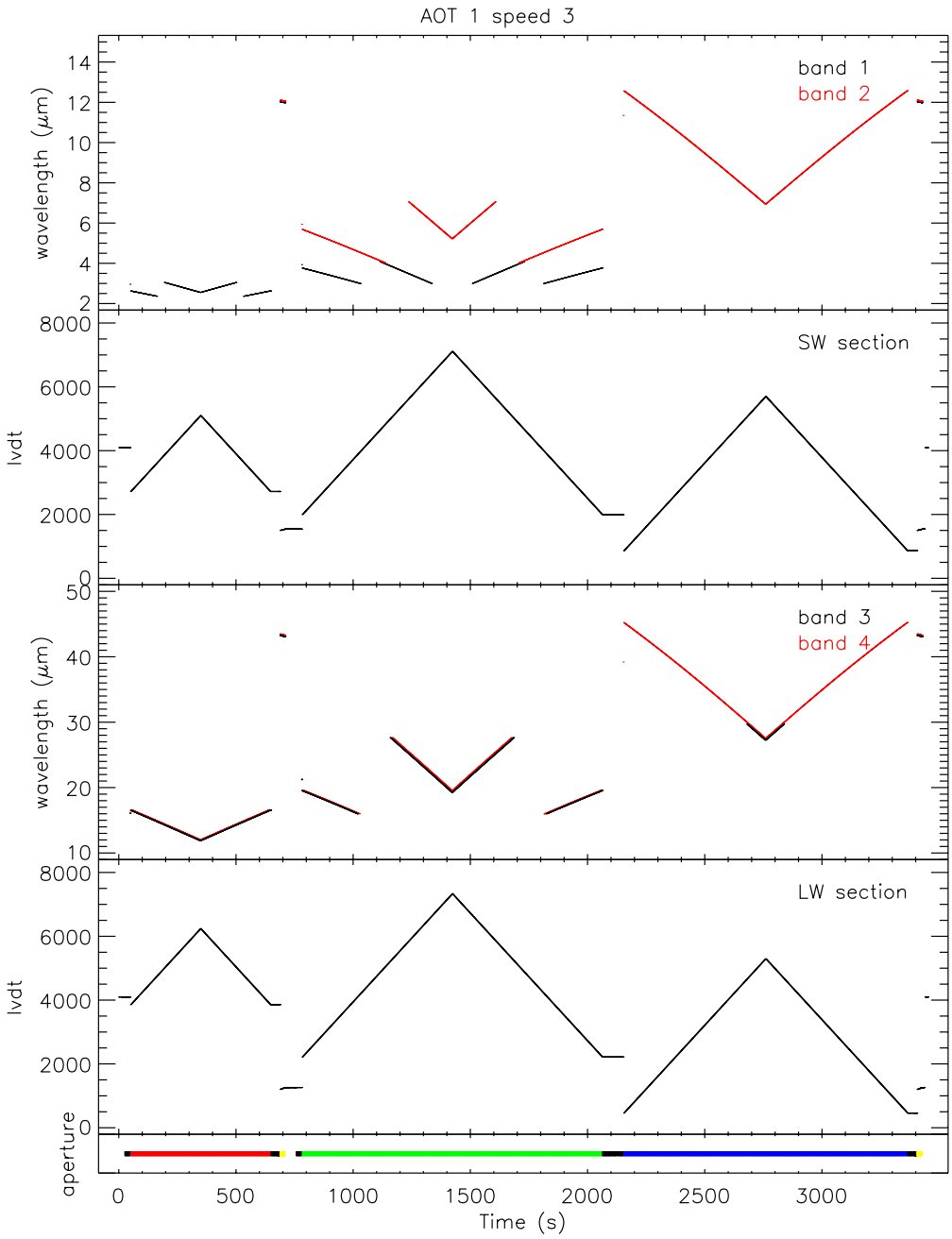

Figure 3.2: *The wavelength layout in all bands during an SWS01. The 2 panels from the top display the layout in the SW section, the wavelength coverage for band 1 and 2 and the corresponding LVDT. In the next 2 panels the same is displayed for the LW section (bands 3 and 4). The small bottom panel indicates which aperture was used: red, green and blue for apertures 1, 2 and 3 resp., black for dark current and yellow for photometric checks. Where there is no colour indication the status of the instrument is officially undefined, although the shutter was closed. In apertures 1 and 2, band 4 covers the same wavelength range as band 3. These ranges are the so-called 'offbands'. They are of less quality and will not normally make it into the AAR. To address them one will have to use OSIA.*

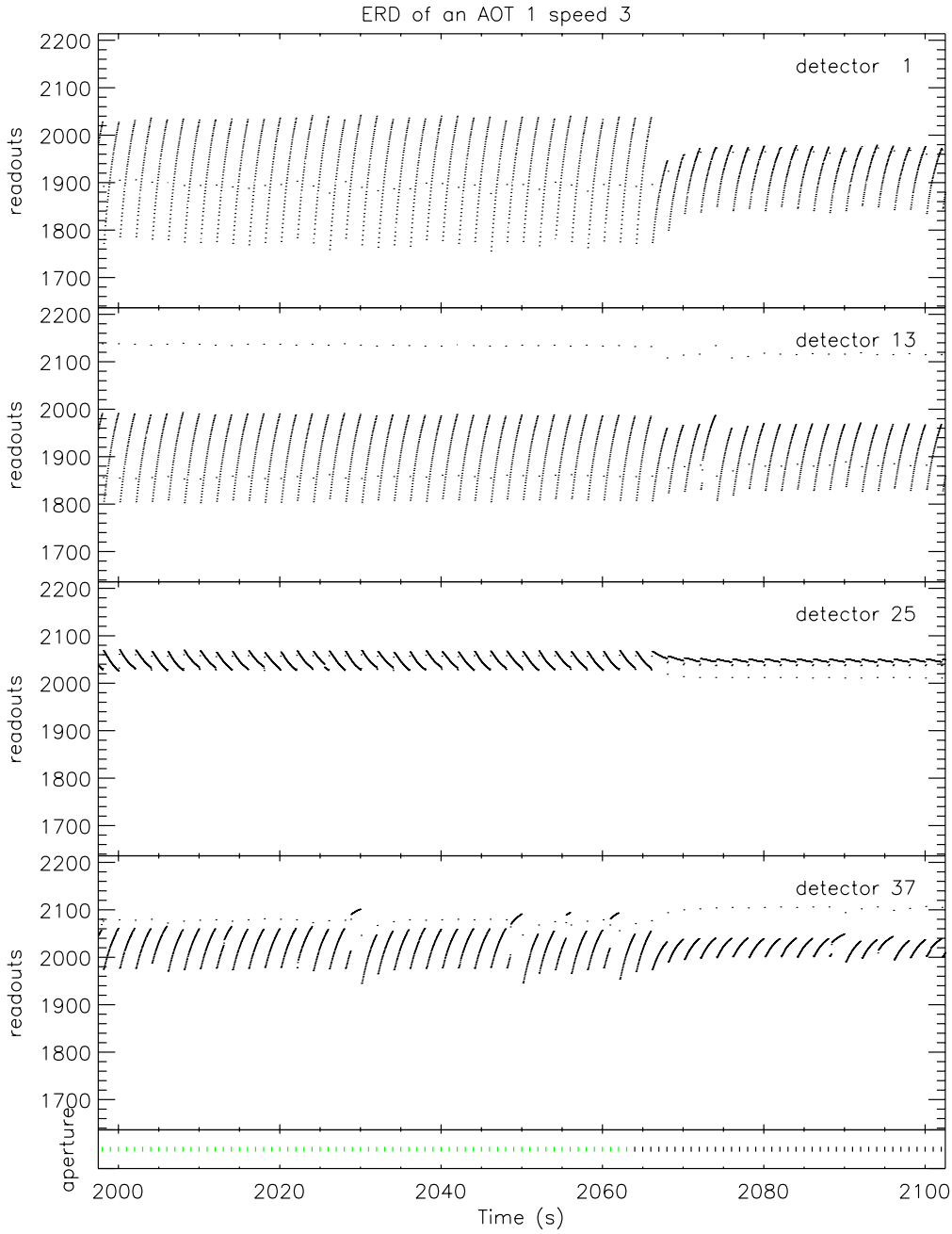

Figure 3.3: *Example of part of an ERD in all bands during an SWS01. The 4 panels display the raw output (in bits) for detectors 1, 13, 25 and 37 resp., the first detectors from each of the 4 grating bands. Only a small section of the ERD is displayed. In band 3 the ramps are downward. In band 4 several glitches can be seen. The small bottom panel indicates which aperture was used: green for aperture 2 and black for dark current. This is the same ERD as in Figure 3.2.*

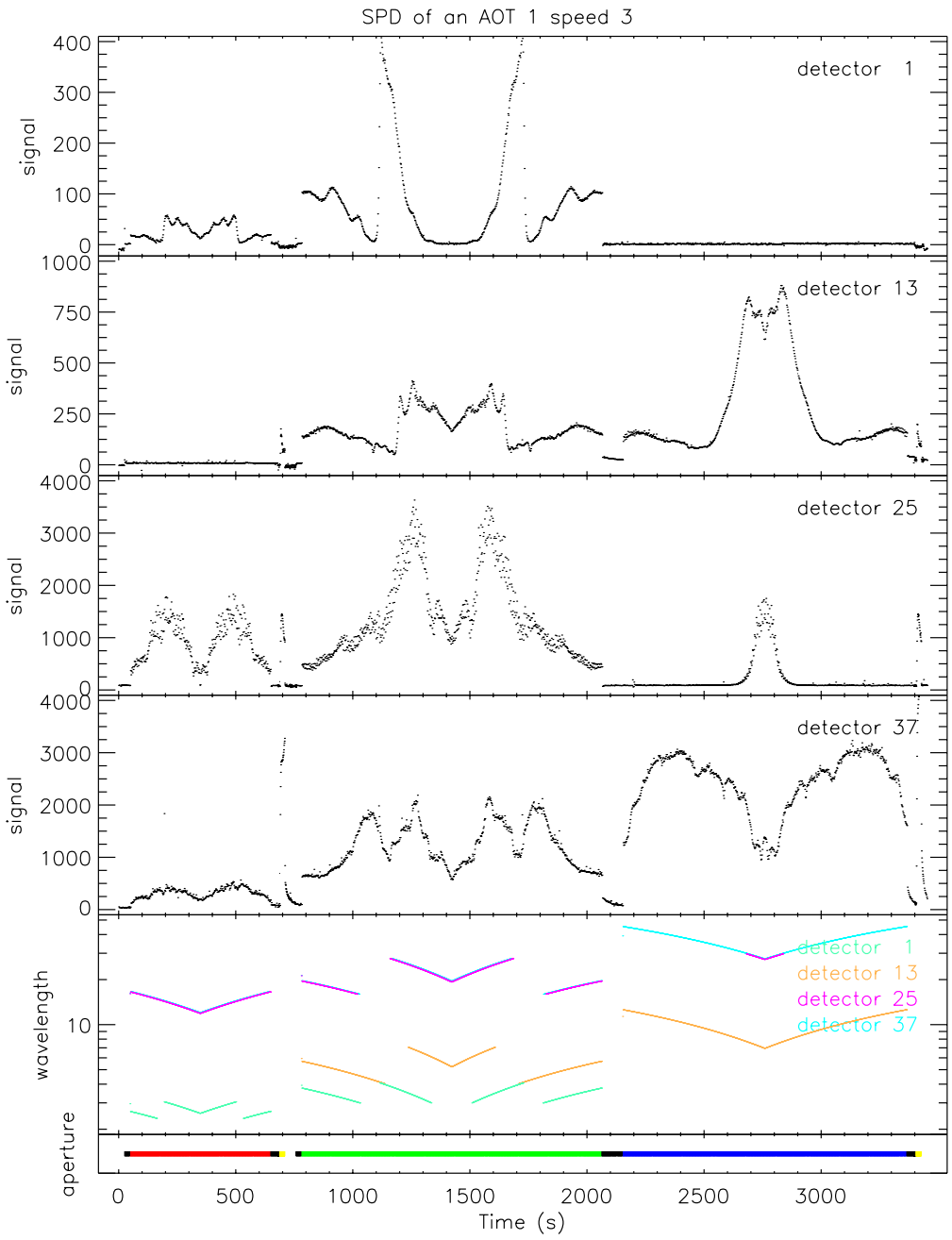

Figure 3.4: *SPD data (in $\mu V/s$) from the first detector of each band during an SWS01. Note the symmetric patterns introduced by the up-down scans for the three apertures. Colour codes for the apertures are the same as for Figure 3.2.*

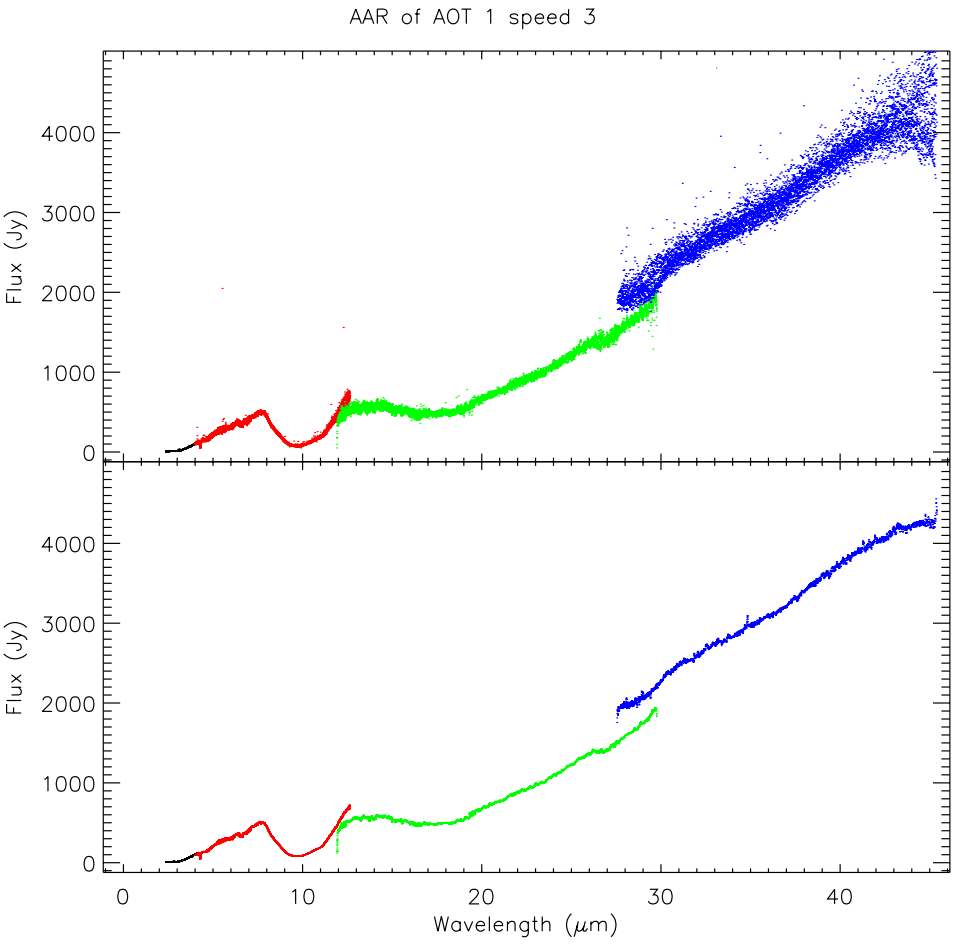

Figure 3.5: *AAR data from all detectors against wavelength during an SWS01 observation. In the upper panel the original AAR is displayed, band 1 detectors in black, band 2 in red, band 3 in green and band 4 in blue. In the lower panel it is shown what further processing (in this case: flat-fielding, σ-clipping, defringing in bands 2C and 3, and rebinning) can achieve. The fact that all of band 3 is somewhat lower than the rest could indicate a small pointing problem.*

3.4 SWS02 – Line Scan

SWS02 was optimised for sensitive observations of single lines. It could observe up to 64 individual small wavelength intervals per spectrum (each one covering approximately 10 resolution elements, i.e., 1500–3000 km/s) using the SWS grating mode. Each range was scanned back and forth to provide redundancy with minimal scan time of 100 seconds. Dark current measurements were performed before and after the spectral scan. And a photometric check was performed at the end, using the internal calibrators. In cases of very long observations (> 3600 sec) there were extra photometric checks.

Table 3.2 shows the reset intervals, dwell times, stepsize and number of up-down scans for SWS02. The dwell time may be higher for some merged scans.

Table 3.2: *SWS02 parameters*

Detector band	Reset interval [s]	Dwell time [s]	Stepsize LVDT	Number of up-down scans
1	1, 2, 4	= reset	1	$n \geq 1$
2,3	1, 2	= reset	1	$n \geq 1$
4	1, 2	= reset	2	$n \geq 1$

Example of an SWS02 observation:

As an example, to observe lines at 10, 12, 35 and 40 μm the SWS02 carried out the following sequence:

1. Acquisition - point aperture 1 to target
2. Dark current measurement (20 sec)
3. Scan line at 12 μm, up (50 sec)
4. Scan line at 12 μm, down (50 sec)
5. Dark current measurement (20 sec)
6. Switch to aperture 3 (10 sec)
7. Dark current measurement (20 sec)
8. Simultaneously scan lines at 10 and 40 μm, up (100 sec)
9. Simultaneously scan lines at 10 and 40 μm, down (100 sec)
10. Dark current measurement (20 sec)
11. Simultaneously scan lines at 10 and 35 μm, up (100 sec)
12. Simultaneously scan lines at 10 and 35 μm, down (100 sec)
13. Dark current measurement (20 sec)
14. Internal photometric calibration (40 sec)

Figure 3.6 shows the wavelength coverage in time of an SWS02. The particular SWS02 is quite a short one, performing only 5 scans. As the individual scans are also short, the up-down character of each of them can hardly be distinguished. Figure 3.7 displays the timeline (SPD) of the first detector in each of the 4 grating bands; not much seems to be happening. Figure 3.8 shows only part of the AAR in the overlap region between band 1D and 2A (upper panel). A faint absorption line is visible in band 1D while it is mostly noise in band 2A. In the lower panel it is shown what can be achieved by post-AAR processing.

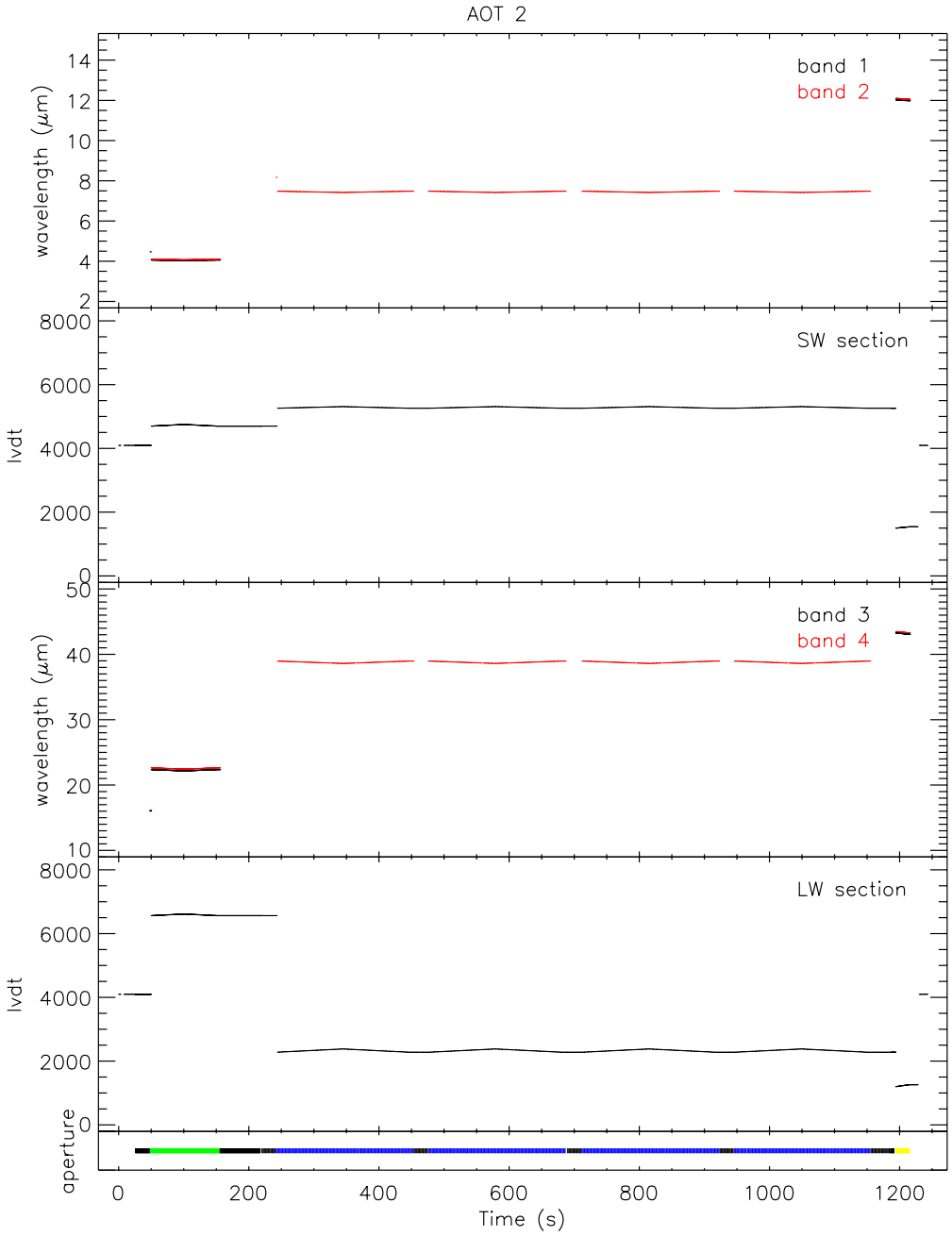

Figure 3.6: *The wavelength layout of an SWS02. A few short scans were planned by the observer. See Figure 3.2 for further explanations.*

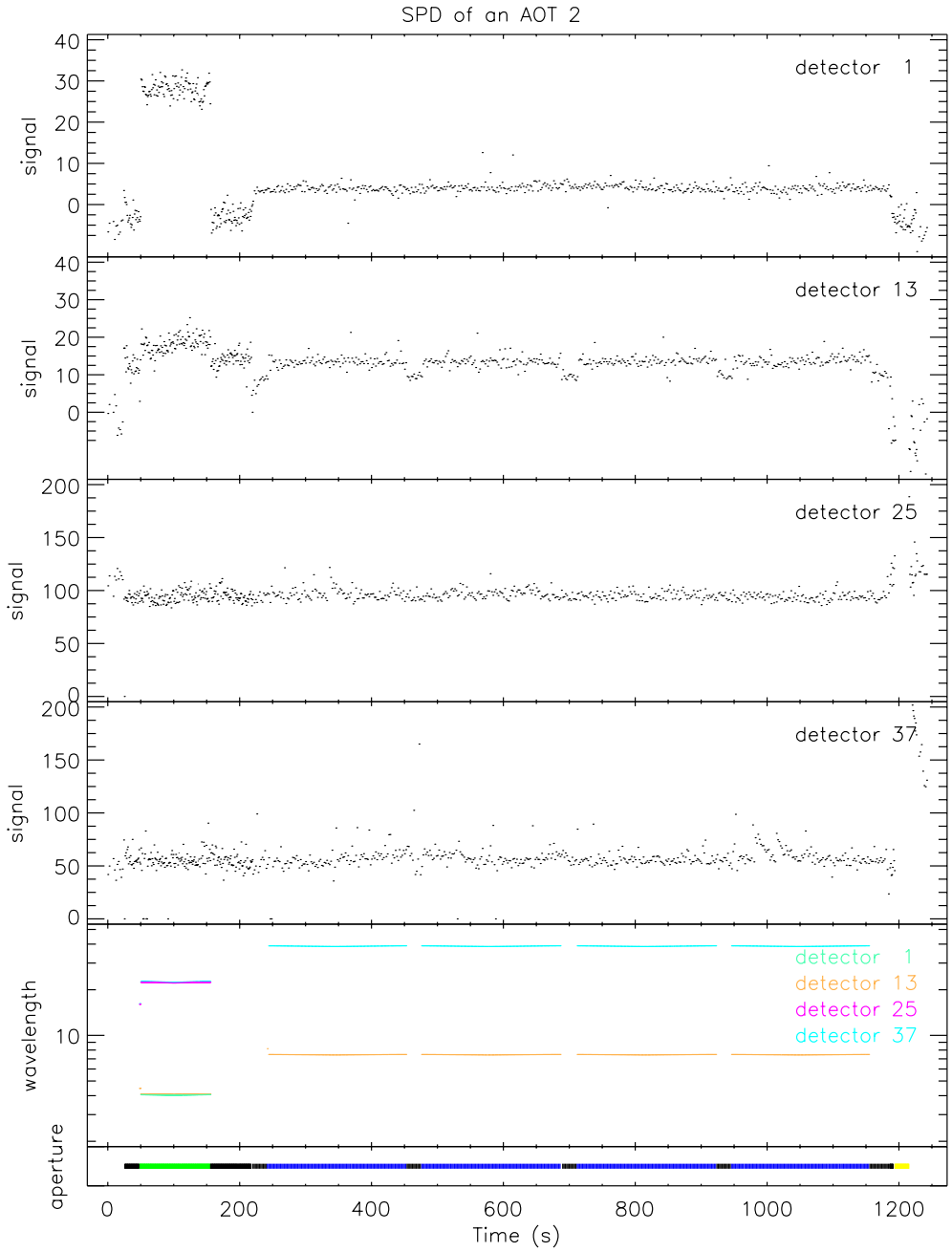

Figure 3.7: *SPD data (in $\mu V/s$) for an SWS02 as a function of time. See Figure 3.2 for aperture colour codes.*

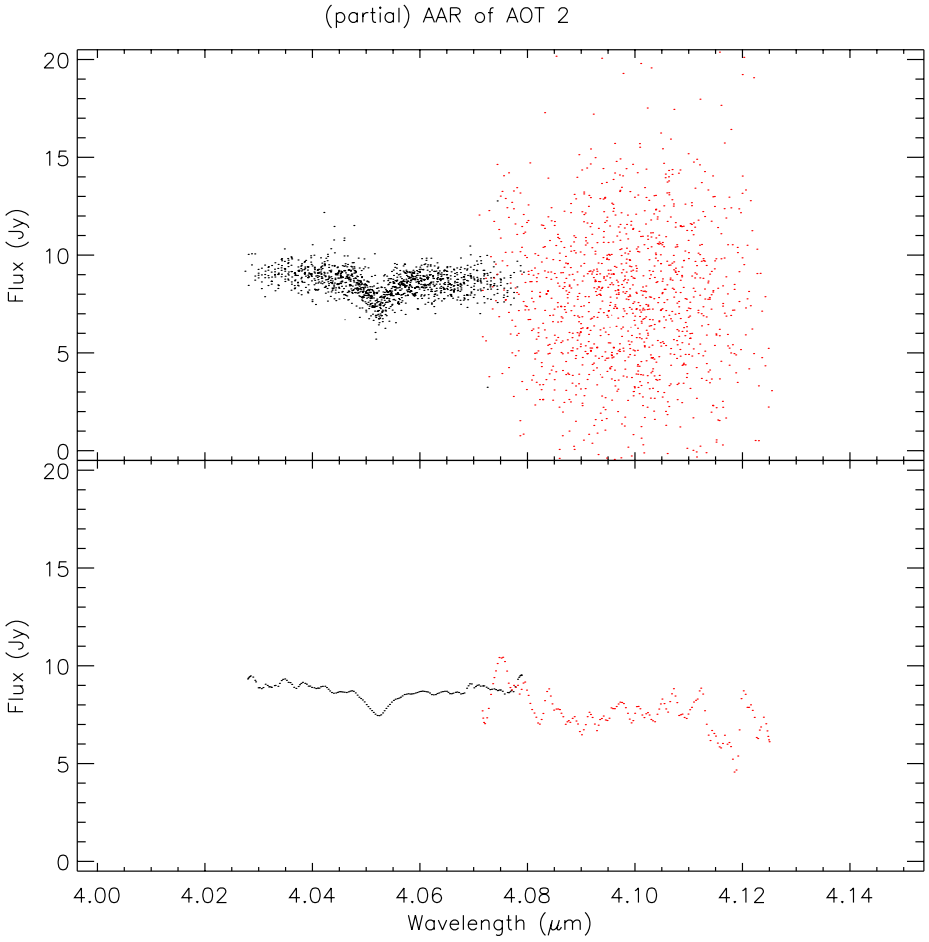

Figure 3.8: *AAR data from overlapping scans of bands 1 (black) and 2 (red) for an SWS02 as a function of wavelength. In the upper panel the original AAR data is displayed while in the lower panel it is shown what can be achieved by post-AAR processing. In this case σ-clipping, flat-fielding and rebinning. No defringing was done in the bands displayed.*

3.5 SWS06 – Wavelength Range Scan

SWS06 was used to make observations over a wider wavelength range, as opposed to observing individual lines. Up to 64 wavelength ranges could be chosen anywhere in the SWS grating range, i.e., between 2.38 and 45.2 μm, under the restriction that each range falls within one of the bands (see Table 2.1).

SWS06 was executed by pointing the telescope to the target position, and then for each wavelength range (or pair of merged ranges) a dark-current measurement was done. If the spectral scan was long enough to need it, a measurement on the reference wavelength was performed. The wavelength range specified in the AOT was observed. Each range was scanned back and forth to provide redundancy. The reference measurement (if any) was repeated after which again a dark current was done. Very long observations were interrupted by wavelength switching to the reference wavelength, as an additional photometric check. If a single up and down scan did not provide enough sensitivity, the measurement sequence was repeated as often as necessary. Photometric checks using the internal calibrator were done at regular intervals, at least once per AOT.

Table 3.3 shows the reset interval, dwell times, stepsize and number of up-down scans for SWS06. The dwell time stops at 4 secs, and for higher sensitivity the scans were repeated. This was not always the case. Earlier versions of the logic (prior to May 1996, see Appendix C) had the dwell time increasing.

Table 3.3: *SWS06 parameters*

Detector band	reset interval [s]	dwell time [s]	stepsize LVDT	Number of up-down scans
1	1, 2, 4	$\geq$ reset	1, 2, 4	n
2, 3	1, 2	$\geq$ reset	1, 2, 4	n
4	1, 2	$\geq$ reset	1, 2, 3, 6	n

Example of an SWS06 observation:

As an example, an SWS06 observation around 10, 12, 33 and 40 μm had the following timeline:

1. Acquisition - point aperture 1 to target
2. Dark current measurement (16 sec)
3. Scan up around 12 μm (24 sec, fast)
4. Scan down around 12 μm (24 sec, fast)
5. Dark current measurement (16 sec)
6. Switch to aperture 3 (10 sec)
7. Dark current measurement (16 sec)
8. Reference scans near 10 and 33 μm (16 sec)
9. Scans around 10 and 33 μm, up (360 sec)
10. Reference scans near 10 and 33 μm (16 sec)
11. Scans around 10 and 33 μm, up, continued (360 sec)
12. Reference scans near 10 and 33 μm (16 sec)

13. Scans around 10 and 33 μm, down (360 sec)
14. Reference scans near 10 and 33 μm (16 sec)
15. Scans around 10 and 33 μm, down, continued (360 sec)
16. Reference scans near 10 and 33 μm (16 sec)
17. Dark current measurement (16 sec)
18. Dark current measurement (16 sec)
19. Reference scans near 10 and 40 μm (16 sec)
20. Scans around 10 and 40 μm, up (96 sec)
21. Scans around 10 and 40 μm, down (96 sec)
22. Reference scans near 10 and 40 μm (16 sec)
23. Dark current measurement (16 sec)
24. Internal photometric calibration (40 sec)

Figure 3.9 shows the wavelength layout and grating positions in both grating sections. Figure 3.10 shows the SPD signals, status data, grating position and wavelength for detectors 1, 13, 25 and 37 during an SWS06 observation. The SPD data is in μV/s. The periods when apertures 1, 2 and 3 are used, times of dark current measurements and photometric checks are indicated.

Figure 3.11 shows the AAR, flux (in Jy) against wavelength, for the same observation (upper panel). What can be achieved after further processing of such data in either ISAP or OSIA is shown in the lower panel.

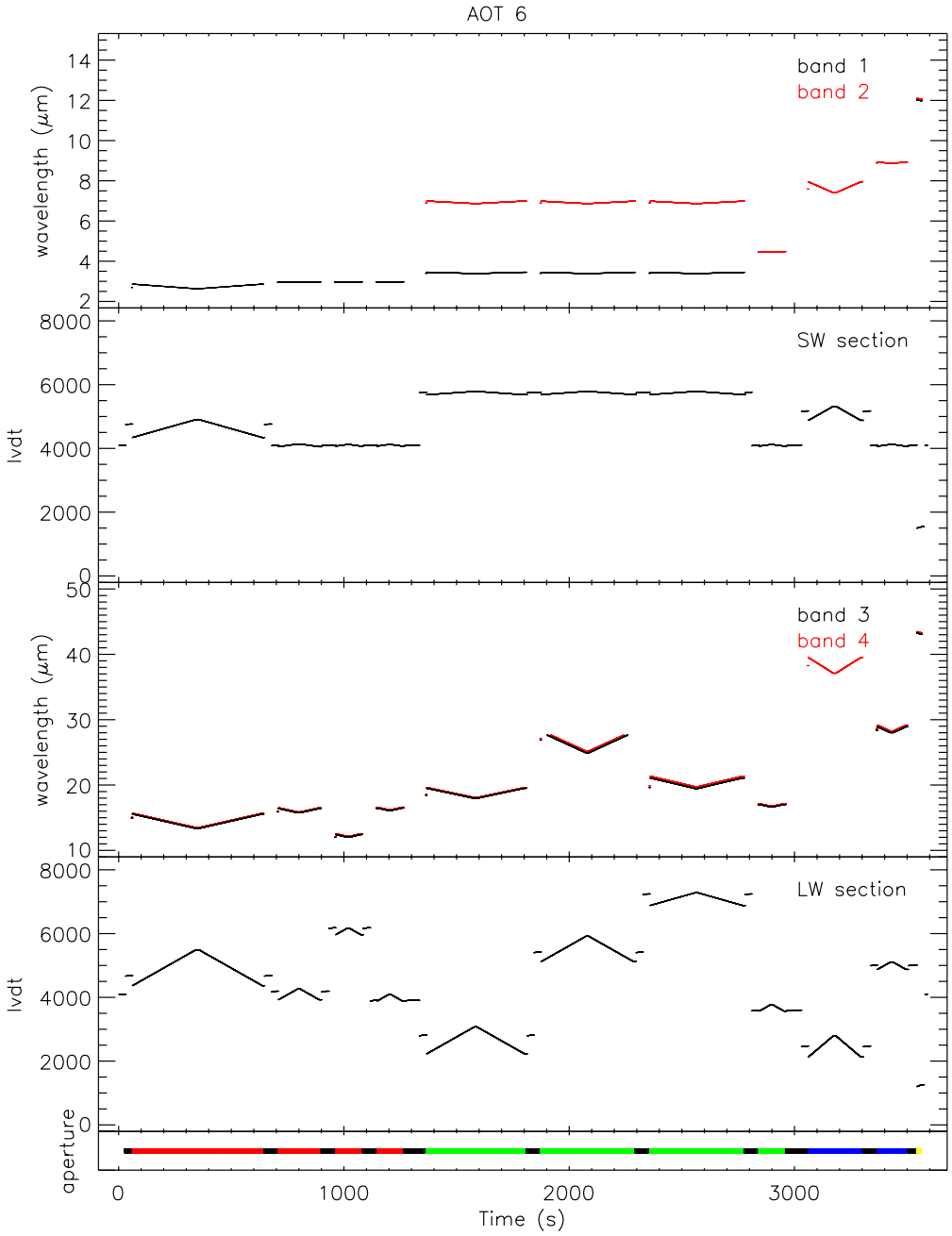

Figure 3.9: *Example of the wavelength layout during an SWS06 observation. See Figure 3.2 for further explanations.*

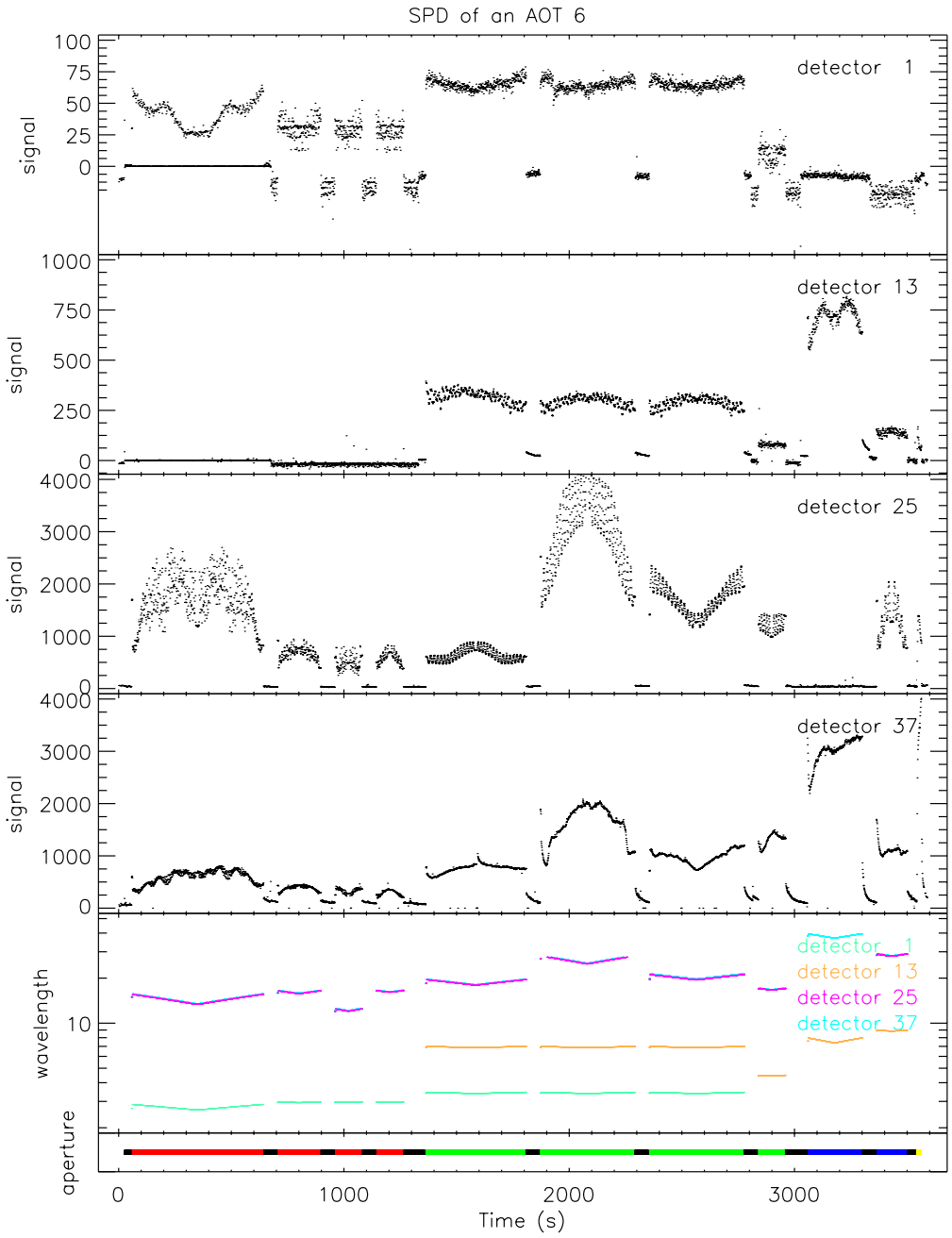

Figure 3.10: *SPD data (in $\mu V/s$) for the first detector of each grating band for an AOT SWS06. Note the symmetric patterns introduced by the up-down scans. Aperture colour codes are the same as in Figure 3.2.*

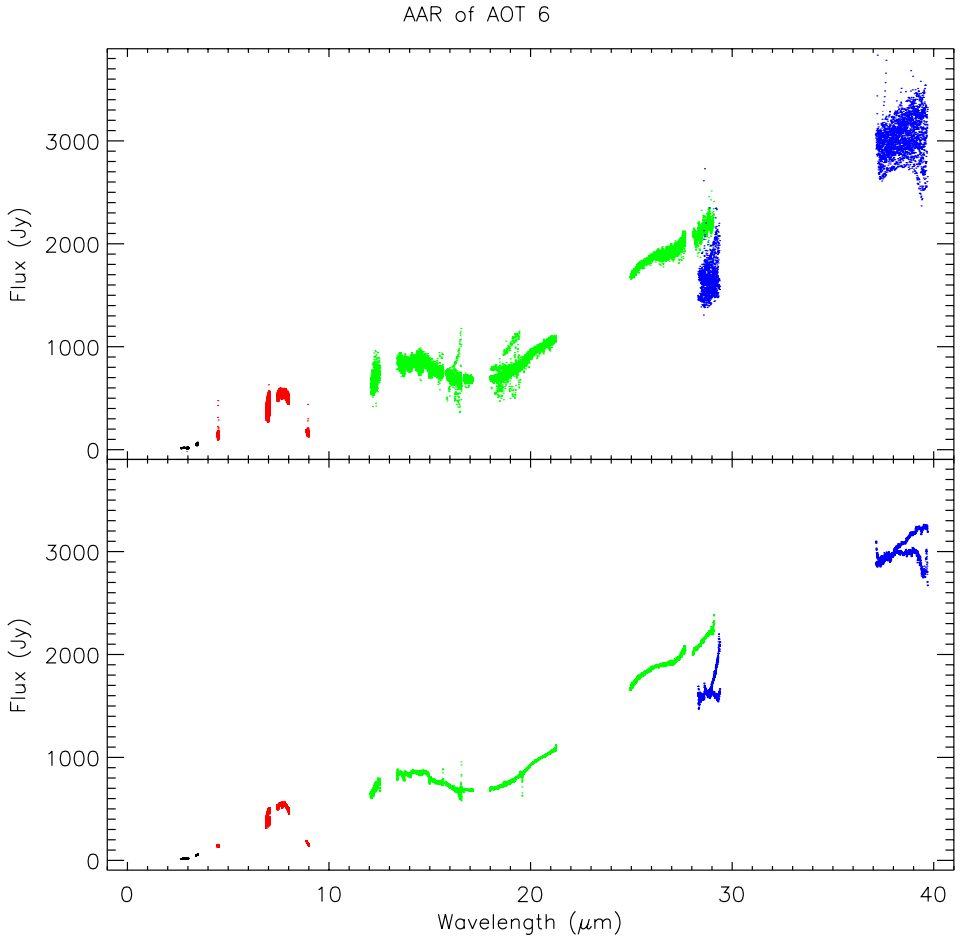

Figure 3.11: *In the upper panel the AAR data from all detectors for an SWS06 observation is shown. In the lower panel it is shown what can be achieved with these SWS06 OLP data after σ-clipping, flat-fielding, defringing in all bands except band 4 and rebinning.*

3.6 SWS07 – Fabry-Pérot Scan

SWS07 was the template used to take measurements using the Fabry-Pérot (FP). If requested, Short Wavelength grating observations of a type similar to those in SWS06 could be made in parallel.

For the FP the stepsize was always two FP units, about 1/4 of an FP wavelength resolution. Reset intervals were 1 or 2 seconds, with the dwell time equal to the reset interval. The number of scans was greater than, or equal to, three, and only up-scans were commanded.

Any requested SW grating observations were carried out in an identical manner to those of an SWS06 measurement, see Section 3.5.

Due to a slight internal misalignment of the Long Wave FP there were problems merging FP observations with grating observations when observing through aperture 3. The 'effective' aperture of the FP was displaced from the centre of the grating aperture by approximately $10''$, causing an approximately 40% drop in throughput of the FP when pointing was determined by the grating. The solution decided on was to define a fourth 'effective' aperture, centred on the FP aperture, and carry out all observations through this. This meant the SW grating lost approximately 40% of its throughput. Therefore LW FP observations (26 – 44 μm) and SW grating observations (7.0 – 13.16 μm) through aperture 3 could not be merged. Any requested aperture 3 grating observations were performed after the FP observations. This change was considered acceptable as the main purpose of SWS07 was FP observations. Merging was still performed on observations using apertures 1 or 2.

However, some early SWS07 observations were carried out before this change was implemented, and the archive contains observations containing FP data merged with SW grating observations in the range 7 to 13.16 μm.

Example of an SWS07 observation:

The SWS07 was executed by pointing the telescope to the target position, where the observation was started with a dark current. The FP lines and grating wavelength ranges specified in the AOT were observed. Each FP line was scanned at least three times and each SW wavelength range was scanned at least twice to provide redundancy. Dark current measurements were performed at regular intervals, at least before and after a set of FP scans on the same line and at least once before the reference wavelength of each SW range. FP scans may had to be broken into segments because the end of the mechanical FP range was reached. Then the scan had to be continued in a different FP order. In all FP scans the LW grating was scanned slowly in coordination with the FP scan to keep the pre-dispersion tuned to the actual wavelength. If the line list contained wavelengths corresponding to different SWS apertures, the aperture was switched accordingly and the satellite re-pointed to bring the source to the centre of the new aperture. At regular intervals, between observations, photometric checks were performed, at least once per AOT.

Figure 3.12 shows the LW grating position, the FP position and the resulting wavelength of light falling on the detector during part of an SWS07 observation.

Figure 3.13 shows ERD, SPD and aperture data for part of an SWS07 observation. The ERD is shown as readouts in bit values against time , and the SPD as signal (in μV/s) against time.

Figure 3.14 shows SPD signal (μV/s) and AAR flux (Jy), both against wavelength, for the same period of the example SWS07. Note the wavelength shift in the location of the peak between the SPD and AAR. This is because the SPD wavelength scale is 'ISOcentric', whereas the AAR is corrected to be heliocentric.

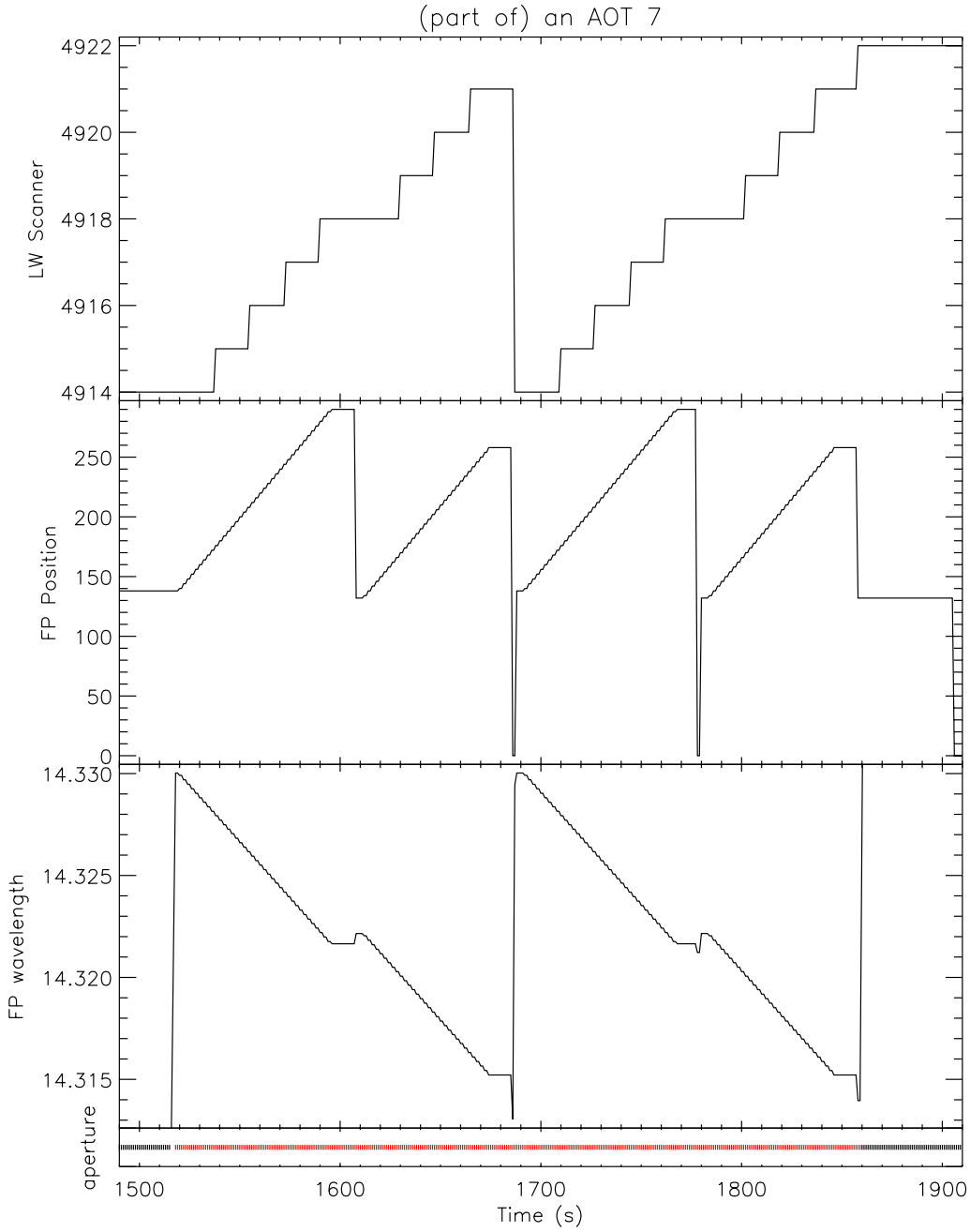

Figure 3.12: *LW grating position, FP position and wavelength (in μm) as a function of time for part of an SWS07 observation. Aperture colour codes are the same as in Figure 3.2.*

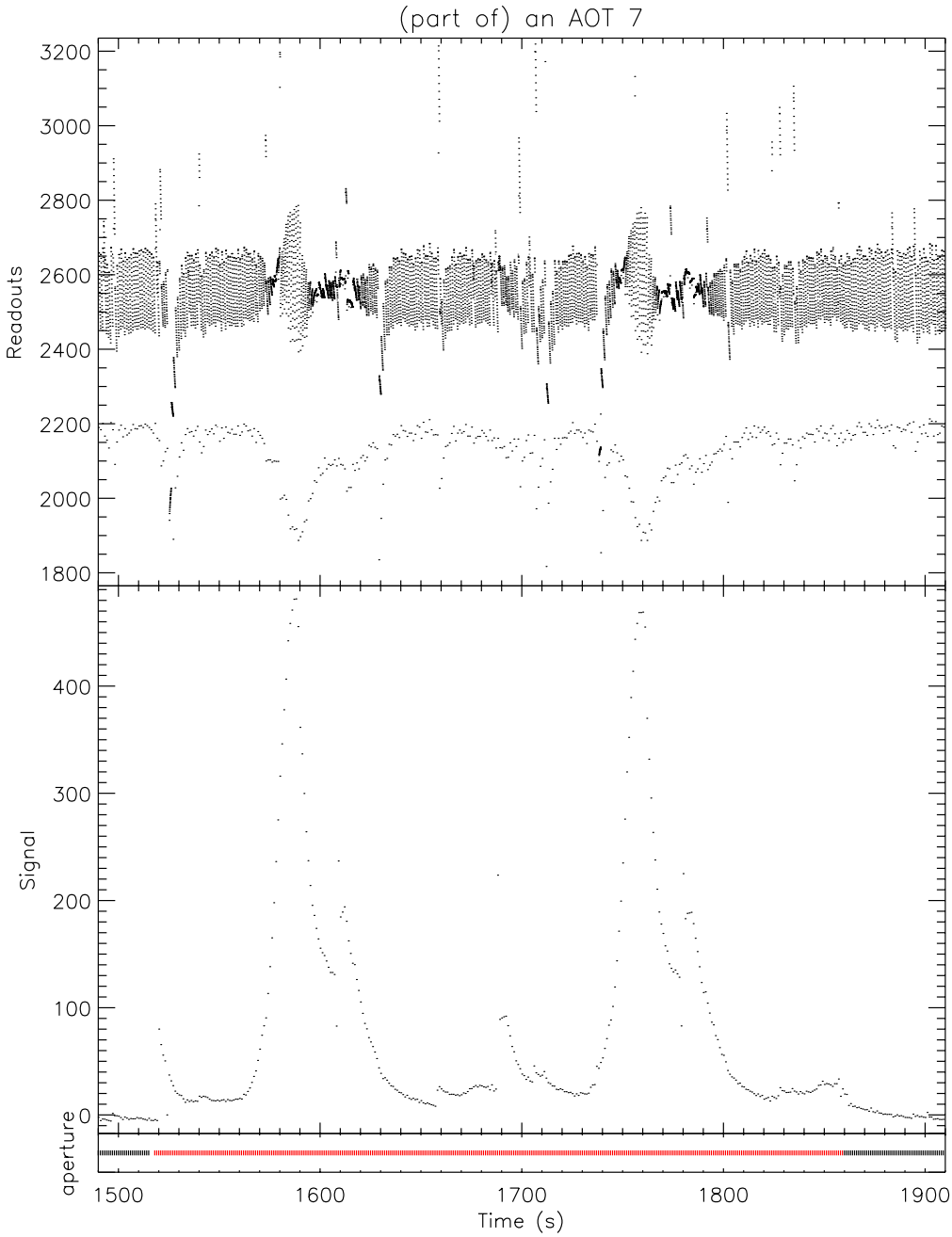

Figure 3.13: *ERD (in bits -upper panel) and SPD (in $\mu V/s$ - lower panel) data for part of an SWS07 observation. The FP is scanning across the line twice, going down in wavelength both times as can be seen from Figure 3.12.*

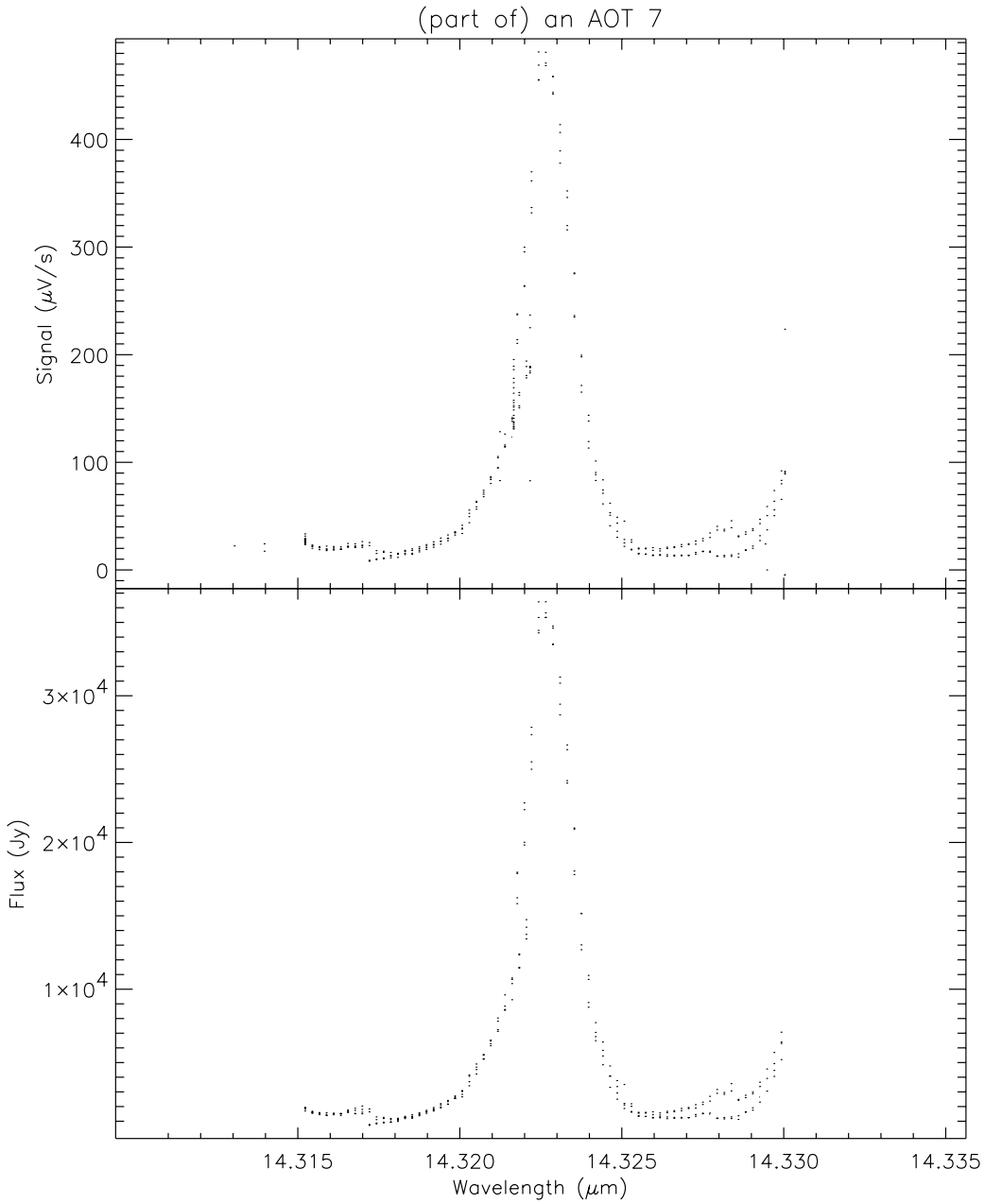

Figure 3.14: *SPD and AAR data for part of an SWS07 observation. Note the wavelength shift in the location of the peak between the SPD and AAR, due to the SPD wavelength scale being 'ISOcentric', whereas the AAR is corrected to be heliocentric.*

3.7 SWS99 – Post-Helium or Calibration Observation

After the liquid helium depletion of ISO, an engineering test programme was conducted on the different satellite systems. Besides functional tests of the various redundant systems, a lot of time was devoted to the testing of alternative pointing strategies in case of failure of one or more gyros.

During this test programme the temperature of the focal plane remained low enough to operate the InSb band 1 detectors of the SWS. The instrument could be operated in some timeslots available during the engineering test programme. This time was used to record spectra of stars between 2.36 and 4.05 μm at medium resolution ($\approx$ 1500 - 2000). As the temperature of the focal plane increased, changes in the position readout of the grating assembly and changes in the response of the instrument could be seen. These changes are detailed in Chapter 6.

3.7.1 The post-helium observation

The astronomical observation templates (AOT) of the nominal operations phase were not appropriate for the post-helium observations. A special observation mode was designed to avoid unnecessary energy dissipation by the long wavelength grating scanner and the heaters in the readout electronics of the detector blocks not used. The grating scanning ranges were limited to the angles corresponding to the wavelengths covered in AOT bands 1A to 1E. The observations were implemented and tested in the Calibration Uplink System (CUS). Therefore post-helium observations appear in the ISO Data Archive with observation type 'SWS99'.

The observation mode exists in two flavours. The fast version had a continuous scanning strategy like the nominal SWS01 speed 4 observation mode with a dwell time of 1/4 sec. The on-target-time was 2352 seconds. The slow version was scanning like in an SWS01 observation but with a dwell time of 1/2 sec. It lasted for 4408 seconds. At the end of the observation a dark current measurement and a photometric check was done. The internal calibration source was used at its maximum brightness.

The complete timeline of an SWS post-helium observation is summarized below.

1. Target Acquisition - point SWS aperture 1 to target
2. Setup the amplifier gain for band 1
3. Single scan up band 1A
4. Single scan down band 1A
5. Single scan up band 1B
6. Single scan down band 1B
7. Point SWS aperture 2 to target
8. Single scan up band 1D
9. Single scan down band 1D
10. Single scan up band 1E
11. Single scan down band 1E
12. Dark current measurement
13. Internal photometric calibration

3.7.2 Calibration observation

The SWS99 identifier was also used during the mission for non-standard calibration observations designed using the Calibration Uplink System (CUS). The CUS allowed Instrument Command Sequences (ICS) to be linked together in a flexible way to perform any kind of observation. While the CUS gave endless possibilities for how the observations would be performed, in practice most observations generated under this system were analogous to the AOTs. Consequently most CUS observations can be processed by the complete pipeline, yielding valuable and accessible scientific information on the sources observed.

3.8 SWS90–SWS98 – Engineering Observation

The SWS90–SWS98 were short sequences of commands for activation, de-activation and routine monitoring of the instrument, under direct control of the instrument operators. They are of little interest for observers but are included here for completeness.

They were:

SWS90: SWS switch-on and complete RAM load. Leave the detector biases switched off.

SWS91: Try and cure the detectors by heating the detector substrates to the maximum values (for this purpose electrical heaters were glued on the substrates).

SWS92: Switch on the detector biases, put the instrument in its default operational state.

SWS93: Try and cure the detectors by irradiating them with photons from the 'flashers'. For bands 2–6 this would have had no effect without the bias switched on.

SWS94: After the instrument has stabilised, or at any other moment, take a dark current measurement and then return the instrument to its default operational state. Introduced at the end of January 1996.

SWS95: SWS post-helium band 1 detector setup sequence.

SWS96: SWS post-helium band 1 internal wavelength calibration sequence.

SWS97: SWS post-helium band 1 internal grating calibration sequence.

SWS98: Switch off.

SWS99: Reserved for the CUS/post-helium.

At the start of a revolution SWS90 to SWS94 were executed in sequence to set the instrument up. SWS98 de-activated the SWS at the end of a revolution. For the post-helium revolutions SWS95 to SWS97 were used to activate the instrument, with SWS98 still used for de-activation.

Chapter 4

Wavelength Calibration and Resolution

4.1 Introduction

The astronomical product from SWS is a spectrum – an array of flux as a function of wavelength. Hence, a relationship must be established between each instrument position (either grating position or FP gap width) and its corresponding wavelength.

The general approach behind the wavelength calibration and its actual application is described primarily in two documents: Valentijn et al. 1996, [37]; and Kester, Beintema & Valentijn 1998, [18]. For the Fabry-Pérot there is a separate document: Feuchtgruber 1998a, [6]. This section is a summary of those papers, which should be read for a further understanding of the wavelength calibration of the SWS.

The gratings and FPs were characterised in the laboratory during a series of Instrument Level Tests (ILT), and a first approximation to the wavelength calibration was achieved. After launch this calibration was checked and updated. Throughout the mission the wavelength calibration was checked and refined.

4.2 Wavelength Models

4.2.1 Grating

For each grating section, rotating scan mirrors were used to vary the angle of incidence onto the gratings. The relation between the incident angles and the resulting reflected wavelength is given by the grating equation:

$$\frac{\lambda \times N}{D} = \sin(\theta + \beta) + \sin(\theta + \delta) \tag{4.1}$$

where β is the angle from the optical axis to the entrance or light source used, as seen from the collimator; δ is the angle from the optical axis to the detector pixel; θ is the angle of incidence on the grating for a beam entering along the optical axis for the current scanner position; D is the grating constant; and N is the spectral order.

The angle of the scan mirror, θ, is measured as a 'grating position' by a Linear Voltage Differential Transducer (LVDT) and colloquially given the units 'LVDT'. As a first approximation the relation between scan angle and LVDT reading is well represented by a linear relation. However, the high wavelength

calibration accuracy required modelling of the non-linear residuals in the θ-LVDT relation. It was found from the ILT calibration that this relation could be adequately described by a fifth order polynomial function. Eighteen constants were needed to be determined for a full description of the wavelength calibration: 6 for the polynome, 3 for the aperture offsets, 6 for the detector arrays and 3 for the offset angles to the grating and FP wavelength calibration sources. The offset angles to the detector bands were described for each array with an offset to the first array elements plus a constant pitch value between the elements.

In ground-based instrument level tests, the relation between grating position readout and physical grating angle was determined by measurement of wavelength references in the form of vapour absorption lines (H_2O, NH_3, HCl). The spectral features provided by the internal grating wavelength calibrator have been tied to that scale.

4.2.2 Fabry-Pérot

A Fabry-Pérot etalon transmits only those wavelengths which fit a whole number of times within the gap between the etalon meshes.

$$\lambda = d/N \tag{4.2}$$

where d is the (optical) gap width and N is an integer number (typically a few thousands). The optical gap is related to the mechanical gap which in turn is derived from the FP position as is explained in Section 7.2.11.2.

For the Fabry-Pérot, the position-gap relation has been determined from the spectrum of the internal FP wavelength calibrator, which is known to high accuracy from Fourier Transform Spectroscopy. H_2O and NH_3 vapour absorption lines have been used for additional checks and for determination of the variation of effective FP gap with wavelength.

In orbit, the grating position-angle relation and the FP position-gap relation was re-established during the PV phase, first using the internal calibrators and then astronomical sources. It was then checked regularly during the mission.

4.3 Wavelength Calibration Methodology

In the pre-flight ILT measurements H_2O, NH_3 and HCl vapour cells and a set of lasers at 4, 10, 16 and 28 μm were used as SWS input sources to obtain wavelength calibration data. Analysis of these data resulted in a set of tables and constants defining accurately the relation between wavelength and scanner angle for the 3 aperture slits and the 6 detector arrays.

4.3.1 Grating

During the ILTs the internal SWS wavelength calibration sources were also used. Two for each grating section, positioned next to the entrance apertures, and one for the FPs. For the grating sections these sources consist of a hot element with a fixed FP, producing a series of fringes. The wavelengths of these fringes were calibrated using the vapour source calibration taking into account a correction needed for the off-aperture location of the internal sources.

In-orbit, first the internal wavelength calibration sources were measured again, to check for possible changes due to launch vibration effects and the effects of zero-gravity, and used to update the θ-LVDT relation. From this measurement a first order correction to the pre-flight wavelength calibration was derived. The difference between the pre-flight and in-flight calibration was mainly a zeropoint shift, 25 LVDT units for the SW section and 10 for the LW.

To establish the wavelength calibration a number of emission lines of Planetary Nebulae (PN) NGC 6543, NGC 7027, IC 2501, NGC 3918 and NGC 6826 were observed (see Table 4.1). All but IC 2501 are extended for the SWS. As most of the PNs filled the slit, pointing errors became irrelevant for the wavelength calibration. These data were used to further update the angles. For the LW section these additional corrections were equivalent to 0.8 LVDT for the wavelength calibration source angle and 0.3 LVDT for aperture 1. For the SW section, the correction was 6.5 LVDT for detector band 1.

Also used were observations towards η Car with the FP in a fixed position and the grating scanning. The wavelength calibration of the FP for the peaks of the fringes from the strong continuum was used to update the wavelength calibration for wavelengths above 35 μm where suitable emission lines in PN are lacking. This relied on the (ground-based) calibration of the FP.

Table 4.1: *Lines used for grating wavelength calibration*

Ion	Wavelength [μm]
[Mg IV]	4.488
[Ar VI]	4.527
[Mg V]	5.608
[Ar II]	6.895
[Ar III]	8.991
[Si IV]	10.510
[Ne II]	12.814
[Mg V]	13.521
[Ar V]	13.102
[Ne III]	15.555
[S III]	18.712
[Ne V]	24.318
[O IV]	25.890
[S III]	33.481
[Ne III]	36.014
plus H recombination lines	

4.3.2 Fabry-Pérot

The situation for the FPs was different. Here the internal wavelength calibration source was a fixed, stable FP, providing a series of very narrow transmission peaks. The in-orbit wavelength calibration of the two FPs relied mainly on the ground calibration of these peaks which was assumed to be unchanged in-orbit. Line observations towards astronomical sources were used for confirmation only.

The SWS Fabry-Pérot calibration source had a fixed FP with twice the thickness of the scanning FP, providing a very fine grid of narrow transmission peaks around 25 μm. The wavelengths of these transmission peaks were accurately determined (0.001 cm^{-1}) at liquid helium temperature using a Fourier Transform Spectrometer (FTS). A few of these peaks were first used for the automatic parallelisation procedure which used the on-board computer and adjusted the plates holding the mesh by maximising the peak intensities. A large number of the transmission peaks were subsequently used to determine the actual gap of the FP and to linearise the gap-position relation. After analysis of these data the on-board drive current lookup table could be updated.

As the LW grating section serves as order filter for the scanning FPs and as the free spectral range of the FPs is close to the grating spectral resolution, the wavelength calibration of the LW grating is critical

for the FP operation and had to be carried out first. However, it does not affect the FP wavelength calibration.

4.4 Wavelength Calibration Accuracy

The goal of wavelength calibration was to achieve an accuracy of between 10 and 20% of a resolution element for the two gratings. An accuracy of 10% was hoped for the LW grating as this is used by the FP wavelength calibration.

4.4.1 Grating

Overall the wavelength calibration stabilisation was kept accurate to within 1 LVDT during the mission. This was achieved by updating the calibration files at irregular intervals. After about one year of operations it became clear from the biweekly quick grating wavelength checks that the calibration was shifting slightly. In revolution 356 and 370 full grating scans, illuminated by the grating calibration source, were therefore performed to check on this, and the shift was corrected by an update of the calibration files. Three more full grating scans were performed in revolutions 475/479, 669/670, and in the last month before helium boil-off. During the Post-Helium Phase partial grating scans were done each day to keep track of the wavelength calibration which in this phase was fast changing due to the increasing temperature in the focal plane. All these scans were analysed resulting in updates to the grating polynome.

As it became apparent that regular updates of the grating polynome would be necessary, it was also decided to have a regular look at some external source with strong emission lines. Between revolution 360 and 800 27 of these observations were performed on NGC 6543, observing 8 lines in the SW section and 5 in the LW section. The lines were analysed, and one noticeable effect was discerned, a slowly increasing trend in LVDT against time. This indicated that a more precise wavelength calibration would be possible by linear interpolation of the calibration files, and this was available from OLP V8.4 onwards.

The errors expected on the wavelength calibration of the grating are shown in Table 4.2. It lists the requirements on ISO, what has been achieved in ground tests and during operations. The limitations on the grating wavelength calibration accuracy appear to come mainly from pointing errors, see Section 8.6.

Table 4.2: *Grating wavelength calibration errors.*

	SW	LW	
		$< 40\mu$m	$> 40\mu$m
Requirements	$< \lambda/10000$	$< \lambda/10000$	$< \lambda/10000$
Obtained in ILT	< 1 LVDT	$< 0.5 - 1.0$ LVDT	2.0 LVDT
	$\lambda/10000$	$\lambda/12000 - \lambda/20000$	$\lambda/6000$
Flight Achieved	1 LVDT	0.5 - 1 LVDT	
	$\lambda/5000 - \lambda/12000$	$\lambda/8000 - \lambda/16000$	

4.4.2 Fabry-Pérot

For the two FPs relevant information concerning wavelength calibration accuracies is shown in Table 4.3. Throughout the mission no wavelength shifts of more than 1 FP scan step were found, within the requirements listed in the table. More information on this can be found in Feuchtgruber 1998a, [6].

The accuracy of the internal wavelength calibration was, as expected, about 1 FP scanner step at $24\,\mu$m, which corresponds to about 10^{-4} μm. However, the effective FP gap is slightly dependent on wavelength,

Table 4.3: *FP wavelength calibration errors.*

	SW-FP1	LW-FP1
Requirements	$< \lambda/100000$	$< \lambda/100000$
Obtained in ILT	$\lambda/125000$	$< \lambda/125000 - \lambda/200000$
Flight Achieved	$\lambda/100000$	$\lambda/100000$

because shorter wavelengths penetrate deeper into the reflecting meshes. During the ILTs, vapour absorption lines were measured to determine this gap correction, which had a maximum of about one FP resolution element over the full wavelength range of the FPs. Remaining uncertainties of this correction and the memory effects of the Si:Sb detector material used in the shortwave FP section cause a final uncertainty in the wavelength calibration of 2 FP scanner steps between 11.4 and 26 μm, and 1 FP scanner step between 26 and 44.5 μm. Regular checks of the internal calibration during PV and routine phase indicate excellent stability.

The verification of the wavelength calibration by observations of external spectral lines suffered from the lack of accurate wavelength standards and radial velocities. However, a few lines could be used to verify the internal calibration and the resulting accuracy was 1/3 of a resolution element or better.

4.5 Instrumental Profile and Resolution

4.5.1 Grating

The instrumental profile intrinsically provided by the grating section of SWS is correctly reproduced in observations done with the SWS02s and SWS06s (and grating observations in SWS07s if such were requested). For SWS01s, grating motions during a detector reset interval are used to speed up execution. These lead to a degradation compared to SWS' physical resolving power. Resolution and other instrumental profile characteristics achieved with SWS are outlined in this section and are reviewed in more detail in the documents by Lutz, Feuchtgruber & Morfill 2000, [29], for SWS02 and SWS06 and by Lorente 1998, [28], for SWS01.

It should be emphasized that resolution values quoted here refer to the resolution as measured by Gaussian fits to the AAR 'dot cloud'. However, essentially all SWS data reduction recipes involve a step of 'rebinning' or 'convolution' aiming at collapsing the dot cloud into a single valued spectrum. Necessarily, this has an effect on the resolution measured in the final spectrum whose magnitude sensitively depends on the chosen parameters and easily reaches 10% or more. Since, for good reasons, different routines and widely varying parameters are chosen, by different users and for different projects, no general 'resolution' can be quoted for a rebinned spectrum. Users who need to base their analysis on accurate linewidths from rebinned spectra should estimate this effect themselves for the exact parameter combination adopted in their data reduction.

4.5.1.1 Resolution and instrumental profile in SWS02 and SWS06

The SWS grating mode spectral resolution is a function of wavelength as well as source size. Figure 4.1 shows the resolution for several source sizes, as derived from an empirical model based on a large set of observations in the ISO database. It is estimated that this model fits the true SWS resolution to an accuracy of about 10%.

The SWS Instrumental Profiles are close to Gaussian in shape from the peak down to 5% of the peak height. The most significant deviations are faint blue wings at the few % level in band 3 which are most likely due to an optical effect in the instrument. Band 2 and more clearly band 4 bright lines have

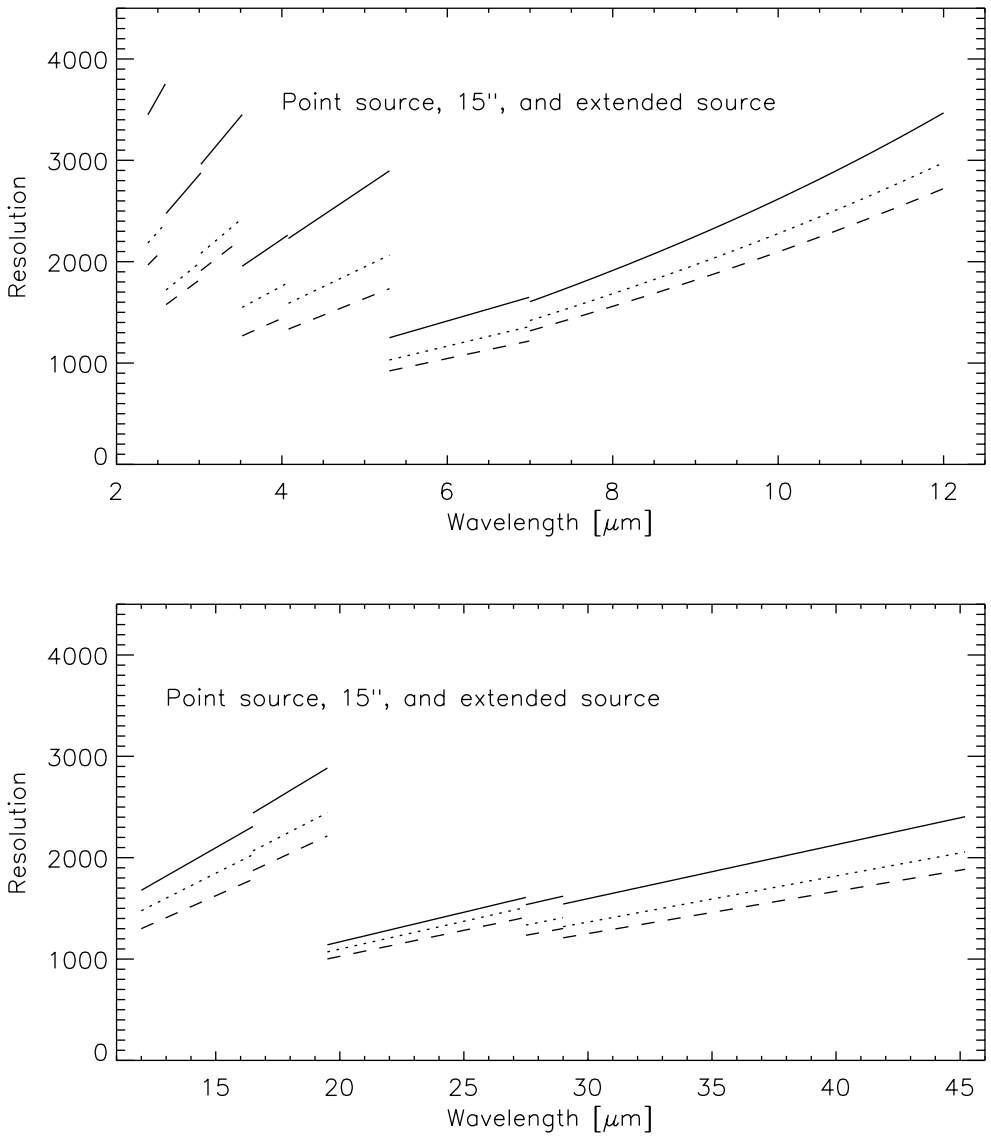

Figure 4.1: *Spectral resolution of SWS02 or SWS06 observations for a point source (continuous), a 15″ diameter source (dotted) and a fully extended source (dashed) as predicted from an empirical model.*

faint (few % level) wings on both sides that can be traced to detector transient effects in the up- and down-scans. The FWHM resolution is effectively unchanged by these transients. No 'ghost' lines have been observed near bright lines.

4.5.1.2 Resolution and instrumental profile in SWS01

The document of Lorente 1998, [28], gives observed and modelled resolving powers, and simulated line profiles for the four observing speeds of SWS01. Modelling of SWS01 line profiles is more complex than a simple convolution in the spectral domain because the pipeline fits straight lines to the detector

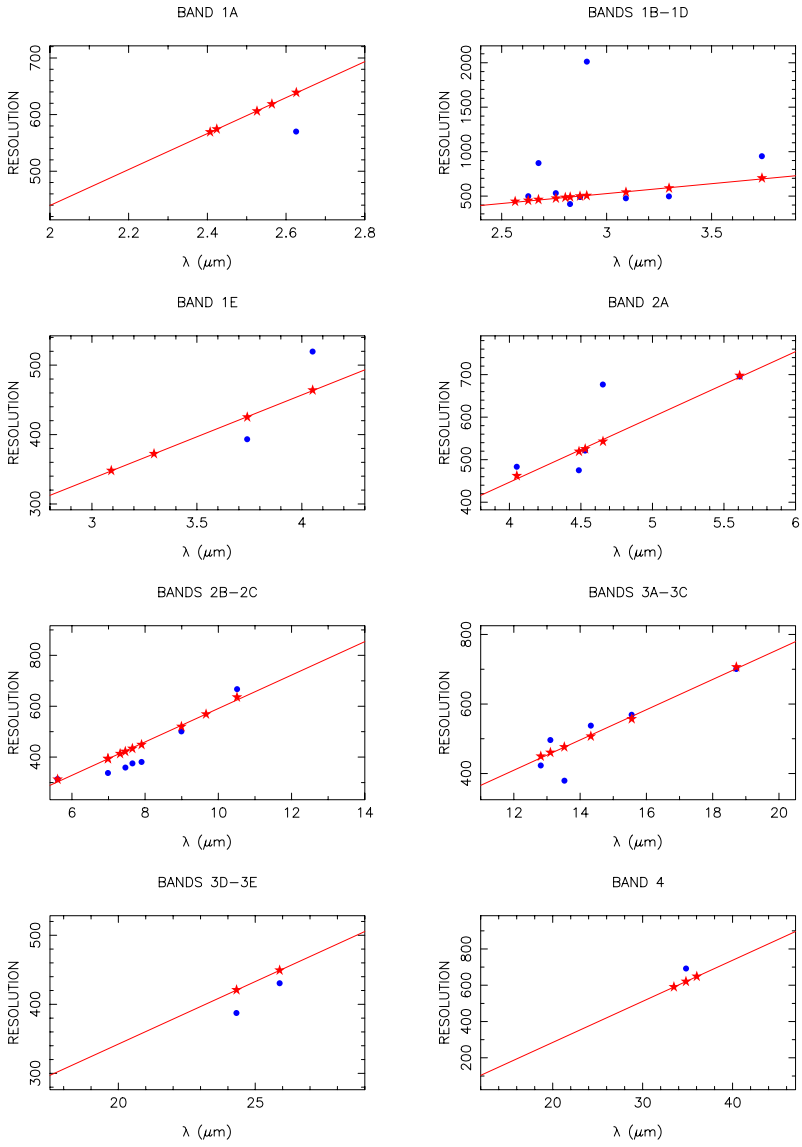

Figure 4.2: *Observed and theoretical resolutions for SWS01 speed 1. Stars correspond to theoretical resolution values, fitted by a straight line. Dots represent observations. Bands which have a continuous trend in the resolution (same detector, slit width, and grating order) have been plotted in the same panel.*

integration ramps, even if they are curved because a line was crossed during an SWS01 reset interval. Figures 4.2 to 4.5 show measured and modelled resolutions for the various SWS01 speeds and the various bands. Note that some of the measured lines are very faint, giving outlying resolution values. Table 3.1 (Chapter 3) gives approximate values for the SWS01 pipeline resolution degradation, i.e. the factor by which the resolution of the spectrometer is degraded for SWS01 data processed by the pipeline. The SWS01 line profiles are noticeably non-Gaussian, but their FWHM is always within 10% of the FWHM to a Gaussian fit.

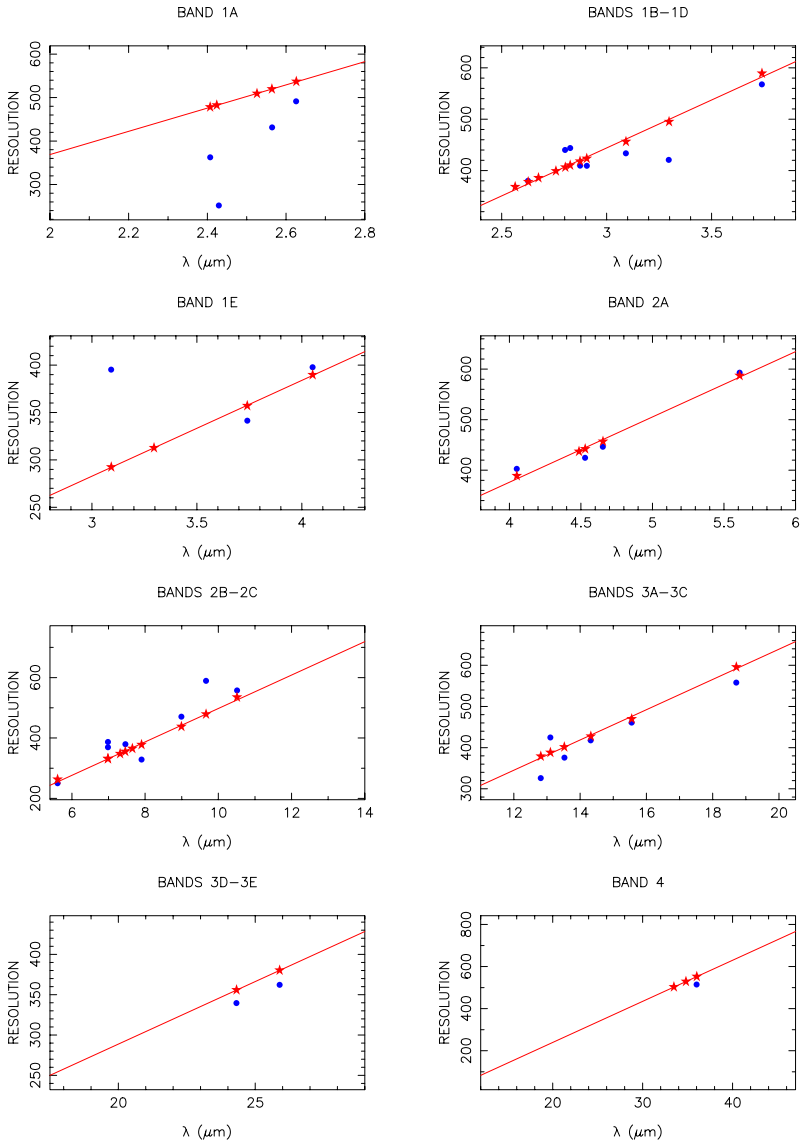

Figure 4.3: *Observed and theoretical resolutions for SWS01 speed 2. See Figure 4.2 for further explanations.*

4.5.2 Fabry-Pérot

4.5.2.1 Spectral resolution

The Fabry-Pérot spectral resolution was measured in laboratory tests at a few discrete wavelengths using solid state laser sources. Figure 4.6 shows the spectral resolution as a function of wavelength, interpolated between these measurements. The spectral resolution decreases towards the short wavelength ends of the wavelength ranges covered by the two Fabry-Pérots, where the wavelengths corresponding to the resonances of the reflective meshes are approached. The Fabry-Pérot spectral resolution depends on precisely parallel FP plates.

Measurements of the Fabry-Pérot spectral resolution in-orbit suffered from the lack of bright, narrow

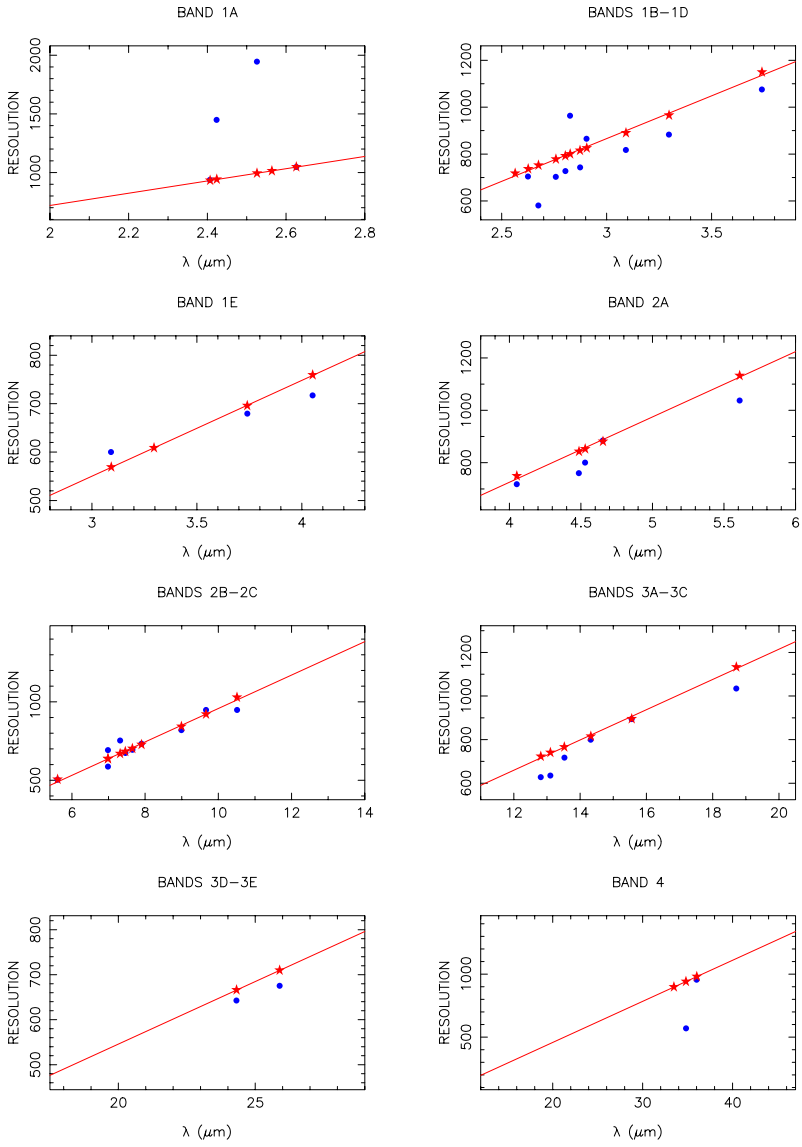

Figure 4.4: *Observed and theoretical resolutions for SWS01 speed 3. See Figure 4.2 for further explanations.*

lines. Three lines were measured and lower limits found to the spectral resolution that were very close to expectations. This is reported in Valentijn et al. 1996, [37]. The lower limits are plotted in Figure 4.6.

4.5.2.2 Tracking noise

The coordination between Fabry-Pérot scans and the movement of the grating that tracks the FP scan is a source of signature (or, loosely, 'noise') that ultimately limits the quality of FP spectra on bright sources. For all but very short FP scans, the wavelength sampled by the FP would soon be no longer tuned to the transmission peak of the grating if there were no tracking. The discrete steps of the grating's tracking movement result in the final FP scan of a pure continuum source looking like a repetition of a small section of the grating instrumental profile.

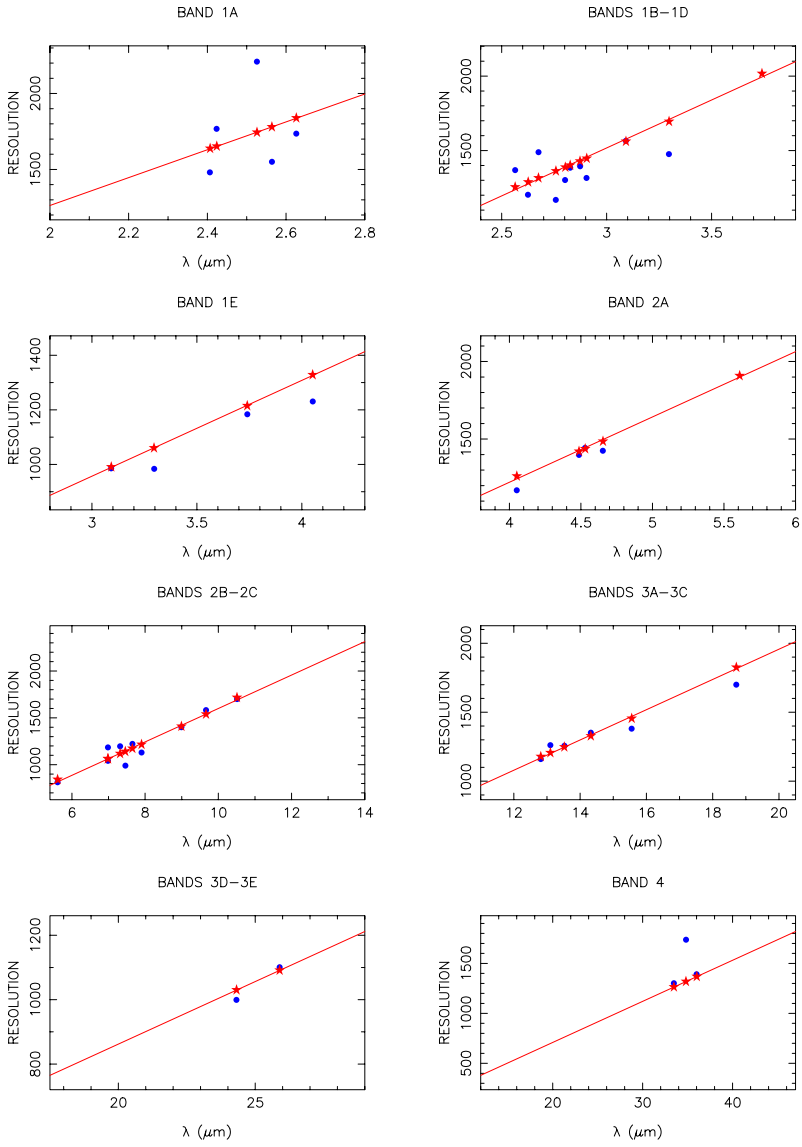

Figure 4.5: *Observed and theoretical resolutions for SWS01 speed 4. See Figure 4.2 for further explanations.*

The amplitude of this 'noise' depends on various factors like quality of grating wavelength calibration, ratio between grating stepsize and line profile FWHM, or pointing stability. It is hence difficult to predict for an observation at a certain wavelength. Instrument level tests with optimised grating wavelength calibration showed 'signal-to-noise' ratios of around 200. In the case of an observation of a single line on a smooth continuum, part of the 'noise' could be calibrated out by observing a larger region of continuum around the line, provided the non-systematic contribution of pointing jitter is not too large.

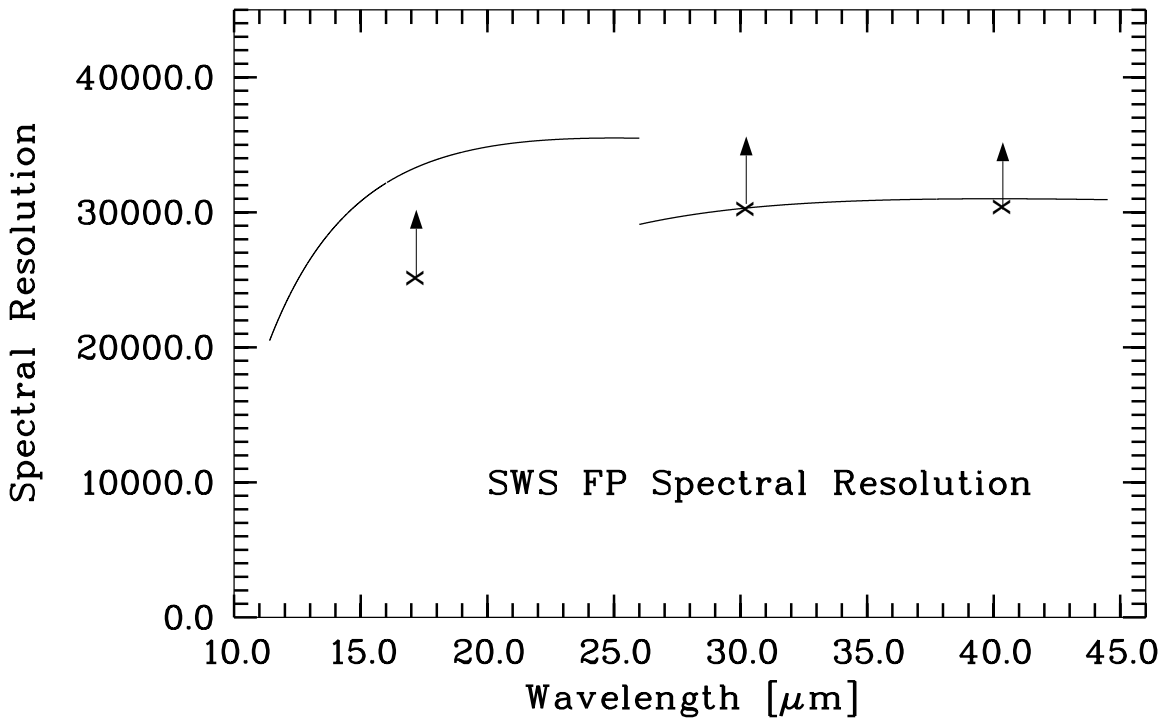

Figure 4.6: *SWS Fabry-Pérot spectral resolution as a function of wavelength, computed from measured mesh properties and confirmed by checks at three wavelengths, as shown by lower limits.*

Chapter 5

Photometric Calibration

5.1 Introduction

This chapter describes the photometric calibration of SWS and the expected accuracy. The chapter is organized to follow the general flow of the pipeline processing (see Section 7.3). In Section 5.3 we discuss the method by which the dark current is measured and the uncertainties associated with the dark current measurement. Section 5.4 discusses the Relative Spectral Response Function (RSRF) and the related uncertainties. Section 5.5 presents the application of the internal calibration measurements to correct for sensitivity drifts in time. Section 5.6 presents the pipeline flat-fielding. Section 5.7 discusses the conversion of the internal SWS signal to astronomical units for point sources while Section 5.8 shows how to derive the surface brightness of extended sources. The final section (5.9) of this chapter presents our best understanding of the uncertainties present in the calibrations and in the AAR products of SWS.

5.2 Photometric Model

This section describes the model used for converting measured slopes in μV/s, (see Chapter 2.4) to absolutely calibrated flux densities (in Jy). The measured slope, S, is a linear combination of the source flux incident on the detectors, instrumental gain G, the dark current D and the Flux conversion factor G_c. This is described by the following equation:

$$F(\lambda) \quad = \quad G(t, block, det, aotband, \lambda) \cdot G_c(aotband) \cdot (S(t, \lambda) - S_d(t)) \tag{5.1}$$

where t is the time of the observation, *block* is the detector block, *det* the detector number, *aotband* is the unique combination of detectors, apertures, and orders to describe a wavelength range, and λ is the specific wavelength. The different types of detectors (e.g., In:Sb) are grouped into 6 different blocks. Blocks 1 through 4 refer to the grating detectors and each block has 12 detectors. Blocks 5 and 6 are Fabry-Pérot detectors and each of these blocks only has 1 active detector.

Note that in Equation 5.1 it is implicitly assumed that *all* memory effects (see section 9.2) can be neglected or have been removed.

The instrumental gain is split into several orthogonal components:

$$\begin{aligned} G(t, block, det, aotband, \lambda) \quad = \quad & G_p(t, block) \cdot \\ & G_f(det, aotband) \cdot \\ & G_r(detector, \lambda, aotband) \end{aligned} \tag{5.2}$$

G_p accounts for time variations in the detectors response at the time of observation but is assumed constant within the observation. This correction brings the measurement to a standard time determined by

the Cal-G 41. The correction is calculated from observations of the internal grating calibrator. Traditionally these observations are called 'photometric checks'.

G_f corrects for the response of an individual detector relative to the average of the detectors. This gain brings the response of all the detectors (within a band) to that of one average detector. The flat-field coefficients are found in the Cal-G 43. The Fabry-Pérots do not have any flat-fielding values applied since they are single detectors and not in blocks.

G_r corrects for the response of a detector at wavelength λ (anywhere within the band) relative to the response of that detector at an optimum system response wavelength of the band. The gain factor, G_r, is called the Relative Spectral Response Function (RSRF).

The Relative Spectral Response Function characterises the wavelength dependent response of SWS. The wavelength range of the grating section of the ISO-SWS is covered in 15 overlapping spectral bands. Each of these channels, sometimes also referred to as AOT-bands, are characterised by a unique combination of the instrument aperture, the grating order, the detectors used and a set of order selection filters in the light path. Therefore every detector has a different RSRF in every band. In each band, a block of 12 detectors is used. Thus, the complete RSRF behaviour of the SWS grating section is characterised by 12×15 RSRF functions. The RSRF functions are retained in calibration files Cal-G 25_xx.

In each of the 10 independent SWS gratings and 5 independent SWS Fabry-Pérot (FP) bands a wavelength and a bandpass have been chosen where the RSRF is at its maximum, and where the spectra of the calibration standards are featureless. These so-called 'key wavelengths' (listed in Table 5.3) were used for determining the scaling constants between signal (μV/s) to flux density (Jy). The grating calibration made use of SWS06 observations of astronomical standards centred at these 'key wavelengths' over the corresponding passbands.

G_c is the conversion factor from corrected signal in μV/s to flux density units in Jy. These numbers are retained in calibration file Cal-G 42.

For the Fabry-Pérot mode, sources considered to be continuum in their emission at the FP key wavelengths were observed. They are listed in Morris 1999, [30].

Following Equation 5.1 the actual source flux $F(\lambda)$ is reconstructed by first subtracting the dark current from the measured slopes, and subsequently applying the instrumental gain and the flux conversion to convert the signal within the band to flux in Jy.

5.3 Dark Current Subtraction

5.3.1 Detector noise & dark current

Nominal detector dark noise and dark current values for individual detectors are stored in calibration files Cal-G 21_n, where n equals one of 1, 2, 4 or 8 for the different reset intervals. Units are μV/s. In the standard processing, this calibration file is used to issue warnings when a particular detector is very different from the nominal value. Note that 4 and 8 second resets were only used early in the mission for calibration measurements.

Checks were made at the start of every revolution for the purpose of characterising the dark current and noise throughout the mission. It was found that they were stable for all bands except band 3. Here, the dark currents increased by up to a factor of three during the mission, while the dark noise hardly increased for most detectors. In most cases the increase in dark currents was gradual, but occasionally the dark current suddenly jumped to a higher level, e.g. detector 36 (band 3 detector 12) in revolution 150. Dark currents also decreased: after 250 revolutions of relative high dark currents, those in detector 36 dropped to one-fifth of their high value.

Some detectors had either an exceptionally high dark current and/or a high noise. These have been dubbed 'bad' detectors. Which detectors in a band are or are not good can change. For example, at the

start of the mission band 3 detector 34 was poor. After PV, when its bias voltage was changed, detectors 30, 31 and 36 were the worst in that band.

The dark currents were higher at the start of a revolution for all bands, decaying with time so that after about four hours they had reached their nominal values. This was the case for bands 2, 4 and 6, with dark currents between 15% and 100% higher than nominal at the start of a revolution. This effect was less important for bands 3 and 5, while for band 1 it was only observed in a few detectors.

Normally all changes in dark current will be automatically corrected during the pipeline processing, see Section 7.3.3. Cases where the continuum is weak can cause problems for dark current subtraction. When the amount of flux falling on the detector is small, there may be cases where the output of the detector from *incident flux + dark current + noise* is less than the output from *dark current + noise*, the end result being negative fluxes in the AAR product.

The straightforward dark current subtraction for bands 1, 3, 4, 5 and 6 is described in Section 7.3.3. No models to correct the data for memory effects could be found for band 4 and, as a consequence, dark current subtraction for this band is the same as bands 1 and 3. For band 2 however, a method was found to model the signal falling on the detectors which incorporates a dark current correction.

5.3.2 Dark current correction for band 2

The band 2 dark current subtraction is closely tied to the band 2 memory effect correction. The memory effect for Si:Ga detectors (band 2) as described by the Fouks-Schubert model (Fouks & Schubert 1995, [10]) is an additive effect. As such, its proper correction takes place during the dark current subtraction.

An adapted version of the Fouks-Schubert model was developed by Do Kester and successfully implemented in the SWS pipeline to correct band 2 data for transient effects. The method can bring the errors (of sometimes up to 20%) down to the few percent level. This is described in Kester 2001, [22] and García-Lario et al. 2001, [11].

Section 9.2 gives a complete description of the implementation of the band 2 memory correction in the SWS pipeline.

5.4 The Relative Spectral Response Function (RSRF)

This section presents a description of how the RSRF was measured during the Instrument Level Tests (ILT) (Feuchtgruber 2001, [9]) before launch, and how it was corrected based on in-orbit measurements of stellar calibration sources. The accuracy of the RSRF calibration is indicated and the remaining artifacts are discussed. More information on the calibration of the RSRF can be read in Vandenbussche et al. 2001, [41], and Vandenbussche 1999, [40].

5.4.1 RSRF measurements before launch

Prior to launch, the RSRF was determined during the instrument level tests. The measurements consisted of SWS spectra of a cryogenic blackbody calibration source at full spectral resolution, fully sampled in every detector. The calibration source fully filled the SWS apertures. Several scans were performed through the different SWS apertures and with blackbody temperatures ranging between 30 and 300 K. The spectra obtained were then divided by a Planck function of the corresponding blackbody temperature to obtain the RSRF. Figure 5.1 illustrates this calibration process.

5.4.2 In-orbit verification of the ILT RSRF

After launch, the accuracy of the ILT RSRF was verified by comparing SWS observations to synthetic spectra, composite spectra or template spectra for various sky calibration sources. This comparison revealed both broadband errors and small-scale errors.

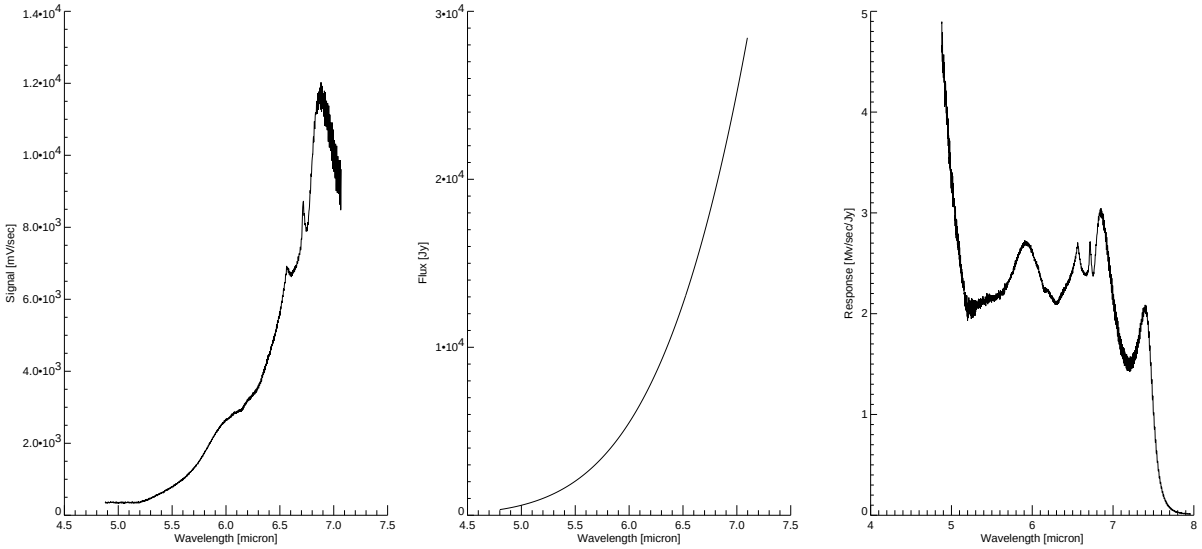

Figure 5.1: *Determining the RSRF from pre-launch SWS measurements of a blackbody in the lab. The left panel shows the response of an SWS detector during a scan in band 2B of a 173K blackbody. The middle panel shows a Planck curve for this blackbody temperature. The right panel shows the division of the two. This is the Relative Spectral Response for this detector in band 2B.*

Figure 5.2 shows the broadband differences between a composite spectrum by Cohen et al. 1992a, [2], and an SWS observation of Sirius.

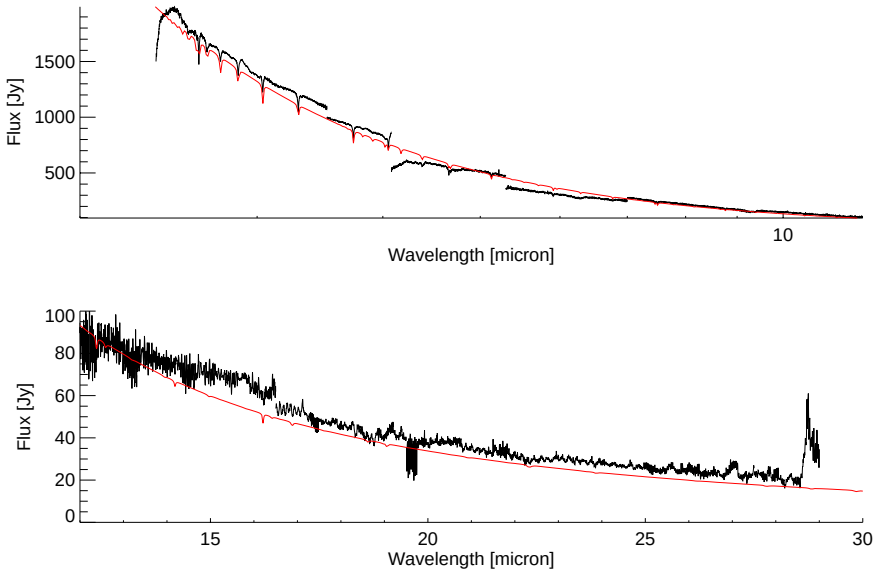

Figure 5.2: *Comparison of a composite by Cohen et al. 1992a, [2], and the SWS spectrum of Sirius. The spectrum was calibrated with the RSRF derived from the pre-launch blackbody scans. Top: SW section; bottom: LW section.*

Several effects e.g., differences in nature of calibration sources (extended vs point source), leaks in laboratory setup filters, diffraction losses and uncertainties or small drifts in the blackbody temperature, are responsible for the broadband errors in the pre-launch RSRF.

The SWS RSRF has been corrected for broadband differences between in-orbit observations and reference spectra, except for band 4, see Section 5.4.5.4. The quality of this correction improved in the course of the project as more SWS spectra of calibration stars were observed and the reference spectra available became more accurate.

5.4.3 Spline smoothing of residues

Fitting polynomes to the residues was clearly not optimal for the variety of shapes present in the residues. The problem with polynomial fits is that a local bias always translates to a global bias, e.g. strong oscillations in the high-order components of a polynomial fit to noisy data. Therefore a method of smoothing the residues with a cubic spline was adopted.

A spline function $S^{(m)}$ of order m with knots x_i, $i = 1..k$ is a set of functions F_j, $j = 1..k-1$ that are defined over the intervals $[x_0,x_1]$, ... $[x_{k-1}, x_k]$ and stitched together in the knots so that the combined function S^m is m times continuously differentiable at the knots. The functions F_j are often cubic polynomes (n=3).

Späth et al. 1995, [36], describes various algorithms to smooth a dataset using splines. An algorithm has been adopted to smooth a dataset (x_i, y_i), $i = 1,..,k$ by determining a cubic spline $S^{(2)}$ for which $w_i(S^{(2)}(x_i) - y_i)^2 < P_i$, $i = 1,...,n$. w_i are weights for the datapoints and P_i is a parameter for the smoothness in knot k_i. w_i and S_i are combined into one knot parameter s_i. Varying this parameter in a knot will result in a smoothing spline which is more 'stiff' or which follows the dataset more accurately in that region.

Cubic spline smoothing allows to make the correction curve follow the features in the residues where they are understood to be instrumental. In regions where the residues are believed to be unreliable (less accurately modelled features in the synthetic spectra, etc...) the spline smoothing curve is forced to be more 'stiff'. Therefore it is necessary that one understands the strong and weak points in the reference spectra and datasets used.

This method was implemented for every band and every detector as follows: for a selected set of calibration sources and reference spectra we calculated ratios *(observation/model)*. The ratios are averaged over bins of $\lambda/\delta\lambda$=200).

The data points in the average ratio are then taken as the knots for a cubic spline smoothing. The local stiffness of the smoothing spline is tuned in an Interactive Analysis widget tool, and the resulting spline is then evaluated in the wavelengths sampled in the ILT RSRF. These factors are multiplied with the responses in the ILT RSRF to obtain the corrected RSRF.

After carefully studying many sources observed by the SWS, four features in the residues (9–9.3, 10.1, 11.0 μm in band 2C and at 12.3 μm in band 3A) were understood as inaccuracies in the RSRF, e.g. the result of a strong memory effect while scanning over a feature in the RSRF during the ILT tests. Therefore, the smoothing spline was allowed to be less strict in this region following the shape of the knots.

5.4.4 RSRF calibration sources

The calibration sources were selected to cover a wide diversity in spectral types. This allowed the avoidance of biases to spectral features typical for different spectral classes. The RSRF used in the processing of the ISO Data Archive (OLP Version 10.1) has been corrected using the stars in Table 5.1. For the shortest wavelength section (< 4 μm and band 5.3–6 μm)) we used synthetic spectra based on MARCS models by Decin 2000, [4]. For bands 2A and 2C only sources with spectral type G9 and earlier

were used. For the long-wavelength section, composites by Cohen et al. 1992a, [2] were used. Composites are pieces of synthetic spectra and real data spliced to photometric points.

Due to a lack of suitable observations (i.e. a decent S/N) of calibration targets with a well known energy distribution in the region 30–45 μm, no correction was applied on the RSRF for band 4.

Table 5.1: *The calibration sources used for the correction of the RSRF in OLP Version 10.1, the version of the ISO data reduction pipeline used for the ISO Data Archive.*

Source	HR	Spectral type	Wavelength range [μm]
α Lyr	HR 7001	A0V	2.3 – 30
α CMa	HR 2491	A1V	2.3 – 30
β Leo	HR 4534	A3 V	2.3 – 4
α Car	HR 2326	F0 II	2.3 – 12
α Cen A	HR 5459	G2 V	2.3 – 30
δ Dra	HR 7310	G9 III	2.3 – 12
α Boo	HR 5340	K1.5 III	2.3 – 4, 5.5 – 7, 10 – 30
ξ Dra	HR 6688	K2 III	2.3 – 4, 5.5 – 7, 10 – 12
β UMi	HR 5563	K4 III	2.3 – 4, 5.5 – 7, 10 – 12
γ Dra	HR 6705	K5 III	2.3 – 4, 5.5 – 7, 10 – 30
α Tau	HR 1457	K5 III	2.3 – 4, 5.5 – 7, 10 – 30
HD 149447	HR 6166	K6 III	2.3 – 4, 5.5 – 7, 10 – 12
β And	HR 337	M0 III	2.3 – 4, 5.5 – 7, 10 – 30
α Cet	HR 911	M2 III	2.3 – 4, 5.5 – 7, 10 – 30
β Peg	HR 8775	M2.5 III	2.3 – 4, 5.5 – 7, 10 – 30

5.4.5 Accuracy of the RSRFs

5.4.5.1 Residues of artifacts in the ILT RSRF

As mentioned in Section 5.4.3, several features in the ILT RSRF of band 2C and one feature in band 3A were understood to be artifacts. Although the RSRFs have been corrected for these features, residues of them can remain in these wavelength regions.

The wavelength regions that therefore deserve special care are:

Band 2C: 9–9.3 μm
Band 2C: 10.1 μm
Band 2C: 11.0 μm
Band 3A: 12.3 μm

5.4.5.2 Fringing

All spectral bands of the SWS show fringing caused by one or multiple sets of parallel surfaces in the lightpath that act as a Fabry-Pérot system. The most obvious fringe pattern is seen in band 3 where the Fabry-Pérot effect is caused by the BIBIB detectors themselves.

Order selection filters cause fringing in bands 1 and 2. Compared to the fringes in band 3, the situation is less severe – the amplitude is smaller and the fringe frequency higher, close to the wavelength resolution of the SWS in those bands.

The fringes in bands 3 were also observed during the instrument level tests (Section 5.4.1) so they are also present in the RSRF and will be divided out in the final SWS spectra. However, the beam from

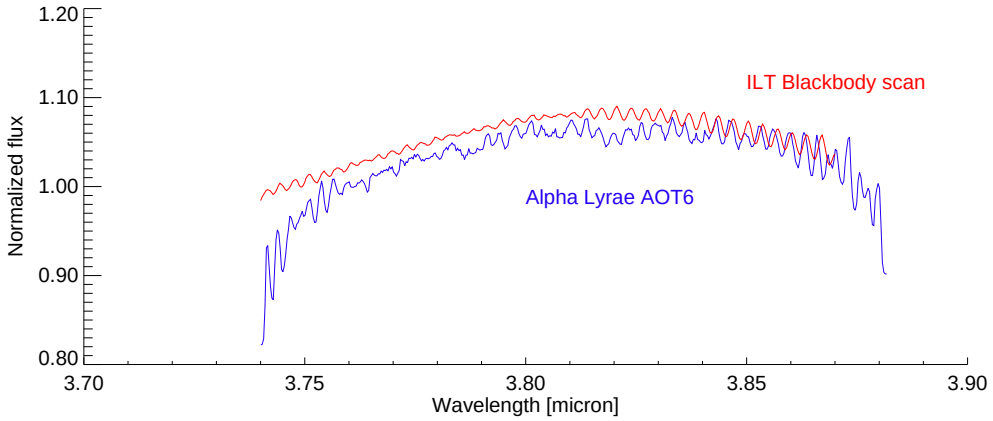

Figure 5.3: *In full-resolution scan SWS06 observations of point-like sources the fringes (here in off-band data band 1D) are better resolved than in the ILT blackbody scans.*

the source used during the pre-launch measurements filled the slit of the SWS entirely. Therefore the RSRF measured during these tests has a slightly lower spectral resolution than in-orbit observations of point-like sources. That is the reason why the fringes seen in band 3 are sharper in observations of point-like sources than in the RSRF. Slight pointing errors will also result in a wavelength shift of the spectrum observed, so that the fringes can be shifted slightly with respect to the fringes in the RSRF. This will result in large fringe residues in the spectra in bands 3A, 3C, 3D and 3E. Within the OSIA and ISAP packages, interactive processing tools are available to deal with the residual fringes (Kester, Beintema & Lutz 2001, [21]). See also Section 9.7.

As illustrated in Figure 5.3 the fringes in bands 1 and 2 are hardly resolved in the RSRF while they are completely resolved in high-resolution SWS spectra of stars. This will often limit the S/N that can be achieved with the ISO-SWS at full resolution in those bands.

5.4.5.3 Wavelength regions showing order leakage

The wavelength range of the SWS grating section extends over several octaves. A set of dichroic beam-splitters and order selection filters are therefore needed to avoid light from other wavelengths to leak in via lower or higher spectral orders. The order selection filters in the light path of band 3D do not cut off the shorter wavelengths efficiently enough. Band 3D therefore shows leakage from the wavelength region around 14 μm. Typically about 10% of the flux at 14 μm will leak to the 28 μm region. The RSRF for band 3D is appropriate for sources that have a relatively low flux at 14 μm compared to 28 μm and hence show no leakage. In spectra of blue sources a false rise at the end of band 3D is seen (Figure 5.4).

Within the OSIA package the RSRF calibration for bands 4A, 4C and 4D is available. These bands contain the data recorded in the band 4 detectors during the scans of bands 3A, 3C and 3D. From the SWS block diagram (see Figure 2.4), it can be seen that there is no order selection filter in the re-imaging optics of the band 4 detectors. For band 4C, this results in very severe leakage from longer wavelengths. Since stellar spectra were used for the RSRF correction, the impact on the RSRF accuracy is minimal. The primary use of this serendipity data is to verify the strength of spectral features in spectra where the band 3 data is problematic due to fringing. In that case one will typically normalise the continuum measured in band 4 to the continuum measured in band 3. The lower sensitivity with respect to band 3 can also be used in the few cases where the SWS observed high flux sources that (partially) saturated the band 3 detectors.

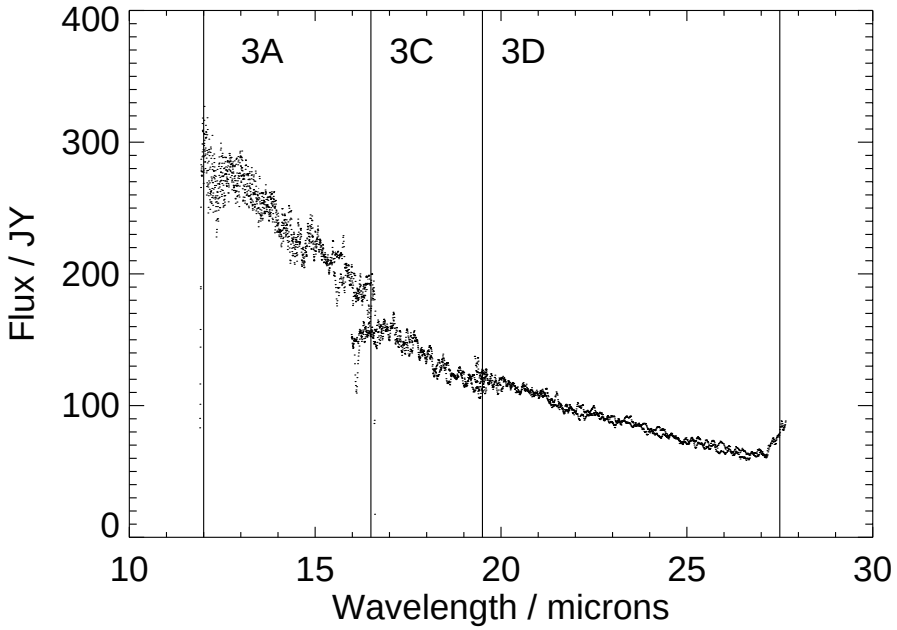

Figure 5.4: *Band 3 data showing the leak around 27μm.*

5.4.5.4 The RSRF for band 4

No in-orbit correction of the band 4 RSRF has been applied due to lack of suitable observations/sources. So the RSRF in band 4 is completely based on laboratory measurement using a very bright, extended source. It is known that the laboratory measurements show a strong de-biasing effect, and it can thus be expected that the shape of the current band 4 RSRF has a global inaccuracy of about 10%.

5.4.5.5 Propagation of RSRF features to the spectra after wrong dark subtraction

The effect on the final spectrum of subtracting a wrong dark-current value depends on the RSRF in the wavelength region affected. The SWS RSRFs are not flat at all. They show steep slopes at the ends of the bands, and various bands show distinct features in their RSRF. The dark current subtraction has to be done properly for a proper RSRF correction.

Dividing poorly dark subtracted data by the RSRF will induce false shapes in regions where the RSRF shows features or where the RSRF has a steep slope. Poor matches between different bands can often be understood (and corrected for) from such a combination of dark current uncertainties and a steep RSRF in the overlap region.

The figures in the next sections show where the RSRF is steep or shows features and thus where the risk for these artifacts exists. If the signal level of a scan is of similar strength as the dark currents for that band, it is wise to check if discontinuities at band overlaps or features whose position coincides with RSRF features are real or artifacts.

5.4.6 Overview of the RSRF curves

In Figures 5.5 to 5.19 we give an overview of the RSRF for one representative detector in each band. The curve plotted below the RSRF is an empirically determined uncertainty on the broadband shape of the RSRF. These uncertainties were determined by examining a large set of observations processed with the appropriate RSRFs (presented in this section) and compared them to the expected spectrum. As such, they do not contain a formal error, but rather an indication of the regions in the RSRFs which are known to be less reliable than other regions. The places where small-scale corrections to the ILT RSRFs were applied can be recognized by a sudden rise in the uncertainty.

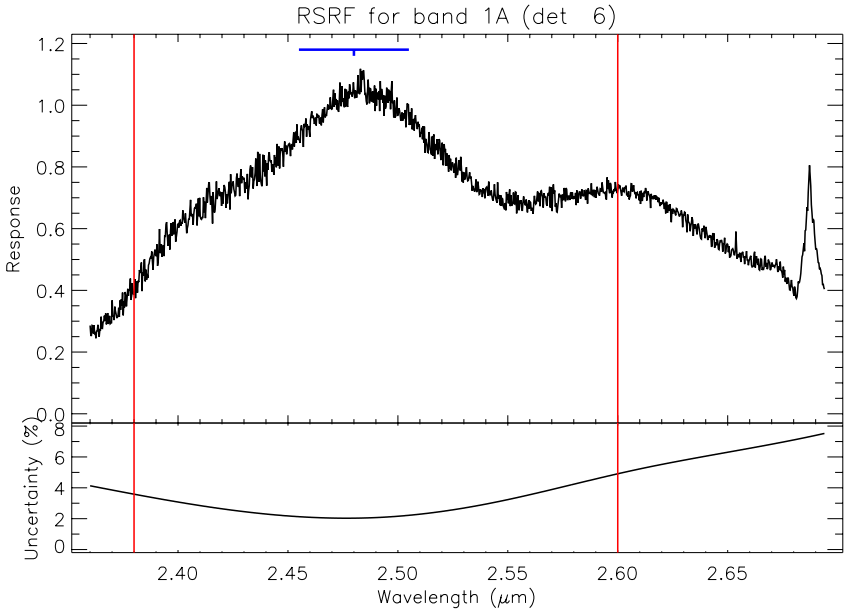

Figure 5.5: *The RSRF for band 1A. The upper panel shows the RSRF while the lower panel displays the relative uncertainty in percent. The red lines indicate the valid wavelength range and the blue bar indicates the key wavelength plus passband.*

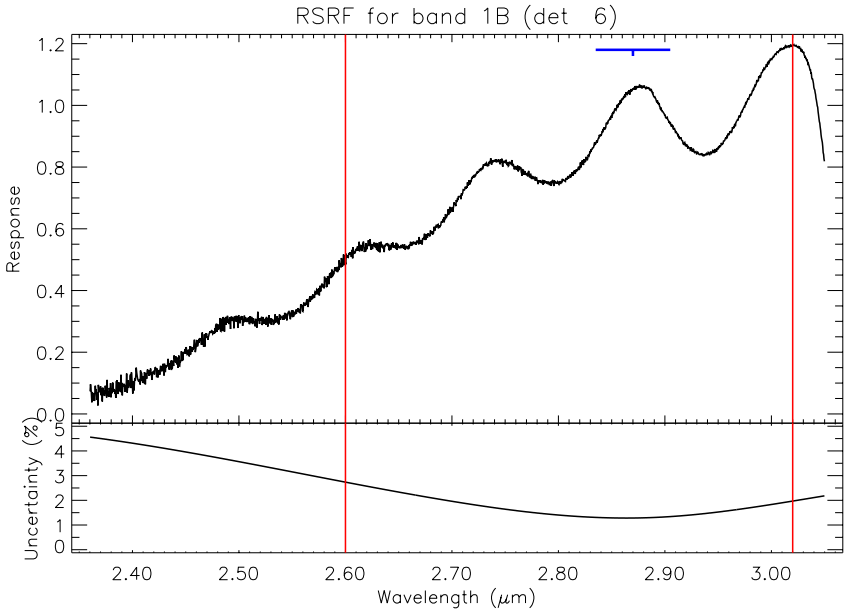

Figure 5.6: *The RSRF for band 1B. See Figure 5.5 for explanation.*

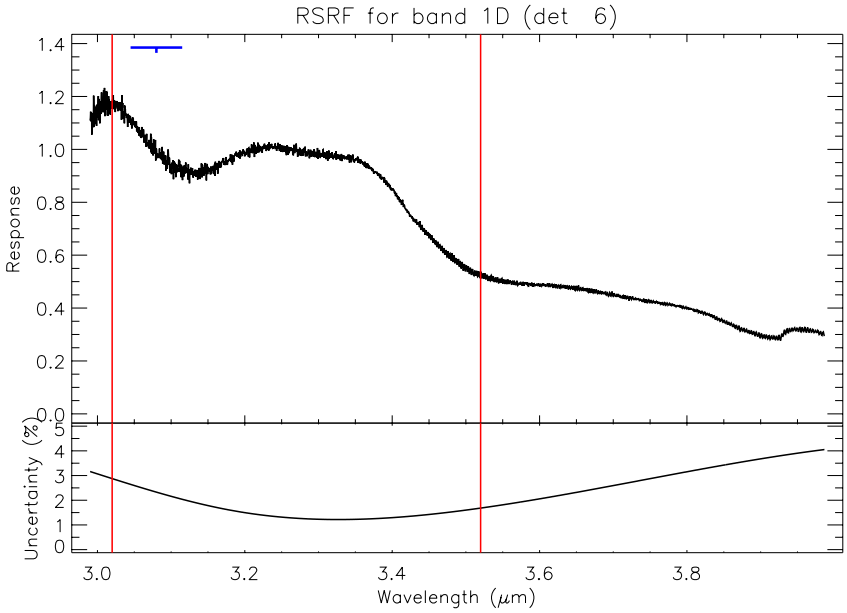

Figure 5.7: *The RSRF for band 1D. See Figure 5.5 for explanation.*

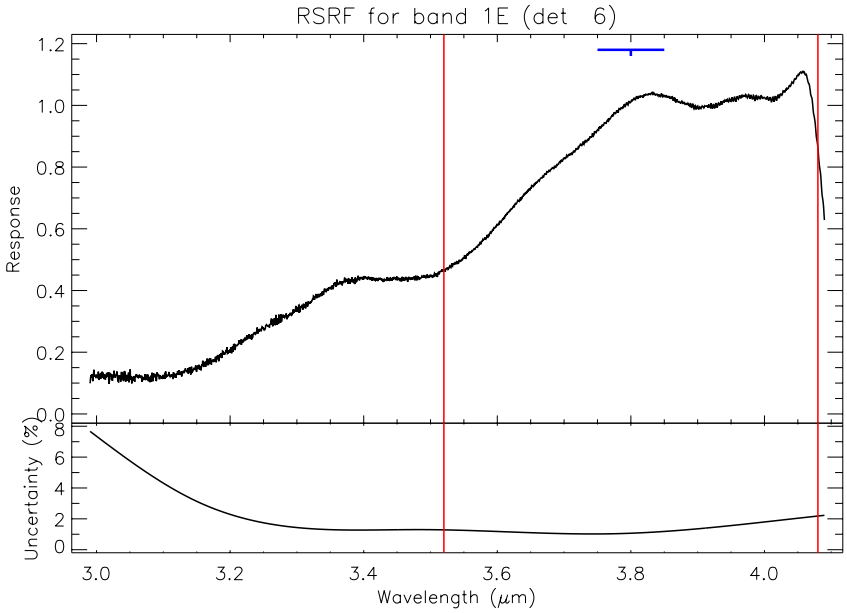

Figure 5.8: *The RSRF for band 1E. See Figure 5.5 for explanation.*

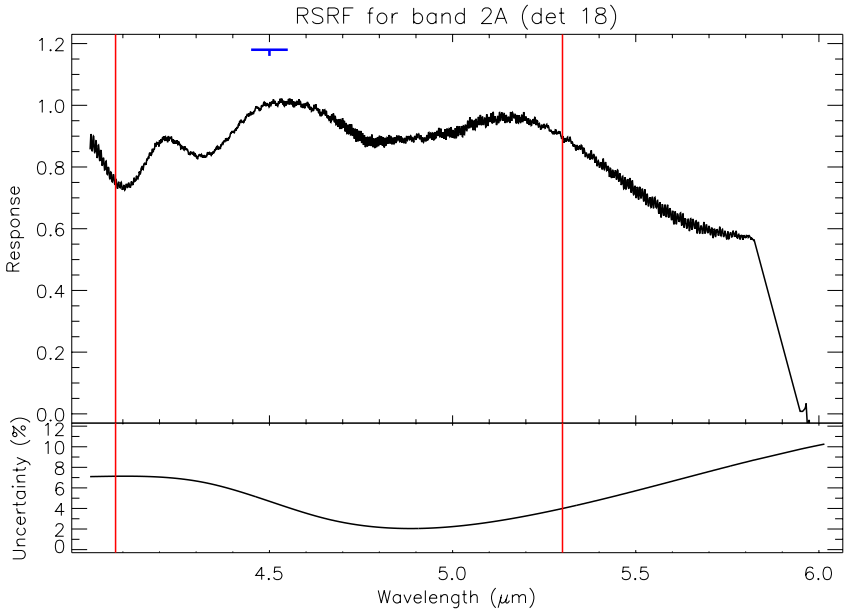

Figure 5.9: *The RSRF for band 2A. See Figure 5.5 for explanation.*

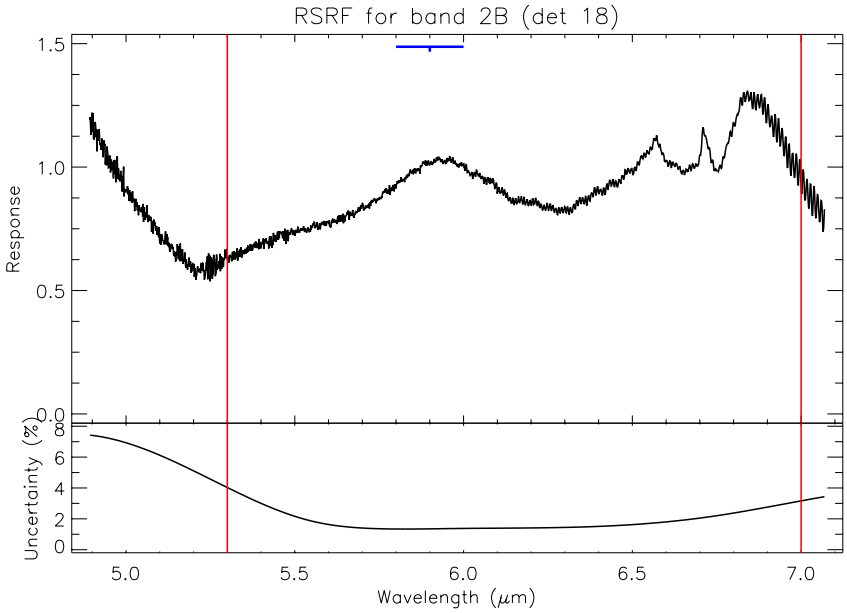

Figure 5.10: *The RSRF for band 2B. See Figure 5.5 for explanation.*

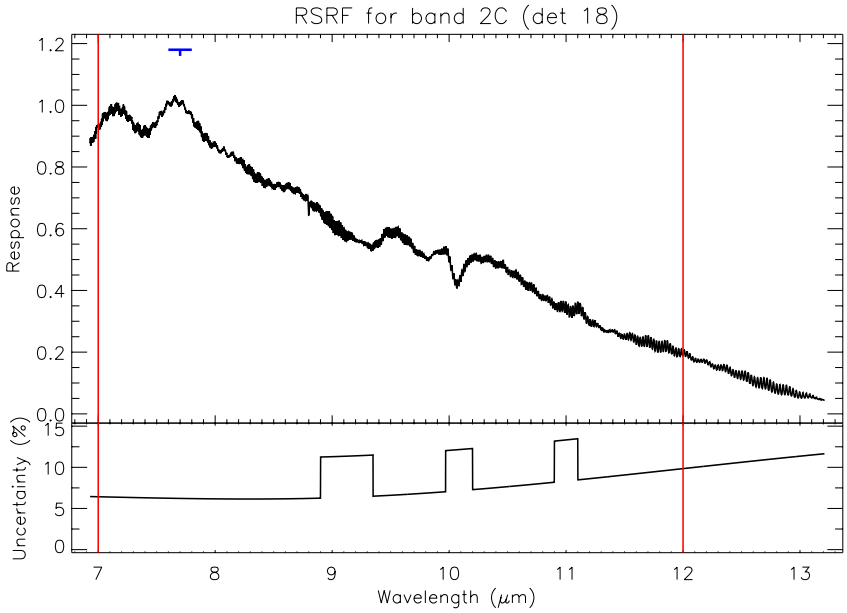

Figure 5.11: *The RSRF for band 2C. See Figure 5.5 for explanation.*

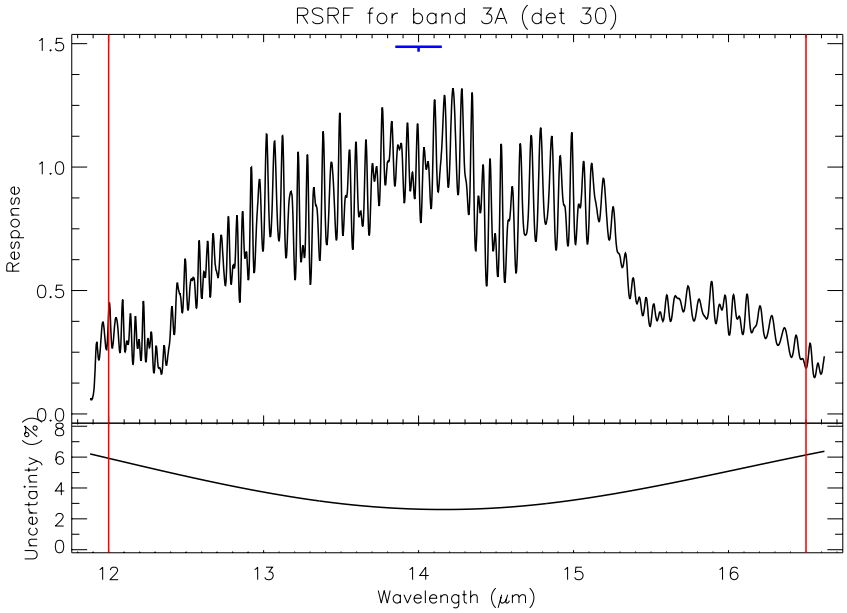

Figure 5.12: *The RSRF for band 3A. See Figure 5.5 for explanation.*

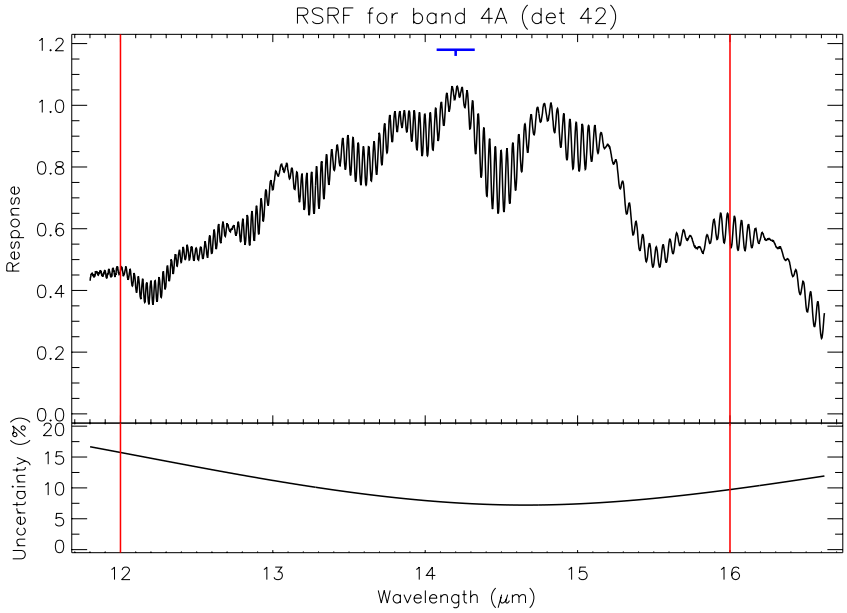

Figure 5.13: *The RSRF for band 4A. See Figure 5.5 for explanation.*

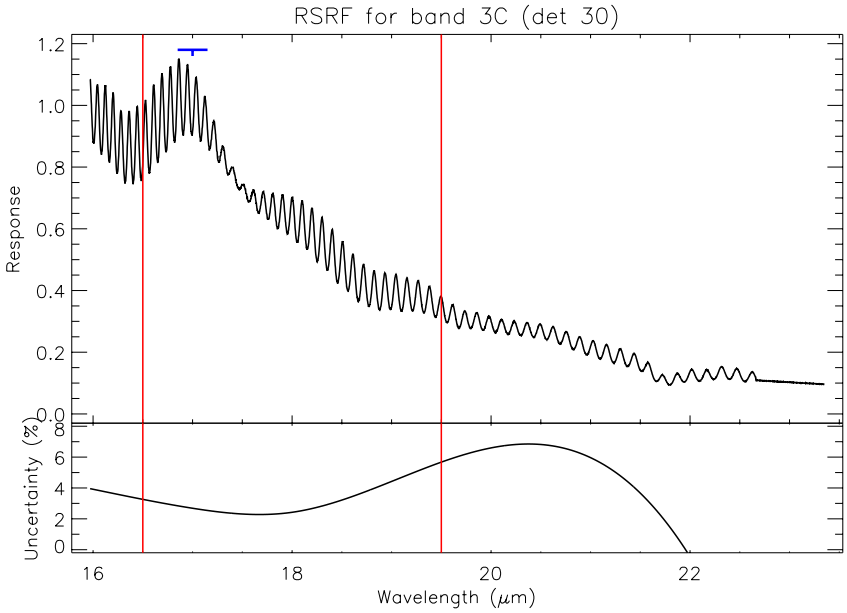

Figure 5.14: *The RSRF for band 3C. See Figure 5.5 for explanation.*

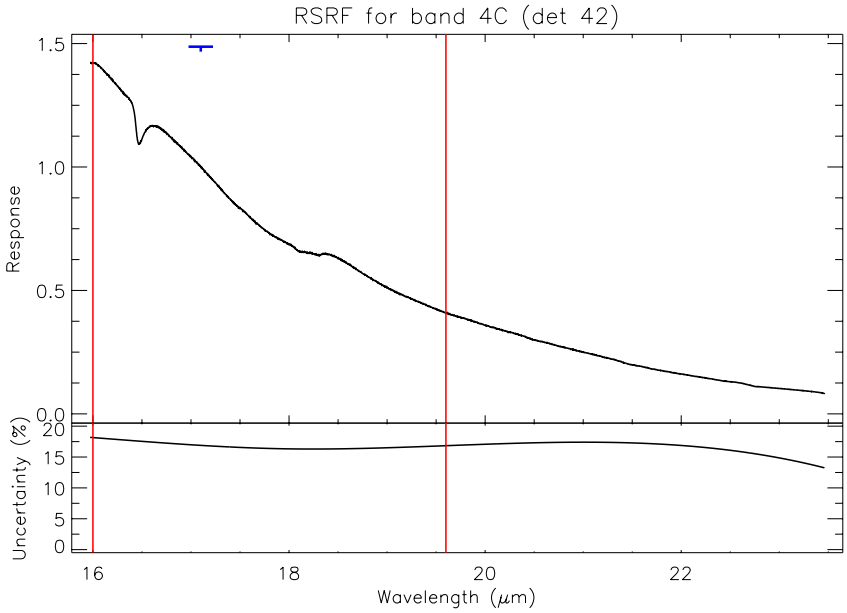

Figure 5.15: *The RSRF for band 4C. See Figure 5.5 for explanation.*

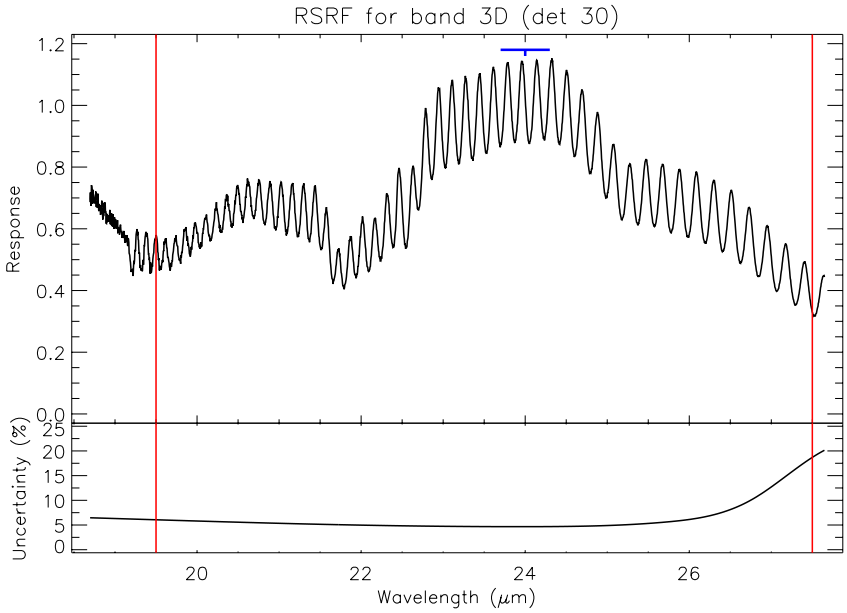

Figure 5.16: *The RSRF for band 3D. See Figure 5.5 for explanation.*

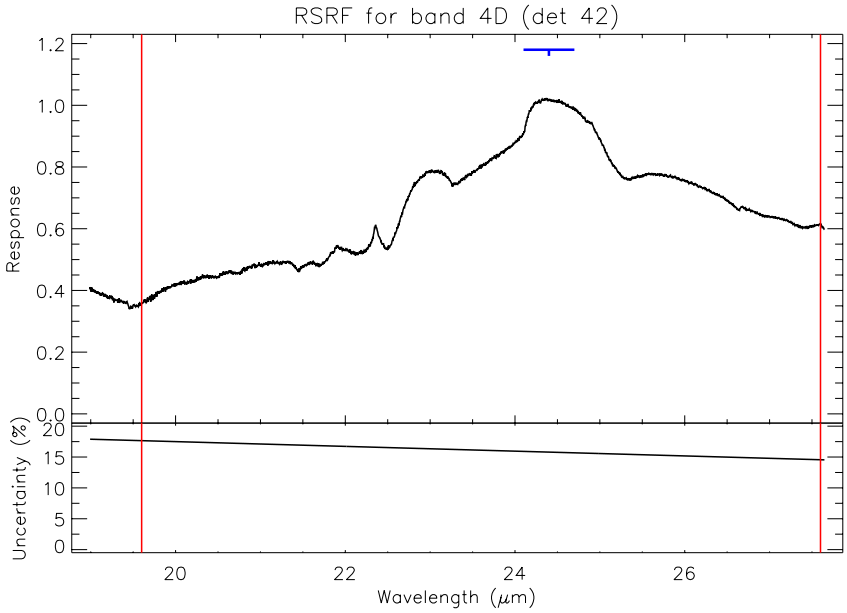

Figure 5.17: *The RSRF for band 4D. See Figure 5.5 for explanation.*

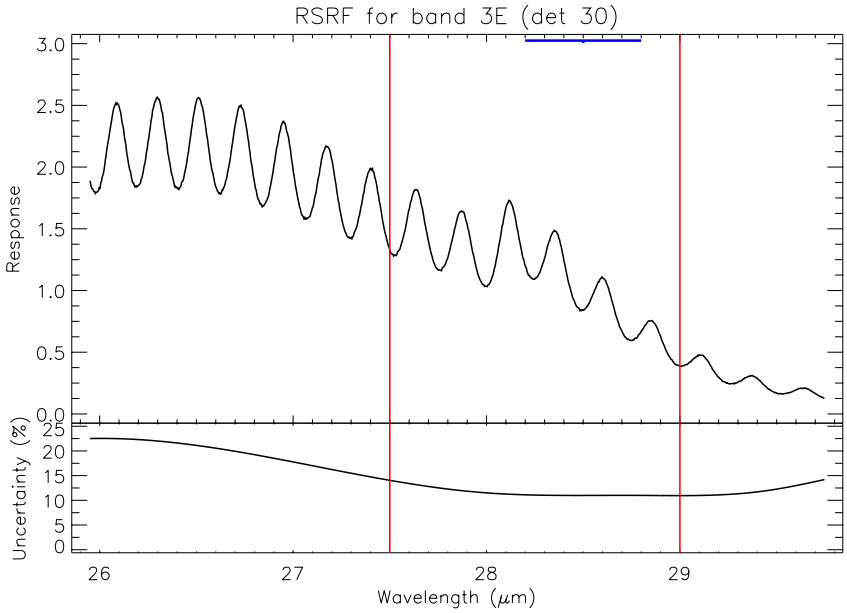

Figure 5.18: *The RSRF for band 3E. See Figure 5.5 for explanation.*

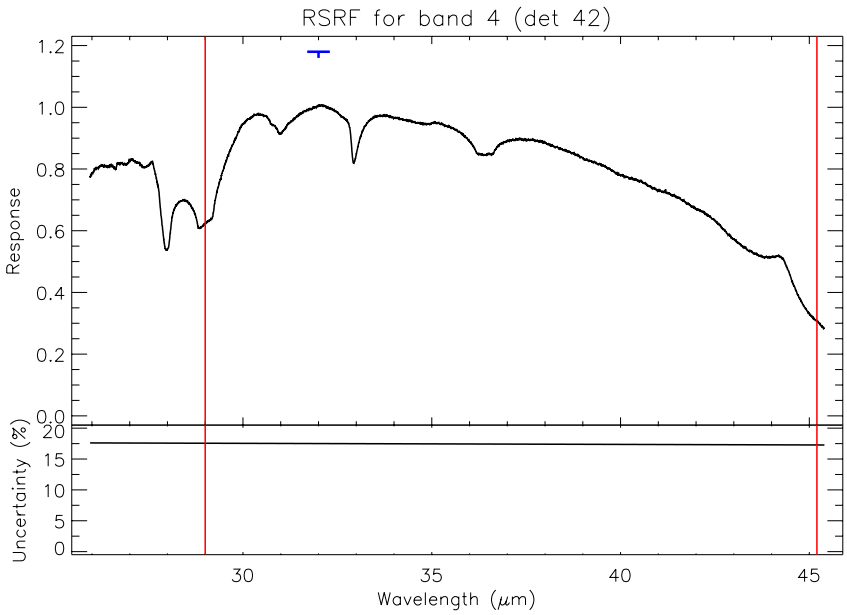

Figure 5.19: *The RSRF for band 4. See Figure 5.5 for explanation.*

5.4.7 Fabry-Pérot RSRF

The Fabry-Pérot sensitivity was characterized in instrument levels tests by doing measurements on a calibrated blackbody source within the test cryostat. Figures 5.20, 5.21, 5.22, 5.23 and 5.24 show the SWS Fabry-Pérot spectral response functions.

The spectral response curve has structure on various wavelength scales. Large scale trends are determined by the counteracting effects of increasing detector spectral response with wavelength (until close to the detector cut-off wavelength) and decreasing transmission of the Fabry-Pérot interferometer. Structures on scales of microns or tenths of microns can be traced to the detector spectral response curves and filter transmission curves. A rapid low-amplitude modulation in the 11.4–16 μm range is caused by reflections between the surfaces of the transmission filter used behind slit 1 in the long-wavelength section of SWS. This 'parasitic Fabry-Pérot' effect is also observed for grating data using the same slit. The stronger modulation detected at $\lambda \geq 40\,\mu$m in the long-wavelength extended range is again caused by a parasitic Fabry-Pérot effect, this time in a reflecting CaF_2 filter. The nearby 'reststrahlen' resonance of CaF_2 causes strong variations with wavelength of the indices of refraction and absorption, leading to the observed modulation pattern. The modulations were characterized with sufficient accuracy to allow good flux calibration in the extended wavelength ranges.

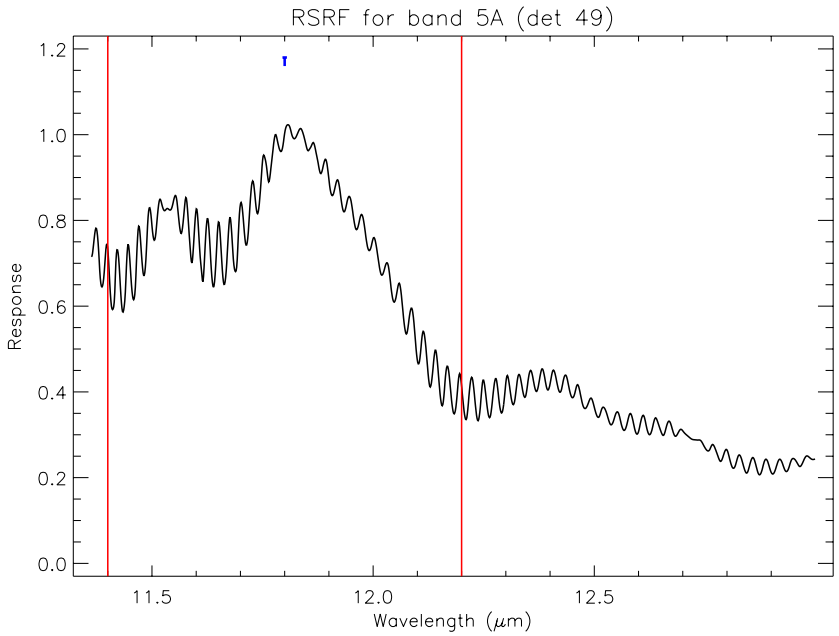

Figure 5.20: *The RSRF for band 5A. See Figure 5.5 for explanation.*

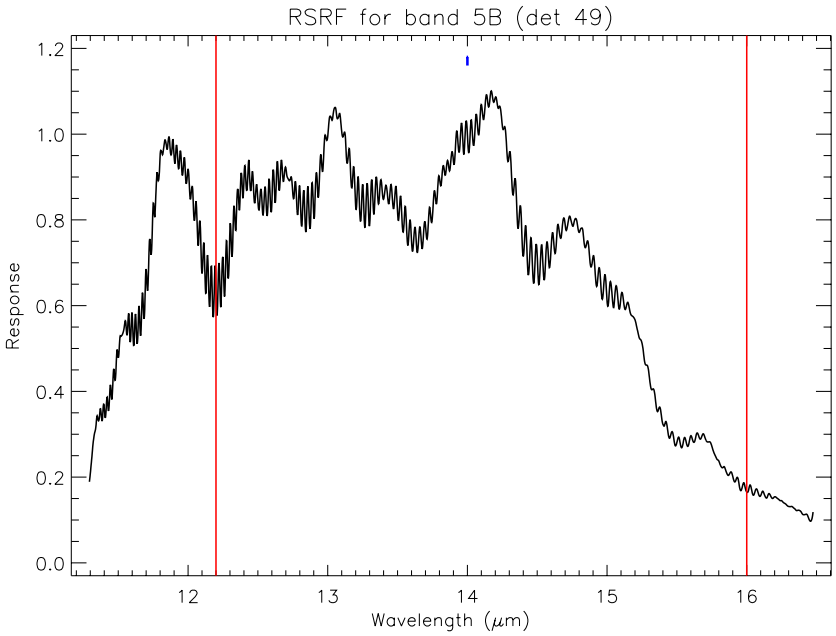

Figure 5.21: *The RSRF for band 5B. See Figure 5.5 for explanation.*

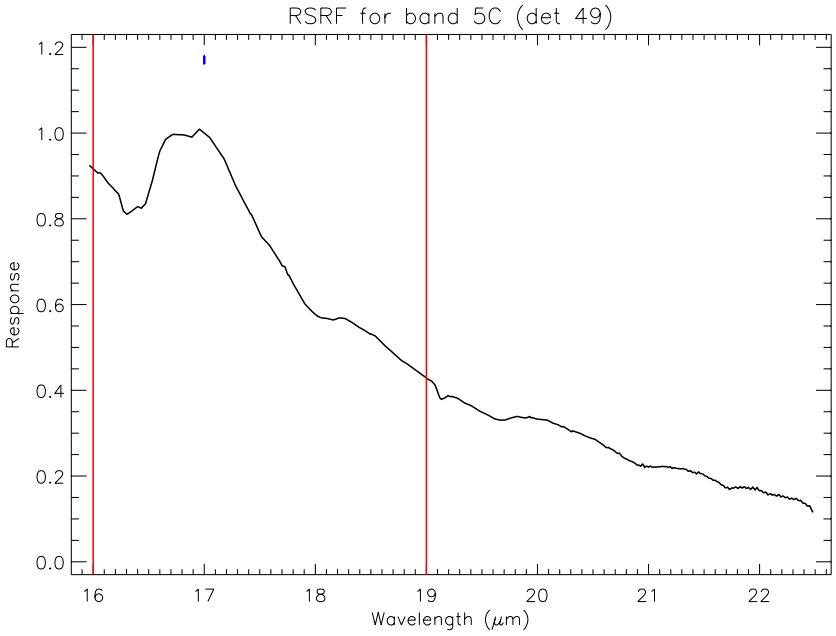

Figure 5.22: *The RSRF for band 5C See Figure 5.5 for explanation.*

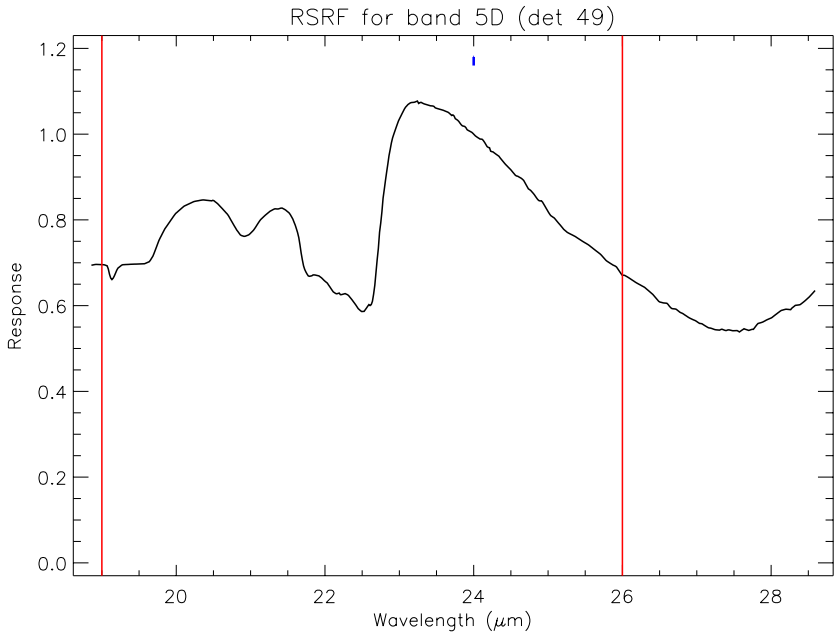

Figure 5.23: *The RSRF for band 5D See Figure 5.5 for explanation.*

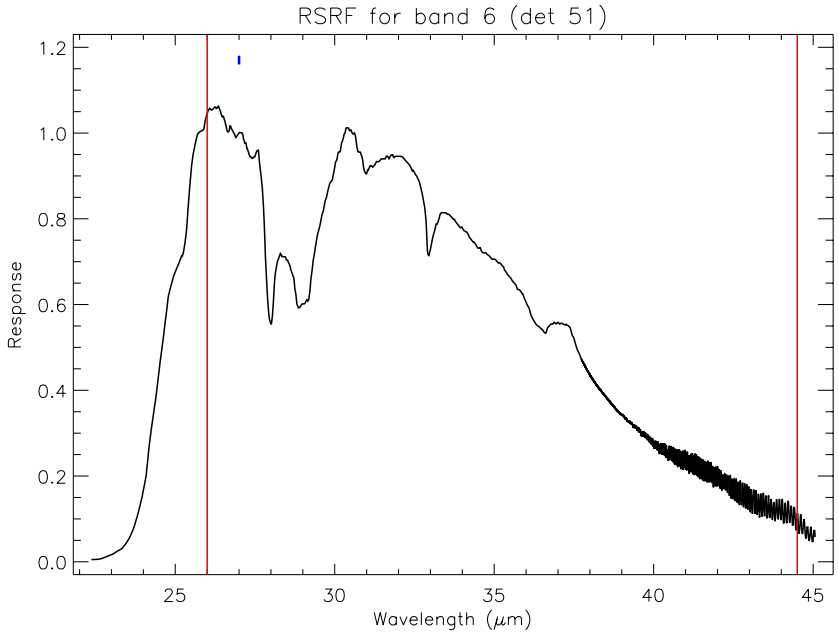

Figure 5.24: *The RSRF for band 6 See Figure 5.5 for explanation.*

5.4.7.1 Diffraction losses

The SWS Fabry-Pérot sub-instrument suffers from diffraction losses caused by the fact that the aperture is comparable in size to the ISO diffraction disk. The effect of these diffraction losses is however not large, and Figure 5.25 shows it as a function of wavelength.

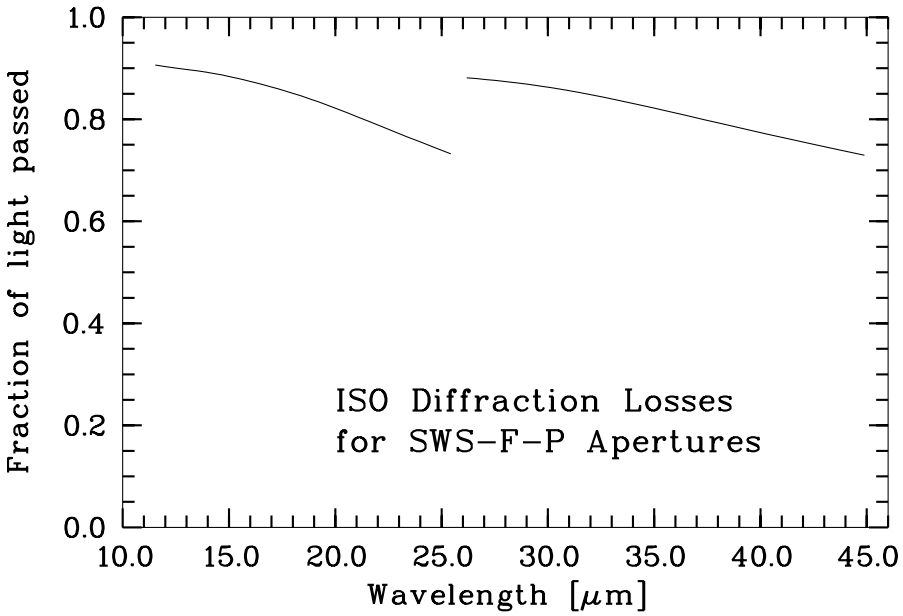

Figure 5.25: *Computed ISO diffraction losses for the SWS Fabry-Pérot channels. The fraction of the ISO diffraction disk accepted by the effective SWS Fabry-Pérot aperture is shown as a function of wavelength.*

5.4.7.2 Leakage in the Fabry-Pérot

The Fabry-Pérot section uses the grating as an order selector that suppresses unwanted FP orders. This suppression is not complete for part of the SWS wavelength range. Neighbouring FP orders 'leak' through the wings of the grating instrumental profile, contributing significantly to the total measured signal (See Figure 5.27). For observations of a single line superposed on a smooth continuum, the only drawback of leakage is a more complicated flux calibration, since leakage will increase the observed continuum but not the line. More serious effects occur in crowded spectra, where strong lines seen in the 'wrong' FP order may significantly distort the observed spectrum, requiring observations of wider wavelength ranges in order to determine the severity of this effect and 'clean' the spectrum.

Leakage has been quantified by analysis of the grating instrumental profile as seen by the FP detectors in scans of solid state laser lines. Figure 5.26 shows the leakage as a function of wavelength. This figure must be used with caution, since it is based on extrapolating the grating instrumental profile from measurements at only a few wavelengths of laser lines.

Figure 5.27 shows the effect of leakage on a observation of a single line specially planned to observe the leakage. Because the observation was carried out over a large wavelength interval two 'ghost' lines appear either side of the real line. Usually these 'ghost' lines would not appear in observations, as they cover a much smaller wavelength range. The observed NeIII line is very strong and, as the FP scans from longer to shorter wavelengths, the line appears non-symmetric because of memory effects in the Si:Sb detector. The 2 leaking orders do not have the same intensity because the grating instrumental profile

is not centred on the main order. This slight deficiency in the grating wavelength calibration, although within specifications, translates into the non-symmetric pattern.

The spectral response data in Section 5.4.7 have not been corrected for the effects of leakage, i.e. they refer to the total signal.

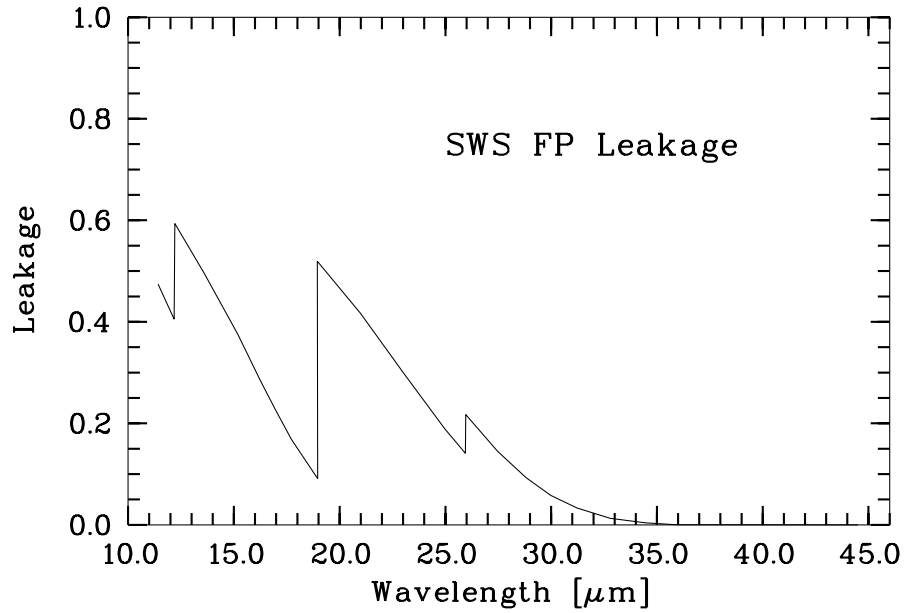

Figure 5.26: *SWS Fabry-Pérot leakage. Leakage is defined here as the fraction of the total detected signal that originates in unwanted Fabry-Pérot orders. The data shown here are based on extrapolation from measurements at a few wavelengths.*

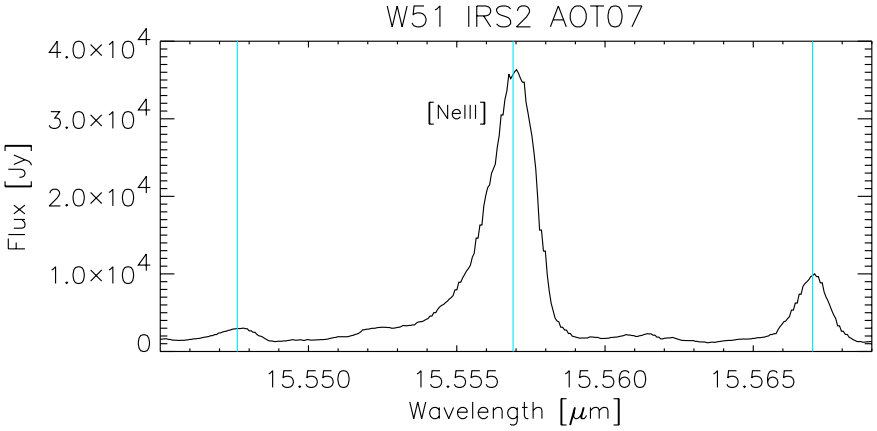

Figure 5.27: *Example of FP leakage on a single line. A large wavelength range was scanned for this measurement, resulting in two 'ghost' lines at approximately 15.548 and 15.567 μm from leakage of the real line at 15.557μm.*

5.5 Detector Response to the Internal Calibration Source

The measured response to an internal stimulator flash is used to calculate a gain factor for each of the detector blocks 2, 3, 4, 5 and 6. Up to revolution 64 (still within the Performance Verification phase) band 1 also received an internal illuminator bright enough for these detectors (InSb). However, the stimulator setting was too high for bands 2, 4, 5 and 6 and introduced transient effects in these bands. Band 1 detectors were also quite stable, within 2% (Heras et al. 2000, [15]), and the decision was made not to use the high stimulator setting after revolution 64.

Figure 5.28 shows a sample (roughly 1000 observations) of the photometric gains based on the internal

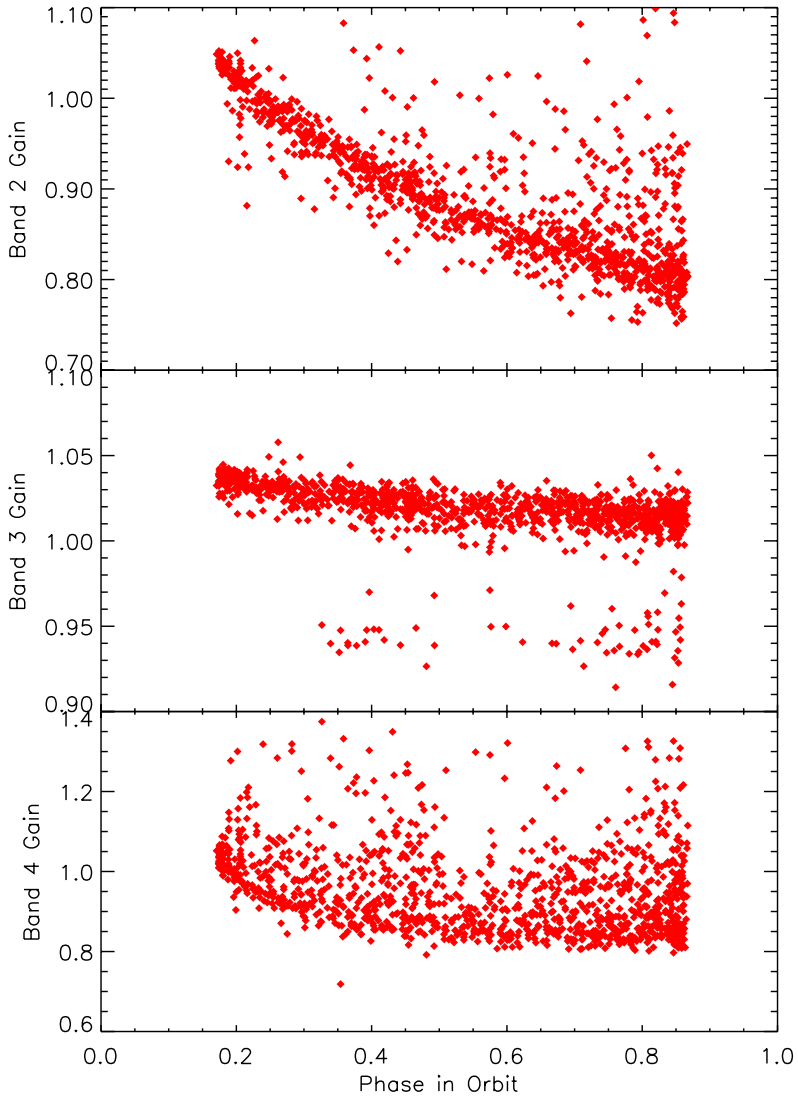

Figure 5.28: *Detector gain plotted against the phase of the orbit. The general trend is for a decay of the response with time in the revolution, with bands 2 and 4 showing the increase in the spread of points near the end of each revolution (approaching perigee), consistent with the increasing number of radiation hits.*

illuminator scans, plotted as a function of phase (time after perige in a revolution). For each of the bands 2 (Si:Ga), 3 (Si:As), and 4 (Ge:Be) the response of the detectors changes systematically throughout the revolution. This is the same trend as seen by Heras et al. 2000, [15], but the gains are now calculated from all 12 detectors. Note that bands 3 and 4 see very similar wavelengths of the illuminator and yet record extremely different variations in their responses. This fact is taken as an indication that the responsivity of the different detectors is changing during a revolution and not the illuminator itself.

The general trend is for a decay of the response with time in the revolution and is related to the long term transient drifts caused by the extreme radiation hits received during perigee. Both bands 2 and 4 also show increase in the spread of points near the end of each revolution (approaching perigee), which is consistent with the increasing number of radiation hits.

Nominally, each observation contains at least two scans of the internal calibrator. Studies show that the 2nd internal calibration scan agrees with the first within the uncertainty of the measurement.

The average response to a stimulator flash is contained in the Cal-G 41 file. Stimulator flash data obtained during a science observation are compared to the average data in this file to determine the 'photometric' gain correction for the science observation.

5.6 Grating Flat-fielding

The 12 detectors of each grating detector block must be individually calibrated such that the resulting spectra from each detector within a block gives the same signal. This step has been dubbed 'flat-fielding' for SWS. In general, the signal to flux calibration per detector should formally account for flat-fielding. However, the variations of an individual detector relative to the average of the detectors can be easily measured from any science observation and not just from the photometric calibration observations. This approach makes use of the entire SWS database of observations to determine the flat-field coefficients.

The calibration of the flat-field is determined from dark subtracted, relative spectral response and photometric gain corrected data of roughly 1000 observations throughout the ISO mission. The average response of each detector in the band is measured against the average response of all the detectors combined. Figure 5.29 shows the flat-field coefficient for bands 1D, 2B, 3A, and 4 throughout the ISO Mission, for sources brighter than 50 Jy (100 in band 4) and median filtered over time for clarity of the trends. Because of the constancy of the flat-fielding, a specific calibration can be applied to correct it. These values are contained in the Cal-G 43 file.

The application of a separate flat-fielding step aids in removing some of the ambiguity of applying an OFFSET or GAIN flat-fielding correction in post processing. The flat-fielding is always a gain correction in the standard processing. In post processing it might be necessary to account for offsets introduced through the dark current application. There remain cases when it is still preferred to apply a flat-fielding correction in post processing, since effects like satellite pointing can also change the flat-fielding. However, the corrections will be smaller.

In Figure 5.29, there are two revolutions which show significantly different flat-field coefficients, these occur at revolutions 244 and 641. In both of these revolutions, a pointing experiment was performed which places and object at a series of different positions within the SWS apertures. From these data, it is clear that mis-pointings will have a significant effect on the flat-fielding.

5.7 Signal to Flux Conversion

Calculation of the conversion factors, G_c, from μV/s to Jy is based purely on observations of the standards listed in Table 5.2. For each band roughly 50 corrected observations at the key wavelengths are compared with model SEDs. Each observation is a measurement of the signal to flux conversion. The final S/F conversion (stored in Cal-G 42) is the average ratio of measured signal to expected flux for each standard at the key wavelength.

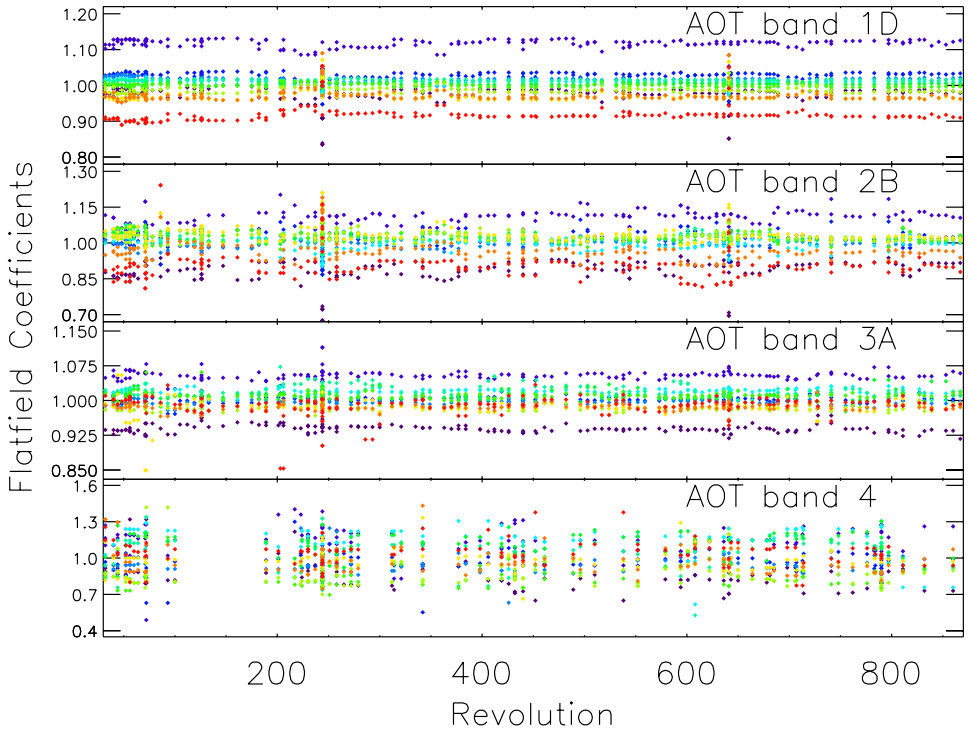

Figure 5.29: *This figure shows the trend in flat-field coefficients throughout the entire ISO mission. Each colour represents the average detector response to the observed object normalised by the average band response to the object. Clearly, a given detector responds systematically differently to the same source relative to another detector. The figure shows the trends for observations in band 1D, 2B, 3A and 4. The flat-field coefficients around 244 and 641 are markedly different. In these two revolutions, pointing exercises were performed to map out the SWS beam profiles. These 'mis-pointings' significantly change the flat-fielding.*

For the purpose of filtering out poor quality data, a number of conditions had to be met by the observations for them to be considered for the calibration. The first condition is that the reconstructed pointing had to be within 1 arcsecond of the intended coordinates. The second condition is that an observation was usable, only if it had high quality data in all the elements of the calibration group. For calibration purposes only, the bands are divided into 4 groups. Group 1 consisted of the short wavelength (SW) section of SWS (bands 1A, 1B, 1D, 1E, 2A, 2B and 2C). Group 2, consisted of bands 3A, 3C and 3D. Group 3 is just band 3E and group 4 is just band 4. The reason for creating these groups is that if and observation failed in any one part of a group, it is suspect in all the others. The final condition is that all points marked as glitches are thrown out. Unfortunately, this filter will not get the glitch tails seen in band 4 (see Section 7.2.8).

5.7.1 Astronomical Calibration Sources (ACS)

Table 5.2 gives an overview of the ACSs used for the photometric calibration of the pipeline products. The table indicates the source name, type of object, and bands which made use of the ACS.

The last 4 columns illustrate the diversity and distribution of observations used for the photometric calibration of the various bands. For each ACS, the number of observations going into the photometric

calibration is given. In the last columns, there are 4 numbers per ACS indicating 4 different band groups. The first group combines bands 1A through 2C, the second group combines bands 3A through 3D, and the last two groups are the bands 3E and 4 respectively. For wavelengths shorter than 12 μm, the SEDs for the ACS were updated with stellar atmospheric models described in Decin 2000, [4]. The absolute calibration of these SEDs is based on the photometry used for the absolutely calibrated composite observed spectra described by Cohen et al. 1992a, [2]. For wavelengths longer that 12 μm the stellar composites themselves are used (Cohen et al. 1992a, [2]). The photometry and composites used for SWS are directly traceable to the published calibrated spectra of Sirius and Vega (Cohen et al. 1992b, [3]).

The stellar calibration sources span a wide range in spectral types from A0V to M0III with the bulk of the sources being K giants. Within each of the SW bands the SEDs cover more than 2 decades in flux. The diversity of the ACSs and the wide flux range increases the reliability of the photometric calibration and reduces the sensitivity to any one object or model.

For bands 3E and 4, models of Ceres (T. Müller, private communication) and Uranus (E. Lellouch, private communication) were used. These models can be obtained from the ISO Data Centre.

As can be seen in Table 5.2, the star, γ Dra, was heavily used. The photometric calibration was checked with and without the inclusion of γ Dra to ensure this one source was not skewing the photometric calibration.

Table 5.2: *Summary of SWS astronomical calibration standards*

Source ID	Alias	Spectral Type	Number Obs. SW[a]	3[b]	3E	4
HR7001	Vega	A0V	5	0	0	0
HR2491	Sirius	A1V	5	5	0	0
HR4534	β Leo	A3Vv	2	0	0	0
HR5459	α Cen A	G2V	1	1	1	1
HR7310	δ Dra	G9III	2	0	0	0
HR6688	ξ Dra	K2III	4	0	0	0
HR5340	α Boo	K2IIIp	8	9	9	9
HR5563	β UMi	K4III	2	0	0	0
HR1457	α Tau	K5III	6	6	6	6
HR6166	HD 149447	K5III	1	0	0	0
HR6705	γ Dra	K5III	24	37	29	0
HR337	β And	M0III	4	4	4	2
HR911	α Cet	M2III	2	2	2	0
HR8775	β Peg	M2.5III	0	7	7	7
HR4763	γ Cru	M4III	0	6	6	6
NML Cyg	IRC+10448	M6IIIe	0	4	3	3
Ceres	210001	Asteroid	0	0	1	1
Uranus		Planet	0	0	1	1

Notes:

[a] SW indicates the short wavelength section of the SWS grating: bands 1A to 2C covering wavelengths from 2.4 to 12 μm. Stellar photosphere models provided by L. Decin (private communication).

[b] 3 indicates bands 3A, 3C and 3D covering wavelengths 12 to 27 μm. All stellar photosphere composites covering 12 to 35 μm are from Cohen et al. 1992a, [2].

5.7.2 Photometric calibration accuracy

An overview of the SWS in-flight photometric calibration for point sources is given in Shipman et al. 2001, [35], from which this section is a summary. The standard processing corrects the observed raw signal for dark current, responsivity changes (monitored with the internal calibrator), RSRF, and flat-fielding. The final step is to convert the signal at all wavelengths from instrumental units (μV/s) to astronomical units (Jy) based on observations of the Astronomical Calibration Sources.

Table 5.3 lists the 1σ uncertainties in the measured signal to flux conversion factors. For each grating band the table lists the key wavelength of the band, the bandpass used around the key wavelength, the 1σ accuracy at the key wavelength, and the 1σ worst accuracy within the band which is usually at the edges of the band. As calculated, the uncertainty is the total absolute uncertainty which has accumulated factors from each of the calibration steps plus estimated contributions from processes which were unprobed or uncorrected. Some examples of these additional uncertainties are, uncorrected memory effects in band 4, higher order memory effects in band 2, and pointing effects. See Section 5.9 for a complete description of the uncertainties in the SWS data.

Table 5.3: *Photometric Accuracies for pipeline products*

Band	Key λ [μm]	Bandpass [μm]	Accuracy 1 σ [%]	Worst 1 σ [%]	λ of worst
1A	2.48	0.05	4	7	edges
1B	2.87	0.07	4	5	edges
1D	3.08	0.07	4	5	edges
1E	3.80	0.10	4	5	edges
2A	4.50	0.10	7	10	6 μm
2B	5.90	0.20	7	9	edges
2C	7.70	0.20	7	8	edges
3A	14.0	0.30	12	14	12μm
3C	17.0	0.30	10	13	edges
3D	24.0	0.60	13	16	19.5μm
3E	28.5	0.60	17	21	edges
4	32.0	0.60	22	23	edges
5A	11.8	0.01	23	23	
5B	14.0	0.01	23	23	
5C	17.0	0.01	23	23	
5D	24.0	0.01	24	24	
6	27.0	0.01	30	30	

The accuracies listed in Table 5.3 are entirely consistent with our current knowledge of SWS and the ISO satellite. A pointing accuracy of 1.5–2" (1σ) will produce more than half of the uncertainty in photometry for bands 1 and 3 and contribute up to half of the uncertainty in bands 2 and 4.

The accuracy expected on the flux calibration of the Fabry-Pérot are the same as that on the grating, but an extra 20% uncertainty needs to be added due to wavelength dependent leakage.

Figures 5.30 to 5.32 show examples of fully calibrated spectra for α Boo. Each spectral segment is made up of 12 detectors. The signal from these 12 detectors is kept separate to demonstrate the flat-fielding. The SED for α Boo is overlaid in red. In Figure 5.31, the up and down scans are shown separately to show the influence of residual memory effects. Figure 5.32 shows bands 3 and 4. In this figure radiation hits (glitches) are quite prevalent in band 4. The residual memory effect introduced by a radiation hit can artificially increase the signal. Also listed in the figures are the ratios of the data to the model at the key wavelength for each of the bands.

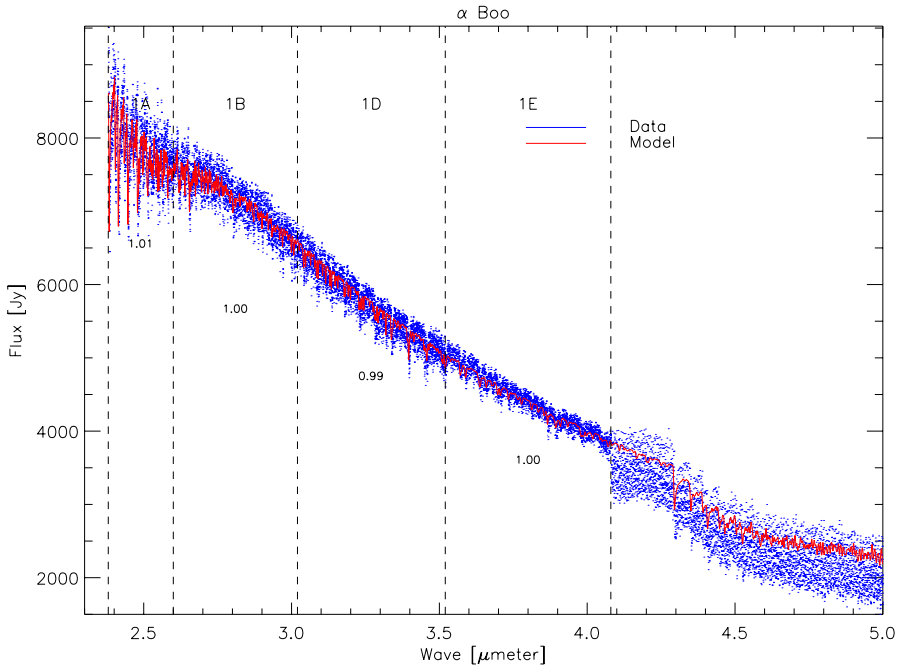

Figure 5.30: *The SWS data are in blue and the SEDs are overplotted in red. The data here are direct pipeline products without flat-fielding or rebinning.*

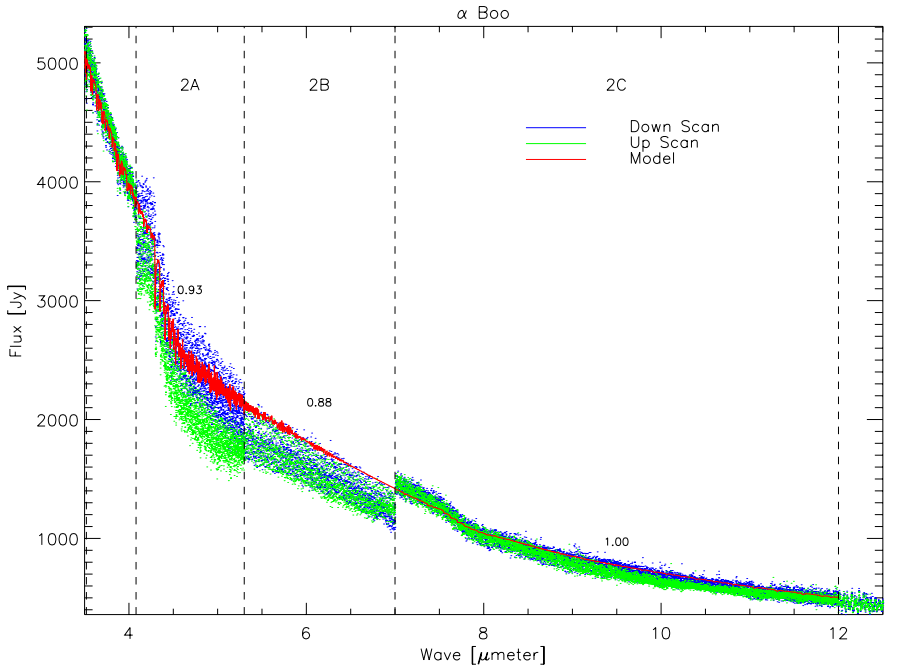

Figure 5.31: *Band 2 for α Boo. Up and Down scans are shown in separate colours (blue and green) while the SEDs are shown in red. The ratio of the observation to SED is indicated. The residual memory effects are clearly seen in this figure as a mismatch between the up and the down scan.*

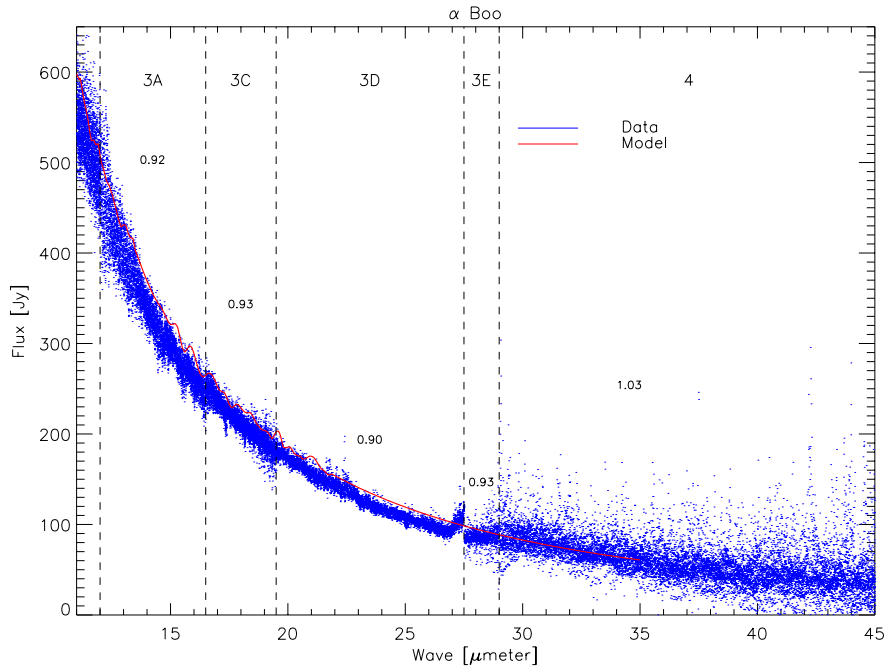

Figure 5.32: *Bands 3 and 4 for α Boo. Note the extreme number of radiation hits in band 4. The band 3D leakage can also be seen around 27 μm)*

5.8 Surface Brightness Derivation

The flux calibration of the SWS instrument has been derived by positioning well known calibration point-like sources at the nominal centre of the instrument beam. The calibration is therefore directly applicable only for point source observations. For extended sources the measured signals have to be converted to surface brightness values rather than flux values.

The derivation of extended source flux from a point source calibration is given by;

$$I_\nu = \frac{F_\nu}{\int_{-\infty}^{+\infty} BP(y,z)\,dydz} \quad (\mathrm{MJy\,sr^{-1}}) \tag{5.3}$$

where F_ν is the (point source) flux density at the frequency ν and $BP(y,z)$ is the detector's Beam Profile, normalised to the value at the position in which the flux calibration has been derived, nominally the (0,0) position. The variables y and z are angles with respect to the spacecraft Z and Y axes.

Table 5.4 lists the conversion factors obtained by integrating the measured SWS beam profiles, according to Equation 5.3. These conversion factors are estimated to be accurate within 10%.

5.9 The SWS Error Budget

In this section, many of the sources of uncertainty in SWS data are pieced together to give an overview of the general errors in SWS data. The discussion presented here cannot replace the detailed analysis of an individual observation. That task is left to the observer.

Table 5.4: *SWS Flux conversion factors for extended sources*

Band	Wavelength [μm]	Conversion factor [Jy] to [MJy sr^{-1}]
1A	2.48	139
1B	2.87	134
1D	3.08	132
1E	3.8	132
2A	4.7	115
2B	5.9	118
2C	7.7	117
2C´	11	114
3A	14	107
3C	17	105
3D	20	97
3E	28.5	65
4	30.9	45
4´	40	42

During the course of the ISO mission, hundreds of calibration observations were obtained. From this database, both the various calibration factors and their uncertainties were determined.

The SWS error budget is presented in 4 main sections. The first section will describe in some detail the sources of uncertainty present in SWS. The second section looks specifically to the uncertainties impacting the photometric calibration. The third section describes the reproducibility of SWS observations. And finally, the last section presents the error budget for a general observation.

5.9.1 Sources of uncertainty

The following is a collection of various sources of errors for SWS from both a calibration and/or a general observation point of view. For example, the discussion on the uncertainty of standard models only really comes to play in describing uncertainties of the photometric calibration. As far as the general observer is concerned the error introduced from the photometric calibration is simply a systematic error.

5.9.1.1 Detector noise

In general, the detector noise is comprised of dark noise, readout noise, and glitches. Detector noise is present in all observations as an additive noise value. Therefore the brighter the source the less important the detector noise. Detector noise will effect the determination of a low contrast feature. As far as the photometric calibration is concerned, detector noise is an important source of uncertainty only if the calibration sources have a low signal in the band. This is true only for bands 3E and 4, where there is a lack of bright calibrators.

The percent uncertainty introduced by dark current noise on the photometric calibration can be estimated by applying typical dark current noise levels to a Monte Carlo simulation of the calibration procedure. The dark current estimates assume dark current uncertainties of 5 μV/s for band 3E and 10 μV/s for band 4 (Heras et al. 2000, [15]). A random component of 5 μV/s and 10 μV/s is added to the brightness (in μV/s) for all the the objects used for photometric calibration. For the bright objects this random component does not change the signal much, for the dimmer objects this procedure can cause significant variations in the signal. The percent uncertainty introduced through detector noise in these bands is estimated as 5% and 2%, respectively.

The calibration for band 3E relies on γ Dra as one of its main calibrators. However, the signal for γ Dra is quite low at 28 μm and the dark current subtraction introduces a large uncertainty due to detector noise and uncorrected glitches. It was decided to use the γ Dra observations for 3E for stability of the photometric calibration.

5.9.1.2 Glitches

Radiation hits (glitches) are events which add/subtract a transient signal to the detector. In general they do not impact the responsivity directly (Wieprecht, Wiezorrek & Haser 2000, [43]). However, glitches can have an impact on the overall photometric calibration through three routes. First they can directly affect the signal of the Astronomical Calibration Source (ACS) during the observation. Second, radiation hits can occur during the internal calibrator scan and or during the dark current measurement. Third, for some detector blocks (2 and 4) there are significant transients (memory effects) caused by the glitch which normally appear as a decaying signal.

In general, most glitches are effectively identified, removed or repaired during standard processing. Each data sample where a glitch was detected is flagged. For the photometric calibration on standard sources, these samples are not used. Furthermore, the SWS design and observation strategies minimized the effects of glitches through the high degree of redundancy (12 detectors each with 2 scans covering the same wavelength range).

This redundancy is used to measure the gain based on the internal calibrator scans. Since the gain measured by the internal calibrator is applied to all data within the detector block, it is vital that glitches not identified by the pipeline get filtered out of the data. This is done for the 12×22 samples in an internal calibrator scan by iteratively filtering significant outlying points (more than 3 σ in one iteration).

Glitches have an impact on the photometric calibration through the residual tails which are present in the observations of the ACSs. band 4 detectors have the strongest glitch tails. The level of these tails taken collectively over all band 4 detectors is estimated at 5 μV/s. For the calibration of band 4, this number is subtracted from the measured signal. This correction only has impact on the low signal sources in band 4, less than 100 Jy, but is applied to every source. It is estimated that the uncertainty introduced by glitches to the calibration of band 4 is on the order of 5%.

5.9.1.3 Internal calibration

For detector blocks 2, 3 and 4, the uncertainties of the internal calibrator scans are determined from roughly 1000 observations taken throughout the mission at all phases in the orbit. These measured uncertainties are indicated in Table 5.5. As mentioned in Section 5.5, the band 1 uncertainty to variations of detector responsivity is taken as 2%.

5.9.1.4 Memory effects

Analysis of the uncertainty introduced by memory effects is complicated. However, one gets a hint from the so-called 'band-border' plots. These plots are made by comparing the flux level at the border of one band with the flux level in the other overlapping band. Note that the band borders may not be used for calibration since the band border itself is defined as a low responsivity wavelength regime of the detectors.

Figure 5.33 shows the band border ratios between 1A-1B, 1B-1D, 1D-1E and 1E-2A. These band-border values have been binned and averaged at flux levels between 0.1 and 10000 Jy. The 1E-2A ratios appear to have a systematic error relative to 1E. Note that this ratio does not suffer from an aperture change. The variation (for signals greater than 100 Jy) increases by 10% and then decreases by 10%. The shape of the trend is probably due to uncorrected memory effects. Based on this figure, the uncertainty is estimated at 5% (1σ). An uncertainty of 5% is also consistent with the standard deviation of the band border ratio between 2A-2B shown in Figure 5.37. The uncertainty for memory effects definitely increases

for signals larger than 1000 Jy. Based on this figure the uncertainty at high flux levels is between 10% and 20% due to memory effects.

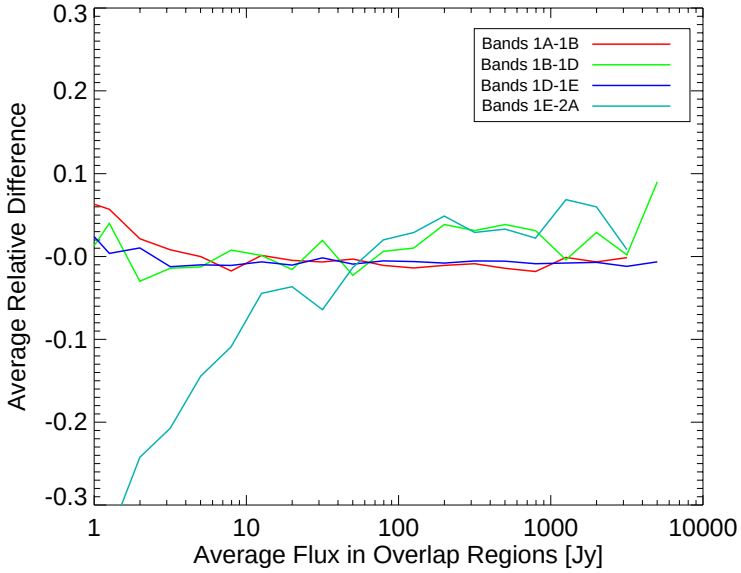

Figure 5.33: *These are the scaled differences between bands at the wavelengths of overlap. Note that 1B-1D and 1E-2A are both overlaps with an aperture change. 1E to 2A also may be showing some residual memory effects or at least the influence of imperfect memory correction at flux levels greater than 100 Jy.*

In Figure 5.34, the band border ratios for band 2 are shown, including band borders 1E-2A and 2C-3A. Note that the overlap between 2A and 2B is the only band 2 border ratio which occurs within the same aperture for the same detector material and should only have memory effects influencing the uncertainty of the ratio. The ratio 2B to 2C suffers from both memory effects and aperture change (i.e. pointing, see 5.9.1.6). This ratio shows a decline which steepens after a few hundred Jy. The 2C to 3A ratio seems noisy but constantly high by 10%, this could be either a problem with absolute calibration or the RSRFs for these two bands.

Also note that band border calculations below 10 Jy, have influences from dark current subtraction as well as any other gain problems and are less useful to check the calibration consistency.

5.9.1.5 Model SEDs

All the stellar model SEDs used in the absolute photometric calibration claim accuracies between 3% and 6% depending on wavelength, except for NML Cyg which is not a good quality calibrator. NML Cyg is likely a variable source so the accuracy of this source as a calibrator is 30%. However, NML Cyg is very bright and can still provide important constraints on the linearity of the detectors.

Bands 1 and 2 are calibrated exclusively against stellar sources. Bands 3A-3D rely mainly on stellar sources with some input of the source NML Cyg.

The uncertainty introduced through the SEDs is reduced only by observing different sources. For example, it is assumed that all stellar sources have an uncertainty of 3%. Assuming the errors in the calibration sources are uncorrelated, a 3% uncertainty is reduced by the observation of 13 different sources. Since every band observed at least 9 different objects, all bands get some benefit. Even bands which partially use NML Cyg (∼30% uncertainty) only show an influence of 3% from the models themselves.

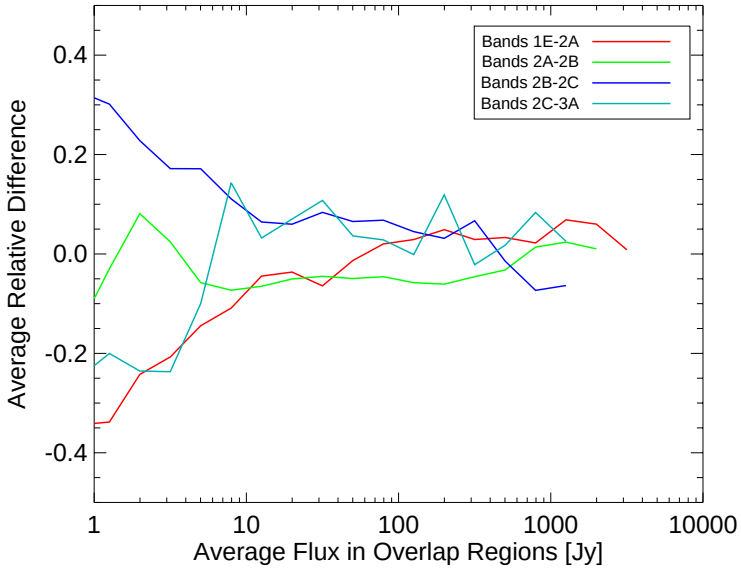

Figure 5.34: *This figure shows the band borders as a function of source brightness. Band 2 has significant memory effects for which a first order correction has been applied. However, the variations seen here are indications that there is a gain component to the memory effect which is not accounted for.*

The assumption of uncorrelated errors between models or between composites does not necessarily hold. Fortunately for the SWS photometric calibration at the key wavelength, the uncertainty of the models is not the limiting factor in the photometric accuracy.

5.9.1.6 Pointing

In this section, we present two separate analyses demonstrating the influence of pointing errors on the absolute photometry of SWS. In Figure 5.35 an analysis of the beam profiles stored in the Cal-G 35 is shown.

For this analysis, the pointing in dispersion and cross dispersion is assumed to have a random error about the zero (perfect pointing) with a Gaussian distribution of width σ. The σs are stepped through 40 different values ranging from 0.1" to 3". A random pair of y and z coordinates are generated from a Gaussian distribution of width σ. The value of the beam profile for this random pair is recorded. For each σ, 10,000 random pairs are drawn and the standard deviation is determined. This standard deviation is labelled as the resulting relative uncertainty in photometry due to pointing and it is shown in Figure 5.35. This figure can be used to estimate the impact of pointing errors on the flux of point sources in each band. The figure can also be used to determine, from the point of view of SWS, the satellite pointing accuracy.

The star γ Dra was observed many times by SWS. The peak to peak variation of the signal at the key wavelength for these observations was 30% in band 3A. According to Figure 5.35, a 1.5" pointing uncertainty would produce such a variation in photometry for band 3A. Assuming that all observations are effected by a 1.5" pointing uncertainty, results in the photometric uncertainties listed in Tables 5.5, 5.6 and 5.7 due to pointing.

It should be pointed out that the variation in the signal from γ Dra was not a random variation. As can be seen in Figure 8.8, the variation appears to by cyclic with a period of one year. Much effort has

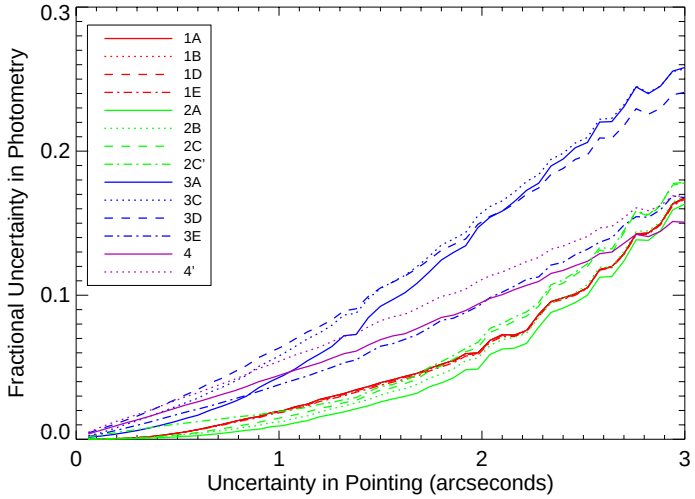

Figure 5.35: *Photometric uncertainty as a function of Pointing Errors for different pointing uncertainties. This figure shows the calculated standard deviation for a sample of 10,000 random draws of pointing errors (in dispersion and cross dispersion directions). Each mispointing is taken as a random number normally distributed with a 1σ. Band 1 is in red. Band 2 is indicated in green (dashed line for 2C'). Band 3 is in blue. Bands 4 and 4' are in purple (4' is dashed).*

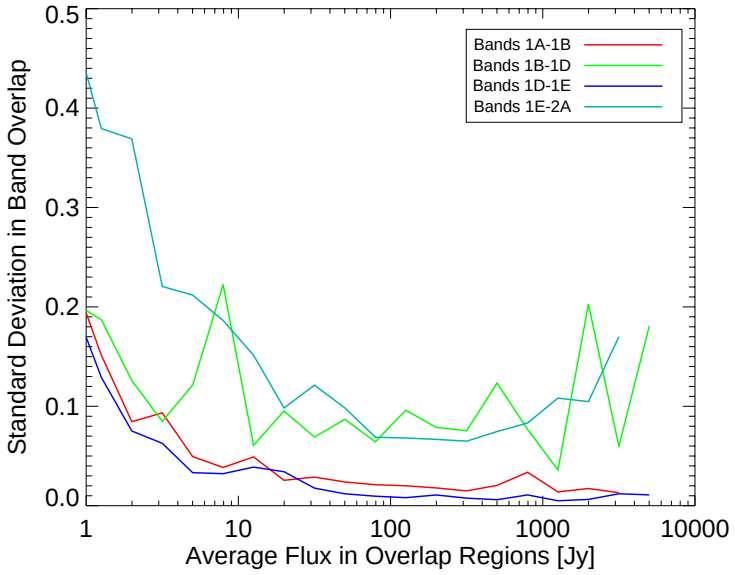

Figure 5.36: *The 1σ fractional uncertainties of the band-border ratios are shown. Different colours are for the different band borders as indicated. Note the significant increase in the uncertainties in the ratios between aperture changes (ratios 1B-1D and 1E-2A) implying that differences in pointings between apertures introduces uncertainties on the order of 5%.*

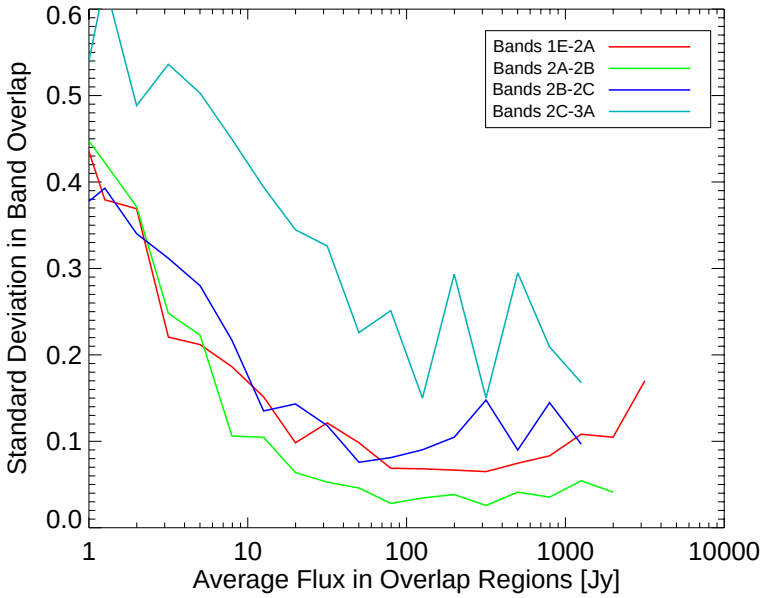

Figure 5.37: *The 1σ relative uncertainties are shown as solid lines. Different coloured lines indicate the different band-border uncertainties. The only band combination for which an aperture change is not present is for the 2A-2B band border.*

been put into identifying the cause of the signal modulation of γ Dra. This effort resulted in significant improvements of the accuracy of the satellite pointing. However, there remains a pointing error on the order 1.5" affecting all SWS observations.

In band 1, the band ratios of 1A-1B and 1D-1E are from bands within the same apertures. Satellite mis-pointings should not have a significant impact on these ratios. Thus the baseline relative uncertainties at fluxes above 10 Jy is worth a closer inspection. From Figure 5.36 the uncertainty is on the order of 1% for the two ratios. This level of uncertainty can be a combination of internal gain changes (which are note probed for band 1) and/or satellite jitter of 0.7".

The band ratio, 1E-2A also occurs within the same aperture. In this case the memory effects play a significant role in band 2.

5.9.1.7 Fringes

For measurements of unresolved lines, instrument fringes will introduce a further uncertainty (see Section 9.7 for a full description of the fringing in SWS bands). In Table 5.6 the percentage of residual fringes after RSRF correction is used to estimate the uncertainty introduced by fringes to line measurements.

5.9.2 The SWS photometric calibration error budget

Since the photometric calibration is the last calibration step (on the responsivity of the detectors) in the pipeline, this calibration will have been affected by all pipeline errors, systematic and random. The dispersion about the average conversion factor in the photometric calibration is then taken as the final photometric uncertainty in the specified band. These are the values already indicated in Table 5.3

The uncertainties in the SWS processing stream appear as systematic errors (uncertainties in calibrations) and random errors. The main wavelength dependent, systematic uncertainties have been discussed in the RSRF section, 5.4.6. The RSRF uncertainties will not be included in the discussions below.

Table 5.5 is the error budget (listed as 1σ uncertainties) for the photometric calibration for the SWS grating at the key wavelengths. This table includes the uncertainties of the SEDs used for calibration as well as the impact of low signal calibration sources on the uncertainty of the photometric calibration.

Table 5.5: *Sources of photometric calibration errors*[a]

Band	1	2A	2B	2C	3A	3C	3D	3E	4
Det. Type	InSb	Si:Ge	Si:Ge	Si:Ge	Si:As	Si:As	Si:As	Si:As	Ge:Be
Dark Noise [μV/s]	1	1.5	1.5	1.5	5	5	5	5	10
Percent Dark Noise	0	0	0	0	0.5	0.5	0.5	5.0	2
Internal Cal.[b]	2	2	2	2	0.5	0.5	0.5	0.5	5
Memory[c]	-	5	5	5	-	-	-	-	15
Glitches [d]	-	-	-	-	-	-	-	-	5
Models/SEDs	1	1	1	1	2	2	2	2	3
Pointing [e]	4	3	3	3	10	10	10	6	7
Uncertainty (rss)[f]	4.6	6.3	6.3	6.3	10.2	10.2	10.2	8.1	18.3
Observed 1σ[g]	4	7	7	7	12	10	13	17	22

Notes:

[a] All uncertainties are 1 σ percentages unless otherwise noted.

[b] Band 1 did not have a useful internal calibration scan after revolution 64 during science observations. Up to revolution 64 the internal calibration for band 1 had a peak to peak variation of 4%.

[c] Estimate of influence on photometric uncertainty. For signals larger than 1000 Jy the estimate is more like 10%

[d] Particle hits influence the photometry based on the residual energies the particles dispose on the detectors. In the SWS terminology these residuals are called 'glitch tails'.

[e] Estimate of pointing uncertainty based on SWS beam profiles and a pointing uncertainty of 1.5" (see 5.9.1.6).

[f] root sum squared values of the different uncertainty components

[g] Taken from Table 5.3

5.9.3 Reproducibility

The reproducibility of SWS observations can be ascertained by the analysis of data available for objects observed many times using the same observing mode. This is true of two objects, γ Dra and NGC 6543. The γ Dra results are shown in Figure 8.8. NGC 6543 was monitored throughout the ISO mission to correct for changes in the wavelength calibration. However, the line fluxes themselves also provide insight into the reproducibility of SWS observations. The results from the line study of NGC 6543 are presented here. The data used for Table 5.6 are standard pipeline AAR products (see Section 7.3) of $\sim$30 observations of NGC6543 after revolution 377. The flux of thirteen separate emission lines is measured by standard line integrating routines. The lines fall within 9 of the SWS bands, only bands 1A, 2B and 3E do not contain emission lines in this data set. See Feuchtgruber 1998b, [7] for a complete description of the dataset and processing.

Table 5.6 shows the expected reproducibility of SWS grating observations based on the known uncertainties in the SWS calibration. The NGC 6543 line fluxes largely confirm the uncertainties in the processing pipeline. For this comparison, the uncertainties introduced by fringes are explicitly expressed since fringing will have a significant impact on the line fluxes.

The uncertainties listed in Table 5.6 are the root sum squared (rss) values of the different uncertainty components. This is likely to produce an over-estimate of the uncertainty for a number of reasons. First,

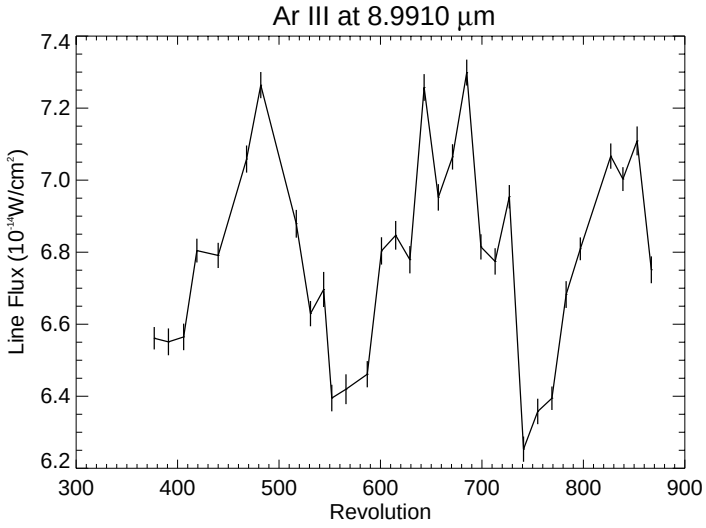

Figure 5.38: *This figure shows the flux of the Ar III line at 9 μm in the planetary nebula NGC6543 as a function of time. Due to the spatial structure of the nebula, different roll angles seem to modulate the Ar III line. The line flux is reproducible at the 4% level. If the modulation is taken into account the line flux is reproducible to within 2%.*

since reproducibility is a question of repeating an observation, instrumental effects like transients are likely to be highly reproducible as well. Pointing is also a component in the uncertainty, but for extended sources the pointing uncertainty will not have the impact that it has for point sources.

As discussed in Feuchtgruber 1998b, [7], NGC6543 is not ideal for determining the reproducibility. The 32 observations were designed to monitor the wavelength calibration and do not cover every band. Furthermore, NGC6543 is extended and has quite a bit of structure in the line emission. Most of the line fluxes show a biannual variability which is consistent with the changing roll angle of the observations. For the lines showing the modulation, fitting out the modulation reduces the uncertainty by 1–3 percentage points. Figure 5.38 shows the Ar III line flux for 32 observations after revolution 377. The Ar III line occurs at 9 μm within band 2C. The biannual modulation is evident in the figure, however, the standard deviation of the line fluxes is only 4%, when the modulation is taken into account the standard deviation drops to 2%. The uncertainties listed in Table 5.6 have not been corrected for this modulation.

Table 5.6: *Reproducibility*[a]

Band	1A	1B	1D	1E	2A	2B	2C	3A	3C	3D	3E	4
Internal Cal.	2[b]	2	2	2	2	2	2	0.5	0.5	0.5	0.5	5
Memory	-	-	-	-	5	5	5	-	-	-	-	15
Fringes[b]	8	3	5	1	2	1	4	5	4	2	2	-
Pointing	4	4	4	4	3	3	3	10	10	10	6	7
Uncertainty (rss)	9	5	7	5	6	6	7	11	11	10	6	17
NGC 6543 1σ	-	6	10	5	9	-	6	8	6	10	-	5

Notes:

[a] All uncertainties are 1 σ percentages unless otherwise noted.

[b] From Table 9.2 in Section 9.7 assuming residual fringes after RSRF correction.

5.9.4 Overall error budget

Table 5.7 is the error budget for a general grating observation at the key wavelength. It lists our best estimates of the major uncertainties on the continuum of any given observation. For line observations, the impact of fringes will have to be taken into account (see Section 9.7). For wavelengths off of the key wavelength the increased uncertainty in the RSRF of the particular band should be root sum squared as well.

There are four main sources of random uncertainties in SWS data:

1 Satellite pointing

2 Memory effects

3 Internal calibrator scans

4 Dark current determination and glitches

The various components to the uncertainties have been discussed in their own sections.

In Table 5.7, we indicate the average dark current noise along with the photometric uncertainties. The dark noise listed is a typical value on 2 sec resets per detector as measured in orbit (Heras et al. 2000, [15]).

The last two columns of Table 5.5 are the root sum squared of the listed uncertainties and the observed standard deviation of the calibration observations. These two columns agree very well, indicating that uncertainties are relatively well understood. The difference between the expected band 3E and the measured value is significant and points to something not yet taken into account.

Table 5.7: *Overall photometric error budget for SWS*[a]

Band	1	2A	2B	2C	3A	3C	3D	3E	4
Det. Type	InSb	Si:Ge	Si:Ge	Si:Ge	Si:As	Si:As	Si:As	Si:As	Ge:Be
Dark Current Noise [μV/s]	1	1.5	1.5	1.5	5	5	5	5	10
Internal Cal.[b]	2	2	2	2	0.5	0.5	0.5	0.5	5
Memory[c]	-	5	5	5	-	-	-	-	15
Pointing[d]	4	3	3	3	10	10	10	6	7
Signal-to-Flux	0.5	0.9	0.9	0.9	1.5	1.5	1.5	1.7	3
Uncertainty (rss)[e]	4.5	6.3	6.3	6.3	10.1	10.1	10.1	6.3	17.6

Notes:

[a] All uncertainties are 1 σ percentages unless otherwise noted.

[b] Band 1 did not have a useful internal calibration scan after revolution 64 during science observations. Up to revolution 64 the internal calibration for band 1 had a peak to peak variation of 4%.

[c] Estimate of influence on photometric uncertainty. For signals larger than 1000 Jy the estimate is more like 10%.

[d] Estimate of pointing uncertainty based on SWS beam profiles and a pointing uncertainty of 1.5" (see 5.9.1.6).

[e] Expected photometric uncertainty (root sum squared) without accounting for detector noise.

Chapter 6

Calibration of SWS after Liquid Helium Depletion

6.1 Introduction

After the liquid helium depletion of ISO, an engineering test programme was conducted on the different satellite systems. Besides functional tests of the various redundant systems, a lot of time was devoted to the testing of alternative pointing strategies in case of failure of one or more gyros.

During this test programme the temperature of the focal plane remained low enough to operate the InSb band 1 detectors of the SWS. The instrument could be operated in some timeslots available during the engineering test programme. This time was used to record spectra of stars between 2.36 and 4.05 μm at medium resolution ($\approx$ 1500 - 2000). As the temperatures of the focal plane increased, changes in the position readout of the grating scanner and changes in the response of the instrument could be seen. In this chapter, the observation mode and the calibration of the changing characteristics of the instrument is presented.

6.2 Temperature Change of the ISO Focal Plane

The temperature of the focal plane steadily increased after the helium boil-off. Figure 6.1 shows how after some days it exceeded the dynamic range of the temperature sensors on the optical support structure. The temperature trend of the focal plane further in the Post-Helium Phase can be inferred from a similar trend seen in the temperatures of the upper baffle of the ISO telescope. It is estimated that the temperature of the SWS detectors increased from the nominal operating temperature (1.8 $\pm$ 0.1 K) to 40 K $\pm$ 5 K over the 30 days of post-helium operations.

Before the helium boil-off, it was anticipated that the temperature of the focal plane would increase sufficiently to allow operating the JFET cryogenic readout without heating. The slow temperature increase however made heating required throughout the entire Post-Helium Phase for the JFETs to function properly. This was verified during every revolution with SWS operations. The instrument controllers manually uplinked a command sequence to the spacecraft to switch off the JFET-heaters for one minute. It was verified offline that this indeed corrupted the detector readout.

6.3 Wavelength Calibration and Spectral Resolution

As the focal plane temperatures of ISO increased, a distinct shift in the position of spectral features could be seen. Fig 6.2 shows how the position of the Hydrogen Pfund-β line shifts in the uncalibrated spectrum

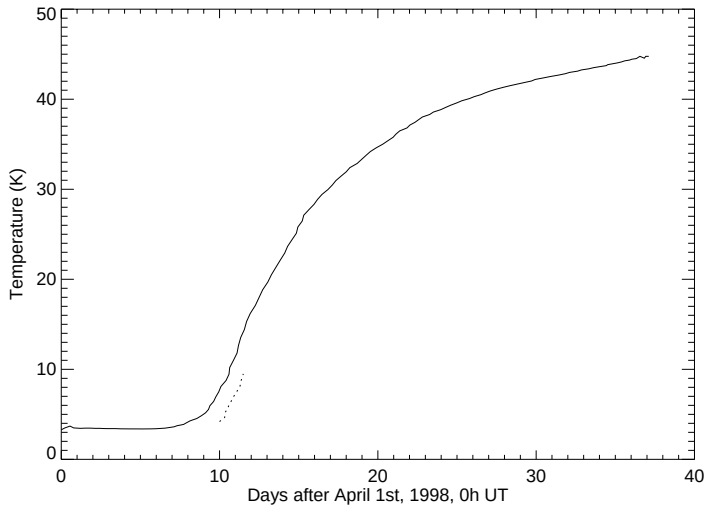

Figure 6.1: *The temperatures of the optical support structure (lower short curve, dashes) and of the upper baffle of the ISO telescope (upper curve, solid line) increased smoothly during the Post-Helium Phase.*

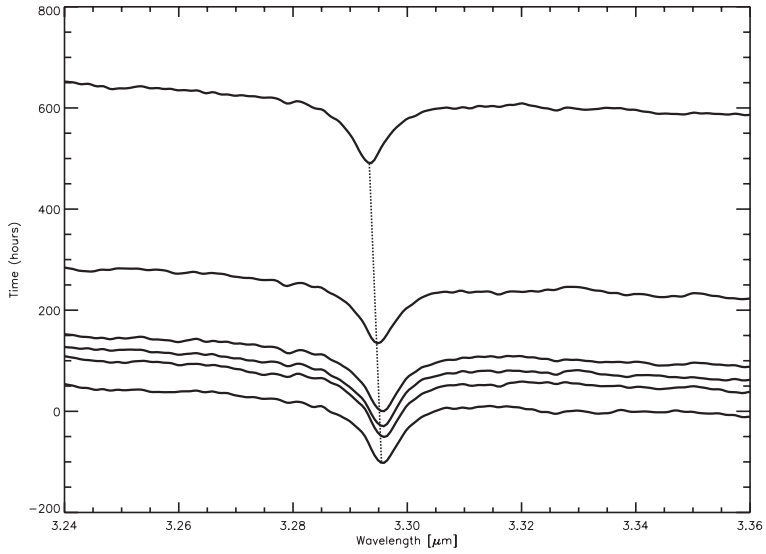

Figure 6.2: *As temperatures changed, geometry changes in the grating scanner mechanism induced a shift in the position of spectral feature like the Hydrogen Pfund-β line in the spectrum of α Lyr.*

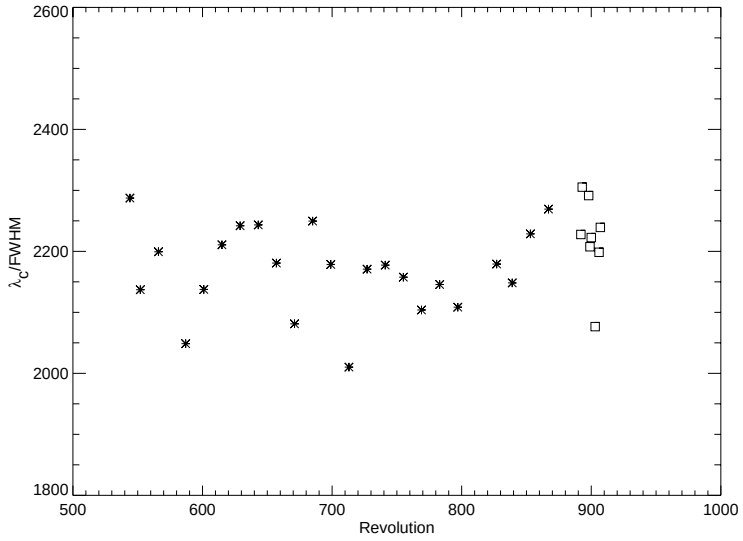

Figure 6.3: *The variation of the spectral resolution as measured from the width of the H95 line [3.297 μm] in NGC 6543. Crosses are the values during the nominal mission. the squares are the values measured during the Post-Helium Phase.*

of α Lyr.

To facilitate the wavelength calibration of the SWS, a fixed Fabry-Pérot is mounted in front of the internal calibration source. During the post-helium operations, a spectrum of the fringes produced by this system was observed at the beginning of every revolution when the SWS was switched on.

Each of these measurements was used to determine a wavelength calibration of the SWS, applicable to the instrument at the time of the calibration measurement. The wavelength calibration for a single post-helium observation can be calculated by interpolating these calibration parameters in time. This results in a wavelength calibration better than 1 resolution element (λ / $\delta\lambda \sim 2200$) and comparable to the grating wavelength calibration of an observation during the nominal part of the mission (Valentijn et al. 1996, [37]).

The spectral resolution as measured from the FWHM of unresolved lines in NGC 6543 varied throughout the post-helium mission, but within the scatter of similar measurements during the nominal mission. For the major part of the ISO mission, this source was visited every two weeks for an SWS02 scan of selected lines. A Calibration Uplink System (CUS) observation was engineered to perform linescans similar to the SWS02 scanning mode. This allowed to continue the monitoring of wavelength calibration stability and resolution on external sources. Figure 6.3 depicts the variation of the spectral resolution of the unresolved H95 line at 3.297 μm in the planetary nebula NGC 6543. One can see that the resolution during the Post-Helium Phase is not drastically different from the values during the nominal mission (Valentijn et al. 1996, [37]).

6.4 Detector Dark Currents

The dark signals and the noise on the dark signals measured after the helium boil-off are not significantly different from those measured during the nominal mission. Figure 6.4 shows the mean of the detector signals during the dark current measurements in the calibration observations during every revolution in the Post-Helium Phase. There is no distinct trend with the temperature increase. This is not so

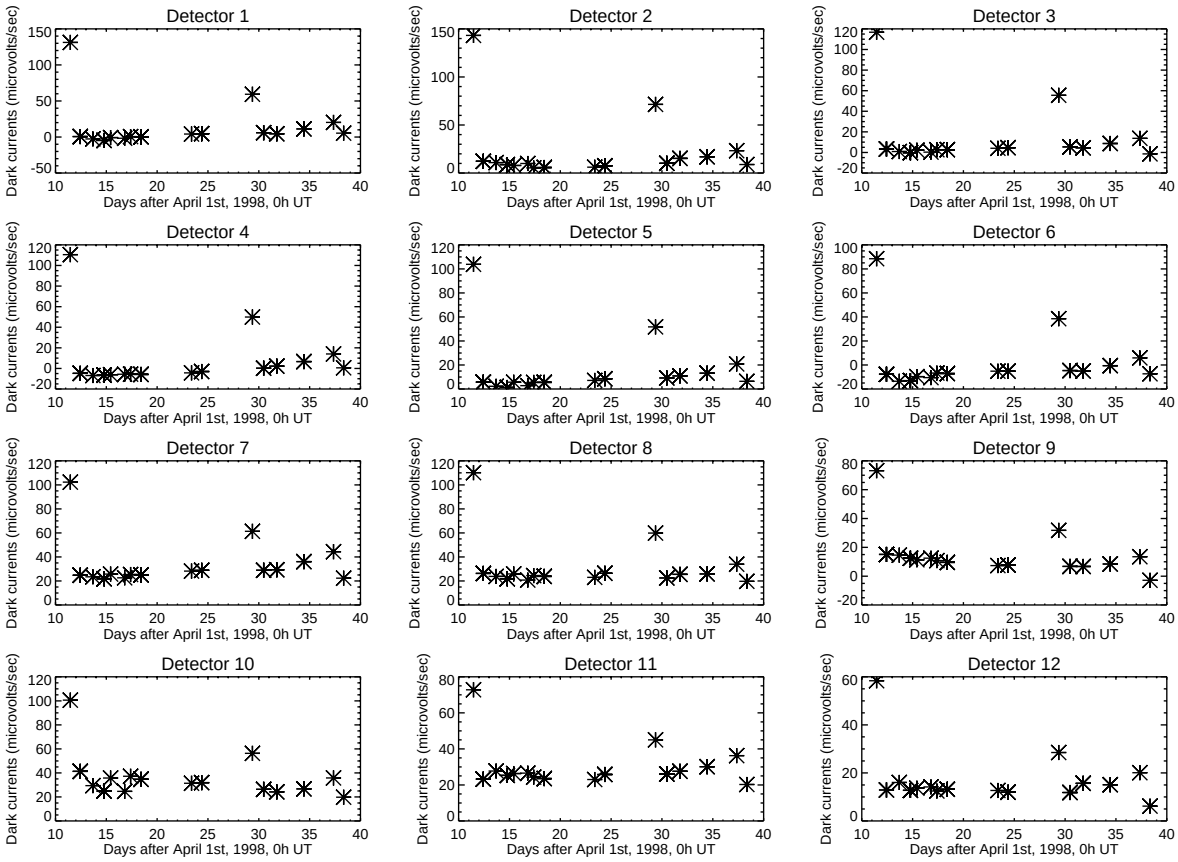

Figure 6.4: *The variation of the mean detector dark signals during the Post-Helium Phase*

surprising, since the output signal of the instrument with closed shutter is dominated by the JFET amplifier offsets rather than the detector dark currents.

6.5 Relative Spectral Response Change

In every post-helium revolution with SWS observations, a full spectrum of at least one calibration star was measured. Section 6.7 gives an overview of the calibration sources used for the flux calibration (both relative and absolute) of the Post-Helium Phase. Comparison of the observed calibration source spectra to a reference spectral energy distribution (SED) shows an increasing tilt of the observed spectrum as the temperatures increases. As can be seen in Figure 6.5, if the spectrum of γ Dra observed in revolution 880 and revolution 907 are divided by the model SED, the linear fit to the residues shows a steeper slope in the later revolutions.

This effect was characterised for every spectral band by fitting a polynome $R(\lambda)$ (n=1) to the division of each calibration star spectrum by its reference SED. The change of the coefficients of these fits in time was then characterised by fitting 2 polynomes $P_n(T)$ to the coefficients of the polynomes $R(\lambda)$. The tilt to apply on a spectrum observed at time t is then $P_1(T) + \lambda P_2(t)$. Figure 6.6 shows the coefficients of the fits to the RFRF residues and the fits to the change of these coefficients.

The characterisation described above minimizes the risk of biasing the correcting tilt to a noisy observation or a specific spectral feature not accurately represented in the synthetic spectra. The different calibration

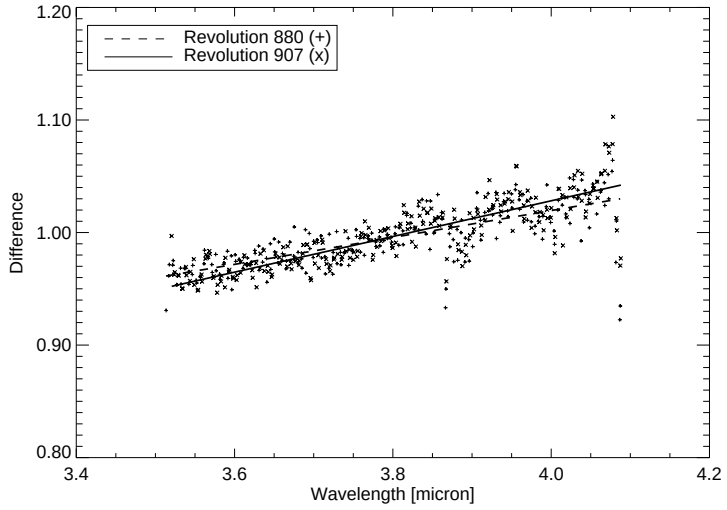

Figure 6.5: *Division of the observed spectrum of γ Dra by a synthetic spectrum in the beginning and the end of the Post-Helium Phase. The Relative Spectral Response of the SWS tilts more as the temperature increases.*

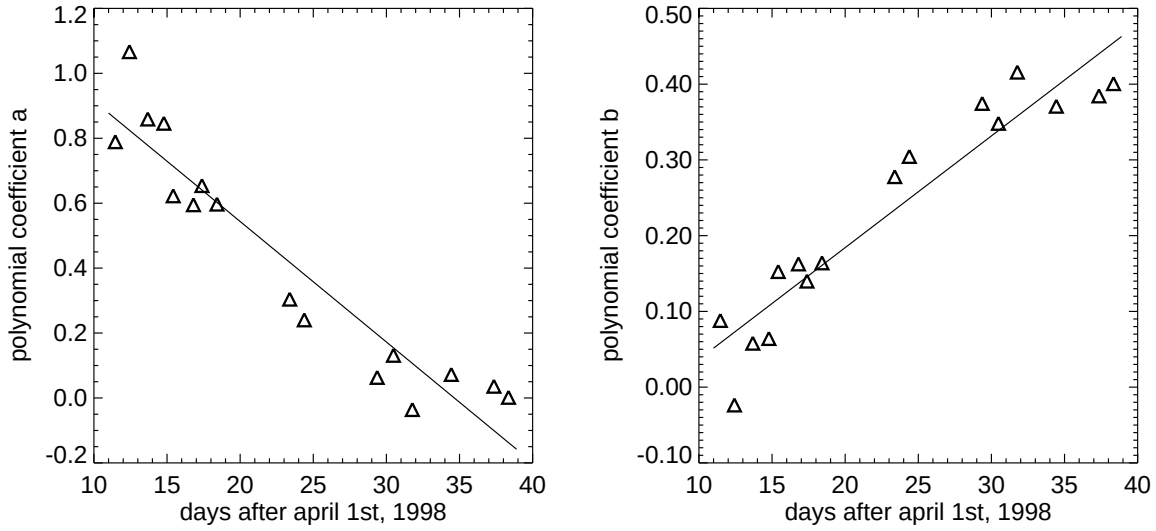

Figure 6.6: *Characterisation of the changing slope of the RSRF for detector 7 in band 1A. The triangles are the polynomial coefficients of the fits to the slope difference between calibration observations and model spectra. The solid line is a linear fit to the coefficients against time.*

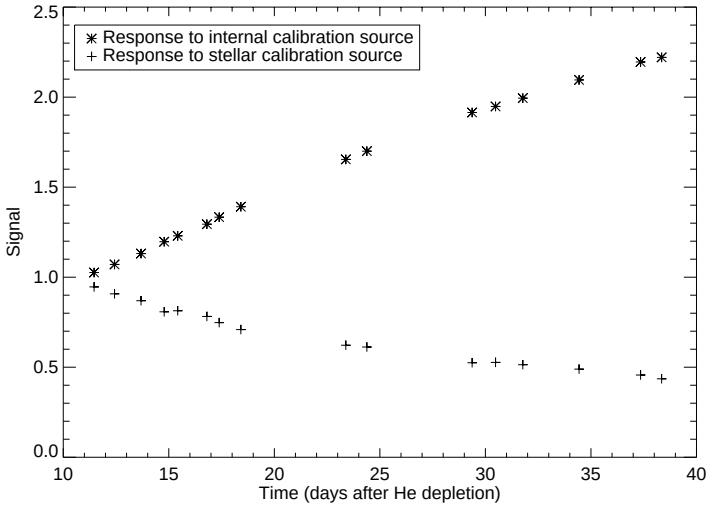

Figure 6.7: *Change of the SWS detector 7 response to the signal of the internal calibration source and to the signal of an external calibration star.*

stars cover a wide range in spectral types. The deficiencies in the synthetic spectra are of a different nature and in different spectral regions (Section 6.7, Decin 2000, [4], Decin et al. 2000, [5]). The double fitting process described above results in some sort of 'averaging out' of the uncertainties in the synthetic spectra and the observations.

6.6 Absolute Flux Calibration

The SWS has built-in calibration sources to tie the flux calibration observations on external sources to frequent internal photometric calibration checks during every observation. During the Post-Helium Phase the signal from these photometric checks increased with the increase of the focal plane temperature. However, the system response to the external calibration sources decreases with time (Figure 6.7). This discrepancy can be understood as a combination of different effects. The increase of temperature of the calibration source could result in a higher flux. Also temperature changes of the telescope could result in a slight defocussing, which could explain (part of) the lower response to the external source. This second effect is likely to be marginal, since no significant change in the wavelength resolution was seen (Section 6.3). Defocussing the telescope, i.e. broadening the profile of the beam entering the instrument, would result in a broader instrumental profile.

The exact reasons for the system responsivity changes cannot be disentangled, but the strategy for an empiric flux calibration is straightforward: for each spectral band signal/flux ratios per detector are determined from the daily observations of standard calibration stars. The calibration sources and reference spectra used are listed in Section 6.7. A polynomial fit (n=2) to those values against time is the flux calibration function. Evaluation of this polynome in the time of a post-helium observation gives the signal/flux ratio to apply on the observation.

Also here the method averages out uncertainties in the accuracy of spectral features in the individual reference spectra and calibration observations.

Table 6.1: *The calibration stars used for deriving the Relative Spectral Response Function and flux calibration of the Post-Helium Phase*

Source	Sp. Type	# obs
α Lyr	A0 VA	6
δ Dra	G9 III	7
γ Dra	K5 III	3

6.7 Post-Helium Flux Calibration Sources

Table 6.1 shows the calibration stars used for the calibration of the RSRF and the flux calibration of the observations obtained during the Post-Helium Phase.

The reference SED used for α Lyr was a composite spectrum by Cohen et al. 1992a, [2] while the synthetic spectra for δ Dra and γ Dra were taken from Decin 2000, [4]. These synthetic spectra are based on the SOS-MARCS model atmosphere code (Gustafsson et al. 1975, [12]) and were generated using the TurboSpectrum programme (Plez, Brett & Nordlund 1992, [31]).

The following fundamental stellar parameters were used for δ Dra: T_{eff} = 4820 K; log g = 2.90; ξ_t = 1.7 km/s; [Fe/H] = 0.00; ϵ(C) = 8.25; ϵ(N) = 8.26; ϵ(O) = 8.83; $^{12}C/^{13}C = 12$; θ_d = 3.31 mas.

In the case of γ Dra the parameters used were: T_{eff} = 3930 K; log g = 1.55; ξ_t = 2.0km/s; [Fe/H] = 0.00; ϵ(C) = 8.22; ϵ(N) = 8.26; ϵ(O) = 8.81; $^{12}C/^{13}C = 10$; θ_d = 10.07 mas.

Chapter 7

Standard Product Generation

7.1 Introduction

The Standard Product Generation (SPG) (also known as Off-Line Processing (OLP) or simply the 'pipeline') processes the raw data telemetered down from ISO (in terms of bits) into more conventional astronomical units of flux against wavelength in a purely automatic procedure. This chapter describes the pipeline and its error propagation. It should give the reader an understanding of what processing has been carried out on the data and why. The ISO Legacy Archive was processed with OLP Version 10.1.

The pipeline is composed of three parts:

• Extracting from the raw data stream the instrument data and placing it into Edited Raw Data (ERD) files. For SWS this process is a reformatting step only and will not be discussed further.

• ERD to Standard Processed Data (SPD) stage, known as Derive-SPD (DSPD). This involves removing all instrumental effects on time scales of less than 1 reset interval, converting detector readouts (bits) into slopes (μV/s) and assigning wavelengths, where possible. Pointing and instrument status files are also read in at this stage. This results in a table of corrected slopes, which should be proportional to the flux density of the target under study, errors and wavelengths in μm. The table is still in time order.

• SPD to Auto-Analysis Results (AAR) stage, known as Derive-AAR (DAAR). This further processes the SPD removing instrumental effects on time scales of greater than 1 reset interval and converts slopes to fluxes (Jy). It results in fully calibrated fluxes as a function of wavelength.

In the course of Derive-SPD and Auto-Analysis several files are used that describe the behaviour of the instrument and its performance. These calibration files are known, for historical reasons, as Cal-G files. They contain such things as the conversion between scanner position and wavelength, the relationship between voltages per second and fluxes, etc.

Examples of the data produced by these steps are given throughout this chapter. In previous chapters examples were given for each of the 4 observing modes of SWS (see Sections 3.3 to 3.6), in raw ERD format or processed to SPD or AAR.

Sections and subsections describe (compound) steps in the pipeline processing. They are in the order in which they occur in the pipeline. Sections 7.2 and 7.3 describe the DSPD and DAAR processing, together forming the complete pipeline. Section 7.4 describes the error propagation for SWS. The last Section 7.5 shortly describes the software elements the pipeline is built of. These elements are runnable procedures within OSIA.

7.2 From ERD to SPD

Derive-SPDs' main input is Edited Raw Data (ERD), 24 Hz data containing detector readout (in bits) of the target's flux, of internal calibration exposures, of wavelength indicators, of dark currents and of housekeeping data. Within the ERD there is also information available from pointing or instrument status files. While processing, the pipeline software reads several Cal-G files.

For each detector, all data for one full reset interval are combined to a single current estimate at single wavelength and are then saved in the Standard Processed Data (SPD) file for that AOT. No attempt is made within Derive-SPD to average measurements of the same type (e.g. dark current measurements) on any time scale longer than one reset interval.

Each measurement for one reset interval of a given AOT is saved separately inside the same SPD product in chronological order of acquisition. The motivation for this is to offer to the observer the possibility of judging the stability and repeatability of SWS measurements. There is a one-to-one correspondence between AOTs and SPD files. That is, one AOT produces one SPD file.

A basic overview of the Derive-SPD processing is given in Figure 7.1, the ERD and SPD files are described in Sections A.2.1 and A.3.1, and each step in the processing is described in the following sections.

7.2.1 Reading the ERD

The ERD data for the observation are read in. As discussed above, each AOT generates different types of data: astronomical measurements from the source, measurements of the currents for the grating and FP positions, measurements of the calibrators and dark currents. Each of these different types of data has a different physical meaning and serves a different purpose. Hence, the data must be flagged according to their type.

Each ERD data record is tagged with an Instrument Time Key (ITK) which points toward a unique record in the Compact Status History (CSH) file (see Section A.2.2). Cross-correlating the ERD ITK with the CSH, Executed Observation History per ICS (EOHI) and General Housekeeping (GEHK) files (both described in the ISO Handbook Volume I, [17]) allows a determination of the status of the SWS instrument at the time of the measurement and therefore of the type of the data recorded and the actual wavelength range covered.

The velocity of the spacecraft is obtained from the IRPH file. It is written into the header file and used later in the Derive-AAR processing stage.

Figure 7.2, top panel, shows 40 seconds of detector 16 ERD data from an SWS02 observation after reading in. This is the same SWS02 shown in Section 3.4.

7.2.2 Determination of the data range

This checks the data values and marks any out of limits. Values are OK when they are larger than 0 and less than 4095. Other data are flagged as out of limit. The values defining the ranges are kept in the calibration file Cal-G 4.

7.2.3 Subtraction of the 'midbit' values

In SWS the detector readout voltages of between -10 and $+10$ V are converted into a bit number ranging from 0 to 4095. The 'midbit' is the bit value that corresponds to 0 Volts. It is set to exactly half of 4095, i.e. 2047.5, for all detectors. This data is stored in the calibration file Cal-G 2A.

The precise value of 'midbit' is not important. It only determines the global level of the samples and also, due to later steps in the pipeline (Section 7.2.5), the overall level of the signal. This overall level is corrected again when subtracting the dark current (Section 7.3.3).

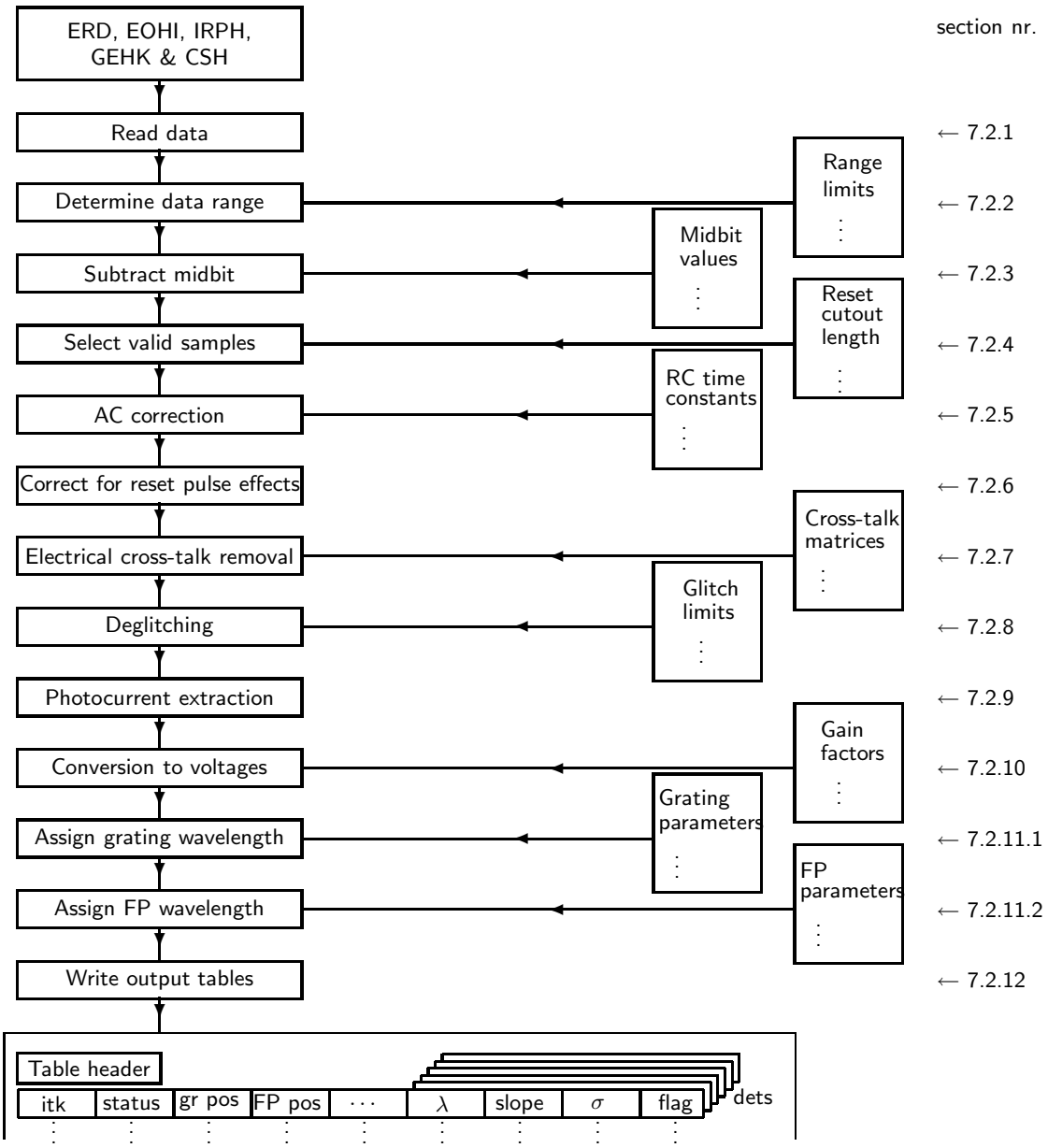

Figure 7.1: *The Derive-SPD flow-diagram*

7.2.4 Selection of valid samples

After each reset a number of samples should be ignored. They are too much affected by the reset pulse. This number is stored in the calibration file Cal-G 3. The values in the file are all set to 6 for OLP 10.

This is not formally a step in the DSPD processing as it is determined in each of the following steps what the valid samples are. It is presented here as henceforth all processing only affects the valid samples.

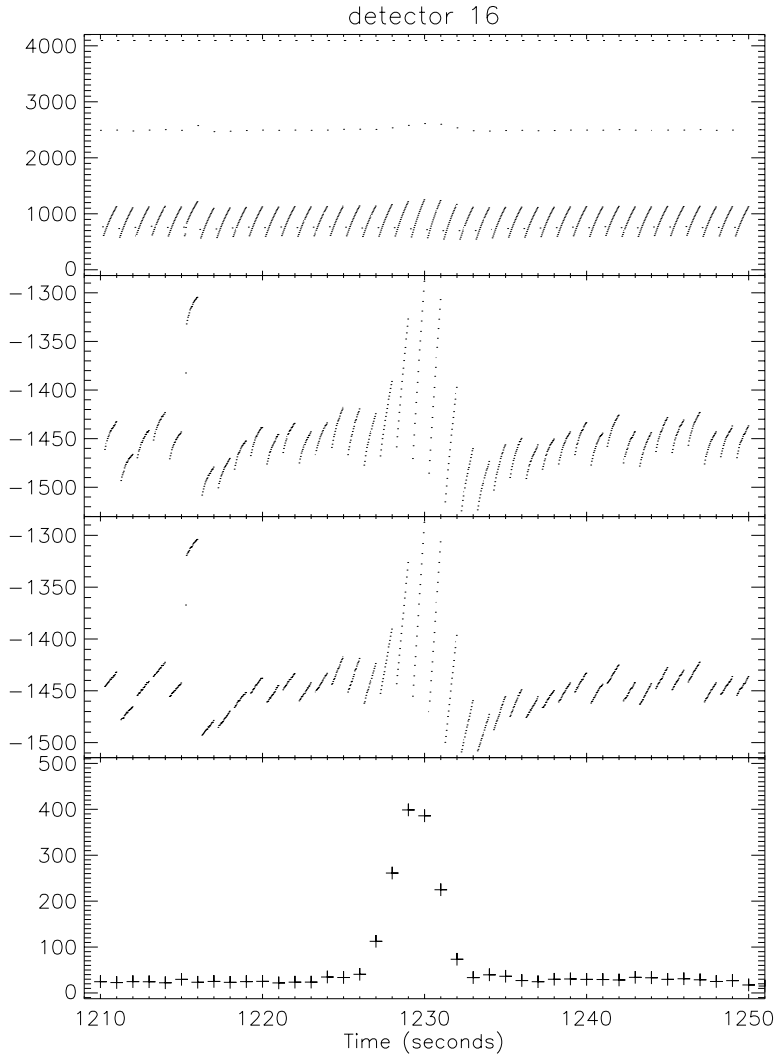

Figure 7.2: *Example data from various sections of the SPD processing. From top to bottom the first panel shows a portion of the raw ERD from detector 16 of an SWS02 observation. The second panel shows the same data after determination of data range, 'midbit' subtraction, valid data selection and correction for RC constant. The next plot shows the ramps straightened by the pulse-shape correction. The final plot shows the SPD output. The top three plots are in bit values against time, whereas the SPD is in $\mu V/s$ against time.*

7.2.5 Correction of the integration ramp for the RC time constant

The amplifier chain contains a high pass filter. For a constant voltage gradient input the response of the amplifier is expected to asymptotically approach a constant value, i.e.

$$\frac{dV(t)}{dt} + \frac{V(t)}{T} = \frac{dV_o(t)}{dt} \tag{7.1}$$

where $V(t)$ is the output voltage at time t, V_o the input voltage across the capacitor due to the accumu-

lation of charges on the detector, and T the detector time constant. In order to later reconstruct the true photo-current, it is first necessary to linearize the ramps, i.e. determine the actual input voltages $V_o(t)$ applied on the detector. Each detector has its own time constant, which is stored in the calibration file Cal-G 2.

Knowing the RC time constant T, it is straightforward to integrate the above formula and derive the input voltage. The trapezium rule is used to calculate the integral.

$$V_k^{corr} = V_k + \sum_{j=3}^{k} \frac{(V_j + V_{j-1}) \cdot \Delta t}{2\tau} \tag{7.2}$$

The time constants stored in Cal-G 2, however, are expressed in terms of frequency, which relates to the τ in Equation 7.2 as $\tau = 1/(2\pi T)$.

The second plot in Figure 7.2 shows 40 seconds of detector 16 after the determination of data range, 'midbit' subtraction and correction for RC constant. The main difference between the first and second plot is due to this correction.

7.2.6 Correction for the reset pulse effects

SWS defines the pulse-shape as the after-effect of the reset-pulse applied after each reset interval. It manifests itself as an exponential curve with typical decay times of 0.25 – 0.5 seconds and a typical amplitude of 20 – 50 μV. The pulse-shape is an additive component to the integrated signal of the detector, while the impact on the observed ramp depends on the gain setting of the instrument. Significant corrections are to be expected for high gain observations only. The pipeline corrects for the pulse-shape on an observation basis. Consequently we do not rely on a fixed calibration file but use the data itself to do the calibration.

While the correction itself is a plain subtraction of the pulse-shape, the difficulty is to find the right pulse-shape. Per detector slopes are fitted to the readouts in each reset interval. The residuals contain the raw pulse-shape after-effects. To the residuals an exponential function is fitted, which determines the decay time for this detector in this observation. With this fixed decay time amplitudes of the exponential are determined, now for each reset interval individually. Subsequently the amplitudes are smoothed to reduce the noise and the resulting shapes are subtracted from the readouts.

More details of the method are explained in Lahuis 1998, [23] and Kester 2000, [20].

The third panel in Figure 7.2 shows 40 seconds of detector 16 after this processing step. Compared to the second panel the slopes have been straightened.

7.2.7 Removal of electrical cross-talk

Due to parasitic capacitance between neighbouring detectors any signal in one grating detector will 'leak' to other detectors (primarily the adjacent ones) in the same array. This 'leak' to the adjacent detector is of the order of 10%.

Assuming the detector response is a linear function of the intensity of the signal, a set of cross-talk matrices can be determined with constant correction factors. The readouts V of each individual detector j in the detector array may then be corrected by applying the following formula:

$$V_j^{corr} = \sum_i C_{i,j} \cdot V_i \tag{7.3}$$

The sum is over all detectors i that are within the same detector block as detector j (12 for the gratings and 2 for the FP). This cross-talk correction matrix, C_{ij}, is held in the calibration file Cal-G 1. It was derived from data taken from charged particle radiation tests in the laboratory and verified in orbit.

There is little effect on the data at this processing step, so a plot is not shown.

7.2.8 Glitch detection

Glitches are sudden jumps in the output signal from a detector. How glitches are recognised in the data depends on which AOT the data is from. For SWS02, SWS06 and SWS07 the grating scanner does not move during a reset interval. Any sudden jump in the output of a detector during a reset interval is probably a glitch and can be recognised as such. For SWS01 however, the grating does move during a detector reset interval. It can scan across an entire line during a reset interval. If the line is strong enough there is a sudden increase in the signal level as the grating scans across it which might be mistaken for a glitch.

Therefore deglitching is handled differently in SWS01s compared to the other AOTs.

7.2.8.1 Glitch detection in general

Glitches are recognized in the differentiated outputs of each detector, $\delta S_k = S_k - S_{k-1}$. For each detector, the median, $m = \text{median}(\delta S_k)$, and the median width, $w = \text{median}(|\delta S_k - m|)$, of the differentiated outputs are calculated. A threshold is defined as $w_t = \max(\alpha \cdot w, w_{\min})$, where α is a numerical factor and $w_{\min}$ is a minimum width. Both of them are held in calibration file Cal-G 6. For OLP 10, α equals 8 and $w_{\min}$ equals 5. Samples are flagged as glitched when $|\delta S_k - m| > w_t$.

As a large fraction of all glitches is spread over more than one sample, the samples preceding and following them are checked again. If they are larger than 40% of the threshold, they are also marked as glitches.

In this processing step glitches are only marked as such. During the slope fitting (Section 7.2.9) a model including slope and glitches is fitted to all samples within the reset interval.

If glitches are detected during a reset this is noted in the flag word. Also the actual number of samples contributing to the slope calculation is decreased by the amount of glitched points found. This number appears in the *offset* tag (`SWSPOFFS`) in the SPD and in the *tint* tag (`SWAATINT`) in the AAR.

The SWS Glitch History (SWGH) file contains the two largest, if any, glitches found in each reset interval. For a description of this file see Section A.3.2.

The accuracy of deglitching depends not only on how well a glitch can be identified, but also on the effects of the glitch with time (the so called glitch-tails, see also Section 9.2.4). Especially in band 4 and in the FP bands glitch tails are occurring frequently. They show as a sudden increase of the flux decaying in about 10 seconds.

Figure 7.3 shows the effect of the deglitching software, showing the ERD and the SPD processed with and without the deglitching software. Where the software has not been used the glitches in the ERD cause the slope in the SPD to vary rapidly in time. Where the software has been used it has identified where the glitches occur, allowing them to be taken into account when calculating the slopes. The resultant SPD is much smoother.

For a further discussion of glitches and their correction see Kester 1999, [19], and Wieprecht, Wiezorrek & Haser 2000, [43].

7.2.8.2 Glitch detection and correction in SWS01

Because in SWS01s the grating is moving during a detector reset interval special care has to be taken reducing the data in order not to confuse narrow lines with glitches. In order to correctly distinguish between glitches and unresolved lines, a source signal is estimated and subtracted from the ramp derivative

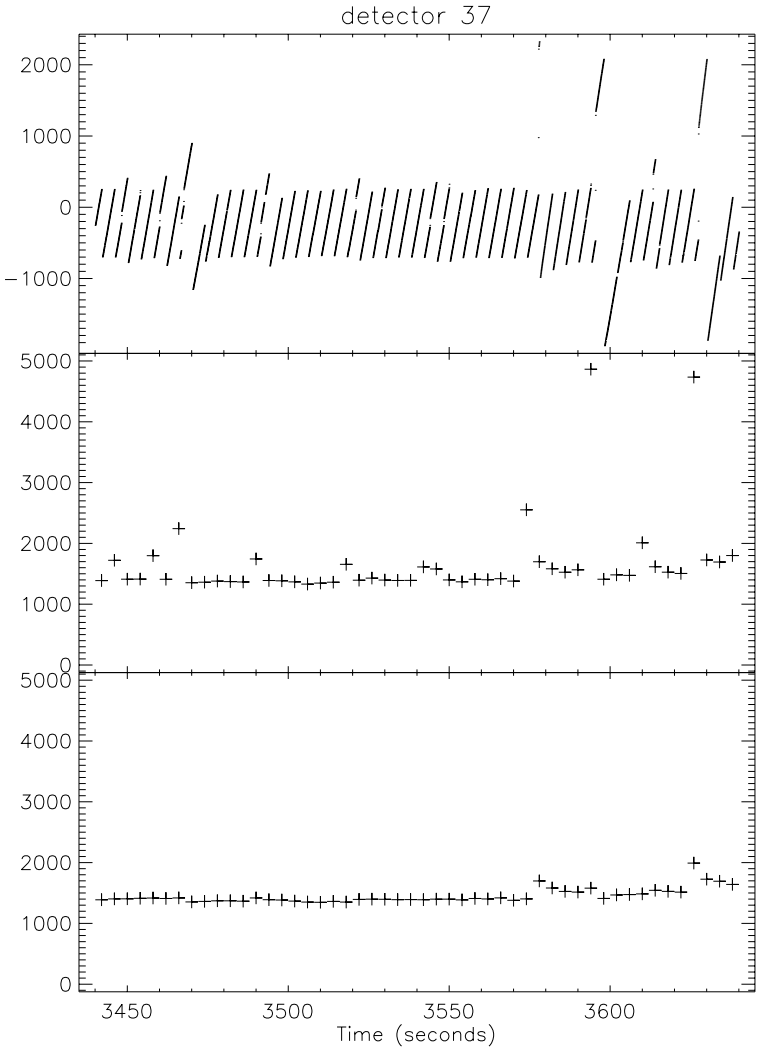

Figure 7.3: *SPD processed with and without deglitching software. The top panel is the ERD (bit values against seconds), processed up until the glitch detection. Glitches can be seen where there are breaks in the sloping lines. The middle panel is SPD (in $\mu V/s$) processed without deglitching. ERD ramps with glitches show very high SPD values. The bottom panel shows SPD processed with the deglitching software in place. The effect of the glitches has been removed, or substantially reduced. Glitch tails, however, are still present, but not at all glitches. The glitch at time 3576 e.g. has a conspicuous tail, while the even higher glitch at 3596 has none at all.*

before deglitching is carried out. This source signal estimate is derived using the knowledge that the source signal should be constant while the grating scanner is not moving (as each detector only sees light in one wavelength). After this step the glitch detection is the same as in the other bands.

In SWS01s glitches are not only detected but also *corrected* with the stepsize found at the detected glitch position. An example of this glitch recognition technique is shown in Figure 7.4.

For more information on how glitches are recognised in SWS01 data see Lahuis, Kester & Shipman 2001, [24].

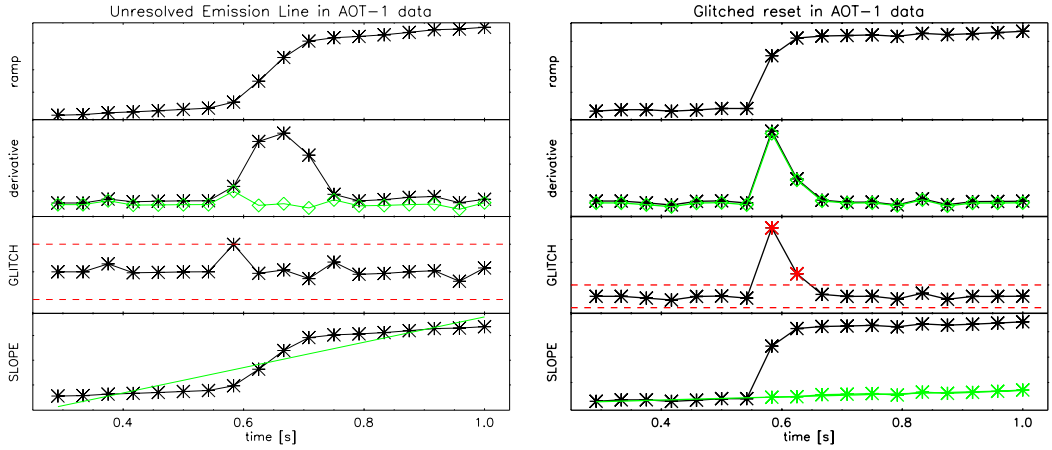

Figure 7.4: *Glitch detection in low resolution data with examples of a reset scanning an unresolved line (left) and a reset with a true glitch (right). From top to bottom we see:*
- the input ramp.
- the uncorrected ramp derivative in black and the corrected ramp derivative in green.
- glitch detection in the pipeline using the corrected ramp derivative. In red the glitch detection limit and the samples identified as glitched are plotted.
- slope fits. In green the pipeline slope fit and the corrected ramp samples.
In the first example the pipeline deglitching using the corrected derivative correctly detects no glitches and fits a single slope. In the second example the glitch is detected and the derived slope is calculated from the corrected ramp.

7.2.9 Extraction of the photo-currents and their uncertainties

The net effect of this processing step is to convert the data from a set of 24 samples per second per detector to 1 point per reset interval per detector. Because of two schemes if glitch detection, also slope fitting come in two variants, one for SWS01 and one for the general case.

7.2.9.1 Slope fitting in general

The current through the detector charges a capacitor. The voltage over the capacitor is measured non-destructively during a reset interval. When there is no glitch within the reset interval we can write the voltage, V_k, as a linear function of the current, S:

$$V_k = S \cdot t_k + O \tag{7.4}$$

where O is the offset caused by the charge at the zero-point of each ramp and the time t_k is counted in seconds since the start of the ramp. V_k and O are in bits and S is in bits/s.

When one or more glitches are present during the interval we add a term for each glitch. For a glitch at sample j we have:

$$V_k = S \cdot t_k + O + p_j \cdot H(t_k - t_j) + \cdots \tag{7.5}$$

where $H(t)$ is the unit step function which step from 0 to 1 at t=0. p_j represents the glitch height at sample j.

This model is fitted to the data D_k by minimising χ^2.

$$\chi^2 = \sum_k (V_k - D_k)^2 \tag{7.6}$$

where the sum is over all valid points within the reset interval, i.e. excluding 6 points after the reset pulse (the reset cutout length) and saturated points, if any. From this fit we find values for the parameters in Equation 7.5, the slope S, the offset O and the glitch heights p_j. Of these only the slope is kept. It represents the current through the detector.

The error in the signal is obtained using the standard method to calculate the standard deviation in a slope:

$$\sigma_S = \sqrt{\frac{\chi^2}{(N-K)}}\sqrt{C_{ss}} \tag{7.7}$$

where N is the number of valid samples in the reset interval, K is the number of parameters to be extracted ($K = 2 +$ number of glitches) and C_{ss} is the element corresponding to the slope, in the covariance matrix spanned by the model in Equation 7.5.

The first factor in Equation 7.7 is the standard deviation of a linear model fit, and the second factor is the amount that has to be assigned to the slope part of the model.

The standard deviation is directly estimated from the fit residuals. Obviously, the accuracy depends not only on the intensity of the source, but also on how well the ramps have been previously linearized and therefore on the measurement error of the RC time constants, the pulse-shape correction and at high gain also digitization plays its role.

For band 3 detectors the slopes are multiplied by -1, as their bias is reversed.

7.2.9.2 Slope fitting for SWS01

Slope fitting in SWS01 is only different in the sense that all detected glitches are corrected in the glitch detection part. So there are no glitches to be fitted, no H-functions. As the glitch heights are estimated from the difference of two consecutive points only, the fits and thus the slopes derived from them, are slightly less efficient in the case where no flux change occurs during the reset interval. It is a trade-off against grossly misfitting the slopes and glitches in the presence of changing flux. In Kester 1999, [19] a more precise method for doing the same is presented. It takes much more time, however.

7.2.10 Conversion to voltages

The electronics amplify the detector voltages with a preselected gain factor before the Analogue to Digital (AD) conversion. Each detector can be operated at three different gains of the amplifier chain. To convert the slopes to currents we have to undo the AD conversion and take into account the gains.

The current in μV/s is related to the output of the AD converter, in bits/s, by

$$S(\mu\text{V/s}) = G_{AD} \cdot G_{pre} \cdot S(\text{bits/s}) \tag{7.8}$$

where G_{AD} is the AD-conversion factor (= 20 10^6 / 4095) and G_{pre} is the pre-amplifier gain which can be one of 225, 900 or 3600 for the grating and a value twice this high for the FP. They are kept in the calibration file Cal-G 5. The resulting signals are stored in the *flux* tag of the SPD (`SWSPFLUX`).

The same conversion is applied to the standard deviations of Equation 7.7. These are stored in the *stdev* tag of the SPD (`SWSPSTDV`). These standard deviations are passed unchanged to the AAR (`SWAASTDV`), see Section 7.4.

The fourth plot in Figure 7.2 shows 40 seconds of detector 16 after this processing step. The data is now in μV/s against time. All that remains for Derive-SPD is to assign wavelengths to the individual data points.

7.2.11 Assigning wavelengths

All reset intervals of all detectors are assigned a wavelength within the limitations described below, even if the band was not requested or contains otherwise useless data. The wavelength is stored in the *wave* tag of the SPD (`SWSPWAVE`) or AAR (`SWAAWAVE`).

7.2.11.1 Grating wavelengths

Within an ERD we have measurements, 24 times per second, of the grating position both for the SW and the LW sections of the grating. The grating position is measured in LVDT, see Section 3.2.1 and Chapter 4.

The grating positions are averaged over the valid samples within each reset interval and for each detector separately as the valid samples may differ from detector to detector. This results for SWS01s in potentially different values for the grating position for each detector. In all other AOTs the scanner does not move during a reset interval.

Subsequently the averaged grating positions are converted into grating angles via the grating polynome. This is a 5th order polynome of which the (time dependent) parameters are stored in the calibration file Cal-G 16ET[1]. The grating angle, θ, is used to obtain the wavelength, λ, via

$$\lambda = \frac{D}{N}(\sin(\theta + \beta) + \sin(\theta + \delta)) \tag{7.9}$$

D is the grating constant. It is taken from calibration file Cal-G 16C. The angle β runs from the optical axis to the entrance slit. It is stored in the calibration file Cal-G 16A. The angle δ runs from the optical axis to the detector pixel. It is stored in the calibration file Cal-G 16B.The spectral order N is determined by calculating all the orders that give wavelengths consistent with the transmission limits of the aperture filters in combination with the detection limits of the blocks (Table 2.1).

A valid wavelength can be assigned only when one order fits the criterion. The order found is incorporated in the flag, which accompanies every flux in the SPD (or AAR), see Table A.7. When no order fits the criterion, a wavelength of 0 is assigned and no order flag bit is set. When multiple orders are found, the wavelength is given its *first* order value while the order flag bits are all set, resulting in a value of 7.

The transmission limits are stored in the calibration file Cal-G 24. The detection limits of the detector blocks are stored in the calibration file Cal-G 23.

The SPD has two more tags related to the (grating) wavelengths: grating position (`SWSPGPOS`) and grating angle (`SWSPGANG`). The position and angle of the *first* sample of each reset interval is stored in there. As explained above, for SWS01s these tags do not convert directly into the wavelengths quoted for each detector because of the movement of the scanner.

[1] Originally they were stored in Cal-G 16E. During the mission we created a time dependent version of this file with quite a different layout. See Chapter 4.

7.2.11.2 Fabry-Pérot wavelengths

When determining the wavelength transmitted by the FPs, the grating wavelength must first be calculated as the LW grating section serves as order filter for the scanning FPs. Once the grating wavelength has been determined, calibration file Cal-G 12 is used to transform the nominal FP-position (an engineering parameter of no interest to the observer) into a FP-gap. This mechanical gap width is then corrected to get the optical gap width (using calibration file Cal-G 18). The wavelength which passes through the FP is the one of which a whole multiple fits exactly in two times the optical gap width.

The FP-position is stored in the SPD as `SWSPFPOS` and the FP-gap in `SWSPFGAP`. There is one more item in the SPD which is related to the FP, the FP-current (`SWSPFCUR`). It is computationally not related to the other FP items. Actually it is not used at all.

7.2.12 Writing the data

The data produced by the processing chain above is written out to the SPD and glitch list SWGH files. Each AOT results in one SPD file. For a definition of the SPD file see Section A.3.1. Note that the SPD file, like an ERD file, contains science data interleaved with dark current measurements, photometric checks etc.

An SPD record is produced for every reset interval. Complexities arise when the reset intervals for the SW and LW sections of the instrument are different, due to the instrumental setup required to obtain the required S/N ratios in the different halves of the instrument. In this case there will be one SPD record (containing data for all detectors) for each of the shorter reset intervals, with the SPD for the longer reset interval having its flag word set to 'No data' for the records when it did not contain a reset (see Table A.7) and contains '0' in the flux — this sometimes confuses plotting programmes. As an example, if the SW grating had a reset interval of 1 second and the LW one of 2 seconds, an SPD record would be produced every second. Every SPD record for the SW detectors (1–24) would contain valid data, while only every other record for the LW detectors would contain valid data, the others being marked as 'No data'.

Figure 7.5 shows the final output of the Derive-SPD stage as detector output against wavelength.

7.3 From SPD to AAR

Auto-Analysis[2] (AA) is the processing stage that starts from SPD, corrects for all instrumental effects lasting longer than one reset interval and generates sets of spectra, fluxes (in Jy) against wavelength (in μm). It applies further corrections to the slope data to transform it into fully calibrated astronomical data. These spectra are generated irrespective of the observation specifications. Figure 7.6 gives an overview of AA processing. Most of the SWS AA processing steps are independent of AOT number as most of the special options (e.g. reference scans) are used in several different AOTs and thus are implemented as part of the main processing flow.

These steps are described in more detail in the following pages.

7.3.1 Reading data from the SPD

The data and header information are read from the input SPD. Contrary to the ERD, where we needed to read in several files, in this stage all information is contained in the SPD. The AOT number, needed for the further processing of the data, is determined from the `EOHAAOTN` keyword in the SPD FITS header. The spacecraft's heliocentric velocity, and, for SWS01s, the scan speed, are also obtained.

[2] 'Auto-Analysis' is a funny misnomer, kept for historical reasons. There is nothing of 'analysis' in it. It better would be called 'Auto-Calibration'.

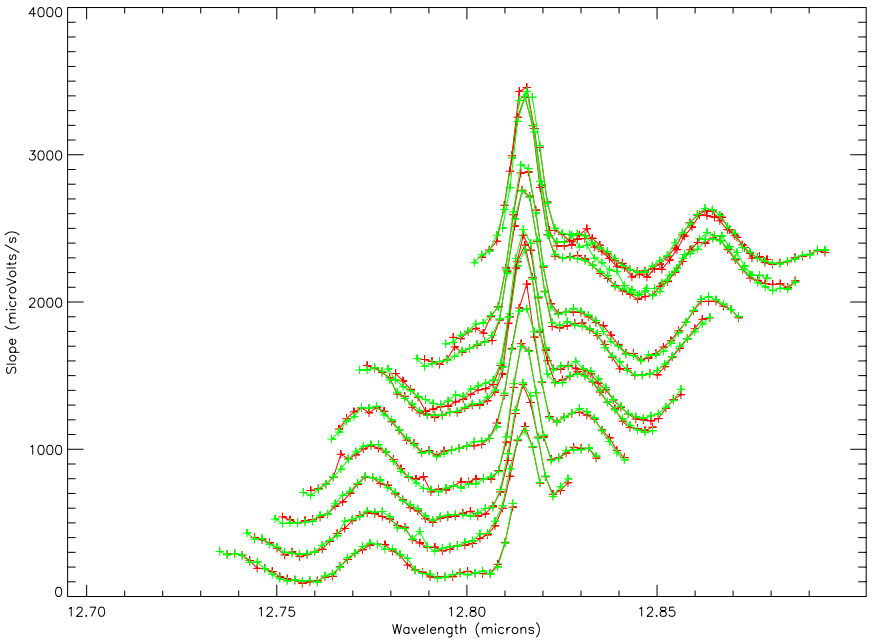

Figure 7.5: *A portion of the SPD data against wavelength for all detectors in band 3A. The detectors are shifted vertically with respect to each other for clarity. In this SWS02 scan not all detectors cover the same wavelength range or even the targeted line. In green the up scans are displayed and in red the down scans. The continuum is not at a constant level due to fringes – see Section 9.7.*

7.3.2 Transient correction

As the first few samples of dark current measurements may suffer from memory effects, or unknown shutter status, the first three datapoints of dark currents for bands 1, 3, 4, 5 and 6 are rejected at this processing step. This is all that is currently done for transient correction in bands other than band 2. We have seen no transient problems in bands 1 or 3. In bands 4, 5 and 6 they are certainly present but no other correction is available. Band 2 transients are treated as changing dark currents, see Section 7.3.3.2.

7.3.3 Subtraction of dark currents

For each observation dark currents are subtracted in all bands for all detectors separately. In band 2 a different dark current model is used than in the other bands because of the transient effects present there and because a model is available which can actually handle these transients.

7.3.3.1 Dark currents in general

For every block of dark current data, the median of valid dark current data is calculated. For every non-dark current scan two dark blocks are selected, one immediately before and one immediately after the scan, which have the same gain and reset lengths as the scan. All AOTs are devised such that this is the case. A linearly interpolated slope connecting the medians of both darks is subtracted from the scan.

In few cases only one dark current block can be associated with a scan. If so, the median of this block is subtracted from the scan. In even fewer cases there is no valid dark current associated with the scan.

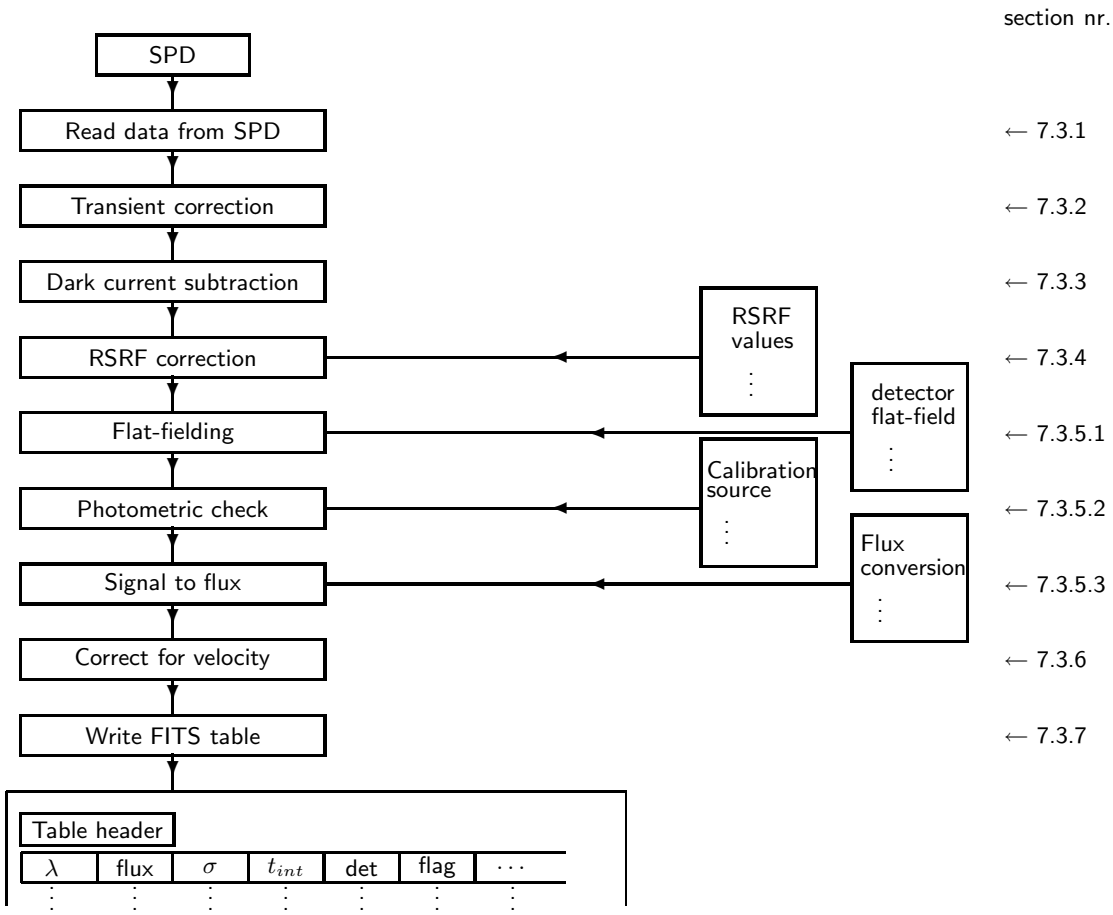

Figure 7.6: *Auto-Analysis flow-diagram*

Then the mean value of all dark currents in the observation with the same gain and reset is used. If there is no valid dark current at all with the same gain and reset length the block is flagged as having no data.

For the photometric checks only the dark current preceding the measurement is subtracted. The calculated dark current values are also subtracted from the dark current frames. The effect on the data of one of the band 1 detectors is shown in Figure 7.7.

7.3.3.2 Dark currents in band 2

The Fouks-Schubert model, as described in more detail in Section 9.2.1, is used to calculate the varying dark current for the band 2 detectors.

$$S_k = \beta S_k^{\infty} + \alpha_k + Z(t_k) \tag{7.10}$$

$$\alpha_k = \frac{(1-\beta)\alpha_{k-1} S_k^{\infty}}{\alpha_{k-1} - (\alpha_{k-1} - (1-\beta)S_k^{\infty}) \exp(-\Lambda\beta S_k^{\infty} \Delta t)} \tag{7.11}$$

Here S_k is the signal through the detector at time k, S_k^{∞} is the relaxed signal at time $t = \infty$. It is proportional to the incoming flux. β is a constant, representing the instantaneous increase at a flux step,

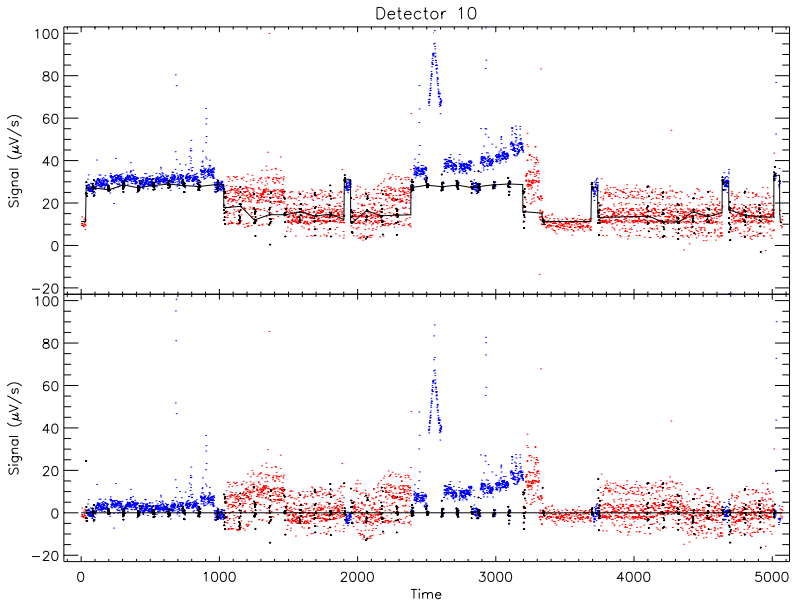

Figure 7.7: *The dark current correction. In the upper panel detector 10 of an SWS02 is displayed. The samples in the dark current blocks are indicated in black. The lines show the linear interpolation. Blue points indicate high gain data and red points indicate low gain data. Note that there is a clear jump between different gains. In the lower panel the dark current is subtracted.*

and α_k comprises the memory effects. α_k is dependant on its previous value, α_{k-1}, on the present relaxed signal, S_k^∞, and on the constants β and Λ. Δt is the duration of the time step from $k-1$ to k. $Z(t_k)$ is the zero level function which represents the level to which the signal would decay when no flux is entering the system. The signal is related to the relaxed signal (or flux) via a constant gain β and a changing dark current α. This changing dark current is subtracted from the data.

The model described in Equations 7.10 and 7.11 is used with a fixed value for $\beta = 0.82$ and $\Lambda = 63\ \mathrm{V}^{-1}$; they are material parameters verified to be constant over the mission. For every observation the zero-level function and the starting value for α had to be estimated anew. They depend on the flux history as seen by the detectors.

The effect on the data of one of the band 2 detectors is shown in Figure 7.8.

7.3.4 Responsivity calibration

A Relative Spectral Response Function (RSRF) has been determined for every band (Section 5.4). It provides the relative response of the instrument as a function of wavelength. They are stored in calibration files Cal-G 25_xx, where 'xx' is the band designation.

For each band the wavelength dependent responsivities are normalised with respect to the key wavelength. This is done per detector. The signals that belong to a certain band are then divided by the normalised responsivities for that band at the corresponding wavelengths. An example of this is shown in Figure 7.9.

Additionally, for SWS01s the responsivities are smoothed by carrying out a flux conserving interpolation to the SWS01 resolution. These factors depend on both the AOT speed and on the band as well as on wavelength, and are stored in the calibration file Cal-G 19.

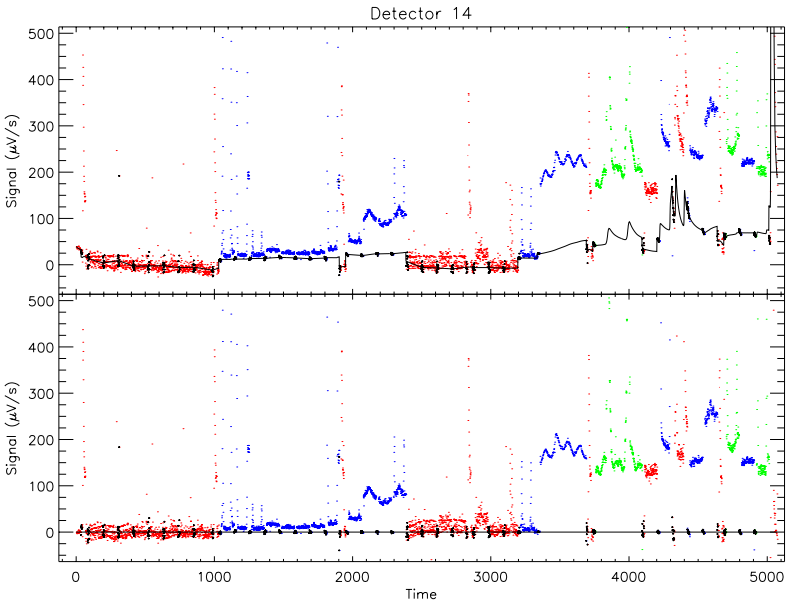

Figure 7.8: *The dark current correction in band 2. The layout in this figure is the same as in Figure 7.7 with the exception that there is medium gain data too, shown in green. Note the changing dark currents and how they make the individual scans in the lower panel much more symmetric; they are all up-down scans. Note also that in cases of low flux there is not much difference with the 'standard' dark current subtraction.*

7.3.5 Flux calibration

The flux calibration comprises three processing steps, which can be done in any order. Flat-fielding brings all detectors to one level. Photometric check removes long term drifts and flux conversion scales the μV/s into Jy.

7.3.5.1 Flat-fielding

In the SWS grating scans, a spectral segment is observed with 12 separate detectors at any one time. In general, these detectors must be individually calibrated such that the resulting spectra from each detector within an AOT band gives the same signal. It was initially recognized that the signal-to-flux calibration per detector formally takes care of the flat-fielding. However, the responsivity of an individual detector relative to the average of the 12 detectors from the same band was found to be quite stable during the mission as determined from ≈1000 observations, see Section 5.6. Therefore, an independent flat-fielding measure was introduced into the pipeline to bring the response of each detector in agreement with the average of all the detectors within an AOT band

The gains of a single detector compared with the average of all detectors in the band are stored in the calibration file Cal-G 43. This flat-fielding step applies a scaling based on Cal-G 43 and results in all detectors being placed on the same scale as an average detector. An example of flat-fielding is shown in Figure 7.10.

Although additional flat-fielding is usually performed in post processing, the application of a separate flat-fielding step here aids in removing some of the ambiguity of applying either a scaling or an offset

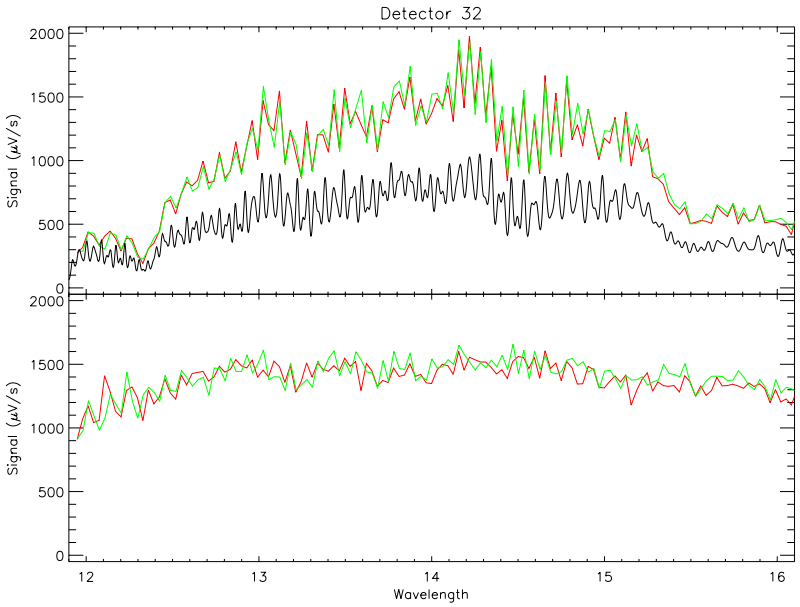

Figure 7.9: *The RSRF correction on an SWS01 observation in detector 32. In the upper panel the data are displayed after dark current subtraction, the up scan is in green and the down scan on red. Also is displayed the (scaled) RSRF for band 3A in black. In the lower panel the data have been divided by the RSRF, removing most of the instrument specific wavelength dependencies like e.g. fringes. Some fringing remains however, see Section 9.7.*

correction. As treated in the pipeline processing, the flat-fielding is always a scaling correction. In post processing it might still be necessary to account for offsets introduced through the dark current subtraction.

7.3.5.2 Photometric check

For almost every observation a photometric check is performed using one of the internal stimulators to correct for any long term drifts of detector sensitivity, assuming that all signal changes can be traced to changes in the detectors and that the illuminator itself is constant. The *wavelength* calibrator was used for this purpose because its flux level was more appropriate. The wavelength calibrator source is scanned over some 20 LVDT steps.

Stimulating the band 1 detectors, however, required a high setting of the calibrator which resulted in significant memory effects in bands 2 and 4. This was noted early in the mission. Photometric checks of band 1 were seen to be quite stable so the photometric check with the high setting was discontinued in revolution 64. Band 1 was periodically monitored throughout the mission with strong illuminator flashes to guard against any possible detector changes. No change was noticed.

The detector signals during the photometric check are compared to the average photometric check over the mission, held in the calibration file Cal-G 41. The signal response is corrected based on an average photometric signal contained in Cal-G 41, see Section 5.5 for more information.

The 6 numbers that are found for the photometric gains are listed in the header of the SPD (to be copied later to the AAR header) under the keywords `PHOT_BD*`, where '*' is a number indicating the band.

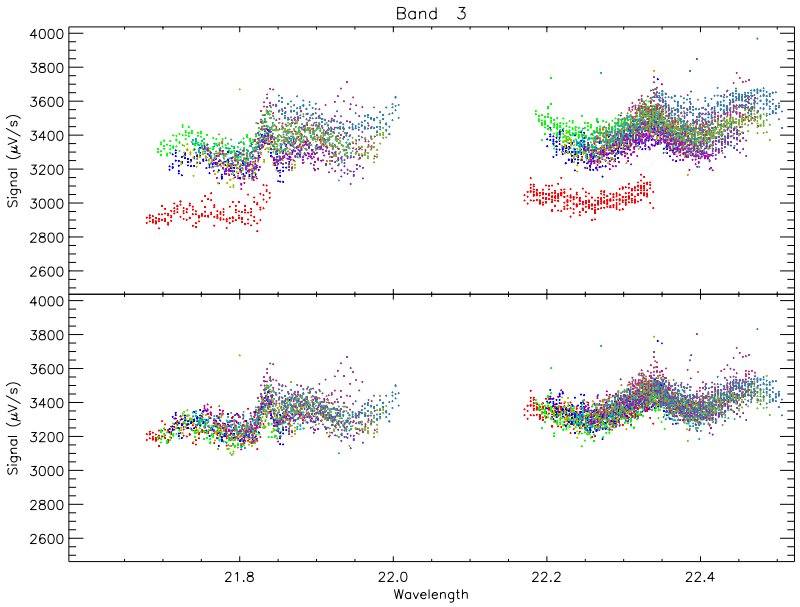

Figure 7.10: *The effect of flat-fielding is shown on a portion of data from band 3. Each detector is shown in a different colour. Before the correction (top panel) the signal levels are widely separated, whereas after (bottom) they more closely approximate each other.*

7.3.5.3 Converting signal to flux

Once the signal, for each band, has been calibrated to a standard time by the photometric check, and to a standard detector using the flat-gain, it can be converted from μV/s to Jy/s. These conversion factors are held in the calibration file Cal-G 42.

The effect of this processing step is shown in Figure 7.11

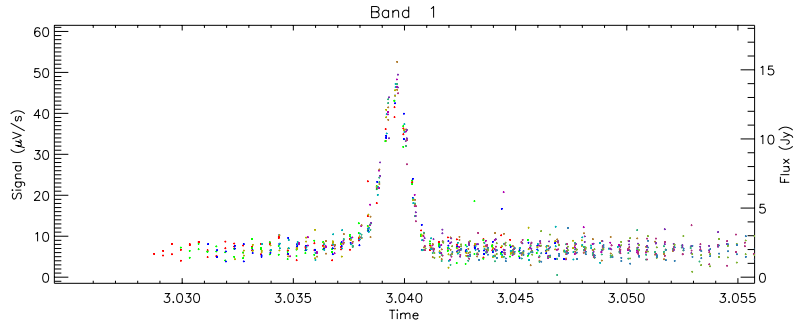

Figure 7.11: *The effect of flux calibration is shown for a line in band 1E. The signal in $\mu V/s$ is read from the left axis while the flux in Jy is read from the right hand side axis.*

7.3.6 Velocity correction

The velocity component (V) in the line of sight towards the target, due to the combined motions of the spacecraft and of the Earth is corrected for in this module. This then ensures that the AAR wavelength is heliocentric.

7.3.7 Output table files

All good data (wavelength, fluxes etc.) are sorted to wavelength and written out to a FITS file. Data for which no wavelength was assigned in Derive-SPD are skipped. The resulting file is a FITS AAR file. For a definition of this file see Section A.4.1, and an example AAR file from an SWS01 observation is shown in Figure 3.5.

7.4 Error Propagation in the SWS Pipeline

The ideas expounded in this section stem from a dissatisfaction with the way the error values were originally delivered to the users: one *error* tag which comprised the full gamut of systematic and random errors. The systematic errors almost always swamped the random ones. More importantly, it prevented the use of the statistical errors as weights in further processing. It was decided to keep three separate error tags in the AAR, one for the statistical errors and two for the more systematic offset and gain errors. This allows the use of the statistical error in various weighting and clipping schemes, which proved fruitful especially at low flux levels (Valentijn & Thi 2000, [38]).

These three tags are not the only source of quality in the SWS products. There is also the flag (`SWAAFLAG` and `SWSPFLAG`, see Table A.7) which provides information about the number of glitches detected within the reset interval. It also holds information whether the flux within the reset interval was (partially) out of limit. And there is the `SWAATINT` tag, see Section A.4.1.2, which contains the number of valid samples within the reset interval. Both glitches and out-of-limit samples diminish the number of valid samples.

Error handling in Calibration Procedures (CAPs), used to derive calibration files and their error, are not discussed in this section.

Of course, some sources of error (e.g. residual fringes) are still present in several bands. The removal of those depends on careful post-pipeline processing.

7.4.1 Basic formalism

The basic formula which describes how the signal S is converted into flux F reads (see also Section 5.5):

$$F = (S - S_d) \cdot G_r \cdot G_f \cdot G_p \cdot G_c \tag{7.12}$$

where S_d is the signal of the dark current measurement(s), G_r is the 'gain' due to the responsivity function, G_f is the flat-field factor, G_p is the photometric gain and G_c is the flux conversion.

To derive the error from this, Equation 7.12 can be rewritten a little, defining $G = G_r \cdot G_f \cdot G_p \cdot G_c$, as:

$$F = (S - S_d) \cdot G \tag{7.13}$$

from which the total error in F can be found. Relative errors in a product add quadratically:

$$\left(\frac{\sigma_F}{F}\right)^2 = \left(\frac{\sigma_{S-S_d}}{S - S_d}\right)^2 + \left(\frac{\sigma_G}{G}\right)^2 \tag{7.14}$$

Multiplying Equation 7.14 by F^2, and expanding σ_{S-S_d} properly, results in:

$$\sigma_F = \sqrt{(G \cdot \sigma_S)^2 + (G \cdot \sigma_d)^2 + ((S - S_d) \cdot \sigma_G)^2} \tag{7.15}$$

where σ_d is the error in the dark current signal.

The right hand side of Equation 7.15 consists of 3 terms below the square-root symbol. The first one is related to the standard deviation (*stdev*) in the slopes. Each slope has its own individual *stdev* which is statistically independent from the others. These standard deviations can be used to assess the quality of the individual slopes. They have to be multiplied by the gain to play its (properly scaled) role in the total error definition of F. The second one is an offset error. It is related to the error in the dark current measurements and as such it is applied to all slopes between two embracing darks. This makes the error a highly correlated one. When the dark current measurement is wrong, all related fluxes are off by the same amount. It also has to be multiplied by the gain to get its contribution to the total error. The third one is a gain error. As is proper for a gain error, this one is stored as a *relative* error. It consists of four parts: errors in the responsivity function; in the flat-field factor; the photometric gain; and the flux conversion. All four are highly correlated errors and except for the photometric gain the others are even correlated over all SWS measurements, i.e. the errors are taken from calibration files which are applied to *all* observations. So errors in the responsivity function, the flat-field and in the flux conversion affect all observations in a similar way. To get the contribution of the (relative) gain error to the total flux error it has to be multiplied by the flux: $F \cdot \sigma_G/G = (S - S_d) \cdot \sigma_G$.

In summary there are three errors, one statistical error and two systematic errors, which will be referred to as 'offset' and 'gain' errors.

7.4.2 Slope error

The error in the signal is calculated when deriving the slope over the rectified ramps, see Section 7.2.9. The standard method is used to calculate the error in the slope:

$$\sigma_S = \sqrt{\frac{\chi^2}{(N-2)} C_{ss}} \tag{7.16}$$

The first factor on the right hand side is the standard deviation of a linear model fit, and the second factor is the amount that has to be assigned to the slope part of the model.

In Figure 7.12 an SPD is displayed with its slope errors, the dark current error, the number of glitches and the number of valid samples.

7.4.3 Offset error

The error in the offset, σ_d is the error in the dark current, multiplied by the gain G.

7.4.3.1 Standard dark current model

To calculate the dark current a preceding dark signal S_1 at time t_1, and one following, S_2 at time t_2 are necessary, see Sections 7.3.3 and referenced sections.

$$S_d(t) = S_1 \frac{t_2 - t}{t_2 - t_1} + S_2 \frac{t - t_1}{t_2 - t_1} \tag{7.17}$$

It is a linear interpolation between S_1 and S_2. The error σ_d now becomes

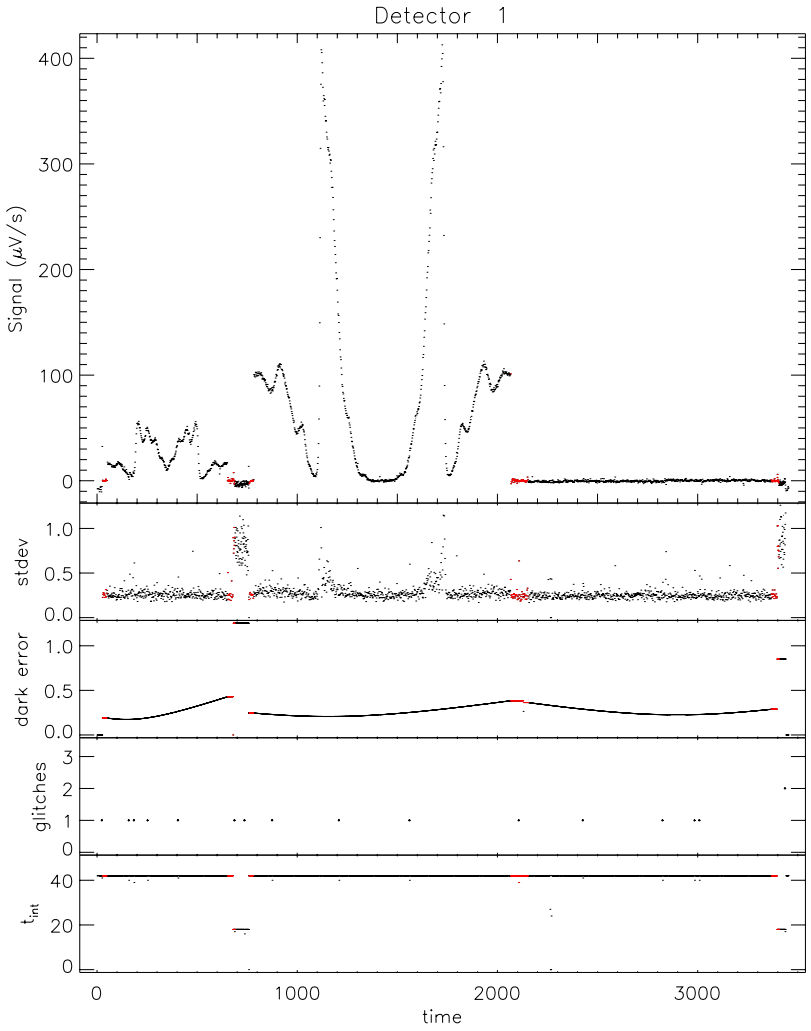

Figure 7.12: *In the top panel we show the signal observed in detector 1 of an SPD. In the second panel is the standard deviation as was derived for this signal. In the third panel the (offset) error due to dark current subtraction is shown. The fourth panel shows the number of glitches found, not all that many in band 1. And in the lower panel the number of valid samples is shown. The actual dark current measurements are displayed in red.*

$$\sigma_d^2 = \sigma_1^2 \left(\frac{t_2 - t}{t_2 - t_1} \right)^2 + \sigma_2^2 \left(\frac{t - t_1}{t_2 - t_1} \right)^2 \tag{7.18}$$

where σ_1 and σ_2 are the errors in both dark measurements. These errors were calculated as Median Absolute Deviates (MAD) to have a more robust estimate of the dark current error. A MAD can be

converted into a standard deviation by division by 0.675, assuming the distribution is Gaussian within the FWHM.

When only one (preceding or following) dark measurement can be found, this dark is subtracted from the signal, and consequently the offset error equals the dark error.

Figure 7.12 shows the signal of detector 1 for an SWS01 SPD, together with the standard deviation of the signal, the offset error due to dark current subtraction, the number of glitches found and the number of valid samples.

7.4.3.2 Transients model in band 2

Band 2 is the only SWS band where a transients model was used to calculate the dark currents. Consequently the errors are also obtained in a different manner. The transients model has a number of parameters that have to be estimated, either for each individual observation or for the database as a whole. The latter are parameters that are assumed to be constant during the mission. See Section 7.3.3.2.

Each of the parameters has its own uncertainty and its own standard deviation. The errors in the dark current model were obtained from a MonteCarlo simulation of 25 cases where the optimal parameters are replaced by a random draw from a Gaussian distribution spanned by the covariance matrix of the model fit – see Kester 2001, [22].

An example of an offset error in band 2 is shown in Figure 9.4, lower panel, red line.

7.4.3.3 Comments

Both in the standard dark current subtraction and in the transient model it is assumed that the dark, or the zero level function in the transients model, changes linearly in time. Actually the standard dark can be seen as a no-model transient, using only the zero level function. This assumption of linearity entails the somewhat funny behaviour of Equation 7.18: it has a dip in the middle (Figure 7.12, middle panel), suggesting that the dark in between two dark measurements is somehow more certain than at the actual measurements. We do not think this is true. The true dark current makes its way from the first measurement to the second by some kind of random walk. We just assume that it is linear because of lack of information otherwise. We decided to keep Equation 7.18 to be mathematically correct.

7.4.4 Gain error

The gain error has four components, one from the responsivity function, one from the flat-field factor, one from the photometric gain and one from the flux conversion. To get the total gain error, the *relative* errors for the four components are added quadratically.

7.4.4.1 Responsivity error

The responsivity error is taken from calibration file Cal-G 25_xx, which has a separate entry where we estimate how good the RSRF is at that wavelength (see Figures 5.5 to 5.19). The RSRF is valid only for one resolution in wavelength. To accommodate the different resolutions possible with SWS, e.g. SWS01s at different speeds, we have to interpolate the RSRF to the proper resolution with a flux conserving interpolation scheme. See Section 5.4. It is assumed that the error follows the same integration formulae as the fluxes, except that the error is divided by the square root of a dilution factor being the ratio between FWHM and the local stepsize in wavelength. Integrating over more wavelengths yields a smaller error, while interpolating over a smaller part of a wavelength interval yields a larger error.

For the FP detectors the error fields in Cal-G 25_xx are not properly filled.

7.4.4.2 Flat-field error

The flat-field error is taken from the calibration file Cal-G 43. It is applied as is.

7.4.4.3 Photometric error

The photometric gain is obtained from fitting a model of a few fringes which are done during the photometric check to the data. This is done with a (robustified) least square fit. See Section 7.3.5.2. The photometric error follows from this fit as

$$\sigma_p = \sqrt{\frac{\chi^2}{N-1}} \tag{7.19}$$

The robustness of the procedure lies in one extra iteration where possibly outlying points are discarded.

7.4.4.4 Flux conversion error

The flux conversion is taken from the calibration file Cal-G 42. In that file also the flux conversion errors can be found.

An example of an AAR with all its pertaining errors is shown in Figure 7.13.

7.5 SWS Pipeline Software

The software of the SWS pipeline Version 10.1 is written completely in IDL. Figure 7.14 presents an overview of the OLP software. There are two global procedures: DSPD which processes and ERD into an SPD and DAAR which takes the SPD and yields an AAR. Each of these processes can be subdivided into other processes as shown in Figure 7.14. Although the SWS pipeline itself does not benefit from this setup, it made it possible to recreate the pipeline and all its constituent parts within OSIA. Each of the parts of the pipeline can be called within OSIA by the names shown in Figure 7.14 and if wished some may be replaced by other more interactive procedures or different calibration files may be connected. E.g. RESPCAL might be replaced by RESP_INTER to get a better handle on the residual fringes in bands 2 and 3.

7.5.1 Implementation of the errors

In the pipeline and OSIA v3 the errors are implemented in three separate parts, one statistical error and two systematic errors. The statistical error is just the *stdev* of the slope, found in `SWSPSTDV` or `SWAASTDV`, see Sections A.3.1 and A.4.1. This *stdev* tag is completely uncalibrated, still in μV/s. We decided to leave it like this to keep the option to use this *stdev* as weight in later processing, or to use it for histogram clipping based on the *stdev* in e.g. low signal processing.

As the decision to keep three kinds of errors was taken quite late in the mission, we had to find room for the two systematic errors. So we (mis)used two spare tags in the AAR for it, both of which were only 1 byte long. So we had to devise some encoding for the offset and gain error. See Section 7.5.2.

In the pipeline the offset error is not completely right according to what is written here, whereas in OSIA v3 it is. Within OSIA there is a routine (DECODE_AA_ERROR) to decode the systematic errors and calibrate the *stdev* tags. It also yields a structure which contains the calibrated errors plus the total error σ_F as in Equation 7.15.

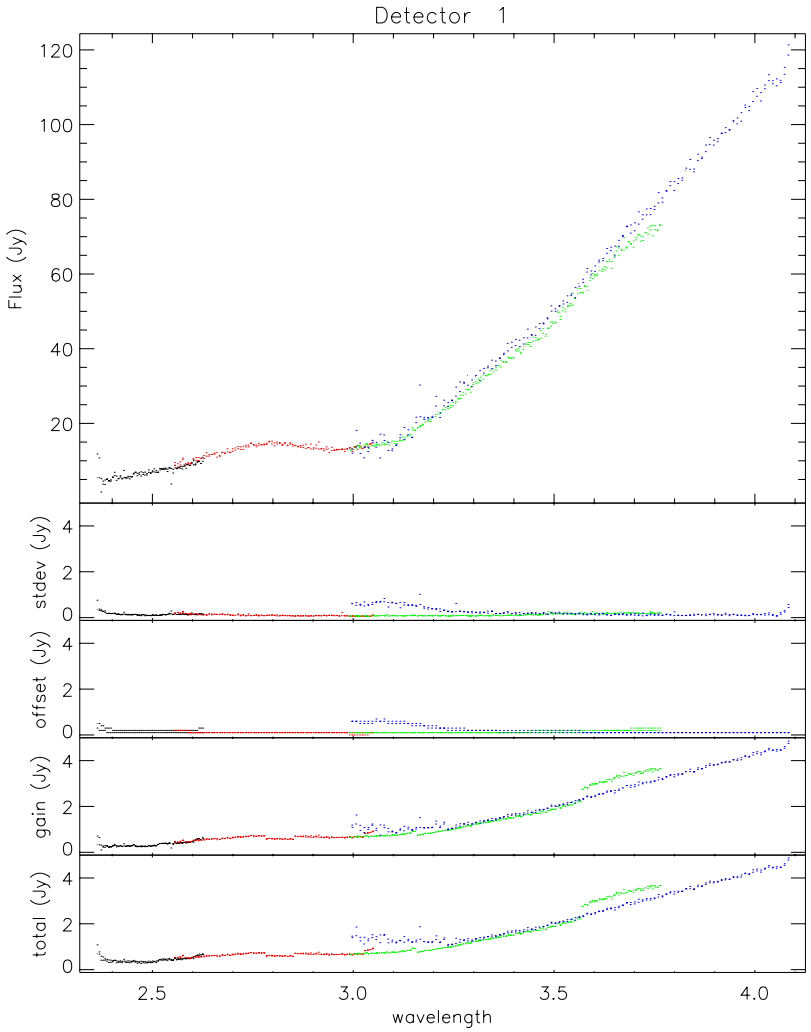

Figure 7.13: *In the top panel we show the signal observed in detector 1 of an AAR as a function of wavelength. It is the same observation as in Figure 7.12. In the second panel we show the standard deviation as was derived for this signal, now converted into Jy. In the third panel the (offset) error due to dark current subtraction is shown, also converted to Jy. The fourth panel shows the gain error. In the lower panel all these errors are added together to form the total (systematic plus random) error in the observation. The four bands which comprises band 1, are colour-coded differently.*

7.5.2 Decoding of error tags in the AAR

Within the AAR there are two spare tags which are used to store error information: `SWAASPAR[1]` contains the gain error in % ranging from 0 to 255 and `SWAASPAR[0]` contains the value of the offset error in Jy using the lookup Table 7.5.2.

For convenient decoding of errors it is possible to use DECODE_AA_ERROR of the SWS IA system

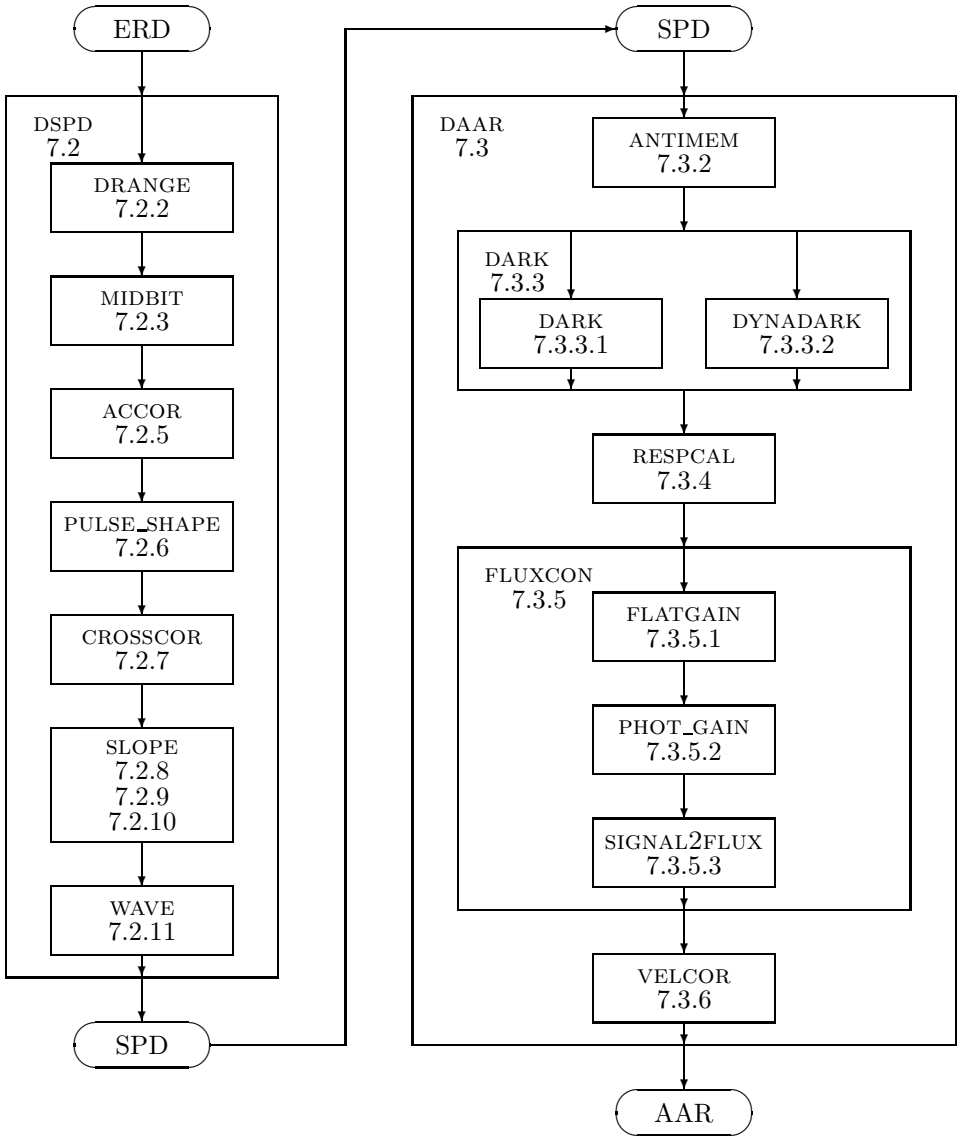

Figure 7.14: *Flow diagram of the SWS pipeline. Boxes represent individual or grouped procedures within the pipeline; ovals represent products. The numbers refer to the sections where the procedures are described.*

or OSIA.

Table 7.1: *Look up table for offset error in* `SWAASPAR[0]`.

parameter value	offset error	generating function
0	0.0	0.1 * value
1	0.1	
⋮	⋮	
10	1.0	
11	2.0	value - 9
12	3.0	
⋮	⋮	
109	100.0	
110	110.0	10 * (value - 109) + 100
111	120.0	
112	130.0	
⋮	⋮	
199	1000.0	
200	1200.0	200 * (value - 199) + 1000
201	1400.0	
⋮	⋮	
255	11200.0	MAX value

Chapter 8

Beam Profiles, Pointing and Focal Plane Geometry

8.1 Introduction

This chapter discusses various issues to do with the pointing, beam profiles and the effect they have on the photometric and wavelength calibration. It is an abridged version of Salama et al. 2001, [33], which should be consulted for more details of the observations, models etc.

Section 8.2 describes the SWS apertures. Section 8.3 introduces the focal plane geometry and Section 8.4 discusses the beam profiles of the various SWS aperture and detector combinations. Section 8.5 presents straylight suppression and Section 8.6 discusses satellite pointing.

8.2 Entrance Apertures and Detector Fields of View

8.2.1 Entrance aperture optics

The SWS instrument has three different physical apertures. A shutter system allows the selection of one aperture, while closing off the other two (the spacecraft pointing has to be adjusted so that the target is imaged onto the selected aperture). There is also a virtual aperture 4, used by the long wavelength FP. This is physically the same as aperture 3, but with its nominal central position offset slightly from aperture 3. Aperture 4 was implemented because of a slight misalignment between the LW grating detectors and the FP detectors. Its introduction increased the amount of light falling onto the FP detectors and hence improved their efficiency (see Section 3.6).

Each aperture is used for two wavelength ranges, one for the short-wavelength section of the spectrometer and one for the long-wavelength section. Since those two sections are otherwise independent, two wavelength ranges can be observed simultaneously. While using the FP virtual aperture 4, however, data from the SW grating section refer to an offset position and are therefore of restricted use only. Table 2.1 indicates which aperture is used for each band.

Beam splitters, consisting of 'reststrahlen' crystal filters (Al_2O_3, LiF and SrF_2), are located behind the apertures. The beams transmitted by the first crystal enter the SW section; the reflected beams enter the LW section, after a second reflection against identical material. As is seen in the schematic (Figure 2.5), the actual entrance slits are located behind the beam-splitting crystal. In this way, each of the 6 possible input beams has its own slit. All slits have been given the same width, except for the SrF_2 reflected input, which has a larger width, adapted to the larger diffraction image at these wavelengths. The slits are in the focus of the telescope, in the plane where the sky is imaged.

8.2.2 Entrance apertures and spacecraft axis

The edges of the apertures are oriented along the spacecraft y- and z-axis.

y-axis (sometimes called m in calibration documents), parallel to the spacecraft y-axis, is the non-dispersion, or cross-dispersion, direction.

z-axis (sometimes called n), parallel to the spacecraft z-axis, is the dispersion direction.

Along the y-axis, the effective size of the aperture is determined by the projection of the detector array on the sky. This amounts to $20''$, $27''$ or $33''$ for bands 1A to 4, and from $39''$ to $40''$ for the FP bands 5A to 6.

Along the z-axis, the aperture size is determined by entrance slit width (14 or $20''$) for bands 1A to 4. For the FP bands 5A to 6, the aperture is effectively as wide as a detector image on the sky, i.e. either $10''$ or $17''$.

Table 2.1 gives the nominal size of the aperture for each band.

8.3 Determination of Focal Plane Geometry

The relative positions of the various entrance apertures and detectors need to be known to ensure that a single grating wavelength calibration can be applied to all combinations of entrance slits and detectors. The determination of the Focal Plane Geometry (FPG) was performed during the ISO Satellite Commissioning Phase Phase (on revolutions 12, 14, 17, 18, 19 and 20).

The offsets between each of the three SWS apertures and the ISO OSS (optical support structure) optical axis were calibrated by making raster maps around point-like sources, with the two SWS grating scanners set at fixed positions, corresponding to selected key wavelengths as defined in the flux calibration programme. In order to ensure the most accurate pointing, five guide stars were used (normally less were used when making observations).

The first measurements to be performed were square rasters around γ Dra, one of the main SWS photometric calibrators, in revolution 17. These were used to calibrate apertures 2, 3 and 1. The calibration derived was verified with a finer square raster on aperture 2 and by cross-like rasters on the other two apertures on the following revolution. In order to avoid possible effects specific to γ Dra and its associated guide stars for that day, another six point-like sources were used for further verifications in revolutions 19 and 20.

The verification and fine tuning rasters were cross-like in order to optimise the use of time. The cross-like axis were parallel to the y-axis (cross-dispersion) and the z-axis of the spacecraft respectively. Each part of the cross consisted in a pair of scans, back and forward, in order to counteract possible detector hysteresis effects.

At the end of revolution 20, SWS02 line scans were performed at each side of the slits. As of revolution 21, the nominal pointing mode with one guide star was used, and the FPG was verified on γ Dra by means of a smaller square raster around it.

The FPG calibration from revolution 19 proved to be accurate to the arcsecond level, and no further updates were requested. The analysis of the revolution 20 raster however (done with one guide star) showed a $-2''$ offset in the z direction on γ Dra. This was judged not worth a further update of the FPG offsets (See Salama et al. 2001, [33] and [16] for more details).

8.3.1 Detector fields of view

In the direction perpendicular to the dispersion, the slits are oversized. There the fields of view are determined by the dimensions of the detectors. The cross-dispersion dimensions are different for almost

all detector bands. Since the imaging of the slits onto the detectors (or *vice versa*) is imperfect due to aberrations, the short sides of the fields of view (detector edges) are more fuzzy than the long sides (the slit jaws).

Small offsets in the fields of view perpendicular to the dispersion direction are caused by alignment errors in the instrument. The internal alignment specification allowed misalignments up to 10% of the detector width and such misalignments have been established.

The monochromatic images of the grating detectors fill about 55% of the slit widths. This means that the spectral resolution for point sources is higher than for extended sources, in a ratio that is affected, of course, by diffraction. See Section 4.5 for more information on this. For extended sources the dispersed detector image fills all of the slit width.

The monochromatic detector images of each Fabry-Pérot detector fills about 50% of the slit width. The FP etalon between the slit and the detector transmits in very narrow wavelength bands at a mutual distance of the order of the spectral resolution offered by the grating spectrometer. The detector image seen in the slit is dispersed by the grating and has fringes parallel to the grating due to the Fabry-Pérot resonances. Thus, the FP detector field of view arises from a dispersed detector image, modulated by the FP fringe pattern.

If the FP is properly tuned, an FP transmission fringe runs through the centre of the slit. The width of this fringe is determined only by the monochromatic detector image. This then is the effective beam width for FP observations on a point source, certainly applicable to the response to a narrow spectral line.

The fringe separation is on the order of the detector width so that there will always be several fringes at least partly visible in the slit. For an extended source the detector is effectively seen to fill the entire slit width, as is the case for all the grating detectors. But the detailed shape of the beam profile should vary rapidly with wavelength, as the FP fringes in the dispersed detector image move across the slit.

Extended sources observed with the FP will have more leakage in unwanted FP orders than point sources. But spatial extent does not affect the spectral resolution of the FP's.

8.4 The Beam Profile

In reality, the situation for the SWS beam profiles is more complex than presented above in Section 8.3.1, which gives the impression that the SWS beam profile was the convolution of this rectangle with the telescope's point spread function. Within the SWS, the apertures are re-imaged twice. Vignetting and diffraction occur both at the focal-plane aperture and at an internal pupil image. These effects influence the beam profile in the dispersion direction: they make the profile narrower than what would be expected from the slit width. In the other dimension the beam profile is affected by geometrical imaging defects. Both these effects were observed in practice, while the instrument was in-orbit.

The profiles were indeed found to be slightly narrower than could be expected from the slit widths and the theoretical telescope beam. In bands 1 and 2 the cross-dispersion imaging defects produced profiles observed to be nearly triangular, rather than more or less rectangular. Cross-dispersion misalignment caused the beams from different detector arrays to be offset from each other. The narrower profiles, the poor cross-dispersion profiles at the short wavelengths and the detector misalignments all contributed to the sensitivity of SWS to pointing errors (see Section 8.6).

8.4.1 Calibration observations

8.4.1.1 Beam profiles: large scale calibration

The beam profiles were fully characterised by observations consisting of rectangular rasters, covering at least one diffraction beam outside the slit, taken at fixed grating scanner positions corresponding to the flux calibration key wavelengths. Target α Boo was used for the grating section and NML Cyg and η Car for the FP section.

8.4.1.2 Beam profiles: small scale calibration

The beam profiles depend on wavelength, clearly from band to band when either detector band or slit size change, but also in general within a band, due to the dependency of the diffraction profile on wavelength. For this purpose SWS01 maps were performed to determine the beam profile at all wavelengths.

The first exercise of this kind was performed early in revolution 126, around γ Dra. This consisted in a series of 7 quick (speed 1) SWS01's performed as a cross-like shape covering the size of the smallest SWS aperture. However, a pointing offset became apparent as well as an offset between detector bands which did not allow observations of both sides of the profile.

A second and finer map was done on α Boo later in revolution 244, but the results showed some inconsistency. This was traced to the brightness of α Boo in the visible causing readout blooming effects on the Star Tracker CCD when used at a time of the year when the orientation of the Star Tracker was parallel to the line of sight defined by α Boo and the guide star used.

This type of exercise was then suspended, waiting for possible improvement of the ISO pointing accuracy. Once achieved, three further exercises were performed to characterise the small scale beam profile close to the peak, via 5×5 rasters done at $2''$ steps on α Boo (revolution 640) and NML Cyg (revolution 742) for the grating and FP sections respectively. A third exercise was done on α Tau in revolution 860, for visibility reasons, to characterise on a fine scale the full wavelength dependency in the Z direction covering both sides of the profile.

8.4.2 Results

8.4.2.1 Beam profiles

Beam profiles for all bands are given in Salama et al. 2001, [33]. Figures 8.1 to 8.4 present the results of the observations, together with the results from the SWS diffraction model. The diffraction model contains a blur model to reproduce the observed cross-dispersion profiles. The presented data are contained in the calibration files Cal-G 35_xx and Cal-G 36_xx. Note that except for the FPs all models and all observations represent the responses to extended sources. The exceptions are the model profiles of the FP, which were computed for a point source. The observed FP profiles are consistent with an FP fringe pattern across the slit.

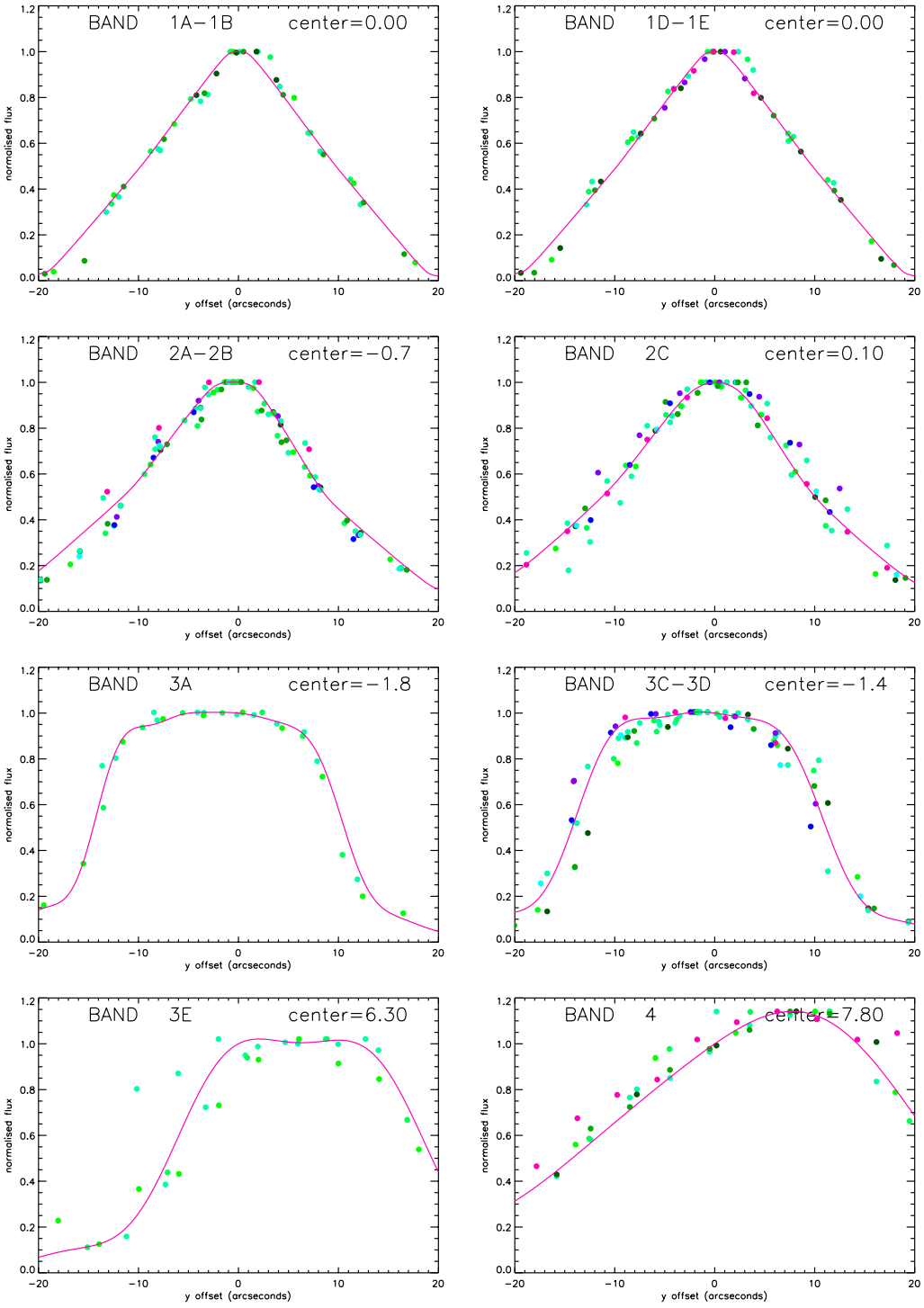

Figure 8.1: *Observations (dots) and calibration file (curves) for the beam profile in different bands in the y-axis (cross-dispersion). Dots with the same colour correspond to the same observation.*

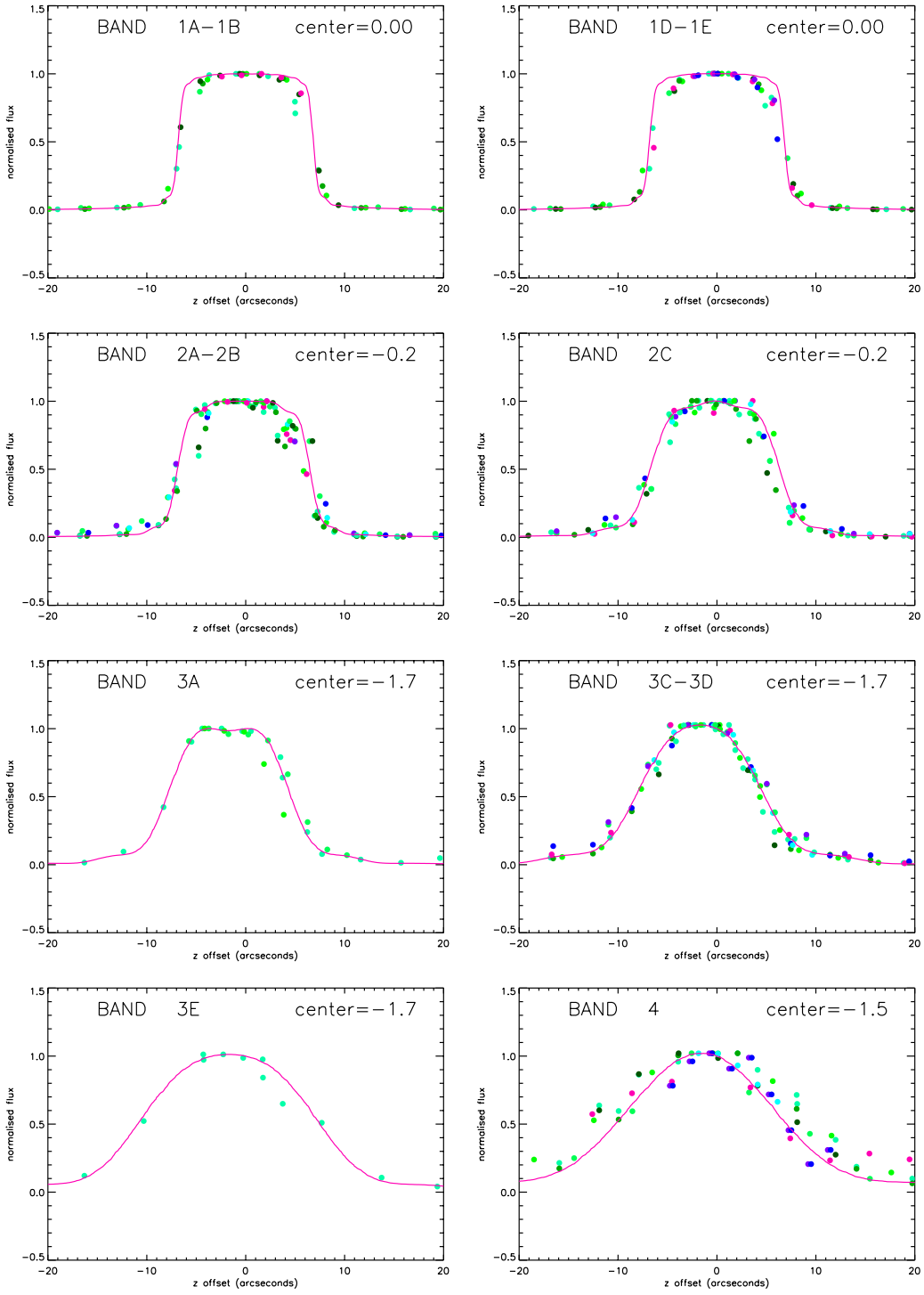

Figure 8.2: *Observations (dots) and calibration file (curves) for the beam profile in different bands in the z-axis (in-dispersion). Dots with the same colour correspond to the same observation.*

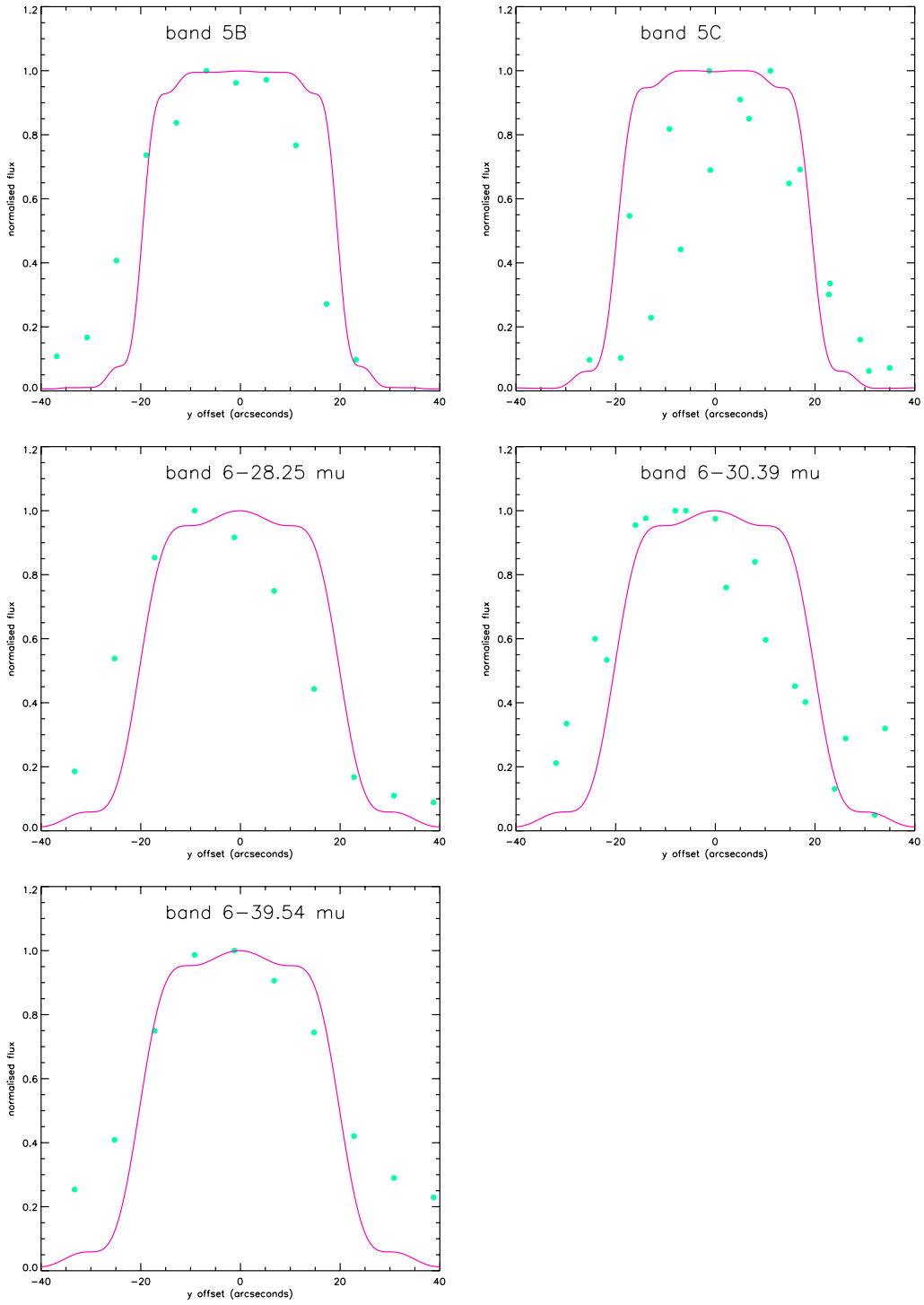

Figure 8.3: *Observations (dots) and model (curves) at different FP wavelengths in the y-axis (cross-dispersion.*

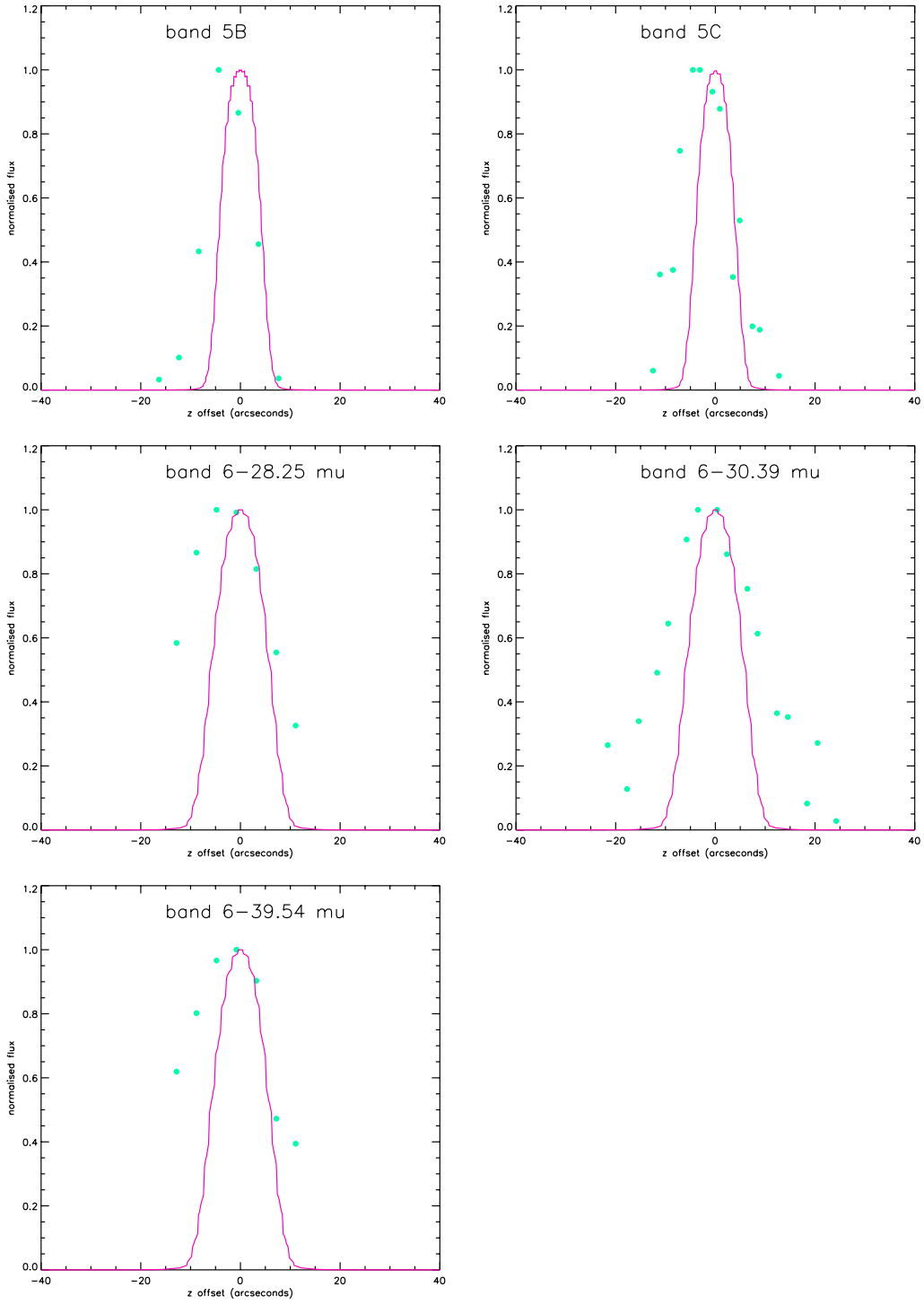

Figure 8.4: *Observations (dots) and model (curves) at different FP wavelengths in the z-axis (in-dispersion). The observed profiles are narrower than the predicted ones (see Section 8.4.2.1).*

8.4.2.2 Subarcsecond scale z-axis beam profile

ISO tracked Solar System Objects (SSO) by means of successive linear rasters. The raster parameters were computed by the mission planning software so that on each raster leg the SSO was allowed to drift from $-1''$ to $+1''$ (prior to the pointing improvement in revolution 290, the tracking was between $0''$ and $2''$). Dedicated measurements were performed in revolution 769 to characterise the beam profile on the subarsecond level, by letting the asteroid Vesta drift within the SWS aperture. The correlation between this experiment and the earlier results is shown in Figure 8.5. See Vandenbussche 1998, [39], for more details.

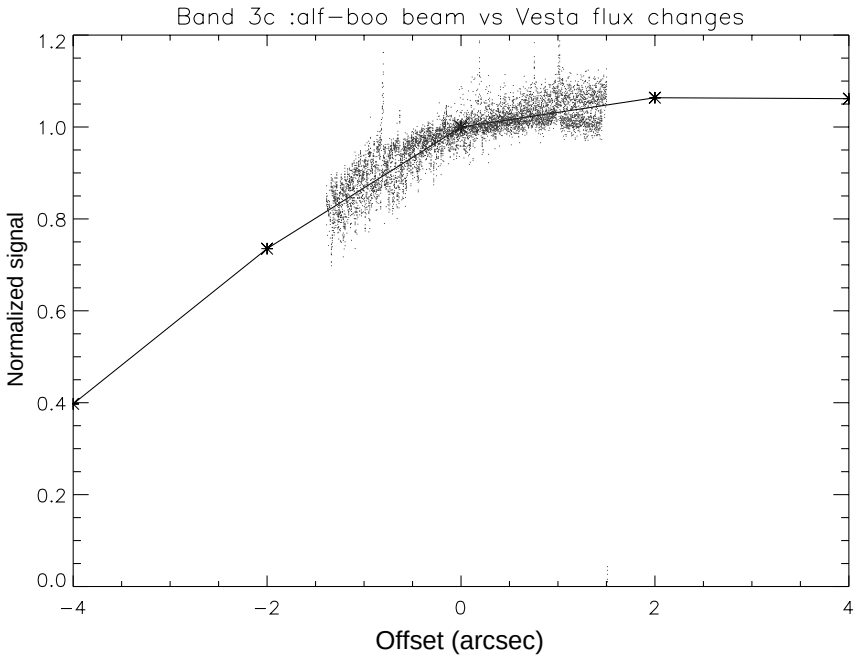

Figure 8.5: *Comparison between the measured (normalised) signal from Vesta as it crosses through the SWS slit and the beam profile as derived from observations on α Boo. The solid line indicates the expected change of the Vesta signal as a function of dispersion (z-axis) offset.*

8.4.2.3 Beam profile wavelength dependency

The SWS01 exercises were used for the characterisation of the beam profile wavelength dependence within a band, done by fitting a first order polynomial to the flux as a function of wavelength.

Only band 2C showed a dependence of the fit parameters on the offset from the target (α Boo, or NML Cyg, shown in Figure 8.6). This is unlikely to be caused by memory effects, as the down scan only has been used in the reduction and also because the pattern is symmetric around the target, but is more likely due to the large wavelength range covered by this band.

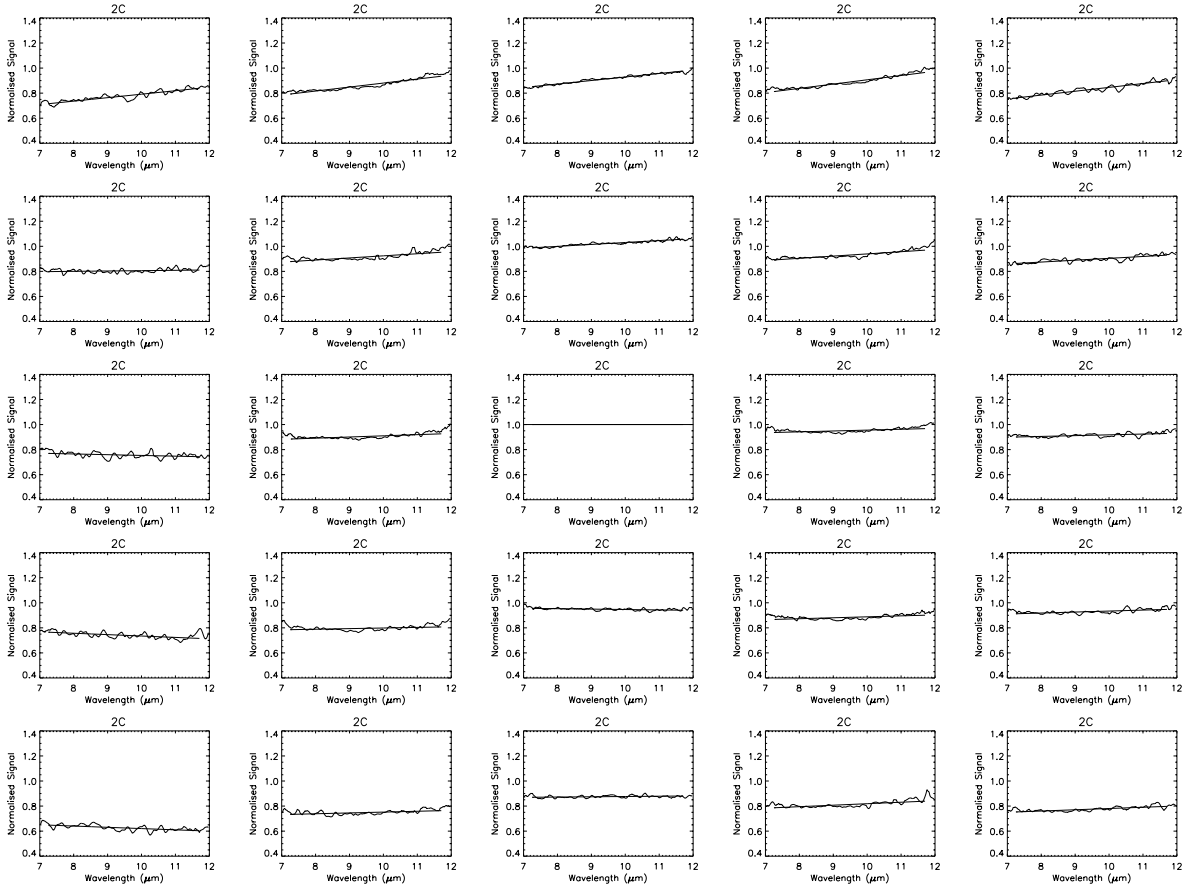

Figure 8.6: *Pointing effects on the spectrum in band 2C, as evidence for wavelength dependence of the beam profile. The data was obtained from an SWS01-like 5×5 raster centred on α Boo in revolution 640. Each box shows the ratio of the spectrum to the centre position. Each box corresponds to one raster point, separated from the adjacent ones by 2′. Y increases from left to right, Z increases from top to bottom.*

8.5 Straylight

Off-axis responses were measured early in the PV phase on the bright source W Hya, out to a distance of 2′. Later in the mission, specific straylight checks were performed, prompted by scientific needs for a better characterization of the influence of straylight from Saturn on planetary satellites such as Titan and Europa.

One measurement of straylight rejection was performed during observations of Titan on revolution 384. The spectral line due to C_2H_4 at 13.7 μm was measured on Saturn and at a position Y_{off} =-87″, Z_{off} =-163″, corresponding to a total displacement of 3′. By comparing the spectral line at these positions a rejection factor of 10^4 was calculated (ref. Salama 1998, [32]).

8.6 Pointing Effects

8.6.1 Introduction

The SWS was designed for a pointing performance consistent with the specification of the telescope optics, but exceeding the specifications of the ISO satellite. Fortunately the satellite pointing was significantly better than specified. Nevertheless, for SWS the data quality was affected by the ISO pointing performance and further improvements on the pointing were triggered by these findings. Even then, pointing problems have remained a limitation for many SWS observations.

The accuracy of the target input coordinates, and of the pointing, have a large impact on the instrumental throughput and the point source flux accuracy, but only a minor impact on the wavelength accuracy of SWS for point sources. Several documents were written covering the pointing accuracy. Leech & Heras 1997, [26], gives examples of what can go wrong when incorrect target coordinates are used. In summary, a star offset from the centre of the aperture by 6″ in the cross-dispersion direction (y-axis) loses approximately 40% in throughput (at 17 μm). A similar offset in the dispersion direction (z-axis) does not result in as large a flux decrease, due to the beam profile (see Section 8.4). An offset in the dispersion direction does, however, affect the wavelength calibration, with a 4″ mispointing resulting in a 1 LVDT (1/8 grating resolution) wavelength offset. As the maximum possible offset is about 2 LVDT, or about 1/4 of a grating spectral resolution element, and within the required wavelength accuracy, errors introduced into the wavelength scale can usually be ignored. Still, random pointing errors are the largest contributors of uncertainty in the wavelength scale. They also impact on the exact fringe patterns, see fringes in Sections 8.6.2 and 9.7.

Heras 1998, [14] extended this study by comparing the ratio of on- and off-source observations of a star with the pointing jitter. It was found that the sudden flux jumps are associated with pointing fluctuations. She noted that even for nominally on-source observations (defined to be those where the pointing error is less than about 4″), there is a correlation between noise in an observation and pointing jitter.

During the ISO mission several stars were observed every few weeks for purposes of wavelength and flux calibration. The flux of one of these targets, γ Dra, was seen to have a modulation that is suspected to be due to pointing errors. The report by Feuchtgruber 1998c, [8], can be read for further information on this.

Information on how the spacecraft pointing can affect observations of extended objects can be read in Feuchtgruber 1998b, [7]. In this case the observed line fluxes varied by 10% over the course of several months. This was attributed to the spatial extent of NGC 6543, the SWS slit size projected on the sky, see Section 8.2.2, and the change in roll angle between the observations.

To derive the position angle of an aperture, information on the spacecraft's position on the sky must be used. This can be found in the header keywords `CINSTRA`, `CINSTDEC`, `CINSTROLL` in ERD, SPD, or AAR products. (see the ISO Handbook Volume I, [17] for a description of these keywords).

8.6.2 Pointing effects on fringes

The effect of pointing offsets on the position and intensity of the instrumental fringes, most prominent in band 3A, was characterised with dedicated spectral scans performed at various positions with respect to NML Cyg as illustrated in Figure 8.7. The dependence of the fringe pattern on the pointing also implies that for extended sources or point-like sources off-axis, a perfect correction for the instrumental response function is not possible.

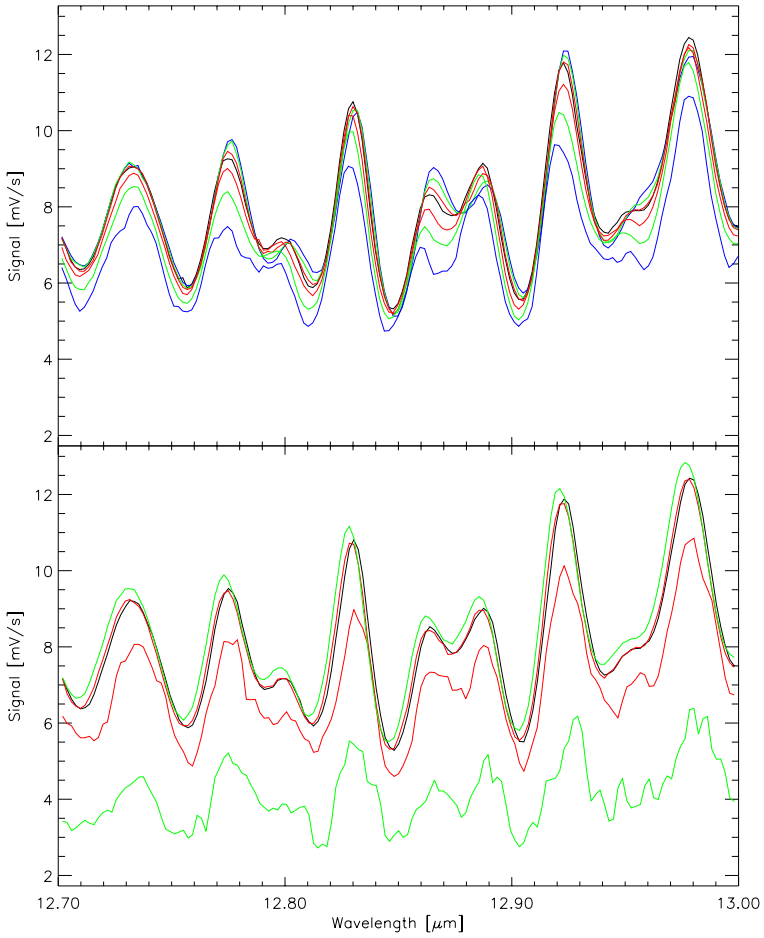

Figure 8.7: *Pointing offset dependence of the fringes seen in detector 26, band 3A, in cross-dispersion (upper panel) and dispersion (lower panel) directions. Each fringe pattern corresponds to a grating scan performed at positions on the sky separated by 2″.*

8.6.3 Pointing jitter induced correlated noise

The ISO pointing jitter is seen by the SWS detectors as the target moves across the beam profile, and results in correlated noise in the band. This correlated noise is discussed in Heras 1998, [14], where the correlation between ISO's pointing jitter and jumps in the flux of SWS observations were first studied. The source DO 24107 was observed off source because of an error in the input coordinates (+4.7″ and −8.6″ off in dispersion and cross-dispersion directions respectively). Such a large discrepancy implies that the observation is carried out at a position where the beam profile is very steep, and therefore small oscillations of the pointing around the average position induce large variations of the measured flux.

8.6.4 Signal modulation on γ Dra

The SWS flux calibration included reproducibility checks on the standard star γ Dra. A total of 120 observations were carried out on this star from revolution 24 to revolution 867. These were systematically processed at the end of the mission and the resulting signals were shown to present flux modulations over

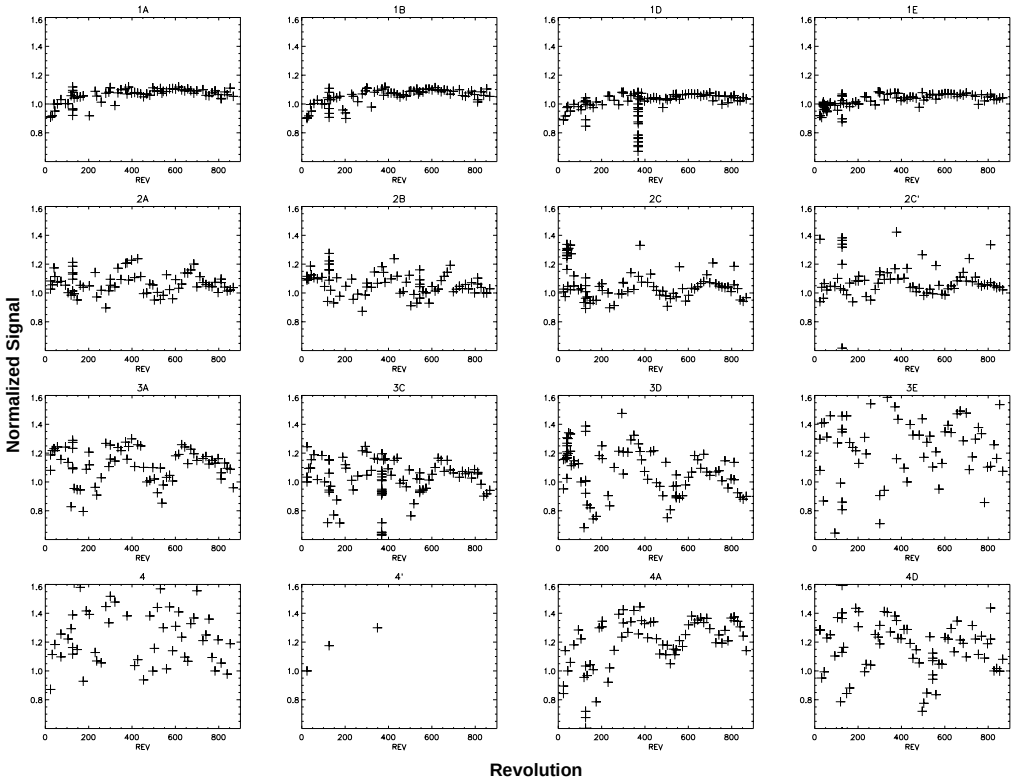

Figure 8.8: *γ-Dra fluxes of all passbands vs. revolution number divided by their median. The flux modulations can clearly be seen in the bands 2A, 2B, 2C, 2C ′, 3A, 3C, 3D, 3E, 4A, 4D. Band 4 and 4′ have too low flux to provide a statement there. No related modulation of comparable amplitude can be seen in band 1.*

the mission (see Feuchtgruber 1998c, [8], for details). Figure 8.8 gives all the derived fluxes within the passbands of the related band versus revolution. The three γ-Dra raster exercises in revolutions 126, 368 and 369 are also included in this sample, clearly to be seen for example in band 1D.

Flux modulations can clearly be seen at the key wavelengths in bands 2A, 2B, 2C, 2C′ (at 11 μm), 3A, 3C, 3D, 3E, 4A (offband data) and 4D (offband data). No related modulation of comparable amplitude can be seen in band 1. Fluxes are heavily affected by pointing inaccuracies, as can be seen in the period before revolution 369, when significant pointing errors happened. Also the use of different guide stars with different accuracies are suspected of introducing additional noise in the flux trends. The best explanation for the flux modulation, still unproven however, is a systematic pointing error towards γ Dra. Band 1 has basically 0 FPG offset, while all the other bands are offset by $2''-3''$. This makes bands 2, 3 and 4 sensitive to even small ($1''$) pointing errors, as they are operated close to the edge of the flat top of the SWS beam profile. Begin centred, band 1 remains rather robust against pointing errors.

Chapter 9

Caveats

9.1 Introduction

This chapter discusses several instrumental effects that have not been discussed elsewhere in this handbook. Most of them are caveats the users should be aware of related to known limitations of the automated pipeline processing of SWS data products. Some of them can be properly accounted for through manual processing using Interactive Analysis software (OSIA or ISAP) while for some others there is currently no correction available. A full list of comon calibration concerns is given in Table B.1 of Appendix B. Section 9.2 discusses transient (or memory) effects in the SWS detectors of bands 2, 4, 5 and 6. It also discusses reference scans and glitch tails. Section 9.3 discusses two forms of detector jumps. In Section 9.4 some remarks are made about the consequences of having (small) apertures of different sizes. Section 9.5 discusses the influence an observation with CAM CVF could have on a subsequent SWS observation. Section 9.6 discusses the influence of the diffuse background of the spectra. The last Section 9.7 discusses fringes and the probably related issue of baseline ripples.

9.2 Memory Effects

The band 2 (Si:Ga), 4 (Ge:Be), 5 (Si:Ga) and 6 (Ge:Be) detectors used in SWS 'remember' their previous illumination history. Going from low illumination to high illumination, or *vice versa*, results in the detectors asymptotically reaching their new output value. These are referred to as memory effects or transients. Bands 1 (InSb) and 3 (Si:As BIBIB) are not affected by memory effects due to the different detector material used.

Figure 9.1 gives an example from all bands during illumination changes. In this figure it can be seen that bands 2, 4, 5 and 6 have severe memory effects, while bands 1 and 3 show no such effects - these detectors instantaneously reach the signal level corresponding to the new illumination levels.

Another example of memory effects is the effect seen in up-down scans of fairly bright sources. For sources with fluxes greater than about 100 Jy memory effects cause the up and down scans in the SPD to differ in response by up to 20% in bands 2 and 4. This effect can be seen in Figure 9.2 for band 2 and in the Figures 9.5 and 9.6 for band 4. Figure 9.2 shows the output of detector 24 against time. Several up-down scans were taken during this measurement, interspersed with dark currents and sometimes reference scans. During a reference scan the grating is moved to a fixed wavelength position to (re)measure the same flux level. This was done to obtain more information on the memory effects, although the scans were never explicitly used for this purpose. The up-down scans have a clear asymmetric shape, the dark currents are not constant and the reference scan do not yield the same flux levels. All this is indicative of serious memory effects.

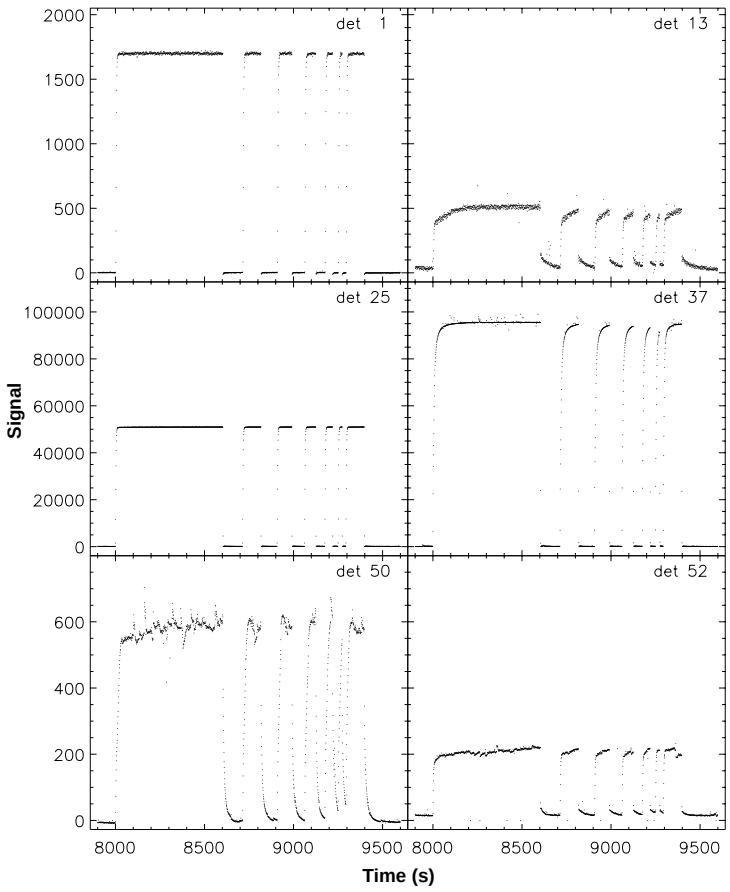

Figure 9.1: *The SPD output of all bands during illumination changes, showing memory effects in bands 2, 4 5 and 6 but none in bands 1 and 3.*

Currently the only memory effects corrected for in the pipeline are those that affect band 2 detectors. They are modelled as changing dark currents. This is mainly discussed in Section 9.2.1. Section 5.3 discusses the general methods used in the dark current subtraction and Section 7.3.3.2 discusses its implementation.

Figure 9.3 shows the result of this in an AAR after application of the transients models described in Section 9.2.1. The up and the down scans overlap quite well and the reference scans find their proper place in the spectrum at 4.5 μm and 7.7 μm.

For transient effects in the longer wavelengths detectors (band 4 and both FP bands) see Section 9.2.2.

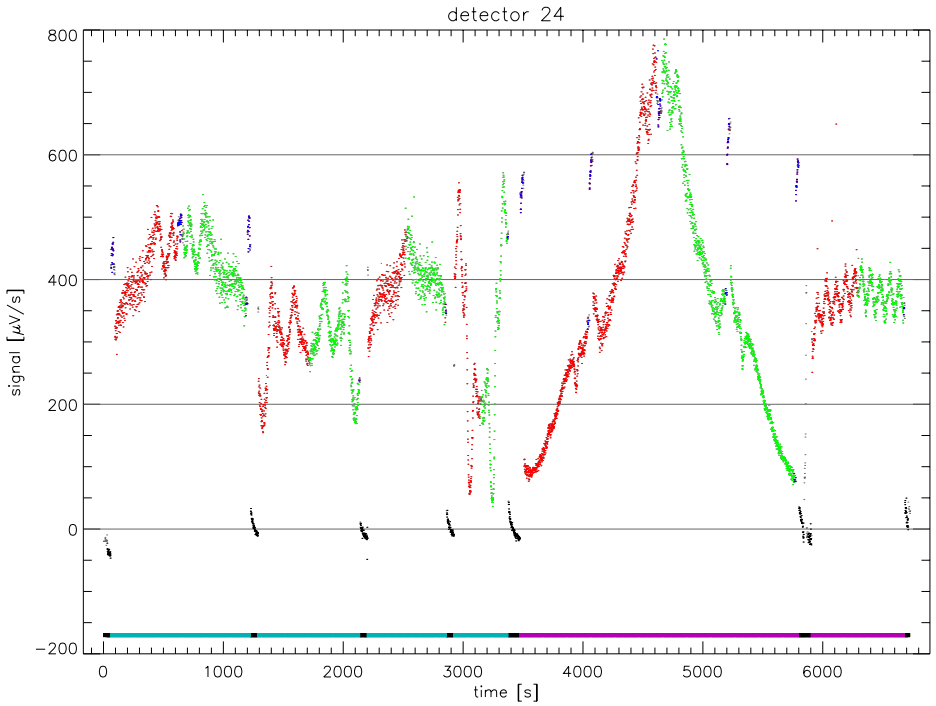

Figure 9.2: *Example of memory effects in band 2 on up-down scans as seen in an SPD of an SWS06. The up and down scans are colour-coded differently: red for the up-scan and green for the down-scan. The so-called 'reference scans' are in blue (see Section 3.2.2 for further discussion). At the bottom is a bar indicating the aperture used: aperture 2 in mint, aperture 3 in purple and black for aperture closed. The asymmetry in up and down scan is evident. Also the reference scans should be at the same flux level (per aperture setting), which obviously they are not.*

9.2.1 Band 2

An adapted version of the Fouks-Schubert model (Fouks and Schubert 1995, [10]) was developed by Do Kester and successfully implemented in the SWS pipeline to correct band 2 data for transient effects. The method brings the errors (of sometimes up to 20%) down to the few percent level.

The Fouks-Schubert model is written for semi-stationary fluxes, where the *semi*-part reflects the fact that the detectors do not have to be in an equilibrium state when the next flux step takes place. For a spectrometer like SWS the flux changes continuously, with every reset interval, or even every step of the grating scanner, giving a new constant flux level. The detectors are (almost) never in an equilibrium state but that is taken into account in the formula. The original Fouks-Schubert formula was therefore rewritten into a form more suitable for SWS.

$$S_k = \beta S_k^{\infty} + \alpha_k \tag{9.1}$$

$$\alpha_k = \frac{(1-\beta)\alpha_{k-1} S_k^{\infty}}{\alpha_{k-1} - (\alpha_{k-1} - (1-\beta)S_k^{\infty})\exp(-\Lambda\beta S_k^{\infty}\Delta t)} \tag{9.2}$$

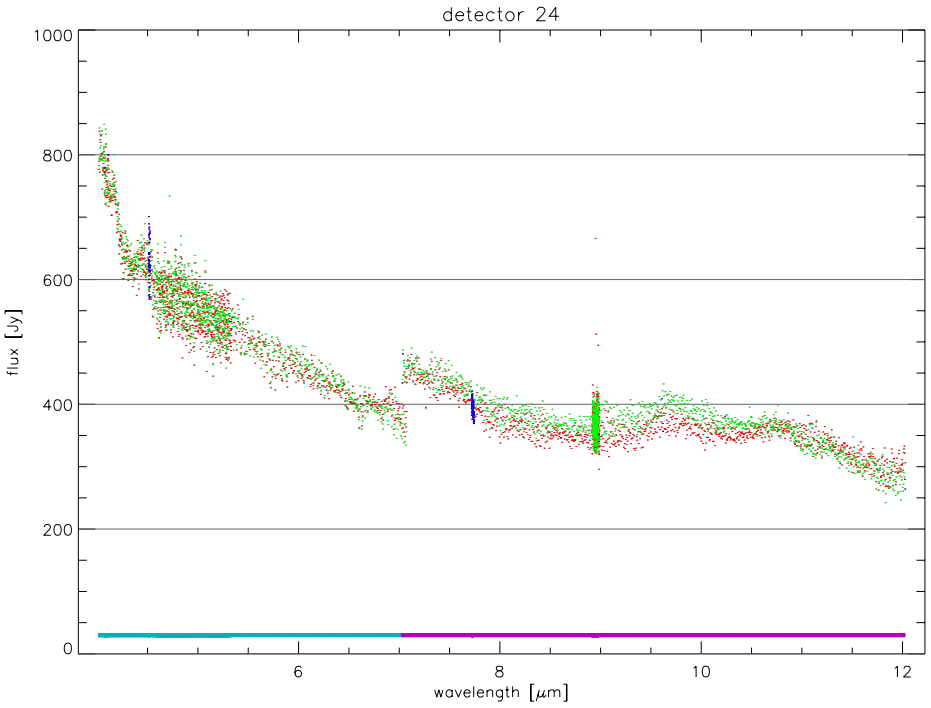

Figure 9.3: *Example of the result of memory correction in band 2 as seen in an AAR of an SWS06. The colours are the same as in Figure 9.2.*

Here S_k is the signal through the detector at time k, S_k^∞ is the relaxed signal at time $t = \infty$. It is proportional to the incoming flux. β is a constant, to be estimated from the data, and α_k comprises the memory effects. α_k is dependent on its previous value, α_{k-1}, on the present relaxed signal, S_k^∞, and on the constants β and Λ. Δt is the duration of the time step from $k-1$ to k. The signal is related to the relaxed signal (or flux) via a constant gain β and a changing dark current α. It is a fortuitous coincidence that we used this gain and dark model already in the pipeline. We can identify the product of βS_k^∞ with the incoming flux as it better reflects our present dark current model of *signal = flux + dark*. The absorption of the constant factor, β, in the subsequent calculations is trivial.

When the incoming flux is zero, i.e. when measuring with a closed shutter (a 'dark current measurement'), the above expression for α breaks down yielding 0/0. Using l'Hôpital's rule we find a new expression for α when $S_k^\infty = 0$:

$$\alpha_k = \frac{(1-\beta)\alpha_{k-1}}{(1-\beta) + \alpha_{k-1}\Lambda\beta\Delta t} \tag{9.3}$$

This expression decays to zero in a more or less hyperbolic manner as observed in the Si:Ga detectors. The constant β is the fraction of the relaxed signal which expresses itself immediately, so β is between 0 and 1. The incoming flux is always positive or zero in case of a dark current. It follows from Equation 9.2 that the values of α are always positive and so is the signal S. We measure, however, (dark) values which are negative for some detectors. So we must conclude that the model is not yet complete, as the zero level in the data cannot be mapped directly on the zero of the model. This is not so disturbing as

the zero in the data can be changed somewhat arbitrarily by changing, for instance, the value of 'midbit'. Also the zero level shifts when the gain setting changes or when the length of the reset interval changes. All these stepwise zero shifts are *artificial* in the above sense.

Thus, we expand the model by adding a model zero level

$$S_k = \beta S_k^\infty + \alpha_k + Z. \tag{9.4}$$

Determining the zero-level function (ZLF) was difficult, as the behaviour at low fluxes is extremely sensitive to the zero level. Piecewise linear functions between dark currents of the same gain setting were used. In this way, the Fouks-Schubert model at low fluxes behaves similarly to the standard dark current subtraction used in all previous pipeline versions, which was deemed correct at low fluxes.

9.2.1.1 Parameter estimation

Now we have a (forward) function which relates the measured signal to the incoming flux in a complicated, non-linear fashion. We only have to invert the relationship, and as the constant β is quite large (≈ 0.8) we can do the inversion iteratively

$$S_k^\infty = (S_k - \alpha_k - Z)/\beta \tag{9.5}$$

where α_k is calculated with the values of S_k^∞ from the previous iteration. For most observations the flux stabilises after half a dozen iterations.

In total we have $3 + N_Z$ parameters: β, Λ, α_0 plus the parameters needed in the ZLF. α_0 is the value of α before the observation started. The first two parameters are material constants, i.e. they might be fixed over the mission and if that is the case they would have to be estimated only once. The others are related to the flux history in some sense. As this history is unknown these parameters have to be estimated for each observation separately. Note however that the ZLF is chosen to be linear. Consequently for each choice of β, Λ and α_0 the ZLF-parameters can be estimated directly, simplifying the non-linear search for the other parameters. All parameters, however, have to be estimated at least once.

To estimate the parameters we use the redundancy in each observation: up-down and 12 detectors covering more or less the same spectral area. The procedure is described in Kester 2001, [22], or García-Lario et al. 2001, [11].

9.2.1.2 Detector constants

The parameters can be estimated properly when an SPD is used with sufficient dynamic range between 100 and 5000 μV/s. For fluxes much larger than 5000 μV/s, other memory effects than the ones we are modelling become important. On the other hand when the flux range is too small ($< 100\mu$V/s) not enough memory effects are present to allow proper extraction of parameters. In that case it is possible, by keeping the parameters β and Λ fixed and fitting the others, to get proper transients, which will not be much different from the dark current the pipeline would yield.

Figure 9.4 shows an example how the memory model changes over time for one detector during an observation of the calibration star γ Dra. In the upper panel the measured data is plotted in black, the relaxed signal in green (symmetric in up-down), the transients, α_k, in red and the zero level in blue. Note that the measured data go below zero and that consequently the model zero level is also below zero. In yellow the model data (relaxed signal + dark) is plotted. They are compared to the true data to calculate χ^2. The memory model has some real impact whenever the flux is more than a few 100 μV/s, e.g. between time 500 and 1000. On the other hand when the flux is below 100 μV/s, e.g. around time 1500, a straight line between the surrounding dark currents is equally good. In the lower panel the

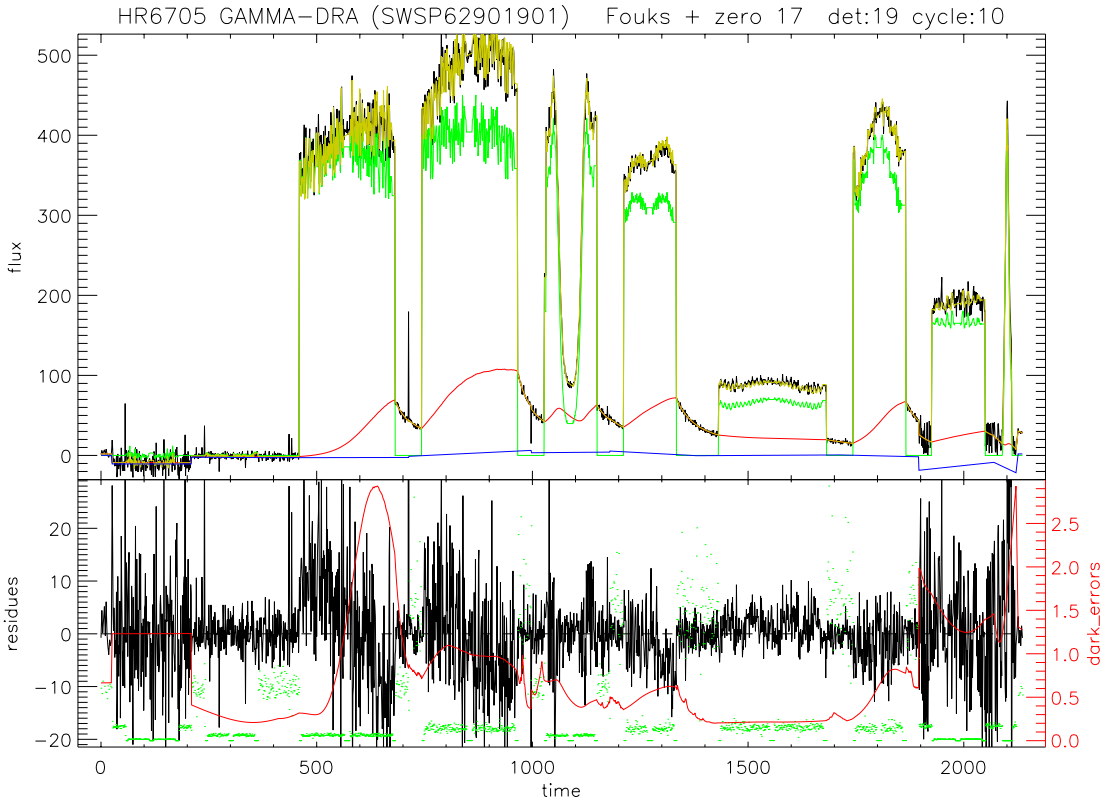

Figure 9.4: *In the upper panel: black is the data, green is an estimated input flux, red is the contribution of the memory model, blue is the virtual zero level and yellow is the sum of the input flux (green) and the memory model (red). It can be compared directly to the actual data (black). In the lower panel: black is the residuals, the difference between black and yellow, above. Green is the weights of the data points to be read on the red scale (on the right) and red is the uncertainty in the memory model also on the red scale.*

residues are plotted in black, the weights of the points in green (scale on the right). There are some systematic effects, but most of the high noise at high flux has to do with the fact that the measured spectrum is fluctuating (or fringing) severely which cannot be properly followed during the rebinning. In red in the lower panel (to be read on the red scale) is a Monte-Carlo estimate of the error in the memory model.

We determined the parameters β and Λ from 65 observations of γ-Dra and checked it afterward on all SWS01 observations which had a median flux in band 2 higher than 100 μV/s. We searched for time variations in the parameters, for variations as function of the flux level and even for variations with temperature, using an extension of the FS formalism. None of the variations was very significant. So we settled for one set of parameters for all of the band 2 detectors, presented in Table 9.1. More details in Kester 2001, [22], or García-Lario et al. 2001, [11].

All pipeline calculations are done with these two parameters fixed. The parameters of the zero-level function and the value for α_0 are estimated for each observation separately.

Table 9.1: *Detector constants for transient correction in band 2.*

constant	value	
β	0.82	-
Λ	63	V^{-1}

9.2.1.3 Error calculation

When we have arrived at the minimum value for χ^2 the standard deviations and covariance matrix for all parameters is calculated, using a Gaussian approximation at $\chi^2_{\rm min}$. Typical errors that we find in a good observation are a few per thousand in β, a few percent in Λ and of the order of 1 μV/s in the other parameters (α_0 and the ZLF). However, we are not so much interested in the formal errors in the parameters but much more in the effects they have on the calculated dark current. We use a Monte Carlo scheme where the dark current is calculated 25 times, each time with another randomized set of parameters, drawn from a multidimensional Gaussian distribution representing the full covariance matrix. At each sample the standard deviation of these 25 dark currents is taken as the formal error. See the red line in the lower panel of Figure 9.4.

9.2.2 Memory effects in bands 4, 5 and 6

The transient effects in band 4 and in both FP bands can be about as severe as in band 2. Various effects can be seen in Figure 9.5. It is an SWS01 speed 4 observation of K3–50. At the start of the up-down scan (at the longer wavelength side) we see a transient. Some detectors, like 37, display a so-called 'hook' effect, some rise faster than others, seeming to get earlier to their relaxed state than the others. At the shorter wavelength there also seems to be some hysteresis effect, where the second part (the down scan in red) seems to stall before getting into the rising mood.

Figure 9.6 displays the same object but then in an SWS01 speed 2 observation, i.e. scanning the spectrum 4 times as fast. It shows the same general trends as in Figure 9.5. In the time domain all detectors react in exactly the same way, which means that in the spectral domain it seems much slower. Both the hook and rise at the start and the hysteresis just after the turning point can be seen. This speed 2 observation has much more glitches; it might have been taken in a more unfavourable part of the orbit. Note that these glitches have their tail, if any, in the time direction, to the left for the up scans (black) and to the right for the down scans (red).

Unfortunately we do not have a proper model to correct for transients in band 4. The FS model applies only to Si:Ga detectors as only for these detectors the assumptions are valid which simplified the full set of interdependent differential equations that describe transients in general. With these assumptions these equations can be integrated into the closed system which yield the FS model. In the future it might be possible to extend the FS equations with first order corrections, which then might successfully be applied to band 4 detectors too.

For the FP detectors (Si:Sb and Ge:Be) the transients can be as serious as in band 4 (Ge:Be). However due to the fact that the flux levels seen by these detectors are generally quite low, the problem is not as severe as in band 4. This is a fortunate situation as we will never be able to correct for transients because we do not have up-down scans for the FPs. The FP scanners could only be driven in one direction with full paralellisation of the meshes. So transient information and spectral information is inextricably mixed.

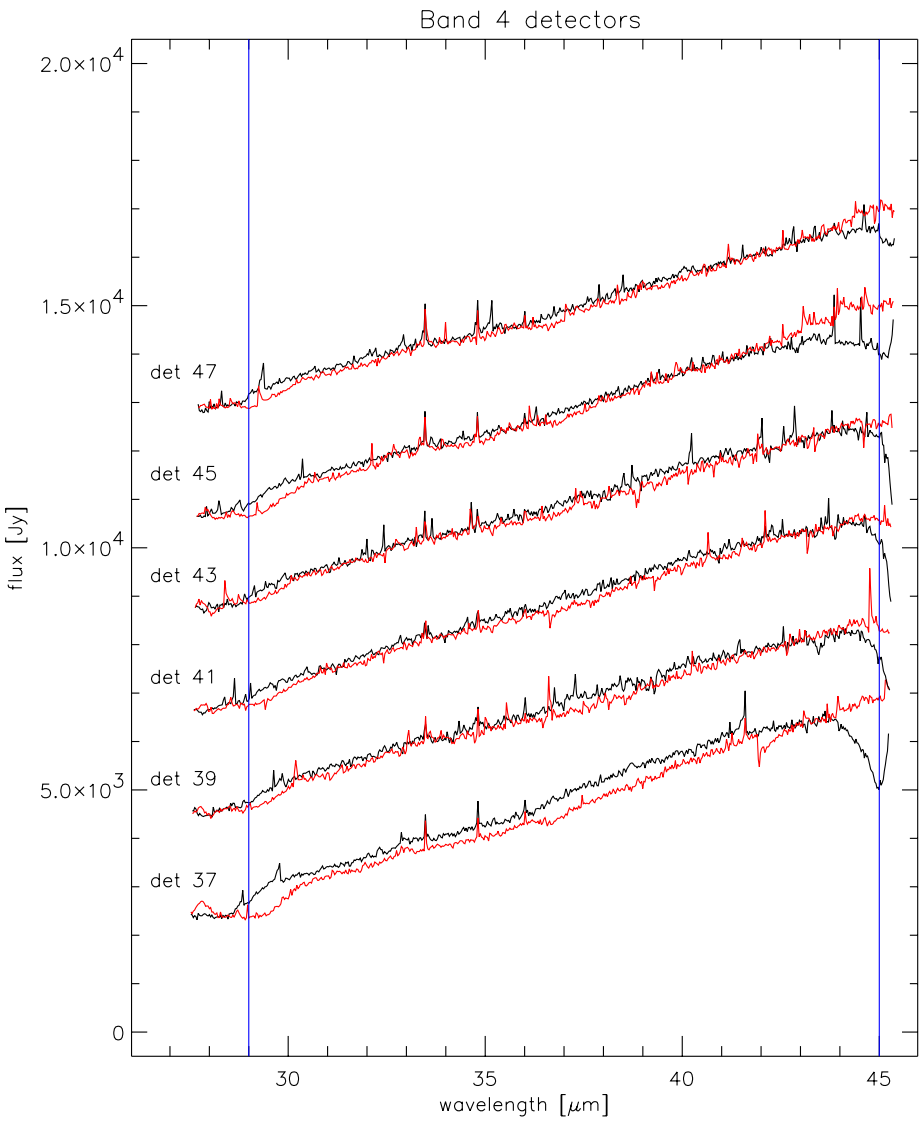

Figure 9.5: *Example of memory effects in band 4 on an up-down scan as seen in an AAR of an SWS01 speed 4. The scans of the different detectors are offset with respect to each other for clarity. At the start of the upscans (black) at the long wavelength side, various memory effects can be seen, some with so-called 'hooks' (dets 37, 45 and maybe 47). The down scans (red, running from short to longer wavelengths) generally show less transient effect. Still there is some systematic difference between up and down scans around 30 μm which is probably attributable to transients. Which one of the up or down scans is affected is unclear. The blue lines show the official borders of band 4.*

9.2.3 Reference scan memory effects

The combined effects of reference scans (described in Section 3.2.2) and detector memory effects produced from band 2 and band 4 detectors during SWS06 observations can be seen in Figure 9.2. Reference scans

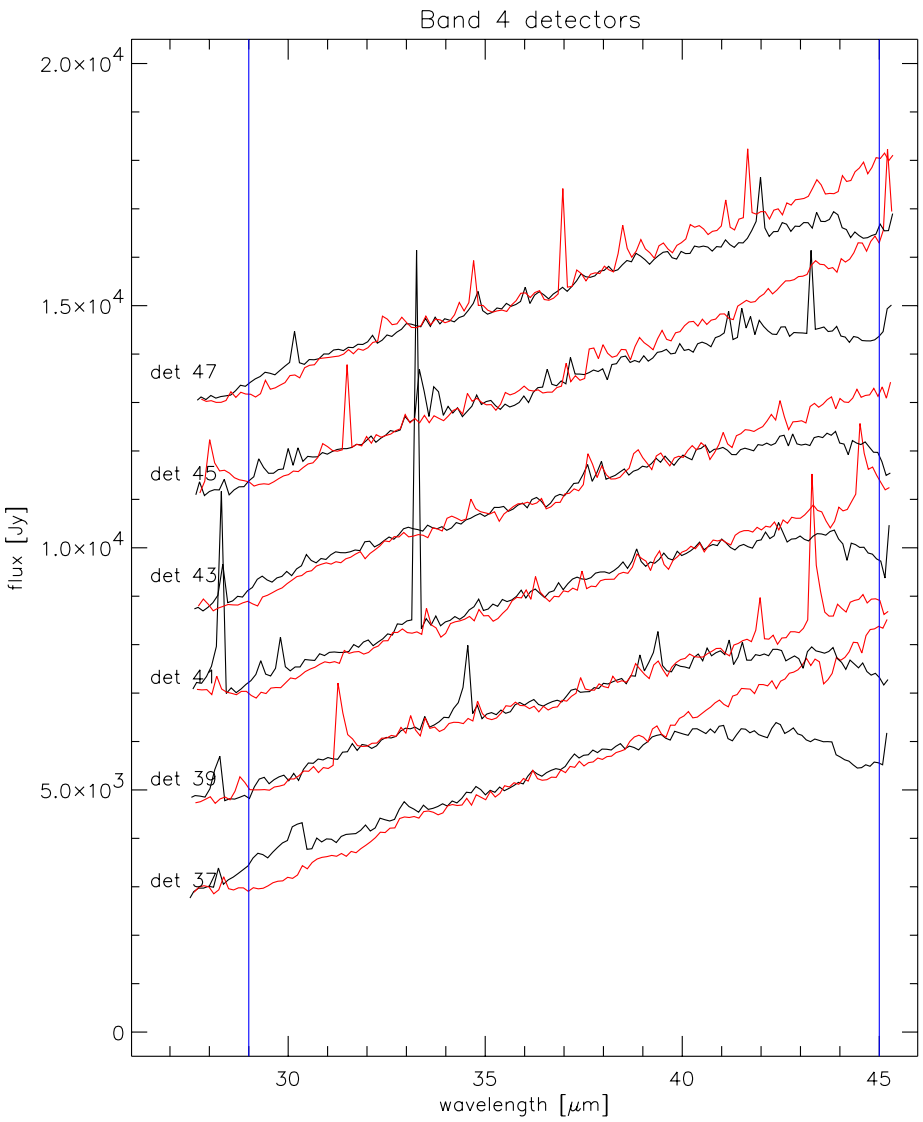

Figure 9.6: *Example of memory effects in band 4 on an up-down scan as seen in an AAR of an SWS01 speed 2. The same colour coding applies as in Figure 9.5. As this observation is done 4 times as fast as the previous one, the transient effects seem to spread out over a much wider wavelength range.*

were introduced to get a handle on the memory effects but as such they were never used due to the lack of an algorithm to do so. Quite early in the mission the number of reference scans per SWS06 was reduced so that only long SWS06 observations had any of them during the up-down scans. They are still present at the beginning and end of an up-down scan. The number was reduced because of the upsetting effect the reference scans had on the rest of the scan.

In band 2 most of the harmful effect of reference scans is removed by the application of the FS model as can be seen in Figure 9.3. In band 4 it just compounds to the transient problems that are already present.

In the document by Leech & Morris 1997, [27], examples of such effects are given and suggestions what to do when they occur[1].

9.2.4 Glitch tails

Glitches are caused by such events as fast moving electrons and ions inside the Earth's magnetic field hitting the detectors. Whatever causes a glitch, the effect of one is a sudden change in the output voltage which causes a step (a 'glitch') in the affected ramp. Most glitches cause an increase in the output voltage, but some can cause a decrease. For small glitches (the majority) the slopes before and after the glitch are indistinguishable from each other. Figure 2.7 shows an example of a glitch in the 24Hz ERD data in the middle of the second ramp of a measurement.

Some glitches, however, are large and have effects that lasts for a long time (they have tails). These tails are especially seen in band 4, due to the detector material and operating conditions, and are probably due to memory effects, see Section 9.2. Figure 9.7 shows two examples of band 4 glitches in the SPD. In both cases the detector requires a long time to stabilise. Note that a strong glitch in one detector can affect other detectors in the same detector array due to cross-talk. More examples of glitches (and tails) can be seen in Figures 9.5 and 9.6. In Figure 9.5 a much rarer negative glitch (with tail) is seen in detector 37 near 42 μm.

Both FP bands are even more affected by glitches than band 4. Their detectors are somewhat larger in size and thus catch more cosmic rays. See Figure 9.1.

Derive-SPD attempts to correct for glitches, and for details of how this is accomplished see Section 7.2.8. No attempt is made to correct for tails.

9.3 Detector Jumps

Detector jumps are another feature seen in the detector responsivities apparently similar to glitches. For unknown reasons the signal level seems to jump, mostly up and then decaying, but also sometimes down. Jumps can be as high as 10 μV/s. They affect the zero level of the detector(s) and therewith dark current subtraction. They occur about once per 5 hours per detector. For low flux observations at high gain they are a big nuisance. In band 1 and 2 about half of the jumps are associated with glitches. However, no correlation has been found between the characteristics of these jumps and those of the glitches.

Part of the jumps are due to sudden changes in the pulse-shape correction. The change can be either in amplitude or in decay time or in both. Why the pulse-shape is suddenly changing is unclear. Since the introduction of pulse-shape correction (Section 7.2.6) in OLP 10, the jumps have lost some of their acuity although they are still present.

Detector jumps come in two different kinds. Either a single detector jumps or the complete detector block jumps.

9.3.1 Single detector jumps

The document by Heras 1997, [13] summarizes a study made on single detector signal jumps. These effects occur in only one detector at a time and can be generally described as a sudden increase or decrease of the signal, which then remains constant or has a long recovering time ($\gg$ 10 s) after the jump. These jumps are normally seen at low signal levels. Examples of such jumps in SPD data are shown in Figure 9.8

[1] Note that this document was written before the FS model was implemented in the pipeline software.

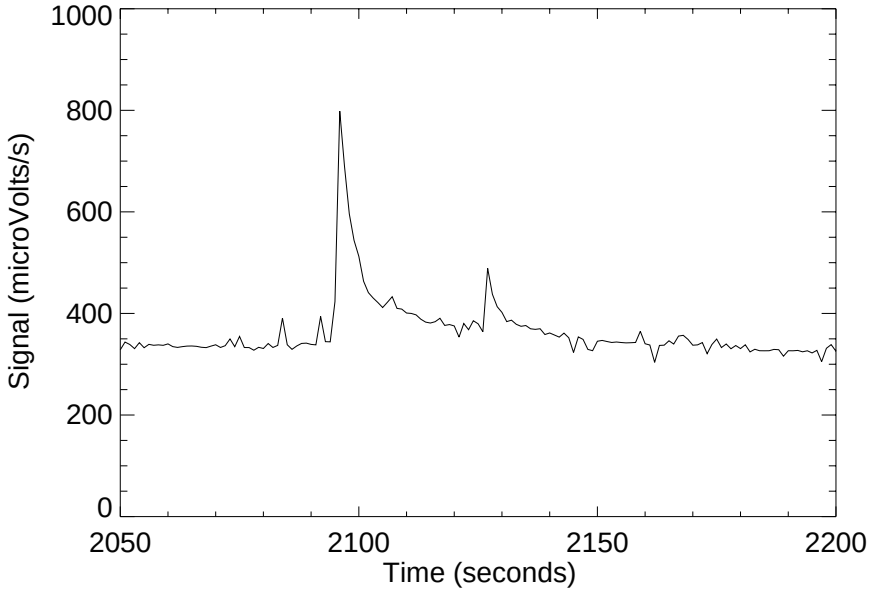

Figure 9.7: *Two examples of less-frequent long lasting glitches. The data shown is SPD from a band 4 detector.*

The signal jumps observed for each detector vary significantly between different cases, and may be negative or positive.

Jumps in band 3 are of different nature from jumps in bands 1 and 2. In band 3 it sometimes has the character op popcorn-noise, jumping up and down between two more or less fixed levels. This popcorn-noise is associated with 'popping' pulse-shape corrections.

Users are recommended to examine the SPD from their observations to look for such jumps. If they are present the user can either throw the affected portions of the data away or try to adjust the baseline of the affected portion to the pre- and post-jump baseline.

9.3.2 Scan jumps

The symptoms are that each detector in a block suffers a sudden rise in sensitivity, which slowly decays with time. They usually only affect one of an up-down scan pair, and the only solution is to throw the affected scan portion away. As they affect an entire detector block they are given the name 'scan jumps'.

9.4 Aperture Size

SWS has three apertures (four if the virtual Fabry-Pérot aperture is counted) of different sizes and, for the grating, four detector bands each with detectors of different sizes. This causes an effect when switching between apertures/detector bands. The fluxes of extended sources may change as the apertures/detector bands change, due to the different areas of the sky observed. The fluxes of point sources may change if the entered coordinates are incorrect by a few arcseconds, as the apertures are slightly offset with respect to each other. For more information about apertures see Section 8.2.

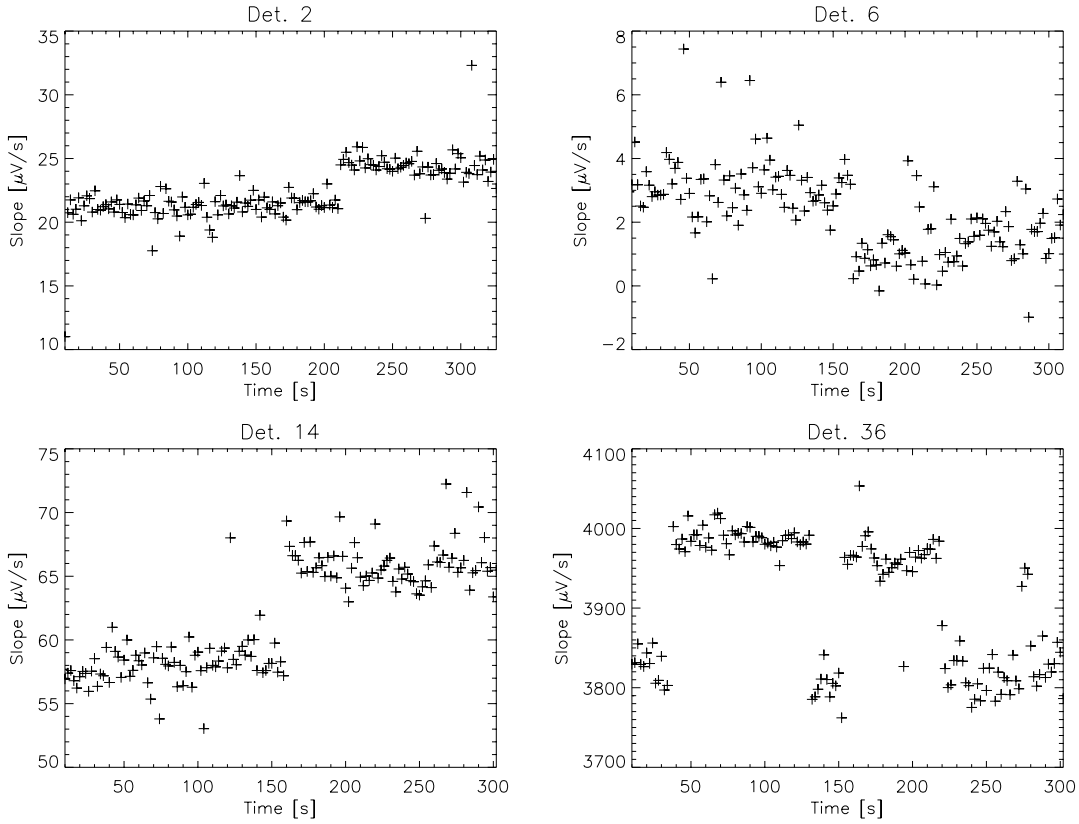

Figure 9.8: *Four examples of single detector signal jumps. In all cases the signal from one detector suddenly jumps to a different value and remains there for a log time. These are pre-OLP 10 plots.*

9.5 The Influence of CAM-CVF Operations on SWS

In May 1997 cases came to light where the action of a CAM-CVF observation before an SWS observation led to an increased SWS band 3 detector dark current. This increase above the nominal value approached a factor of 100 in some cases. The dark current decreased with time during the SWS observation and reached the nominal dark current less than 30 minutes after the CAM-CVF observation. This effect can be seen in affected observations by selecting and plotting all the dark currents from the data - the dark currents are enhanced and decrease with time. In severe cases this effect can manifest itself in the AAR by band 3 fluxes being negative and in the SPD by the band 3 up and down scans having different shapes.

No correlation between the dark current and the operation of any other instrumental AOT was seen.

This could only affect observations made before June 1997. After this date SWS observations were not scheduled until after 30 minutes of a CAM-CVF observation.

9.6 Diffuse Background Emission

SWS does not use spatial chopping, hence all spectra will contain some contribution by zodiacal light and galactic background. In most cases, this will be negligible compared to the source flux. The zodiacal background component is the most important over the largest part of the SWS wavelength range, with a continuous spectrum corresponding to a dust temperature of about 260 K, that does not affect searches

for line emission. As an order of magnitude estimate, a typical zodiacal light flux density seen within an SWS aperture will be about 0.3 Jy.

9.7 Fringes and Baseline Ripples

All SWS bands show fringes to some extent. They are a modulation, with wavelength, of the flux falling on the detectors and originate on parallel plane surfaces in the light path which act as Fabry-Pérot etalons. Plane parallel surfaces at a distance of a few mm up to a few cm are perfect for generating FP effects in the infrared wavelength range. It is assumed that etalons are formed inside filters, on plane mirrors and, most conspicuously in band 3, in the BIBIB detectors themselves. Combinations of all these effective etalons result in a sometimes wild fringe pattern. Every reflecting surface which is added to the light path can add N-1 extra fringe components excluding all the overtone options. Bands 1, 2 & 4 are only lightly affected by fringes, whereas they are more pronounced in band 3. An example of fringes in the band 3D spectrum of a star can be seen in Figure 9.9.

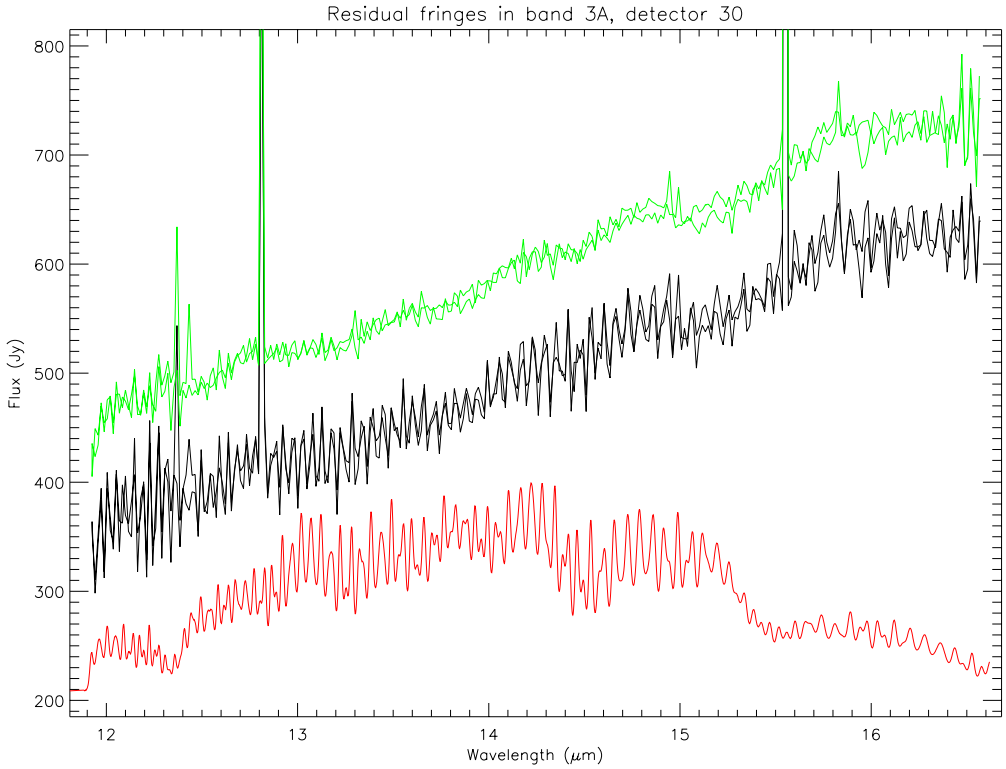

Figure 9.9: *Example of residual fringes in band 3A. The (scaled and shifted) RSRF is displayed in red to show that the residual fringes are indeed leftovers of the RSRF. In green is a defringed version of the same scan, shifted up by 100 for clarity. The baseline ripples show as a slow modulation on the spectrum.*

Most of the observed fringe patterns disappear in the calibration process where the observation is divided by a similarly fringed relative spectral response function (RSRF). Some residual fringing still remains in the calibrated spectrum. However, its exact pattern is presumably determined by the location of the source in the slit. The fringe pattern does not shift as a whole when moving from one spot within the slit to another. Instead different components of the fringe pattern shift by different amounts, resulting in a completely altered fringe pattern. See also Figure 8.7. Another cause of extra fringing is found in

the combination of the size of the observed object and the speed at which its spectrum is scanned. This combination determines the smoothing in the spectrum. Ideally the RSRF should match exactly the smoothness of the observation, which unfortunately is almost never the case. The RSRF was observed at full spectral resolution during ground tests using a black body source which filled the slit completely. For SWS02 and SWS06, and for slow SWS01s, we have an RSRF where the fringes are not sharp enough and for fast SWS01s the RSRF is not smooth enough. In the pipeline processing we try to remedy this by smoothing or peaking up the RSRF according to the speed of the observation. The three reasons mentioned above (location, speed and extent) can cause a *residual* fringe pattern in some bands of up to 10%. Table 9.2 lists the main residuals and the bands in which they occur.

Fringes can have an unknown effect on both the continuous flux level and on line fluxes. For monochromatic light the amplitude of the fringe pattern can be much higher. So line emission might so to say sneak through the fringing FPs with much higher (or lower) amplitude than the surrounding continuum flux, depending on where on the fringe the line is located. No study has been carried out the assess this effect.[2]

For continuum flux another effect is present. When the signal passes through the fringing FPs some of the flux is reflected backward and other is passing through, but in essence we loose flux. When the signal is divided by a perfect RSRF this lost signal is restored. Such a perfect state is not given to us. The signal is divided by a not quite adjusted RSRF and any of the following things might happen. When dividing by a too weak RSRF which is properly aligned in wavelength we still miss signal in the original fringes. When the RSRF has too strongly peaked fringes we actually end up with too much signal; the fringes invert. And finally when the amplitude of the fringes is perfect but the fringes are out of phase, we get a signal which is on average okay but still has shifted fringes. So in all cases we have residual fringes, but we do not know what was the cause. After removal of the residual fringes we could have either too little continuum flux or too much or we might be lucky. Indeed baseline ripples have been found when comparing bright calibration sources with stellar models (Van Malderen et al. 2002, [42]). These baseline ripples have an amplitude of a few percent and they are shaped quite like the envelope of the fringe pattern on the RSRF.

Tools exist in OSIA and the ISO Spectral Analysis Package (ISAP) to carry out defringing of AAR data. The OSIA tool FRINGES removes (residual) fringes in a completely automated way from SPD or AAR data.

For more information on fringes, how they are modelled and how well they can be removed, see Kester, Beintema & Lutz 2001, [21].

[2] On the other hand no rumours have reached us which would spur such a study.

Table 9.2: *Main fringe components per band. The second column gives the effective etalon thickness for the main components. Sometimes there is more than one component. These are listed separately when the components are quite distinct. Column 4 and 5 list the compound amplitude in percent, of the fringe components in resp. the RSRF and of the residual fringes in some observations on point sources. The last column list the AOT numbers where these residual fringes might be found.*

band	D [mm]	range of D [mm]	RSRF [%]	Residual [%]	AOT nr.
1A	4.20	4.1 – 4.3	-	8	6,2
1B	4.30	4.2 – 4.4	-	3	6,2
1D	4.45	4.3 – 4.5	2	5	6,2
1E	4.58	4.4 – 4.6	-	1	6,2
2A	4.43	4.4 – 4.6	1	2	6,2
	0.89	0.8 – 0.9	0.5	-	
	2.39	2.3 – 2.4	0.3	-	
2B	4.50	4.4 – 4.7	2	1	6,2
	0.89	0.8 – 0.9	0.6	-	
2C	5.86	5.6 – 6.1	4	4	all
	0.89	0.8 – 0.9	2	-	
3A	3.37+3.25	3.2 – 3.4	25	5	all
	5.26+5.72	5.0 – 6.0	10	5	
3C	3.25+3.38	3.2 – 3.4	17	4	all
3D	3.25	3.2 – 3.4	17	2	all
3E	3.28	3.2 – 3.4	19	2	all
4	13.25	13.2 – 13.3	0.2	-	-
4A	5.27+5.73	5.0 – 6.0	10	3	all
4C	6.67	6.5 – 6.8	1	-	all
4D	-	-	-	-	-

Appendix A

Product Description

A.1 Introduction

This appendix describes the products available from the ISO Data Archive (IDA). It is split into five sections describing the Raw data (ERD and CSH) files; the standard processed (SPD) files; the Auto-Analysis Results (AAR) files; the other product files available from IDA; and the Calibration-G files. Note that the format for all these files is binary FITS format and that most of them are described in the IDPD, [34].

A.2 Raw Data Files

Two files are described in this section: the SWS Edited Raw Data (ERD) and the SWS Compact Status (CSH).

A.2.1 Edited Raw Data (ERD)

These files are normally named swer*.fits, where '*' is an eight-digit number generated from the revolution the observation was made, the order the observations were performed in that day and the order it appeared in the proposal.

A.2.1.1 Headers

The ERD files contain primary headers described in Table A.1. In this table example information is used to fill the header.

Most keywords are self-explanatory. Those that are not include:

`TMRATE` The Telemetry Rate can only be 32, indicating 32 kbps.

`EOHAAOTN` This can take the values S01, S02, S06 or S07, for AOTs 1, 2, 6 and 7, or S90 to S99 for calibration/post-He observations. This is copied from the field of the same name in the EOHA file for the observation, see the ISO Handbook Volume I, [17] for an explanation of this file.

`EOHAPCAT` indicates the proposal category as entered by the user in PGA. The categories were European GT, NASA GT, ISAS GT, OT or Calibration, and these are coded in `EOHAPCAT` as numbers 1 to 5 respectively. This is copied from the field of the same name in the EOHA file for the observation.

`EOHATTYP` indicates the scientific category as entered by the user in PGA. The categories were Solar System, Interstellar Matter, Stellar Physics, Extragalactic Systems or Cosmology, and these are coded in `EOHATTYP` as numbers 001 to 005 respectively. This is copied from the `EOHASCAT` field in the EOHA file for the observation.

`ATTUTCS` should be close in value to `EOHAUTCS`. If the observation contains micro-slews (e.g. SWS aperture changes) this value will refer to the first pointing.

`ATTOTFTH` is the AOT on target threshold in arcsec. When the pointing is within this accuracy of the target the on target flag is set.

`ATTTYPE` Can be set to 'T' for solar system tracking, 'P' for fine pointing (single target) or 'R' for a raster operation.

Time keys The various time keys, referred to by `TREFUTK`, `TREFITK` and `TREFITKU`, are described in the ISO Handbook Volume I, [17].

`VERSn` indicates the version numbers of the various files used to generate this product.

Table A.1: *ERD primary headers*

Header keyword		Contents		Comment
SIMPLE	=	T	/	file does conform to FITS standard
BITPIX	=	8	/	number of bits per data pixel
NAXIS	=	0	/	number of data axes
EXTEND	=	T	/	FITS dataset may contain extensions
COMMENT	FITS (Flexible Image Transport System) format defined in Astronomy and			
COMMENT	Astrophysics Supplement Series v44/p363, v44/p371, v73/p359, v73/p365.			
COMMENT	Contact the NASA Science Office of Standards and Technology for the			
COMMENT	FITS Definition document #100 and other FITS information.			
ORIGIN	=	'ESA '	/	European Space Agency
TELESCOP	=	'ISO '	/	Infrared Space Observatory
INSTRUME	=	'SWS '	/	Instrument used
COMMENT	SWS Edited Raw Data			
FILENAME	=	'SWER67801301'	/	File name
DATE	=	'2001-12-14'	/	Creation date 2001/348
FILEVERS	=	'2690 '	/	Version ID (derived from creation date)
OLPVERS	=	'OLP_101 '	/	SOC OLP system version
CALGVERS	=	'CALG_71 '	/	SOC OLP CAL-G files version
USERNAME	=	'PIPEPAR'	/	Product not catalogued
VERS1	=	'2518/EOHA678'	/	Version ID of each input file
VERS2	=	'2518/EOHI678'	/	Version ID of each input file
VERS3	=	'1120/APPH678'	/	Version ID of each input file
OBJECT	=	'HR7001 ALPHA-LYR'	/	Target ID as given by proposer
OBSERVER	=	'SWS_CAL '	/	Proposer ID in ISO Mission DB
EQUINOX	=	2000.0	/	Equinox
TMRATE	=	32	/	Telemetry rate in Kbps (Kbits/s)
EOHAUTCS	=	'97266235847'	/	Approx. UTC of start of observation
EOHAUTCE	=	'97267011121'	/	Approx. UTC of end of observation
EOHAAOTN	=	'S06 '	/	AOT name
EOHAPLID	=	'SWS_678 '	/	Proposal ID
EOHAOSN	=	'01 '	/	Observation sequence number

```
EOHAPSN  =                 '00 '  /  Pointing sequence number
EOHAPCAT =                 '5 '   /  Proposal category
EOHACIND =                 ' '    /  Calibration indicator
EOHATTYP =                '001 '  /  Target type
AOTVERS  =              '03.70 '  /  AOT-to-OCT logic version
TREFCOR1 =             275443127  /  UTC of 1st reference time
TREFPHA1 =              678.40749 /  Orbital phase at TREFCOR1
TREFCOR2 =             275445304  /  UTC of 2nd reference time
TREFPHA2 =              678.43275 /  Orbital phase at TREFCOR2
TREFCOR3 =             275447481  /  UTC of 3rd reference time
TREFPHA3 =              678.45801 /  Orbital phase at TREFCOR3
ATTUTCSL =          '97266235519' /  UTC of start time of slew to intended target
ATTUTCS  =          '97266235820' /  UTC of time of first arrival at intended target
ATTOTFTH =                 10.0   /  On-target flag threshold (arc secs)
ATTRA    =              279.23442 /  Intended Right Ascension of instrument viewing
ATTDEC   =              38.78350  /  Intended Declination (with ATTRA)
ATTTYPE  =                 'P '   /  Type of attitude operation (P/R/T)
ATTGUIDE =                101570  /  Guide star reference number
ATTSAANG =                 96.8   /  Solar aspect angle (degrees)
ATTERROR =                    0   /  Contingency flag(0=success; 1=target not acq'd)
TREFUTC1 =             275443127  /  UTC (whole seconds since 01-01-1989)
TREFUTC2 =                951300  /  UTC (remaining fraction of second)
TREFUTK  =            1437003072  /  ISO Uniform Time Key (UTK)
TREFITK  =            1437003072  /  ISO INSTRUMENT Time Key (ITK)
TREFITKU =      0.04166666666667  /  ITK unit length in seconds (= 1/24)
END
```

A.2.1.2 Records

The ERD file contains records (24 per second) with the fields described in Table A.2.

Table A.2: *Records in the ERD file*

Field name	Number	Format	Comment
GPSCTKEY	1	I*4	Instrument time key
GPSCRPID	2	I*1	Raster point ID
GPSCFILL	1	I*2	Filler
SWERDR5	12	I*2	5-micron array readouts
SWERDR10	12	I*2	10-micron array readouts
SWERDR20	12	I*2	20-micron array readouts
SWERDR35	12	I*2	35-micron array readouts
SWERDRFP	4	I*2	FP detector readouts
SWERHK1	1	I*2	SW scanner - actual position (if mode = 0,1)
SWERHK2	1	I*2	SW scanner - LVDT output (if mode = 0,1)
SWERHK3	1	I*2	SW scanner motor current (if mode=1)
SWERHK4	1	I*2	SW scanner DAC output (if mode=1)
SWERHK5	1	I*2	LW scanner - actual position (if mode = 0,2,3)
SWERHK6	1	I*2	LW scanner - LVDT output (if mode = 0,2,3)
SWERHK7	1	I*2	LW scanner motor current (if mode=2)
SWERHK8	1	I*2	LW scanner DAC output (if mode=2)
SWERHK9	1	I*2	Last received internal command (if mode=3)
SWERHK10	1	I*2	Temp. sensor FP cal. source (if mode=3)
SWERHK11	1	I*2	Fabry-Pérot main current
SWERHK12	1	I*2	Fabry-Pérot correction current 1
SWERHK13	1	I*2	Fabry-Pérot correction current 2
SWERSLHK	1	I*2	Slowly commutated Housekeeping (HK)
SWERIRC	1	I*2	Internal readout counter
SWEREXEC	1	I*2	'Execute' flags

Notes:

1. The five SWERDR fields contain the detector readouts, whereas the thirteen SWERHK fields allow the wavelength falling on each detector to be calculated.
2. The two GPSCRPID fields should always contain '1's for SWS, unless a SSO is being tracked.
3. The selection of which of fields SWERHK1 to SWERHK10 contain valid information is mode-dependent. The 'mode' can be 0 (default), 1, 2 or 3. A change in mode implies the start of a new measurement period, and the value of the mode is contained in the corresponding Compact Status field SSTAHKMD. In practice the mode is completely ignored and the only SWERHK information that is used is the actual positions of the scanners: SWERHK1 and SWERHK5.
4. Whereas all other fields repeat at the rate of 24 Hz, SWERSLHK repeats at 0.5 Hz. The meaning of any individual readout depends on the accompanying value of SWERIRC.
5. SWERIRC begins at 1 (for the first readout cycle of a new format), then increments up to 48. It is derived from the 'SWS internal frame counter' and indicates the sequence of information in SWERSLHK.
6. SWEREXEC is extracted from the more significant byte of the SWERIRC. They appear only in ERD records for which SWERIRC is a multiple of 2, as the flags are telemetered at a rate of 12 Hz, and are set to zero for the intervening records. The more significant byte of SWEREXEC is always set to zero, e.g. the sign bit for the flags is not extended.

A.2.2 Compact Status History (CSH)

These files are normally named ssta*.fits.

A.2.2.1 Headers

The CSH files primary header are very much the same as the ERD headers. No new keywords need to be explained.

A.2.2.2 Records

The Compact Status file contains records with the fields described in Table A.3. The records are defined in the binary header of the FITS file.

Table A.3: *Records in the CSH file*

Field name	Number	Format	Comment
CSGPUKST	1	I*4	UTK start time
CSGPUKEN	1	I*4	UTK end time
CSGPIKST	1	I*4	ITK start time
CSGPIKEN	1	I*4	ITK end time
CSGPUTST	2	I*4	UTC start time
CSGPUTEN	2	I*4	UTC end time
CSGPOSN	1	I*1	Observation Sequence Number
CSGPFILL	15	I*1	Spare
SSTASHUT	1	I*2	Shutter position (0=closed, or 1/2/3)
SSTAGAIN	6	I*2	Nominal gain in each of the bands (1/4/16)
SSTACALS[1]	4	I*2	Calibration source status
SSTARESP	2	I*2	Reset interval in frames (SW/LW)
SSTAHKMD	1	I*2	House keeping mode
SSTAFPS	1	I*2	FP selection (1=FP1, 2=FP2)
SSTASPAR	9	I*2	Spare

1. The four elements of SSTACALS are:
   1: Grating calibrator, 2: Flusher, 3: FP calibrator and 4: Diffuse calibrator.
   A zero in a SSTACALS field indicates that the respective calibrator is off. 1 indicates it is on low, 2 that it is on high.

A.3 First Stage of the Pipeline

There are two files in this section: the SWS Standard Processed Data (SPD), and the SWS Glitch History Data.

A.3.1 Standard Processed Data (SPD)

These files are normally named swsp*.fits by the IDA.

A.3.1.1 Headers

The SPD files contain primary headers described in Table A.4. In this table example information is used to fill the header.

Most keywords are self-explanatory, or have been described above. Those that are not are `INSTRA`, `INSTDEC` and `INSTROLL`. These are the instruments pointing direction and roll, and are described in the ISO Handbook Volume I, [17].

Table A.4: *SPD primary headers*

Header keyword		Contents		Comment
SIMPLE	=	T	/	file does conform to FITS standard
BITPIX	=	8	/	number of bits per data pixel
NAXIS	=	0	/	number of data axes
EXTEND	=	T	/	FITS dataset may contain extensions
COMMENT	FITS (Flexible Image Transport System) format defined in Astronomy and			
COMMENT	Astrophysics Supplement Series v44/p363, v44/p371,v73/p359,v73/p365.			
COMMENT	Contact the NASA Science Office of Standards and Technology for the			
COMMENT	FITS Definition document #100 and other FITS formation.			
ORIGIN	=	'ESA '	/	European Space Agency
DATE	=	'2001-12-17'	/	Creation date 2001/351 2001/303
TELESCOP	=	'ISO '	/	Infrared Space Observatory
INSTRUME	=	'SWS '	/	Instrument used
COMMENT	SWS Standard Processed Data			
FILENAME	=	'SWSP62400216'	/	File name
FILEVERS	=	'2693 '	/	Version ID (derived from creation date)
OLPVERS	=	'OLP_101 '	/	SOC OLP system version
CALGVERS	=	'CALG_71 '	/	SOC OLP CAL-G files version
USERNAME	=	'PIPEPAR'	/	Product not catalogued
OBJECT	=	'200400 MARS'	/	Target ID as given by proposer
OBSERVER	=	'TDEGRAAU'	/	Proposer ID in ISO Mission DB
EQUINOX	=	2000.0000	/	Equinox
TMRATE	=	32	/	Telemetry rate in Kbps (Kbits/s)
EOHAUTCS	=	'97212233059'	/	Approx. UTC of start of observation
EOHAUTCE	=	'97213001349'	/	Approx. UTC of end of observation
EOHAAOTN	=	'S06 '	/	AOT name
EOHAPLID	=	'MARS_A '	/	Proposal ID
EOHAOSN	=	'16 '	/	Observation sequence number
EOHAPSN	=	'00 '	/	Pointing sequence number
EOHAPCAT	=	'1 '	/	Proposal category
EOHACIND	=	' '	/	Calibration indicator
EOHATTYP	=	'001 '	/	Target type
ATTUTCSL	=	'97212233032'	/	UTC of start time of slew to intended target
ATTUTCS	=	'97212233041'	/	UTC of time of first arrival at intended target
ATTOTFTH	=	10.000000	/	On-target flag threshold (arc secs)
ATTRA	=	200.20242	/	Intended Right Ascension of instrument viewing
ATTDEC	=	−8.9580800	/	Intended DEClination (with ATTRA)
ATTTYPE	=	'T '	/	Type of attitude operation (P/R/T)
ATTGUIDE	=	72040	/	Guide star reference number
ATTSAANG	=	73.200000	/	Solar aspect angle (degrees)
ATTERROR	=	0	/	CONTINGEncy flag(0=success; 1=target not acq'd)

TREFUTC1	=	270775859	/	UTC (whole seconds since 01-01-1989)
TREFUTC2	=	8492230	/	UTC (remaining fraction of second)
TREFUTK	=	1324988640	/	ISO Uniform Time Key (UTK)
TREFITK	=	1324988640	/	ISO INSTRUMENT Time Key (ITK)
TREFITKU	=	0.041666667	/	ITK unit length in seconds
TREFCOR1	=	270775859	/	UTC of 1st reference time
TREFPHA1	=	624.25378	/	Orbital phase at TREFCOR1
TREFHEL1	=	−146.18	/	Heliocentric correction +(s) at TREFCOR1
TREFDOP1	=	−29.50	/	ISO velocity towards target (km/s) at TREFCOR1
TREFCOR2	=	270777144	/	UTC of 2nd reference time
TREFPHA2	=	624.26868	/	Orbital phase at TREFCOR2
TREFHEL2	=	−146.30	/	Heliocentric correction +(s) at TREFCOR2
TREFDOP2	=	−29.46	/	ISO velocity towards target (km/s) at TREFCOR2
TREFCOR3	=	270778429	/	UTC of 3rd reference time
TREFPHA3	=	624.28359	/	Orbital phase at TREFCOR3
TREFHEL3	=	−146.42	/	Heliocentric correction +(s) at TREFCOR3
TREFDOP3	=	−29.42	/	ISO velocity towards target (km/s) at TREFCOR3
ISRRSEV	=	1	/	RTA maximum severity level = WA
ISRQSEV	=	1	/	QLA maximum severity level = WA
ISRRWARN	=	'OK '	/	RTA warning flag from IS user
ISRNOOSL	=	0	/	No. of out-of-soft-limit errors
ISRNOOHL	=	0	/	No. of out-of-hard-limit errors
ISRNMW	=	0	/	No. of monitor warnings
ISRNCVW	=	0	/	No. of command verification errors
ISRNBTW	=	0	/	No. of bad telemetry errors
ISRNMVW	=	0	/	No. of memory verification errors
ISRNSQLA	=	0	/	No. of severe QLA errors
INSTRA	=	200.20242	/	Reference instrument J2000 right ascension (deg
INSTDEC	=	−8.9580700	/	Reference instrument J2000 declination (deg)
INSTROLL	=	292.04000	/	Reference instrument J2000 roll angle (deg)
CINSTRA	=	200.20250	/	Corrected reference instrument J2000 right asce
CINSTDEC	=	−8.9579100	/	Corrected reference instrument J2000 declinatio
CINSTROL	=	292.04000	/	Corrected reference instrument J2000 roll angle
AOTVERS	=	'03.70 '	/	AOT-to-OCT logic version
VERS4	=	'ssta62400216'	/	Version of each input file
VERS5	=	'gehk62400216'	/	Version of each input file
VERS6	=	'eohi624 '	/	Version of each input file
VERS7	=	'swer62400216'	/	Version of each input file
VERS8	=	'irph62400216'	/	Version of each input file
VERS10	=	'cal04_010.fits'[1]	/	CAL04: isp_drange
VERS11	=	'cal02a_010.fits'	/	CAL02A: isp_midbit
VERS12	=	'cal02_010.fits'	/	CAL02: isp_ac_correction
VERS13	=	'cal03_010.fits'	/	CAL03: isp_ac_correction
VERS14	=	'cal03_010.fits'	/	CAL03: isp_self_pulse
VERS15	=	'cal05_010.fits'	/	CAL05: isp_self_pulse
VERS16	=	'cal06_010.fits'	/	CAL06: isp_self_pulse
VERS17	=	'cal01_010.fits'	/	CAL01: isp_cross_correction
VERS18	=	'cal03_010.fits'	/	CAL03: isp_slope
VERS19	=	'cal05_010.fits'	/	CAL05: isp_slope
VERS20	=	'cal06_010.fits'	/	CAL06: isp_slope
VERS21	=	'calibration_structure'[2]	/	CAL16ET: isp_slope
VERS22	=	'cal03_010.fits'	/	CAL03: isp_wave

```
VERS23          =          'cal16a_011.fits'  /  CAL16A: isp_wave
VERS24          =          'cal16b_010.fits'  /  CAL16B: isp_wave
VERS25          =          'cal16c_010.fits'  /  CAL16C: isp_wave
VERS26          =  'calibration_structure'    /  CAL16ET: isp_wave
VERS27          =          'cal23_011.fits'   /  CAL23: isp_wave
VERS28          =          'cal24_010.fits'   /  CAL24: isp_wave
VERS29          =          'cal12_010.fits'   /  CAL12: isp_fpgap
VERS30          =          'cal18_010.fits'   /  CAL18: isp_fpwave
END
```

Notes:

1. Calibration file can be listed with their complete path.
2. Due to architectural mismatch between VAX-VMS doubles and IEEE doubles the calibration file containing the grating polynome was connected to the OLP system somewhat differently than all other calibration files.

A.3.1.2 Records

The SPD file contains records with the fields described in Table A.5. In the FITS file they are defined in the binary header.

Table A.5: *Records in SPD file*

Field name	Number	Format	Unit	Comment
GPSCTKEY	1	I*4		Instrument time key
GPSCRPID	2	I*1		Raster point ID
GPSCFILL	1	I*2		Filler
SWSPSTAT	1	I*4		Status of this record
SWSPGPOS	2	R*4		Average positions for gratings 1/2
SWSPGANG	2	R*4	degrees	Angles for SW & LW gratings
SWSPFPOS	1	I*4		Position of FP
SWSPFCUR	3	R*4		Average main current for FP coils
SWSPFGAP	2	R*4	μm	Gaps for FP
SWSPWAVE	52	R*4	μm	Detector wavelength
SWSPFLUX	52	R*4	$\mu V/s$	Detector slopes
SWSPOFFS	52	R*4		Number of 24 Hz samples used to calculate the slope
SWSPSTDV	52	R*4	$\mu V/s$	Standard deviation of the detector slope
SWSPFLAG	52	I*4		Flags per detector

Notes:

1. One record is generated every reset interval (1, 2 or 4 seconds).
2. Because SWS has no raster AOTs, the raster point IDs will always be set to 1 except when tracking a Solar System Object.
3. The I*4 status number SWSPSTAT, one per measurement, can be decoded by referring to Table A.6.
4. The I*4 flag number SWSPFLAG, one per detector, can be decoded by referring to Table A.7.

A.3.1.3 Status Word (SWSPSTAT and SWAASTAT)

The meaning of the value of the status word SWSPSTAT and SWAASTAT) is listed in Table A.6. Different bits summed together may represent the status word value.

Table A.6: *Decoding of status word*

Meaning	Bits set 10987654 32109876 54321098 76543210	Value
dark	00000000 00000000 00000000 00000000	0
aperture 1	00000000 00000000 00000000 00000001	1
aperture 2	00000000 00000000 00000000 00000010	2
aperture 3	00000000 00000000 00000000 00000011	3
reset in SW section	00000000 00000000 00000000 00000100	4
reset in LW section	00000000 00000000 00000000 00001000	8
reset all bands	00000000 00000000 00000000 00001100	12
diffuse cal normal	00000000 00000000 00000000 00010000	16
diffuse cal high	00000000 00000000 00000000 00110000	48
fp check normal	00000000 00000000 00000000 01000000	64
fp check high	00000000 00000000 00000000 11000000	192
flusher normal	00000000 00000000 00000001 00000000	256
flusher high	00000000 00000000 00000011 00000000	768
grating check normal	00000000 00000000 00000100 00000000	1024
grating check high	00000000 00000000 00001100 00000000	3072
fp nr 2 active	00000000 00000000 00010000 00000000	4096
band1 requested	00000000 00000000 00100000 00000000	8192
band2 requested	00000000 00000000 01000000 00000000	16384
band3 requested	00000000 00000000 10000000 00000000	32768
band4 requested	00000000 00000001 00000000 00000000	65536
band5 requested	00000000 00000010 00000000 00000000	131072
band6 requested	00000000 00000100 00000000 00000000	262144
fp execute flag	00000000 00001000 00000000 00000000	524288
fp run flag	00000000 00010000 00000000 00000000	1048576
low resolution scan	00000000 00100000 00000000 00000000	2097152
reference scan	00000000 01000000 00000000 00000000	4194304
photometric check	00000000 10000000 00000000 00000000	8388608
defined dark measurement	00000001 00000000 00000000 00000000	16777216
SW grating run flag	00000010 00000000 00000000 00000000	33554432
LW grating run flag	00000100 00000000 00000000 00000000	67108864
SW down scan direction[1]	00001000 00000000 00000000 00000000	134217728
LW down scan direction[1]	00010000 00000000 00000000 00000000	268435456

Notes:

1. If the run flag is set and the down flag is *not* set, the scanner is moving in the up direction.

A.3.1.4 Flag Word (SWSPFLAG and SWAAFLAG)

The meaning of the value of the flag word SWSPFLAG and SWAAFLAG) is listed in Table A.7. Different bits summed together may represent the flag word value.

Table A.7: *Decoding of flag*

Meaning	Bits set	Value
No glitch	00000000000	0
1 glitch	00000000001	1
2 glitches	00000000010	2
3 glitches	00000000011	3
Partly Out of limit	00000000100	4
Totally Out of limit	00000001000	8
No data	00000010000	16
Order 1	00000100000	32
Order 2	00001000000	64
Order 3	00001100000	96
Order 4	00010000000	128
Multiple orders (confused)	00011100000	224
Gain bit 1 = gain 1	01000000000	512
Gain bit 2 = gain 4	10000000000	1024
Gain bit 3 = gain 16	11000000000	1536

Notes:

1. No order flag set indicates no order could be calculated for the data.
2. Bit number 31 (value 2^{30}) is used to flag (user selected) suspicious data in post-AAR processing.

A.3.2 SWS Glitch History Data

This product has been produced from OLP Version 5, with the files named swgh*.fits.

A.3.2.1 Headers

The SWGH files contain primary headers described in Table A.8, filled with example information. Most keywords are self-explanatory, or have been described before.

Table A.8: *SWGH primary headers*

Header keyword		Contents		Comment
SIMPLE	=	T	/	
BITPIX	=	8	/	
NAXIS	=	0	/	
EXTEND	=	T	/	
ORIGIN	=	'ESA '	/	European Space Agency
DATE	=	'2001-12-17'	/	Date of writing: YYYY-MM-DD
TELESCOP	=	'ISO '	/	Infrared Space Observatory
INSTRUME	=	'SWS '	/	Instrument used

```
COMMENT         SWS Glitch History Data
FILENAME        =    'SWGH62400216'   /   File name
FILEVERS        =                ' '  /   Version ID in ISO archive
OLPVERS         =          'OLP-101 '  /   SOC OLP system version
USERNAME        =                ' '  /   Unofficial data product
CALGVERS        =          'CALG_71 '  /   SOC OLP system version
END
```

A.3.2.2 Records

The SWGH file contains records with the fields described in Table A.9.

Table A.9: *Records in the SWGH file*

Field name	Number	Format	Unit	Comment
GPSCTKEY	1	I*4		Instrument time key
SAMPLES1	52	I*2		1st Sample start
SAMPLEE1	52	I*2		1st Sample end
HEIGHT1	52	R*4	bits[1]	1st Sample height
SAMPLES2	52	I*2		2nd Sample start
SAMPLEE2	52	I*2		2nd Sample end
HEIGHT2	52	R*4	bits[1]	2nd Sample height
GLNUMBER	52	I*2		Total glitches

Notes:

1. Bits can have values between 0 and 4095.

A.4 Second Stage of the Pipeline

There is one file in this section, the SWS Auto-Analysis Results file.

A.4.1 Auto-Analysis Results (AAR)

A.4.1.1 Headers

The AAR files, normally named swaa*.fits by the IDA, contain primary headers, very much the same as those of the SPD-files with some obvious exceptions and some more calibration files listed. See Section A.3.1. No example of an AAR-header is presented here.

A.4.1.2 Records

The AAR file contains records with the fields described in Table A.10. In the FITS file they are defined in the binary header.

Table A.10: *Records in the AAR file*

Field name	Number	Format	Unit	Comment
SWAAWAVE	1	R*4	μm	Wavelength of data point
SWAAFLUX	1	R*4	Jy	Flux
SWAASTDV	1	R*4	$\mu V/s$	Standard deviation of the slope
SWAATINT[1]	1	I*4	samples	Number of samples used
SWAADETN	1	I*4		detector number
SWAAITK	1	I*4		SWS instrument time key
SWAAUTK	1	I*4		ISO uniform time key
SWAARPID[2]	2	I*1		raster point id
SWAASPAR[3]	2	I*1		Contains error information
SWAALINE[4]	1	I*4		line number
SWAASDIR[5]	1	I*4		scan direction
SWAASCNT[4]	1	I*4		scan number
SWAASTAT[6]	1	I*4		status word
SWAAFLAG[7]	1	I*4		flag word

Notes:

1. SWAATINT is the total number of 1/24 second samples used in the calculation of the flux of this data point.
2. SWAARPID, the raster point id, is copied over from the GPSCRPID in the SPD. As SWS has no raster AOTs it is always (1,1) (unless a Solar System Object is being tracked), but is included so that the format of SWS AAR is compatible with LWS AAR.
3. These two bytes contain the error information described in Section 7.4.
4. Section A.4.1.3 discusses SWAALINE and SWAASCNT.
5. SWAASDIR is used to identify if the data point is from an up-scan (1) or a down scan (-1). 0 is undefined (and do not use the data). See Section 3.2.1 for a definition of up-down scans.
6. SWAASTAT is copied over from SWSPSTAT. For a description of this see Table A.6.
7. SWAAFLAG is copied over from SWSPFLAG. For a description of this see Table A.7.

A.4.1.3 SWAALINE and SWAASCNT

SWAALINE and SWAASCNT are both counts of the valid data present in an AAR. All valid data means data that are flagged as 'Data', with the 'SW', 'LW' or 'FP' runflags set but without being flagged simultaneously as 'darkcurrent', 'photometric check'. Additionally the data should have a valid order assigned.

SWAALINE is a count of the valid ranges in a dataset. For SWS01, it is filled with the band number (see Table 2.1). For an SWS02 observing X lines it will count from 1 to X, with 0 reserved for any datapoints not associated with a line. Note that the datapoints associated with SWAALINE set to, e.g. 1, may not correspond to the first entered line number in your AOT as the logic may re-arrange them to increase efficiency. For SWS06 it effectively counts the number of scans, including reference checks etc. For an example see Table A.11.

SWAASCNT has nothing to do with the number of scans required for an AOT. It is a count of the number of lines/bands containing requested (i.e. what was requested in the AOT) data, starting with 1. Any data outside the requested ranges will have SWAASCNT set to 0. Note that even if SWAASCNT is greater than 0, the flag and status word should be checked to ensure the data is okay. For SWS01 SWAASCNT is filled with 1.

The decision whether to increment SWAALINE or SWAASCNT depends on whether a scan starts and ends at the same grating position as the preceding scan. Initially both are set to one. If a scan starts and ends at

Table A.11: *Line number against detector band*

Operation	line number for detector band			
	1	2	3	4
REF	1	2	3	4
SCAN UP	5	6	7	8
REF	9	10	11	12
SCAN DOWN	13	14	15	16
REF	17	18	19	20
.	.	.	.	.

Note that this is an example of an 'old' (pre mid-1997) SWS06 and that the scans may be different for a different SWS06 operation.

the same grating position as the preceding scan the line counter is not incremented but the scan counter is. If the wavelength range is different the line counter is incremented and the scan counter is (re-)set to one. Users should note that this effectively results in a difference in the behaviour of `SWAALINE` for SWS02's and 6's. For SWS02 there is one value per each up-down pair, whereas for an SWS06 there is one value per individual up- or down-scan.

A.5 Calibration-G Files

An overview of all calibration files present in either the IDPD or in the OSIA system, is given. For each of these files there can be several versions, one for each phase in the mission. Which version is used to process a dataset is defined in the STIMEDEP file.

Table A.12: *SWS Cal-G files*

archive	name	use[1]	Description
SC01	Cal-G 1	S	Electrical cross-talk matrices
SC02	Cal-G 2	S	RC correction time scales
SC02A	Cal-G 2A	S	'Midbit' values
SC02B	Cal-G 2B	SO	Pulse-shape correction values
SC03	Cal-G 3	S	Reset cutout lengths
SC04	Cal-G 4	S	Data range limits
SC05	Cal-G 5	S	Switchable gains
SC06	Cal-G 6	S	Glitch reject levels
SC07	Cal-G 7	C	Grating detector noise characteristics
SC08	Cal-G 8	C	Grating calibration spectrum
SC09	Cal-G 9	CO	LVDT-Angle relation
SC10	Cal-G 10	O	Key wavelengths
SC11	Cal-G 11	C	FP calibration spectrum
SC12	Cal-G 12	S	Gap-position relation
SC13	Cal-G 13	C	Key wavelength and passbands
SC14	Cal-G 14	CO	Intensity of internal calibration sources
SC15	Cal-G 15	CO	maximum allowable shift in wavelength
SC16A	Cal-G 16A	S	Aperture offsets
SC16B	Cal-G 16B	S	Detector offsets

SC16C	Cal-G 16C	S	Grating constants
SC16D	Cal-G 16D	C	Telescope area
SC16E	Cal-G 16E	SO	Scanner curve coefficients
SC16ET	Cal-G 16ET	S	Scanner curve coefficients as function of time
SC18	Cal-G 18	S	Effective gap correction
SC19	Cal-G 19	A	SWS01 resolution factors
SC20	Cal-G 20	C	Relative detector responsivity
SC21_n[2]	Cal-G 21_n	A	Detector dark current/noise for reset interval of n sec
SC22	Cal-G 22	C	Detector response to internal diffuse source and flusher
SC23	Cal-G 23	SA	Wave limits for bands
SC24	Cal-G 24	SA	Wave limits for apertures
SC25_xx[3]	Cal-G 25_xx	A	Spectral responsivity for band xx - RSRF file
SC35_xx[3]	Cal-G 35_xx	I	Beam profile (fine grid) for band xx
SC36_xx[3]	Cal-G 36_xx	I	Beam profile (coarse grid) for band xx
SC40	Cal-G 40	U	Scanner stops
SC41	Cal-G 41	A	Average shape of flux calibration sources
SC42	Cal-G 42	A	Signal to flux conversion
SC43	Cal-G 43	A	Flat-fielding parameters
STIMEDEP		All	Time dependency file

Notes:

1. The use-column indicates the primary usage of the calibration file:

   A DAAR.

   C Calibration or trend analysis procedures.

   I OSIA.

   O Obsolete, not in use any more or maybe never was...

   S DSPD.

   U Uplink purposes.

   All these calibration files are present in OSIA, except for Cal-G 10 which has been replaced by Cal-G 13. As such they can all be used in OSIA.

2. Possible reset intervals are 1, 2, 4 and 8 seconds.
3. xx indicates one of the bands: 1A, 1B, 1D, 1E, 2A, 2B, 2C, 3A, 3C, 3D, 3E, 4A, 4C, 4D, 4, 5A, 5B, 5C, 5D or 6. The offband (4A, 4C, 4D) beam profiles are not available.

Not all of these calibration files are actually used in the OLP. Some of them were only for calibration purposes, like Cal-G 8 and Cal-G 16D. Others have become obsolete in the course of the mission, like Cal-G 2B and Cal-G 16E.

In all cases the ISO Data Product Document, [34] should be referred to for the exact file layout. The files are given the names 'SCNN_XXX.FITS' in the archive, where 'NN' denotes the calibration file number, like '01', '02A', '25_3C' etc, and 'XXX' denotes the version number of that file (different versions may be used for different revolutions as already mentioned), and can be '010', '021' etc.

A.5.1 SWS Cal-G 1 Electrical Cross-talk Matrices

This file is used in Derive-SPD to correct for the effects of electrical cross-talk (see Section 7.2.7).

The file contains 12 records, each 52 integers in length. The first 12 numbers in each record contain the cross-talk for band 1, the next 12 for band 2 etc. Record 1 contains the cross-talk between detector 1 in each band and the other detectors in that band, record 2 contains the cross-talk between detector 2 in each band and the other detectors in that band, etc. Only records 1 and 2 contain information for bands 5 and 6 (the FP bands with only 2 detectors in each).

A.5.2 SWS Cal-G 2 RC Correction Time scales

This file, used in Derive-SPD, contains the time constants for the high pass filter in the amplifier chain (see Section 7.2.5). It contains 52 numbers, the time scales per detectors in seconds.

A.5.3 SWS Cal-G 2A 'Midbit' Values

This file, used in Derive-SPD, contains the 'midbit' value for each detector (see Section 7.2.3). The detector readouts are between 0 and 4095 (bits) corresponding to -10 to $+10$ Volts. The 'midbit' is the bit value that corresponds to 0 Volts, approximately 2048, and is different for each detector.

Currently this calibration file is filled with 2047.50.

A.5.4 SWS Cal-G 2B Pulse-Shape Correction Values

This is an obsolete calibration file. The pulse shapes are never constant. Consequently they could not be caught into a single calibration file. Since OLP 9 they are corrected for each observation individually. See Section 7.2.6.

A.5.5 SWS Cal-G 3 Reset Cutout Lengths

This file, used in Derive-SPD, contains the number of 24Hz readouts to ignore after a reset (short circuit of the capacitor) (see Section 7.2.2). It contains 52 numbers, one number per detector.

A.5.6 SWS Cal-G 4 Valid Data Range Limits

This file, used in Derive-SPD, contains the limits of the digital data range (see Section 7.2.2). There are 52 records, each of which contains the minimum and maximum values (in bits between 0 and 4095) for the three gains.

A.5.7 SWS Cal-G 5 Switchable Gains

This file, used in Derive-SPD, contains the actual gain applied to the signal before AD-conversion (see Section 7.2.10). There are 52 records, one per detector. Each record contains three numbers, one for each gain.

A.5.8 SWS Cal-G 6 Glitch Reject Levels

This file, used in Derive-SPD, contains information used to recognise glitches and reject them (see Section 7.2.8). It contains 52 records, one per detector. Each record contains four numbers: α, the signal-to-noise level above which a point is marked as a glitch; the number of readouts to ignore before and after a glitch; and the minimum noise level in the signal. In the glitch detection algorithm of OLP v10 only the α-number and the minimum noise is used. See Section 7.2.8.

A.5.9 SWS Cal-G 7 Noise Characteristics

For each of the 6 SWS bands noise characteristics are given, split in 3 items: read-noise, dc-noise and signal noise.

A.5.10 SWS Cal-G 8 Grating Calibration Spectrum (high)

Lists for each of the 48 grating detector elements the measured LVDT, the intensity (μV/s) and the wavelength of the peaks produced by the grating calibrator source, with the source intensity HIGH for all bands. This file was used for regular updates of the grating polynome in the SW section resulting in updates for Cal-G 16E and Cal-G 16ET. For the LW section Cal-G 8a was used.

A.5.11 SWS Cal-G 8A Grating Calibration Spectrum (low)

Lists for each of the 48 grating detector elements the measured LVDT, the intensity (μV/s) and the wavelength of the peaks produced by the grating calibrator source, with the source intensity LOW for all bands. This file was used for regular updates of the grating polynome in the LW section resulting in updates for Cal-G 16E and Cal-G 16ET. For the SW section Cal-G 8 was used. The SW section (dets 1 to 24) of Cal-G 8A is still filled with data from an outdated version of Cal-G 8.

A.5.12 SWS Cal-G 9 LVDT-Angle Relation

This file lists the relation between LVDT and the grating angle, both for the SW and the LW sections. It is not in use any more. It is replaced by the grating polynome using values from Cal-G 16ET.

A.5.13 SWS Cal-G 10 Key Wavelengths

This file should list the key wavelengths for each of the bands. It has been replaced by Cal-G 13. The file is not present in the archive.

A.5.14 SWS Cal-G 11 FP Calibration Spectrum

This file contains the fixed FP transmission peak wavelengths for the FM. These peaks are used as reference during the FP wavelength calibration. The peak wavelengths are determined at high accuracy in the laboratory by a Fourier Transform Spectrometer.

A.5.15 SWS Cal-G 12 Gap-Position Relation

This file, used in Derive-SPD, contains information on the gap, current and position relationship of the two FPs (see Sections 7.2.11.2 and 4). Each record contains the FP position (a number calculated from slow housekeeping data) applicable to both FPs, and for each FP the size of the gap. It also contains the main current and two correction currents pertaining to the FP position, but these are not used as the FP position is not obtained from the FP currents.

A.5.16 SWS Cal-G 13 Key Wavelengths

This file is used in Auto-Analysis for determining key wavelengths and passbands e.g. when normalising the RSRF. There is one row per key wavelength. Each row has the name of the band, the key wavelength, two numbers defining the passband used.

It contains more information which was used in previous versions of the OLP for the flux calibration. These numbers have been replace by information from Cal-G 42. This extra information consists of conversion numbers for each detector in that band (by default 12, with 10 blank for FP bands) in μV/s/Jy, 12 internal calibration signals (in μV/s), 12 relative flux calibrations (in Jy), errors on the conversion numbers (in μV/s/Jy), errors on the internal calibrations (in μV/s), errors on the relative flux calibrations (Jy) and finally the grating start and end position.

A.5.17 SWS Cal-G 14 Intensity of Calibration Sources

The intensity for each of the calibration sources (in both settings, low and high) is given at a specified wavelength. This calibration file has never been in actual use. The file is not available within IA.

A.5.18 SWS Cal-G 15 Maximum Allowable Wavelength Shift

For the grating and the FP the maximum wavelength shift is given which is permitted for an observation. This calibration file was never in actual use as the wavelengths were very stable from observation to observation. The file is not available within IA.

A.5.19 SWS Cal-G 16A Aperture Offsets

This file, used in Derive-SPD, contains the angles, in degrees, from the optical axis to the entrance or calibration source used, as seen from the SW and LW collimators (see Section 7.2.11.1).

A.5.20 SWS Cal-G 16B Detector Offsets

This file, used in Derive-SPD, contains the angles, in degrees, from the optical axis to each of the detectors (see Section 7.2.11.1).

A.5.21 SWS Cal-G 16C Grating Constants

This file, used in Derive-SPD, contains two grating constants, in μm, for the SW and LW gratings (see Section 7.2.11.1).

A.5.22 SWS Cal-G 16D Telescope Area

This file contains the size of the telescope area, in m^2. It is nowhere used in the data processing.

A.5.23 SWS Cal-G 16E Scanner Curve Coefficients

This file contains the scanner curve coefficients derived at several time intervals during the mission. It is not used anymore in Derive-SPD, where it has been replaced by Cal-G 16ET (see Section 4).

A.5.24 SWS Cal-G 16ET Scanner Curve Coefficients

This contains the scanner curve coefficients needed to transform the LVDT values into incidence angles. The values are presented at a number of intervals suited for linear interpolation in time within Derive-SPD (see Section 7.2.11.1).

A.5.25 SWS Cal-G 18 Effective Gap Correction

This file, used in Derive-SPD, contains information of the effective gap correction. For each possible FP wavelength there is a gap correction for each of the two FPs. All units are μm.

A.5.26 SWS Cal-G 19 SWS01 Resolution Factors

Cal-G 19 is used in the processing of all speed SWS01s. It contains the factors needed to smooth the RSRFs of each band down to the spectral resolution of the SWS01 being processed and hence match the resolutions.

A.5.27 SWS Cal-G 21_n Detector Dark Current/Noise for n sec Reset

These 4 files, Cal-G 21_1, Cal-G 21_2, Cal-G 21_4 and Cal-G 21_8 contain information on the dark current. There is one file per reset interval. Each file contains 52 records, each containing the detector number, the average measured dark current (from ground and PV phase tests), the noise in the dark current and finally the minimum and maximum valid dark currents. Dark currents are measured in μV/s. They are used in Derive-AAR to check whether the observed dark currents are within the bounds. If not a warning is issued (and subsequently completely ignored).

A.5.28 SWS Cal-G 23 Wavelength Limits for Bands

This file, used in Derive-SPD, contains information on the wavelength limits for the six detector bands. There is one row for each band, and each row contains the lower and upper wavelength limits in μm. See also the next entry, Cal-G 24.

A.5.29 SWS Cal-G 24 Wavelength Limits for Apertures

This file, used in Derive-SPD, contains information on the wavelength limits for the three apertures. There are five rows, one row for each aperture plus two for calibrators, and each row contains the lower and upper limit wavelength limit for the two subsystems, in μm. Together with Cal-G 23 they determine which order is seen for all grating settings by each of the bands, essentially which band is seen.

A.5.30 SWS Cal-G 25_xx Spectral Responsivity for Band xx

These files, Cal-G 25_1A, Cal-G 25_1B, Cal-G 25_1D, Cal-G 25_1E, Cal-G 25_2A, Cal-G 25_2B, Cal-G 25_2C, Cal-G 25_3A, Cal-G 25_3C, Cal-G 25_3D, Cal-G 25_3E, Cal-G 25_4, Cal-G 25_4a, Cal-G 25_4c, Cal-G 25_4d, Cal-G 25_5A, Cal-G 25_5B, Cal-G 25_5C, Cal-G 25_5D and Cal-G 25_6, contain the spectral responsivity information (RSRF) for each band.

Each is composed of the number of detectors in that band (twelve for grating, two for the FP files Cal-G 25_5x and 25_6) times three numbers. These are the wavelengths at which the responsivity is measured (in μm), the responsivity and the error on it, both in $\mu V/sec/Jy$.

Files Cal-G 25_4A, Cal-G 25_4B and Cal-G 25_4C are used for off-band data. They are not in the OLP products but can only be reached with OSIA.

A.5.31 SWS Cal-G 35_xx Fine Beam Profile for Band xx

These files, Cal-G 35_1A, Cal-G 35_1B, Cal-G 35_1D, Cal-G 35_1E, Cal-G 35_2A, Cal-G 35_2B, Cal-G 35_2C, Cal-G 35_3A, Cal-G 35_3C, Cal-G 35_3D, Cal-G 35_3E, Cal-G 35_4, Cal-G 35_5A, Cal-G 35_5B, Cal-G 35_5C, Cal-G 35_5D and Cal-G 35_6, contain the beam profile information for pointing and jitter correction. There is one file for each of the bands. The beam profile is given at a sampling of 0.1 arcsec in the y-axis (cross dispersion) and z-axis (dispersion) for the key wavelength over an area of $\pm$10 arcsec. In some bands the beam profile is given at two key wavelengths.

A.5.32 SWS Cal-G 36_xx Coarse Beam Profile for Band xx

These files, Cal-G 36_1A, Cal-G 36_1B, Cal-G 36_1D, Cal-G 36_1E, Cal-G 36_2A, Cal-G 36_2B, Cal-G 36_2C, Cal-G 36_3A, Cal-G 36_3C, Cal-G 36_3D, Cal-G 36_3E, Cal-G 36_4, Cal-G 36_5A, Cal-G 36_5B, Cal-G 36_5C, Cal-G 36_5D and Cal-G 36_6, contain beam profile information for extended source flux correction information. There is one file for each of the bands. The beam profile is given at a sampling of 1 arcsec in the y-axis (cross dispersion) and z-axis (dispersion) for the key wavelength over an area of $\pm$6 arcmin. In some bands the beam profile is given at two key wavelengths.

A.5.33 SWS Cal-G 40 Scanner Stops

Cal-G 40 contains the extreme positions in LVDT for both scanners. It was used for deriving uplink tables for SWS01 observations, and also to monitor the instrument. It has no use in data processing.

A.5.34 SWS Cal-G 41 Shape of Calibration Source

Cal-G 41 contains for every detector the average flux at each of the 22 grating positions that were used during a photometric check. These fluxes are compared bandwise with the observed fluxes to determine the relative sensitivity of the band. See Section 7.3.5.2.

A.5.35 SWS Cal-G 42 Converting Signal to Flux

This contains the factors used in converting from signal, in μV/s, to flux, in Jy. The errors in the flux conversion are also stated. It is used in the flux calibration stage, see Section 7.3.5.3.

A.5.36 SWS Cal-G 43 Flat-Fielding

Cal-G 43 contains the flat-fielding factors for all detectors within each of the bands. Flat-field errors are also given. It used in pipeline Section 7.3.5.1.

A.5.37 STIMEDEP Time Dependency File

The Time Dependency file defines which version of the Cal-G files is used to process an observation. It lists the file (or files) which are valid for what observations.

Appendix B

List of Calibration Concerns

This appendix tries to list for different kind of observations, what kind of problematic areas there might be and it points to the relevant sections. It is certainly not a complete list. Most common concerns are addressed.

Table B.1: *List of calibration concerns*

Observing	Concern	Section
Band 1 in SWS06	Fringes	9.7
Band 2	Memory effects	9.2.1
	Fringes	9.7
	RSRF artifacts	5.4.5.1
Band 3	Fringes	9.7
	Leakage in 3D	5.4.5.3
Band 4	Memory effects	9.2.2
	Glitches + tails	9.2.4
	RSRF	5.4.5.4
FP bands	Memory effects	9.2.2
	Glitches + tails	9.2.4
	Diffraction loss	5.4.7.1
	Order leakage	5.4.7.2
extended source	band-border discontinuity	9.4
	RSRF (for point sources)	5.4
Low flux	Detector jumps	9.3
	Dark current	5.4.5.5
High flux	Saturation & de-biasing	2.4.2
Line flux	Fringes	9.7
All	Pointing, loss of flux	8.6
	—, band borders	5.9.1.4
	—, fringes	8.6.2

Appendix C

Uplink History

C.1 Summary of Uplink Changes

This appendix gives details of any changes to the uplink software used to control the instrument. A list of changes is given in Table C.1 with a more complete explanation given below.

Table C.1: *SWS uplink history*

Uplink system	Revolution	SPR/SCREW	Comment
21.3	36+	SPR 1383	band 3 bias reduced from setting 4 to 2.
21.5	40+	-	more accurate wavelengths in uplink tables.
21.6	44+	-	more accurate wavelengths in uplink tables.
22.0	60+	SCREW 116	uplink time overhead reduced.
22.3	64+	SCREW 144	exact match of up and down scans in SWS01.
		SCREW 145	more precise control of the run flags at the end of a down scan.
		-	improved system sensitivities and noise parameters.
		-	scan ranges in SWS01 adjusted.
		-	less frequent photometric checks.
		-	hi-level photometric checks no longer used.
		-	3E transition moved from 28 to 27.5.
22.6	71+	-	intervals between photo checks increased.
		-	intervals between ref scans increased.
		-	scan lengths in AOT1 50 instead of 40 steps.
23.1	71+	-	better FP gap calibration.
??	78+	-	band 3 bias reduced to setting 1.
23.7	101+	SCREW 169	dark currents measured in activation.
24.0	103+	SCREW 162	maximum reset of 4 seconds allowed for band 1.
		SCREW 163	longer darks in SWS01.
		SCREW 164	disabling of reference scans in AOTs 6 and 7.
		SCREW 165	wavelength-dependent FP gap width.
		SCREW 166	FP scan repetition rate minimally 3.
		SCREW 167	avoid breaking up short FP-scans.
25.1	150+	SPR 1689	more accurate FP control table.
		SPR 1691	more ref scans for band 3.
28.0	191+	SCREW 188	grating tracking also for short FP scans.

		SCREW 189	further suppression of unnecessary ref scans in SWS07
		SCREW 190	make sure that all scans are followed by proper dark measurements.
		SCREW 191	delay photo checks as much as possible within the AOTs.
		SPR 1548	improved FP velocity correction.
		SPR 1787	band 1 edge moved from 4.05 to 4.08 μm.
29.0	161, 237+	SCREW 187	acknowledge misalignment of bands 6 and 4.
30.0	336+	SCREW 232	replace very slow scans in AOTs 6 and 7 by repeated faster scans.
33.2	584, 590+	SPR 2307	ref scans in AOTs 6 and 7 finally disabled.

C.2 From Revolution 36 (Early in the PV Phase)

Reduction of the bias for the band 3 detectors from 3.0 V to 2.25 V. This was done to cope with radiation damage in the BIBIB detectors (further reduction in revolution 78). This was a major change, essential for optimal sensitivity.

C.3 From Revolution 40

Improved wavelength accuracy in the uplink tables.

C.4 From Revolution 44

Again, improved wavelength accuracy in the uplink tables.

C.5 From Revolution 60

Slightly less time lost between ICSes.

C.6 From Revolution 64 (Late in the PV Phase)

1. Scan ranges in SWS01 adjusted, to increase the overlap and to optimise redundant coverage.
2. Dark-current measurements made longer, to improve the measurements.
3. Level-high photometric checks deleted, to avoid upsetting band 2, band 4 and FP detectors. This makes the checks useless for band 1, but that band is as stable as the internal calibrator source. The effect is better initial detector behaviour in AOTs executed immediately after another SWS AOT.
4. Reduced frequency of photometric checks, giving marginally better data quality in bands 2, 4, 5 and 6.
5. Fewer reference scans in SWS06, again giving marginally better data quality.
6. Resets limited to 1 or 2 seconds (instead of 1, 2, 4 or 8 seconds). In orbit, reset intervals of 2 seconds give the highest sensitivity, at least in bands 2-6. Longer intervals catch too many particle glitches.
7. Band limits of 3D, 3E and 4 adjusted, to minimise leakage from the second-order spectrum.

C.7 From Revolution 71 (End of PV Phase)

1. Intervals between photometric checks and between reference scans in SWS06 adjusted. This leads to fewer breaks in AOT 6 scans.
2. AOT 2 scan length increased from 40 to 50 steps, giving better baselines.
3. Better FP gap calibration, resulting in a better matching between grating and FP control. Should reduce tuning jitter in FP scans.

C.8 From Revolution 78[1]

Further reduction of the bias for the band 3 detectors now to 1.8 V, to cope with radiation damage in the BIBIB detectors (first reduction in revolution 36). This is a major change, essential for optimal sensitivity.

C.9 From Revolution 101

Dark currents measured during activation, to allow trend analysis on band 3 damage.

C.10 From Revolution 103

1. Reset intervals of 4 seconds allowed for band 1 detectors. This occasionally gives better sensitivity.
2. Further change to longer dark-current measurements. This gives better baselines for some cases.
3. Reference scans bracketing short scans suppressed in SWS06. This gives higher observing efficiency for some cases.
4. FP minimum scan repetition changed from 2 to 3-fold giving more redundancy.
5. Wavelength-dependent FP gap correction giving improved tracking between FP and grating, especially at shorter wavelengths. Worth mentioning

C.11 From Revolution 150

Spacing between reference scans in band 3 in SWS06 was reduced from 8000 sec (effectively disabling reference scans) to 1000 sec. The purpose was to monitor baseline changes during long scans, to alleviate fringing problems. These reference scans were disabled again from revolution 590. The effect of this was detrimental in some cases, potentially helpful in some other cases (but only for users willing to use OSIA, since reference scans are treated as normal data by the pipeline).

C.12 From Revolution 191

1. The transition from band 1 to band 2 moved from 4.05 μm (Bracket-α) to 4.08 μm. This significantly improved measurements of Bracket-α.

[1] No records of these changes could be found in the SOC files.

2. Dark-current measurements now follow all grating scans Previously only the dark measurement preceding a grating scan was guaranteed to be performed. This was a significant improvement, especially in AOTs 1 and 6.

3. Photometric checks delayed, to prevent detector memory effects from these measurements. This gave somewhat better data in some cases.

4. Velocity correction for FP measurements amended, giving better centring of AOT 7 line observations, but no effect on data interpretation.

5. Improved precision in the FP calibration tables, giving significantly better tracking between grating and FP.

6. Switch to spectral order 4 in FP measurements below 12.2 μm. The effect of this was to give better grating resolution and less leakage.

7. Grating tracking introduced also for the shortest FP scans, significantly improved tracking for short scans.

C.13 From Revolution 237

Aperture 4 introduced for the FP band 6. This gave better pointing for band 6 observations, but no simultaneous band 2 grating observations.

C.14 From Revolution 336

In AOTs 2, 6 and 7 very slow scans are replaced by repeated scans at normal rates, giving more redundancy and fewer baseline problems.

C.15 From Revolution 590

Reference scans effectively disabled in SWS06. This was a final acknowledgement that reference scans do not improve any measurement.

Appendix D

List of Acronyms and Symbols

This appendix lists acronyms and symbols specific to SWS in Tables D.1 and D.2. For a more general list of acronyms we refer to the ISO Handbook Volume I.

Table D.1: *List of acronyms*

acronym	Description
AA	Auto Analysis – software used to process data, see Section 7.3
AAR	Auto Analysis Result file - output of AA, defined in Section A.4.1
AIT	Assembly and Integration Tests
AIV	Assembly and Integration Verification
AOT	Astronomical Observation Template – see Chapter 3
CAM	ISO Camera – one of the four instruments on board ISO
CoCo	Configuration Control
CSH	Compact Status History file, defined in Section A.2.2
CUS	Calibration Uplink System
DAAR/Derive-AAR	The OLP stage that processes SPD data to the AAR level. See Section 7.3
DIDAC	Dutch ISO Data Analysis Centre at SRON in the Netherlands
DSPD/Derive-SPD	The OLP stage that processes ERD data to the SPD level. See Section 7.2
EMC	Electro-Magnetic Compatibility
EOHA	Executed Observation History per AOT (CHECK)
EOHI	Executed Observation History per ICS
ERD	Edited Raw Data – raw data from the satellite, defined in Section A.2.1
FITS	Flexible Image Transport System
FM	Flight Model (of SWS)
FPG	Focal Plane Geometry
FS	Fouks-Schubert transient model
FWHM	Full Width at Half Maximum
FP	Fabry-Pérot Spectrometer
FPU	Focal Plane Unit
GEHK	General House Keeping
IA/SIA	Interactive Analysis – a software package to analyse SWS data
ICS	Instrument Command Sequence
IDA	ISO Data Archive – the legacy archive in VILSPA, Spain
IDPD	ISO Data Product Document – see [34]
IDT	Instrument Dedicated Team

ILT	Instrument Level Test (SWS laboratory test)
IRPH	Instrument Reference Pointing History
ISAP	ISO Spectral Analysis Package
ISO	Infrared Space Observatory – home of SWS, LWS, CAM and PHOT
ISOSDC	ISO Spectrometer Data Centre at MPE, Garching (Germany)
ITK	Instrument Time Key – see the ISO Handbook Volume I for a description of this key
JFET	Junction Field Effect Transistor
LW	Long Wavelength section of SWS
LWS	ISO Long Wavelength Spectrometer – one of the four instruments on board ISO
LVDT	A measure of the angle of the scan mirror for the gratings. It is given the term 'LVDT' as this angle is measured by a Linear Voltage Differential Transducer
OLP	Off-Line Processing – the pipeline, also known as SPG
OSIA	Observers SWS Interactive Analysis – IA without the specific calibration parts
PA	Product Assurance
PHT/PHOT	ISO Photo-polarimeter – one of the four instruments on board ISO
QLA	Quick Look Analysis – a quick assessment carried out on the data
PV	Performance Verification – Early phase in the mission
RC	Resistor-Capacitance circuit responsible for curvature in the integration ramps
RSRF	Relative Spectral Response Function
RTA	Real Time Assessment – a quick assessment carried out on the data
SED	Spectral Energy Distribution
SIDT	SWS Instrument Dedicated Team
SNR	Signal-to-Noise Ratio
SOC	Science Operations Centre (Villafranca)
SPD	Standard Processed Data file – output of DSPD, defined in Section A.3.1
SPG	Standard Product Generation – the pipeline, also known as OLP
SPOPS	SWS Post-Operations
SSO	Solar System Object.
SW	Short Wavelength section of SWS
SWGH	SWS Glitch History Data file – output of DSPD, defined in Section A.3.2
SWS	ISO Short Wavelength Spectrometer – one of the four instruments on board ISO
TDATA	Transparent Data
TDF	Telemetry Distribution Format
TDT	Target Dedicated Time
UTK	Uniform Time Key – see ISO Handbook Volume I for a description of this key
ZLF	Zero Level Function in FS model

Table D.2: List of symbols

symbol	Description
α	Memory factor in FS transient model (μV/s)
β	Instantaneous gain in FS transient model
	Angle between optical axis and aperture (degree)
C	Cross talk matrix
	Covariance matrix
χ^2	Quadratic misfit between model and data
d	Fabry-Pérot gap width
D	Grating constants (lines/mm)
D_k	Data samples, measured readouts from the ERD. (bits)
δ	Angle between optical axis and detector (degree)
Δt	Time interval (s)
F	Flux density (Jy)
G	Gain factor
G_{AD}	Analogue to Digital conversion factor
G_c	Flux conversion factor (Jy s/μV)
G_f	Flat-field gain
G_p	Photometric gain factor
G_{pre}	Pre-amplifier gain
G_r	Gain factor due to RSRF
$H(t)$	Unit step function at t=0
L_{AOT}	Number of scan steps per band
L_F	Number of scan steps per FWHM of spectral resolution
L_s	Step size in scanner steps
λ	Wavelength
Λ	Decay time in the FS transient model
mas	Milliarcseconds
n	Fabry-Pérot order
n_i	Number of integrations
n_{int}	Number of samples taken from a single spectral resolution element
n_{scan}	Number of scans
n_{step}	Number of steps
N	Grating or FP order
N_D	Dark current noise
O	Offset
p	Glitch height
R	Spectral Resolution
S	Signal Strength (μV/s)
S_d	Signal in the dark current
σ	Standard deviation
t	time (sec)
t_r	Detector reset interval (sec)
τ	AC time constant
V	(Modeled) readouts
Z	Zero level function in FS model

Appendix E

Connections and Snapshots

E.1 Connections

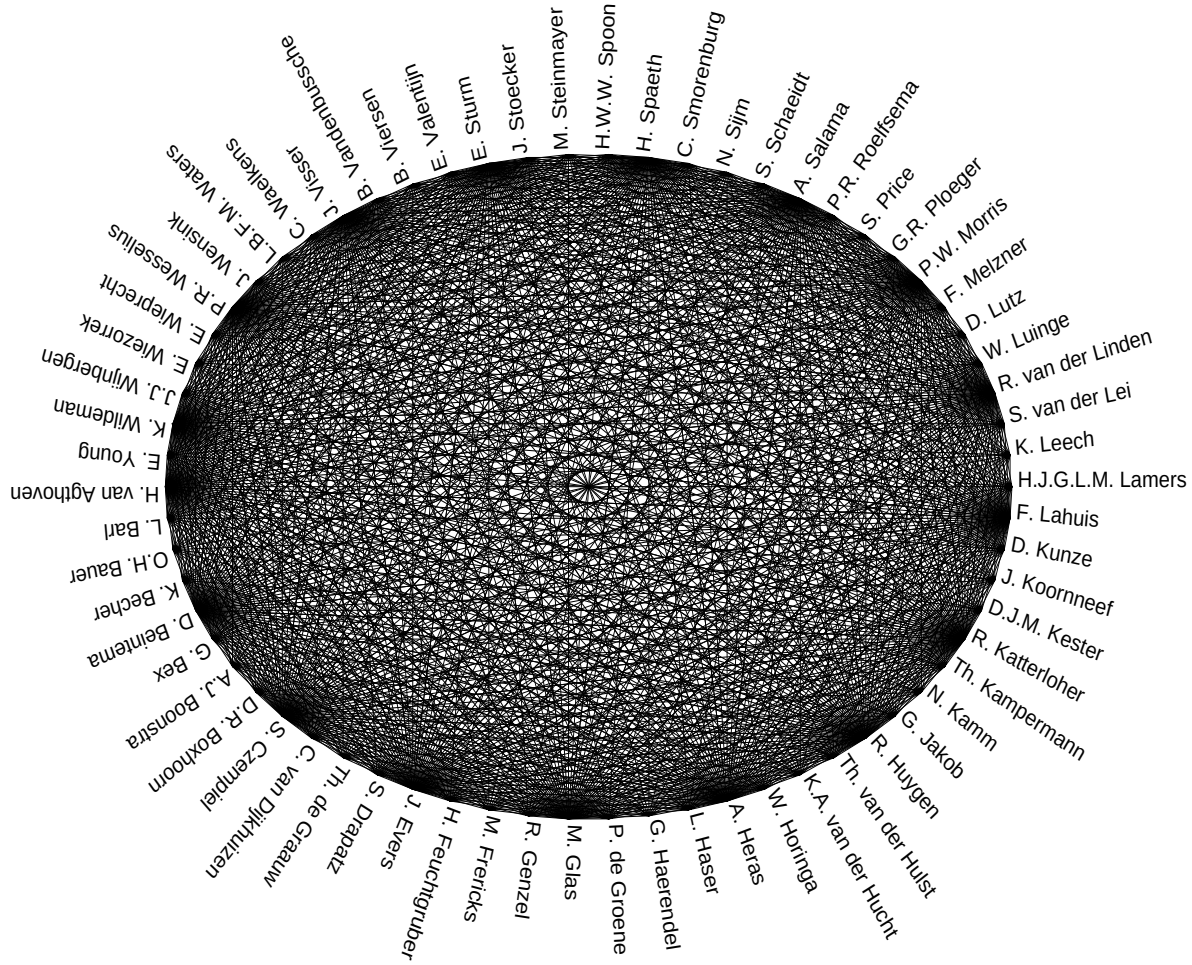

Figure E.1: *This diagram, showing the connections between the SWS team members, was derived by H. Feuchtgruber from an earlier work.*

E.2 A Snapshot in Time 1

Figure E.2: *A snapshot of the SWS Instrument Dedicated Team (SIDT) and Instrument Support Team (SIST), taken soon after the launch of ISO at the ESA VILSPA, Spain, ground station. From left to right: H. Spoon, E.A. Valentijn, D.A. Beintema, R. Huygen, N. Sijm, D.R. Boxhoorn, D. Levine (NASA liaison with ISO), A.M. Heras, O.H. Bauer, H. Feuchtgruber, P.R. Roelfsema, A. Salama, B. Vandenbussche, S.G. Schaeidt & K. Leech. Not all team members were present for this photo.*

E.3 A Snapshot in Time 2

Figure E.3: *A snapshot of the SWS Team during the final SPOPS meeting in September 2001. From left to right: top row – B. Vandenbussche, E. Wiezorrek; middle row – I. Yamamura, H. Feuchtgruber, O.H. Bauer, E. Stürm, R. Shipman, Jeroen Valk (Boat Captain), P.R. Roelfsema, T. de Graauw (PI); bottom row – D. Kester, R. Huygen, F. Lahuis, A. Heras, Karlieke de Jong (ship mate), A. Salama, D. Lutz, D.A. Beintema, A. Verma & E. Wieprecht. Not all team members were present for this photo.*

Bibliography

[1] Beintema D.A. & Kunze D. 1996 *SWS AOT design description*, SWS Internal Report issued 24 June 1996 (see SWS documentation under: `http://www.iso.vilspa.esa.es`)

[2] Cohen M., Walker R.G., Barlow M.J. & Deacon J.R. 1992a, *Spectral irradiance calibration in the infrared. I - Ground-based and IRAS broadband calibrations*, AJ 104, 1650

[3] Cohen M., Walker R.G. & Witteborn F.C. 1992b, *Spectral irradiance calibration in the infrared. II - α Tau and the recalibration of the IRAS low resolution spectrometer*, AJ 104, 2030

[4] Decin L. 2000, *Ph.D. Thesis*, Katholieke Universiteit Leuven, Belgium

[5] Decin L., Waelkens C., Eriksson K., Gustaffson B., Plez B., Sauval A.J., van Assche W. & Vandenbussche B. 2000, *ISO impact on stellar models and viceversa*, in 'ISO Beyond the Peaks: The 2nd ISO Workshop on Analytical Spectroscopy'. Eds. A. Salama, M.F. Kessler, K. Leech & B. Schulz, ESA-SP 456, 289

[6] Feuchtgruber H. 1998a, *Status of SWS Fabry-Pérot wavelength calibration and instrumental profile*, IDC Internal Report issued 5 May 1998 (see SWS documentation under `http:www.iso.vilspa.esa.es`)

[7] Feuchtgruber H. 1998b, *Status of study of AOT02 line profiles and fluxes on NGC6543*, IDC Internal Report issued 2 June 1998 (see SWS documentation under `http://www.iso.vilspa.esa.es`)

[8] Feuchtgruber H. 1998c, *Status of study on Gam-Dra fluxes and related pointing errors*, IDC internal Report issued 10 June 1998 (see SWS documentation under `http://www.iso.vilspa.esa.es`)

[9] Feuchtgruber H. 2001, *The ground-based calibration of SWS*, in 'The Calibration Legacy of the ISO Mission'. Eds. L. Metcalfe & M.F. Kessler, ESA-SP 481 (in press).

[10] Fouks B.I. & Schubert J. 1995, *Precise theoretical description of photoresponse for detectors of ISOPHOT's Si:Ga array*, SPIE 2475, 487

[11] García-Lario P., Coulais A., Kester D. & Caux E. 2001, *Transients Working Group Final Report*, IDC Report, SAI/2000-057/Dc, Version 0.7

[12] Gustafsson B., Bell R.A., Eriksson K. & Nordlund A. 1975, *A grid of model atmospheres for metal-deficient giant stars. I*, A&A 42, 407

[13] Heras A.M. 1997, *Single detector signal jumps*, IDC Internal Report issued 9 June 1997 (see SWS documentation under `http://www.iso.vilspa.esa.es`)

[14] Heras A.M. 1998, *The effects of the pointing jitter on SWS observations*, IDC Internal Report issued 6 August 1998 (see SWS documentation under `http://www.iso.vilspa.esa.es`)

[15] Heras A.M., Wieprecht E., Feuchtgruber H. et al. 2000, *The ISO-SWS detectors: Performance trends and space radiation effects*, ExA 10, 177

[16] *ISO Launch and Early Orbit Phase & Satellite Commissioning Phase Report*, D/TOS-ISO-LEOP/SCP/JF, Issue 1, 31 October 1997.

[17] Kessler M.F., Müller T.G., Leech K. et al. 2002 *The ISO Handbook: Volume I, ISO – Mission & Satellite Overview*, ESA SP-1262, SAI/2000-035/Dc, Version 2.0

[18] Kester D., Beintema D.A. & Valentijn E. 1998, *End-of-Mission Report: Wavelength Calibration Status*, SWS Internal Report issued 2 July 1998 (see SWS documentation under `http://www.iso.vilspa.esa.es`)

[19] Kester D. 1999, *Straight lines*, in 'Maximum Entropy and Bayesian Methods'. Eds. W. van der Linden et al. (Kluwer Acad. Pub.) p. 179

[20] Kester D. 2000, *Improving the SWS spectrum of Titan. Correcting for the reset pulse aftermath*, in 'ISO Beyond the Peaks: The 2nd ISO Workshop on Analytical Spectroscopy'. Eds. A. Salama, M.F. Kessler, K. Leech & B. Schulz, ESA-SP 456, 275

[21] Kester D., Beintema D.A. & Lutz D. 2001, *SWS fringes and models*, in 'The Calibration Legacy of the ISO Mission'. Eds. L. Metcalfe & M.F. Kessler, ESA SP-481 (in press)

[22] Kester D. 2001, *Memory effects and their correction in SWS SI:GA detectors*, in 'The Calibration Legacy of the ISO Mission'. Eds. L. Metcalfe & M.F. Kessler, ESA SP-481 (in press)

[23] Lahuis F. 1998, *Pulse shape correction*, SWS Internal Report issued 11 March 1998 (see SWS documentation under `http://www.iso.vilspa.esa.es`)

[24] Lahuis F., Kester D. & Shipman R. 2001, *Deglitching of SWS low resolution data*, in 'The Calibration Legacy of the ISO Mission'. Eds. L. Metcalfe & M.F. Kessler, ESA SP-481 (in press)

[25] Lahuis F., Feuchtgruber H., Golstein H., Kester D., Luinge W. & Wieprecht E. 2001, *SWS Signal capture: from flux to signal*, in 'The calibration Legacy of the ISO Mission'. Eds. L. Metcalfe & M.F. Kessler, ESA SP-481 (in press)

[26] Leech K.J. & Heras A.M. 1997, *Effects seen in data induced by incorrect target coordinates or crowded fields*, IDC Internal Report issued 12 June 1997 (see SWS documentation under `http://www.iso.vilspa.esa.es`)

[27] Leech K.J. & Morris P. 1997, *Possible detector memory effects in SWS grating range spectra (AOT 6) due to SWS reference scans*, IDC Internal Report issued 27 May 1997 (see SWS documentation under `http://www.iso.vilspa.esa.es`)

[28] Lorente R. 1998, *Spectral resolution of SWS AOT 1*, IDC Internal Report issued 30 September 1998 (see SWS documentation under `http://www.iso.vilspa.esa.es`)

[29] Lutz D., Feuchtgruber H. & Morfill J. 2000, *ISO-SWS grating resolution and instrumental profile as measured by the full resolution modes SWS02 and SWS06*, SWS Internal Report issued 18 February 2000 (see SWS documentation under `http://www.iso.vilspa.esa.es`)

[30] Morris P. 1999, *SWS photometric calibrations at End of Mission. I.*, IDC Internal Report issued 15 January 1999 (see SWS documentation under `http://www.iso.vilspa.esa.es`)

[31] Plez B., Brett J.M., & Nordlund A. 1992, *Spherical opacity sampling model atmospheres for M-giants. I - Techniques, data and discussion*, A&A 256, 551.

[32] Salama A. 1998, *SWS beam profiles and ISO pointing*, SWS Internal Report issued 9 September 1998 (see SWS documentation under `http://www.iso.vilspa.esa.es`)

[33] Salama A., Beintema D.A., Lloyd C. et al. 2001, *Beam Profile and Pointing Working Group Final Report*, IDC Report, SAI/2001-027/Dc, Version 1.0

[34] Saxton R.D. 2000, *ISO Data Products Document (IDPD)*, SAI/94-1266/Dc, Issue 12

[35] Shipman R.F., Morris P., Beintema D.A. et al. 2001, it SWS in-flight calibration, in 'The Calibration Legacy of the ISO Mission'. Eds. L. Metcalfe & M.F. Kessler, ESA SP-481 (in press)

[36] Späth H. 1995, *One dimensional spline interpolation algorithms* (A.K. Peters, Ltd, Wellesley, USA) ISBN: 1-56881-016-4

[37] Valentijn E., Feuchtgruber H., Kester D. et al. 1996, *The wavelength calibration and resolution of the Short Wavelength Spectrometer*, A&A 315, L60

[38] Valentijn E. & Thi W.F. 2000, *ISO's Short Wavelength Spectrometer - Ultimate sensitivity. Reducing the effects of cosmic weather*, ExA 10, 215.

[39] Vandenbussche B. 1998, *The SWS Z-beam-profile for SSO tracking correction*, SWS Internal Report issued 11 June 1998 (see SWS documentation under `http://www.iso.vilspa.esa.es`)

[40] Vandenbussche B. 1999, *The ISO-SWS Relative Spectral Response Calibration*, SWS Internal Report issued 29 October 1999 (see SWS documentation under `http://www.iso.vilspa.esa.es`)

[41] Vandenbussche B., Morris P., Valentijn E. et al. 2001, *The relative spectral response calibration of the ISO-SWS*, in 'The Calibration Legacy of the ISO Mission'. Eds. L. Metcalfe & M.F. Kessler, ESA SP-481 (in press)

[42] van Malderen R. et al. 2002, *Modeling band 3 of the ISO-SWS calibration sources* (to be published in A&A)

[43] Wieprecht E., Wiezorrek E. & Haser L. 2000, *SWS-detector glitch effect correction*, ExA 10, 199

Index